Zirconia Toughened Alumina Femoral Head and Acetabular Socket: Process optimization, Designing, Fabrication and Properties

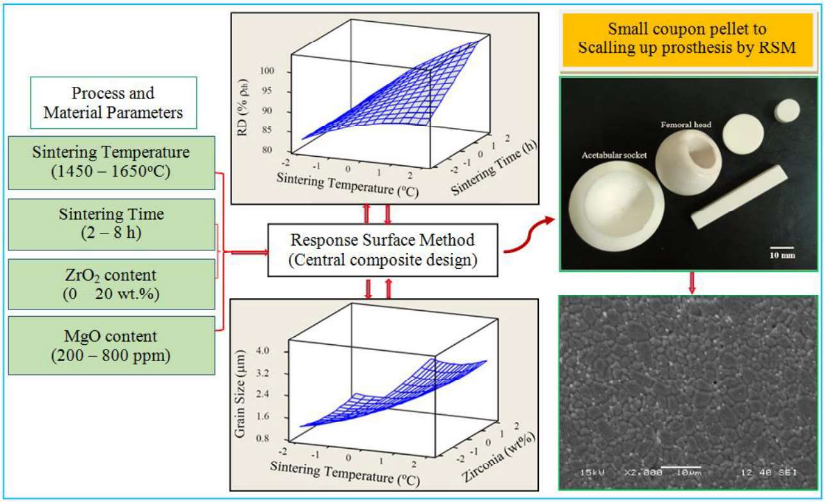

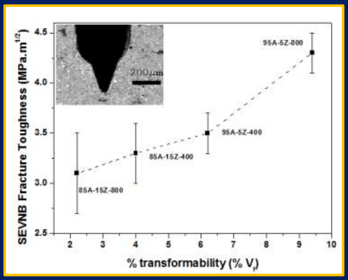

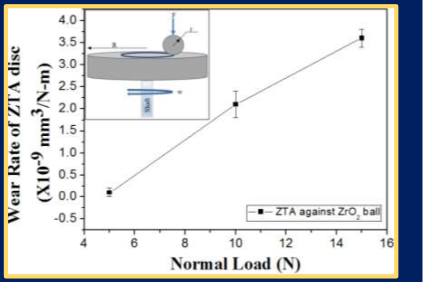

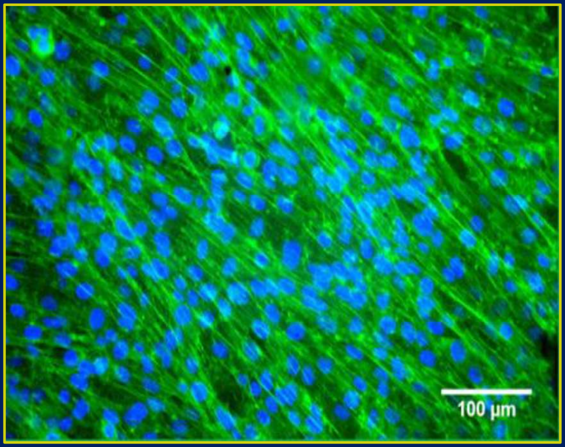

BHIMAVARAPU SAMBI REDDY

Department of Ceramic Engineering

National Institute of Technology Rourkela

Zirconia Toughened Alumina Femoral Head and Acetabular Socket: Process optimization, Designing, Fabrication and Properties

A THESIS SUBMITTED IN PARTIAL FULFILMENT
OF THE REQUIREMENT FOR THE DEGREE OF

Doctor of Philosophy
in
Ceramic Engineering

By

Bhimavarapu Sambi Reddy
(512CR109)
Under the Supervision of

Dr. Debasish Sarkar
Associate Professor, Department of Ceramic Engineering
National Institute of Technology, Rourkela, India

and

Dr. Bikramjit Basu
Professor, Materials Research Center,
Associate Faculty, Center for BioSystems Science and Engineering,
Indian Institute of Science, Bangalore

Department of Ceramic Engineering
National Institute of Technology
Rourkela

April 2016

To my wife

Sangeetha

Declaration of Originality

I, Bhimavarapu Sambi Reddy, Roll Number *512CR109* hereby declare that this dissertation entitled "Zirconia toughened Alumina based Femoral Head and Acetabular Socket: Process Optimization, Designing, Fabrication and Properties" represents my original work carried out as a doctoral student of NIT Rourkela and, to the best of my knowledge, it contains no material previously published or written by another person, nor any material presented for the award of any other degree or diploma of NIT Rourkela or any other institution. Any contribution made to this research by others, with whom I have worked at NIT Rourkela or elsewhere, is explicitly acknowledged in the dissertation. Works of other authors cited in this dissertation have been duly acknowledged under the section "Bibliography". I have also submitted my original research records to the scrutiny committee for evaluation of my dissertation. I am fully aware that in case of any non-compliance detected in future, the Senate of NIT Rourkela may withdraw the degree awarded to me on the basis of the present dissertation.

NIT Rourkela

Bhimavarapu Sambi Reddy

Acknowledgment

I wish to express my deep sense of gratitude and indebtedness to Prof. Debasish Sarkar, Department of Ceramic Engineering, N.I.T Rourkela and Prof. Bikramjit Basu, Material Research Center, IISc Bangalore, for assigning me the project "Zirconia toughened Alumina based Femoral Head and Acetabular Socket: Process Optimization, Designing, Fabrication and Properties" and for their inspiring guidance, constructive criticism and valuable suggestion throughout this research work.

I express my sincere thanks to Prof. Bibhuti Bhusan Nayak, Head, Department of Ceramic Engineering for providing me all the departmental facilities required for the completion of the thesis. I am also thankful to all other faculty members of Ceramic Engineering Department, N.I.T. Rourkela for their constructive suggestions and encouragement at various stages of the work.

I am thankful to Mechanical Engineering Department, Industrial Design Department, Metallurgical & Materials Engineering Department, N.I.T. Rourkela for facilitate to conduct various characterizations. I am thankful to Department of Materials Research Center, IISc Bangalore for permitting me to carry out biological test and other mechanical characterizations.

I am thankful to Prof. M. Ravi Sankar, Department of Mechanical Engineering Department, IIT Guwahati for providing acetabular socket polishing facilities.

I am also thankful to Director, N.I.T. Rourkela, for providing the Ph.D. opportunity in Ceramic Engineering Department.

I would like to acknowledge the financial support provided by Department of Biotechnology, Government of India under 'Centres of Excellence and Innovation in Biotechnology' scheme through the center of excellence project - Translational Center on Biomaterials for Orthopedic and Dental Applications.

I am also thankful to Ms. Sangeetha, Mr. Raju Mula, Mr. Sarat Chandra, and all the research scholars in the Department of Ceramic Engineering for their kind help and providing all joyful environments throughout this work.

NIT Rourkela
Bhimavarapu Sambi Reddy
512CR109

Abstract

Despite several decades of research for new materials for articulating joints in orthopedic applications, the efforts to develop patient-specific prototype of such biomaterial devices are rather limited. While addressing this aspect, the present work demonstrates an integrated manufacturing approach how to fabricate zirconia toughened alumina femoral head and acetabular socket initiation with composition and process optimization, and designing of prototypes. The properties and performance of a such ceramic components significantly depend on the microstructue (grain size) and sinter density, it is therefore important to optimize both the process parameters (sintering temperature, sintering time) and material parameters (sinter–aid addition and reinforcement content) to obtain tough and strong materials. Based on considering the fundamental densification-grain size relationship and using the predictive linear, quadratic or interactive response among the process and material parameters, the adopted response surface methodology (RSM) approach is shown to provide excellent capability to predict sinter density and grain size with significant statistical correlation between experimental and predicted values. Summarising, the optimization study establishes that sintering of 5 wt.% zirconia toughened alumina sintered with 800 ppm MgO sinter-aid at 1600^{o}C for 6h can exhibit a great combination of relative density, compressive strength (1100 MPa), tensile strength (200 MPa) and SEVNB fracture toughness (4.3 MP m$^{1/2}$). In order to assess the cytocompatibility properties, C2C12 mouse myoblast cells were grown on the ZTA composite having the best combination of mechanical properties. The results of MTT assay reveal an increase in the number of mitochondrially active cells with time in culture for a period of up to 3 days. The fluorescence microscopic observations also confirmed good cell attachment and cell-to-cell contact with cellular bridge formation. In view of the importance of the wear resistance properties in the performance and durability of prototypes in total hip joint replacement application, the unlubricated sliding wear experiments with commercial cubic zirconia, and stainless steel counterbody reveal that a combination of steady state COF of 0.5 and 0.42 and wear rate of 10^{-9} mm^3/N m observed for the optimized ZTA composite with having the best combination of mechanical properties. The wear mechanism is dominated by abrasive wear and cracking induced delamination of tribolayer. In commensurate with the computer aided-design (CAD) of prototypes after optimization of process and properties of ZTA, the custom made modular steel-die mould assembly was fabricated to produce high strength green powder compact of Al_2O_3-5 wt% ZrO_2 (3 mol %Y_2O_3)-800 ppm MgO without any geometric distortion at uniaxial pressure of 18 - 22 ton. In line with design consideration, green compact of the femoral head / acetabular socket was presintered at 1200^{o}C in air for 2h in a conventional sintering furnace and subsequently computer numerical control (CNC) machined to a limited extent. The final stage of prototype development involved the multi-step sintering of the compact at 1600^{o}C for 6h in air, followed by polishing using tailor made arrangement. The process quality was closely monitored by measuring dimensional changes at each manufacturing stage as well as the circularity measurement of final polished prototype. The microstructure as well as the physical properties in terms of hardness, indentation toughness, and burst strength is also reported. Taken together the present manufacturing approach appears to be a scalable and commercially viable fabrication strategy to make bioceramics based femoral head and acetabular socket biomedical devices.

Keywords: Zirconia Toughened Alumina, Femoral Head, Acetabular Socket, Response Surface Method, Rapid Prototype.

Contents

List of Figures

List of Tables

Page No.

Chapter -1

Introduction

This chapter introduces the clinical aspects as well as various orthopedic biomaterials for total hip joint replacement applications. An emphasis is placed on the development of new bioceramics for the femoral ball head and acetabular socket. The existing challenges are highlighted, and the objectives are stated towards the end of this chapter together with the structure/scope of this dissertation.

1.1 Background of Total Hip Replacement (THR) Materials

The hip joint is one of the most important flexible articulating joints, which allow us to get a wide range of motions, and also experience compressive stress in static/dynamic conditions. From an engineering perspective, the functioning of this joint can be better described as the whole 'ball-bearing' mechanism and typically, a hip-joint bears body force of the strong hip and leg muscles. The round concave acetabulum cup and round convex femoral head project the socket and bearing arrangement for total hip replacement (THR) that impart compressive stress around the articulating contact in the range of 3 – 10 MPa during walking, stair climbing, and sitting.[1,2]

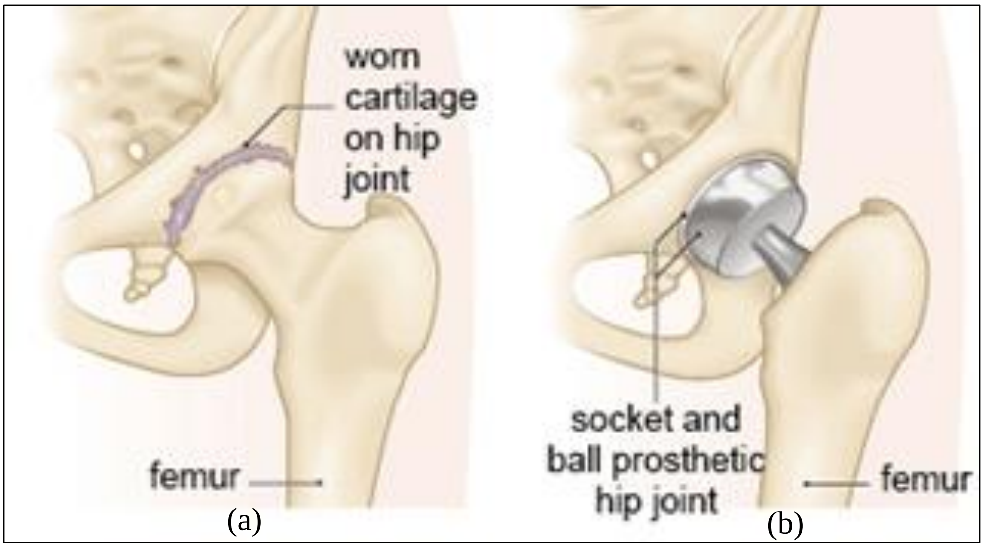

Fig. 1.1: HIP with arthritis (a) and with a replaced joint implant (b).[3]

Typically, the THR surface is smooth and coated with cartilage under normal health conditions. Arthritis, injury, dislocation or irregular activity causes about wear and tear of the surrounding cartilage inside a hip joint and hence, causes pain to patients. This additional debris leads to friction between the bones as they rub against each other, and the hip joint becomes severely damaged in this process. This unexpected damage demands the replacement of THR by a synthetic biomedical device assembly in a diseased patient.[4] Such assembly contains acetabular socket with a conforming femoral head and a long stem, whose neck is closely fitted into the inner cavity of the femoral head (see Fig. 1.1). Typically, individual component of a THR assembly is fabricated separately and then assembled to obtain the entire device.[5] The demand for durable femoral head and the acetabular socket has been the driving for new material development. With the increasing life expectancy in many of the developing nations around the world, the demand for hip replacement surgery is on a rise. For example, 3,00,000 patients undergo primary or revision arthroplasty in a year in India and around 1,00,000 patients undergo knee surgery.[6] While new materials in specific ceramic composites with better properties are widely researched in the materials community, the attempts to make prototypes are rather limited. These prototypes are generally made of the combination of metal, polymer, ceramics and composites. In recent times, several attempts have been concentrated to optimize the materials in order to develop a sustainable and life time performance of articulating surfaces. Herein, the brief about probable materials and dimensions of THR are discussed;

1.1.1 Metal-on-Metal Hip Prosthesis

Metal on metal in specific medical graded stainless steel 316L (SS316L) implants are durable and popular for younger patients because of outstanding mechanical, corrosion resistance, and biocompatibility properties.[7] However, this class of prosthesis is very poor in tribological properties that lead to the high friction stress on articulating surface and forms wear debris. In the long run, stainless steel is subjected to pitting corrosion and releasing the Cr and Ni ions which induce the cell toxicity in the human body, i.e. metallosis.[8] Furthermore, the next generation hip joints are also prepared with cobalt-chromium alloys (Co-Cr alloys) to replace the stainless steel. Co-Cr alloys have preferentially high wear resistance due to surface hardness, as well as chromium oxide act as a self-replenishing agent in body fluids.[9] Past-Co–Cr alloy femoral components experience severe wear and thus scratches on the surface because of third body abrasion and releasing the debris.[10] The next generation lightweight, high corrosion resistance and biocompatible implants (Ti and their alloys) are preferred choice for orthopedic load bearing bioimplant.[11] It is worthwhile to mention that the Ti has analogous stress shielding effect to bone, but the presence of TiO_2 on Ti surface reduces the bioactive interaction in a physiological environment.[12]

A major concern in metal-on-metal bearings is the probability of metal ions release in comparison to the other combinations of THR. Such metal ions are carried to a filtered location in the body, and thus found in urine and serum from the patients. Load bearing and performance efficacy of THR is preferred to increase through restricting both the metal ion release rate and abrasion wear and hence the different combination of materials are considered in the perspective of biomaterials research and surgery.

1.1.2 Hybrid Hip Prosthesis

The hybrid hip prosthesis is the combination of metal, polymer, and ceramic materials in order to achieve minimum friction, potential load bearing efficiency and uncompromised biocompatibility properties. The hybrid hip prosthesis can be classified as metal on polyethylene, ceramic on polyethylene, ceramic on the metal prosthesis, etc. In an example, the UHMWPE liner in Ti alloy acetabular socket, CoCr femoral head and Ti6Al4V alloy femoral stem are used for THR bioimplants. Such hip implantations, in general, are preferred for less active patients and older in their 70s so that it can stop the pelvic bone loss.[13]

Recently, an attractive combination like ceramic on polyethylene has been introduced to minimize the metal ion release and formation of debris particles. Also, oxide ceramic (alumina, zirconia, or ZTA) has high wear resistance properties that minimize the osteolysis. Also, ceramics can withstand high compressive stress strength and poor in fracture toughness.[14] The prime concern in such combined joint is that polyethylene (PE) wear debris causes periprosthetic osteolysis and aseptic loosening, which leads to implant ultimately failure. [15] Polytetrafluoroethylene (PTFE) and Ultra-high molecular weight polyethylene (UHMWPE) are hydrophobic in nature along with chemical stability and low coefficient of friction. However, in the long run, the polymers delivering the high wear debris causes for tissue reaction and granuloma formation. Such a phenomenon occurred due to low resistance in compressive strength and stiffness that leads the debris formation under bearing action.[16] In view of the above, the research on UHMWPE reinforced with carbon fiber, graphene oxide, PMMA, hydroxyapatite, Al_2O_3, ZrO_2, and SiC are under progress to simulate the best properties *in vivo*.[17,18,19]

1.1.3 Ceramic-on-Ceramic Hip Prosthesis

The ceramic hip prosthesis is generally prepared with alumina, zirconia, or ZTA composite materials because they show high hardness, scratch resistance, and bioinert wear debris compared to polyethylene and metal counterpart. This class of hip prosthesis was introduced to minimize the foreign element contamination and to overcome the wear debris related problems, which are reported for other biomaterials. In view of this, the bioceramic composites are hydrophilic in nature, which improves the lubrication effect, reduce the frictional coefficient, and abrasion wear rate. The alumina femoral head and socket linear are known for their durability and reliability when US FDA approved in early 1980. However, they are not popular because of low fracture toughness and high failure rate.

The performance of pure ZrO_2 ceramics for an orthopaedic prosthesis is confusing and controversial because of unexpected phase transformation after 8 to 13 years of implantation thus, need revision surgery. This phase transformation is attributed to dopant ion release *in vivo* and acceleration of monoclinic phase clusters around the surface that initiates early fracture and failure. The recent literature published by pioneer orthopaedic implant manufacturers has also emphasized that several researchers and clinicians found higher rates of osteolysis with zirconia – UHMWPE couple.[20]

In early 2000, first ZTA composite was designated as BIOLOX and was developed by Ceram Tec AG, USA.[21] This ZTA composite (BIOLOX) is primarily composed of ~25% yttria stabilized tetragonal polycrystalline zirconia and ~75% alumina. The improved strength and toughness of ZTA composite are attributed to the stress-induced transformation-toughening mechanism, caused by finely dispersed zirconia particles in the alumina matrix.[22] The phase transformation mechanism contributes to improve the fracture toughness of zirconia and zirconia composites. Martensitic phase transformation of tetragonal zirconia around the crack tip, restrict the crack propagation that further require more energy to propagate into the transformed compressive layer. Moreover, this room temperature tetragonal to monoclinic phase transformation associate with 3-5% volume expansion and 7% shear strain that induced microcrack toughening mechanism. Thus, incorporation of zirconia in alumina matrix bearings is an excellent choice for young and active patients that are capable to withstand high compressive strength and wear resistance.[23] Although ceramic hip prosthesis is introduced and is popular for wear resistance, these may produce squeaking noise and shattering because of faulty design and improper articulate interaction, inadequate mechanical response, and low quality surface finish.

1.2 Geometrical features of Femoral Head – Acetabular Socket

Design and geometrical feature of the spherical femoral ball head are characterised by the 3/4th truncated concave surface and the circular tapered blind hole that experience compressive load through the pelvis and femoral shaft, respectively. An articulating surface conformity depends on the contact mode within the concave femoral head and semi-spherical convex acetabular socket, whereas a tapered femoral stem is accommodated in the femoral head blind hole to complete the THR. In the present market, both cementless and cemented acetabular sockets are being used. The probability of failure of screw loosening is common for the cementless socket, whereas the polymethyl methacrylate (PMMA) cement joined socket provides better post-surgery performance. Thus, the proper dimension of the articulating femoral head and acetabular socket impart the expected performance after surgery. Thus, several schools and manufacturers developed different design and dimension to fulfil the post-surgery competency of the prosthesis.[24,25,26,27,28] The available geometrical features and materials are listed in Table 1.1. Under this circumstance, an effective design and dimension have been considered to develop a representative the ball - and - socket joint prosthesis in the current state-of-art and their details are described in Figure 1.2 and 1.3.

Table 1.1: Dimension and material of commercial femoral head and acetabular socket

Manufacturer	Size of femoral head (mm)	Material	Size of acetabular cup (OD/ID) (mm/mm)	Material	Ref.
Beijing AKEC Medical Co., Ltd.	22, 28, 32, 36	Co-Cr-Mo alloy	42/34, 44/36, 46/38, 64/54	Ti Alloy Co-Cr-Mo UHMWPE*	29
Ceram Tec (Biolox)	28, 32, 36	ZTA	36/28, 38/30, 54/40	ZTA, XPE, Ceramic	30
Sharma Pharmaceutical (India) Pvt Ltd	28, 32	SS-316 and Co-Cr	48/28, 50/28, 52/32, 54/32	UHMWPE & Stainless Steel	31
Medacta International, Switzerland	22, 28, 32, 36, 40	Co-Cr ZTA	46/38, 64/56	N_2 treated SS-316L cup	32
Smith-Nephew, USA	22,26, 28,32, 36	OXINIUM**, CoCr, Biolox Forte, Biolox Delta	40/22, 61/22 52/36, 64/36 increment 3 mm	XLPE***, Ceramic	33

UHMWPE*- Ultra high molecular weight polyethylene; OXINIUM**oxidized zirconium; XLPE***- Cross-linked polyethylene;

Fig. 1.2 shows the projected cylindrical borehole femoral head with geometrical features namely, femoral head diameter, truncated femoral head height, cylindrical taper borehole length, open-end borehole, and blind end borehole diameter, and fillet radius at blind end borehole. In a real sense, the femoral head is globular in structure, which has perfect three forth geometry of the sphere. The artificial bioimplant mimics the natural femoral head that can retrieve the function of the partially or fully damaged joint. In a similar fashion, Fig. 1.3 demonstrates the orthographic and prospective view of the artificial acetabular cup which has an articulating concave surface, outer convex surface, the height of the hemisphere and thickness. In consideration of design and fitting aspects, the following dimensions have been considered to develop the prototypes;

Table 1.2 Typical dimensions of femoral head and acetabular socket

Femoral Head	**Acetabular Socket**
Outer diameter – 26mm	Outer Diameter – 37mm
Truncated femoral head height – 22.25mm	Inner diameter – 26.5mm
Tapered cylindrical borehole length – 15mm	Height – 18.5mm
Open-end borehole diameter – 12 mm	Thickness – 5.25mm
Blind end borehole diameter – 10 mm	
End fillet of bore – 2mm	

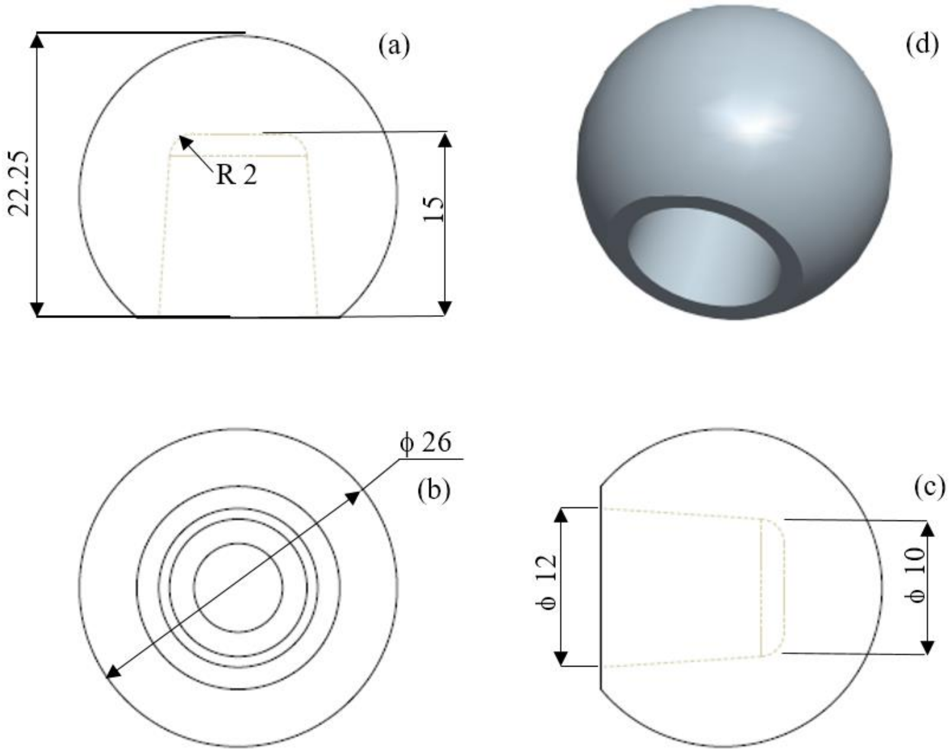

Fig. 1.2 Projected orthographic view (a) top view (b) front view (c) side view and (d) isometric view of the selected femoral head

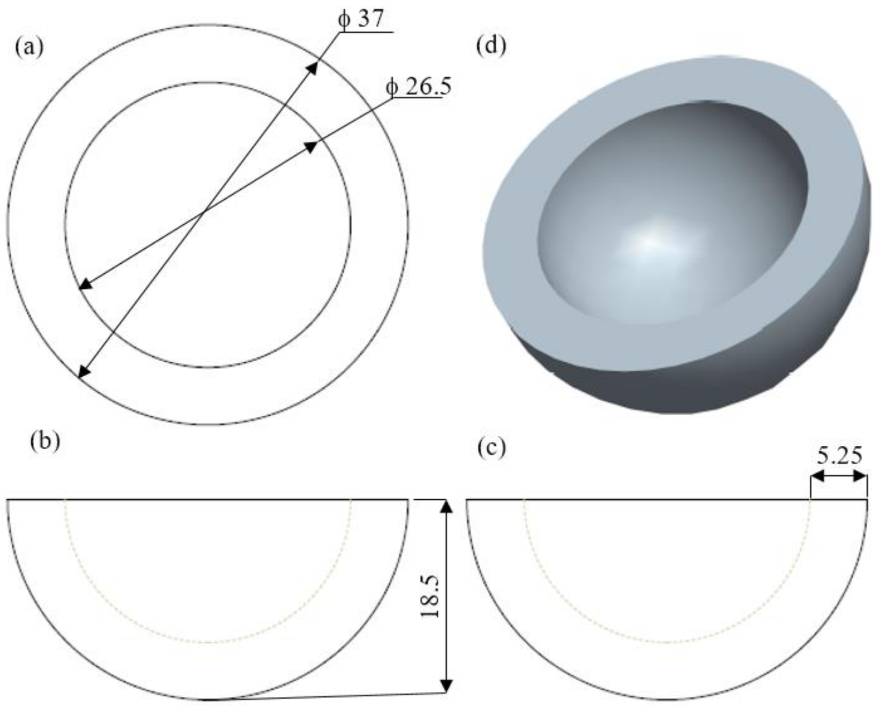

Fig. 1.3 Projected orthographic view (a) top view (b) front view (c) side view and (d) isometric view of the selected acetabular socket

Fig. 1.4 illustrates the exploded (Fig. 1.4 a) and assembled (Fig. 1.4 b) view of the hip joint prosthesis and consists of femoral stem, femoral head, and the acetabular cup. The convex outer surface of truncated femoral head is preferred to conform in the concave socket and maintain smooth relative motion with the acetabular surface. Other side of the femoral head has cylindrical taper borehole on the truncated side which permits to build contact either with the neck of the femoral stem. All the relevant male and female part maintain same Morse taper which is helpful to fix and removal of the components each other in the surgical environment.

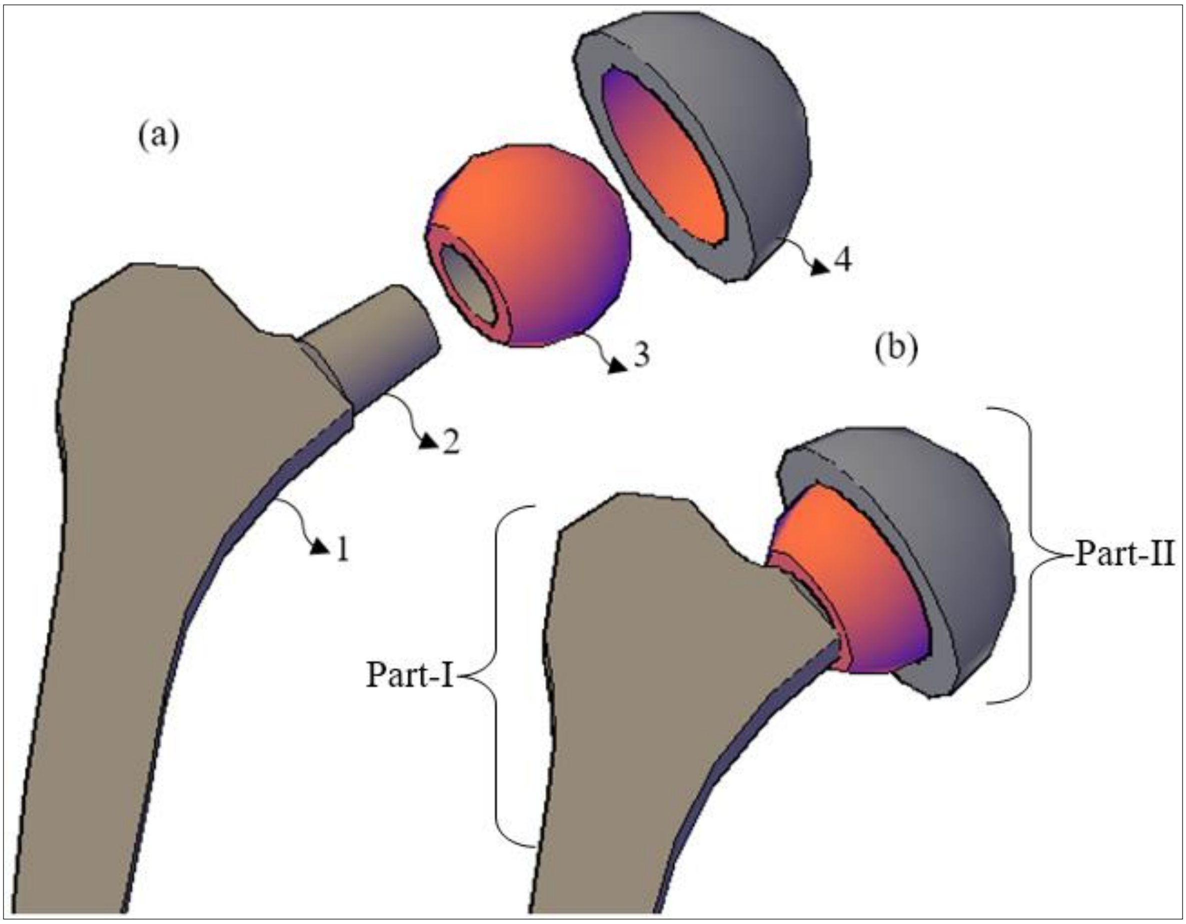

Fig. 1.4 Exploded view of Total Hip Prosthesis (THR) including (1) femoral stems (2) femoral stem neck (3) femoral head (4) acetabular cup (a) and assembly of THR (b)

The interference fit of femoral head and stem act as a single unit which restricts the translation motion between the parts of the system. Such an entire assembly receives the acetabular cup that allows the rotational motion within part-I and part-II (see Fig. 1.4).

1.3 Objectives

The major objective of this thesis is to optimize the ceramic composition, sintering parameters, mechanical and biocompatibility property of zirconia-toughened alumina based femoral head and acetabular socket for orthopedic applications. Some specific objectives include,

i. To optimize the composition and sintering parameters in order to achieve high relative density and optimum grain size of zirconia toughened alumina (ZTA) composites.

ii. To study the different mechanical responses (hardness, compression, tensile strength), including fracture resistance using SEVNB technique.

iii. To assess Cytocompatibility property of sintered ZTA composites with C2C12 mouse myoblast muscle cells.

iv. To evaluate the friction and wear behavior of optimized ZTA against zirconia as well as steel and correlate the observed wear mechanism with the established theory.

v. To develop a representative 26mm (OD) ZTA femoral ball head from optimized composition through uniaxial pressing, presintering, machining, sintering, and polishing as well as to assess critical properties including dimension stability and burst strength.

vi. To fabricate a representative 26.5mm (ID) ZTA acetabular cup by an integrated manufacturing approach and assess their properties.

1.4 Scope of the Thesis

In order to fulfill the aforesaid objective, the entire scope of the dissertation has been elaborated in seven chapters (see Fig. 1.5). **Chapter–1** presents a brief background on the basic and technical importance of this research. **Chapter–2** deals with the detailed literature review on the following aspect, (a) process and composition optimization, b) mechanical and biological behaviour, c) tribological behaviour of different ceramic-ceramic interaction and d) different existence fabrication methods for the both femoral head and acetabular socket. **Chapter–3** describes the detail composition and sintering parameters optimization by response surface method (RSM) to achieve high relative density and optimum grain size of ZTA. In view of the demonstrated robustness, the adopted analytical approach can be extened to other ceramic systems. **Chapter–4** illustrates the mechanical responses including SEVNB fracture resistance, hardness, compressive strength, and cytocompatibility *in vitro*, thus establishing a favourable choice for biomedical applications. **Chapter–5** discusses the tribological behaviour of optimized ZTA against zirconia and steel at various loads and time. The combination of tribological properties suggests that the investigated ZTA can be used for load bearing articulating joints, particularly against ceramic like ZrO_2 mating surface. **Chapter-6** presents the integrated manufacturing approach is for the design and fabrication of bioceramics based femoral ball head and acetabular socket for total hip joint replacement. Various surface and bulk properties of the prototype are also discussed. **Chapter-7** contains the concluding remarks and the scope of future work.

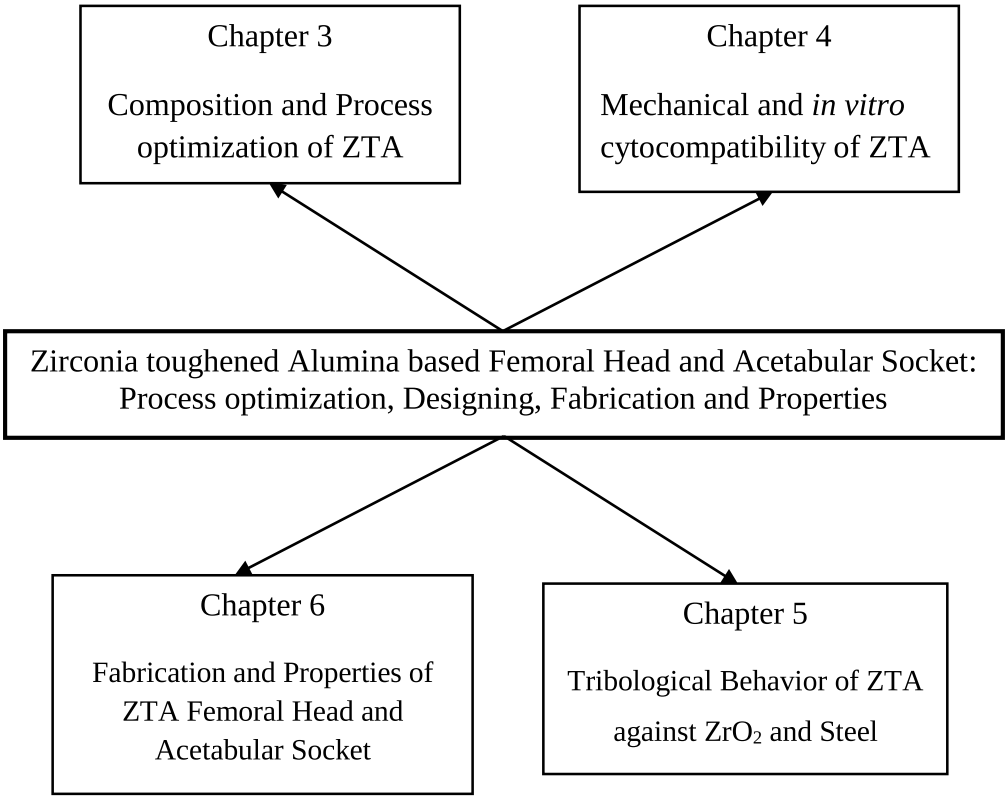

Fig. 1.5 Bird's eye view of the present dissertation

1.5 Reference

---

[1] H. Yoshida, A. Faust, J. Wilckens, M. Kitagawa, J. Fetto, and Edmund Y-S. Chao, "Three-Dimensional Dynamic Hip Contact Area and Pressure Distribution during Activities of Daily Living," J. Biomech., 39, 1996-2004 (2006).

[2] C. L. Abraham, S. A. Maas, J. A. Weiss, B. J. Ellis, C. L. Peters, and A. E. Anderson, "A New Discrete Element Analysis Method for Predicting Hip Joint Contact Stresses," J. Biomech. 46, 1121-1127 (2013).

[3] http://www.bupa.co.uk/health-information/directory/h/hip-replacement

---

[4] K. J. Lee, and Stuart B. Goodman, “Identification of Periprosthetic Joint Infection after Total Hip Arthroplasty,” J. Orthop. Translat., 3, 21-25 (2015).

[5] H. A. Gorman, “Hip joint prosthesis,” U.S. Patent 2,947,308, (1960).

[6] M. K. Babu, T. Srinivas, and G Prasad, "Indian Healthcare Sector-Competitive Advantage in International Markets", Int. J. Comm. Bus. Manage., 1, 2319–2828 (2012).

[7] M. Javidi, S. Javadpour, M. E. Bahrololoom, and J. Ma, “Electrophoretic Deposition of Natural Hydroxyapatite on Medical Grade 316L Stainless Steel,” Mater. Sci. Eng. C, 28, 1509-1515 (2008).

[8] J. Walczak, F. Shahgaldi, and F. Heatley, “In vivo Corrosion of 316L stainless-Steel Hip Implants: Morphology and Elemental Compositions of Corrosion Products,” Biomater., 19, 229-237 (1998).

[9] A. A. Liudahl, S. S. Liu, D. D. Goetz, C. R. Mahoney, and J. J. Callaghan, "Metal on metal Total Hip Arthroplasty using Modular Acetabular Shells," J. Arthroplasty, 28, 867-871 (2013).

[10] K. Maezawa, M. Nozawa, T. Hirose, K. Matsuda, M. Yasuma, K. Shitoto, and H. Kurosawa, “Cobalt and Chromium Concentrations in Patients with Metal-on-Metal and other Cementless Total Hip Arthroplasty,” Arch. Orthop. Traum. Su., 122, 283-287 (2002).

[11] M. Geetha, A. K. Singh, R. Asokamani, and A. K. Gogia, “Ti Based Biomaterials, the Ultimate Choice for Orthopaedic Implants–A Review,” Prog. Mater. Sci., 54, 397-425 (2009).

[12] D. Najjar, M. Bigerelle, H. Migaud, and A. Iost, “Identification of Scratch Mechanisms on A Retrieved Metallic Femoral Head,” Wear, 258, 240-250 (2005).

[13] T. P. Schmalzried, and W. H. Harris, “Hybrid Total Hip Replacement. A 6.5-year follow-up study,” J. Bone Joint Surg. -BR., 75, 608-615 (1993).

---

[14] I. Thompson, and R. D. Rawlings, “Mechanical Behaviour of Zirconia and Zirconia-Toughened Alumina in a Simulated Body Environment,” Biomater., 11, 505-508 (1990).

[15] J. Furmanski, M. Anderson, S. Bal, A. S. Greenwald, D. Halley, D., B. Penenberg, M. Ries, and L. Pruitt, “Clinical Fracture of Cross-Linked UHMWPE Acetabular Liners,” Biomater., 30, 5572-5582 (2009).

[16] N. D. L. Burger, P. L. D. Vaal, and J. P. Meyer, “Failure Analysis on Retrieved Ultra High Molecular Weight Polyethylene (UHMWPE) Acetabular Cups,” Eng. Fail. Anal., 14, 1329-1345 (2007).

[17] X. Dangsheng, "Friction and Wear Properties of UHMWPE Composites Reinforced with Carbon Fiber," Mater. lett., 59, 175-179 (2005).

[18] Z. Tai, Y. Chen, Y. An, X. Yan, X. and Q. Xue, “Tribological Behavior of UHMWPE Reinforced with Graphene Oxide Nanosheets,” Tribol. Lett., 46, 55-63 2012.

[19] D. S. Xiong, and N. Yuan, “Biotribological Properties of UHMWPE Reinforce by Nano-ZrO_2 Particle,” Key Eng. Mater., 330, 1211-1214 (2007).

[20] M. Hamadouche, C. Blanchat, A. Meunier, L. Kerboull, and M. Kerboull, “Histological Findings in a Proximal Femoral Structural Allograft Ten Years Following Revision Total Hip Arthroplasty,” J. Bone Joint Surg., 84A, 269-273 (2002).

[21] R. H. J. Hannink, P. M. Kelly, and B. C. Muddle, “Transformation Toughening in Zirconia-Containing Ceramics,” J. Amer. Ceram. Soc., 83, 461-487(2000).

[22] S. M. Kurtz, S. Kocagöz, C. Arnholt, R. Huet, M. Ueno, and W. L. Walter, “Advances in Zirconia Toughened Alumina Biomaterials for Total Joint Replacement,” J. Mech. behav. Biomed. Mater., 31, 107-116 (2014).

[23] A. H. De Aza, J. Chevalier, G. Fantozzi, M. Schehl, M. and R. Torrecillas, “Crack Growth Resistance of Alumina, Zirconia And Zirconia Toughened Alumina Ceramics for Joint Prostheses,” Biomater., 23, 937-945 (2002).

---

[24] B. Al-Hafez, “Hip Prosthesis,” US 6361566 B1, (2002).

[25] MCMINN, D. J. Wallace, “Femoral Head Prosthesis,” WO 2013/011290 A1, (2013).

[26] Y. Li, Y. Li, “Artificial Hip Joint Consisting of Multi-Layer Shell Core Composite Structural Components,” US 2013/0190889 A1, (2013).

[27] A. Battault, “Bone Prosthesis Made of Sintered Alumina,” U.S. Patent 3,977,026, (1976).

[28] K. S. Ely, A. C. Khandkar, R. Lakshminarayanan, and A. A. Hofmann, “Hip Prosthesis with Monoblock Ceramic Acetabular Cup,” U.S. Patent 7,695,521, (2010).

[29] http://akec.gmc.globalmarket.com (Beijing AKEC Medical Co., Ltd.**).**

[30] https://www.ceramtec.com/biolox/ (Biolox delta ceramic).

[31] http://sharmaortho.com/ (Sharma Pharmaceutical (India) Pvt Ltd).

[32] https://www.medacta.com (Medacta International, Switzerland).

[33] www.smith-nephew.com (Smith-Nephew, USA).

Chapter 2

Literature Review

In order to fulfil the stated objectives, as explained in the preceding chapters, a systematic literature review has been discussed into four subsections. The extensive survey demonstrates that the process parameter and composition optimization of MgO doped ZTA, following their mechanical, tribological and biological properties are limited. Despite the material optimization, the reported research results on THR prototypes, with specific processing and properties are also summarized.

2.1Composition and Process Optimization of ZTA

There has been an increasing need to develop engineering ceramics with better fracture toughness and strength properties for structural applications.[1] Such properties are greatly influenced by the sintered density or the porosity and amount of second phase reinforcement. In particular, the presence of porosity reduces both the strength and elastic modulus of a ceramic.[2] It is generally known that the size of pre-existing cracks in ceramics scales with grain size and for many non-transforming ceramics like alumina, the fine microstructure is therefore desired. Also larger is the crack length, greater is the stress concentration at the crack tip and more will be the driving force for crack propagation.[3] Intuitively, fine scale microstructure is therefore desired to obtain better toughness properties. For ceramic exhibiting transformation toughening like ZrO_2, the grain size of transforming phase (t–ZrO_2) needs to be in the critical size window, which depends on the amount of stabilizing dopant (e.g. Y_2O_3, CeO_2,etc.).[4] For many oxide and non-oxide ceramics, sinter-aid or sinter additivesare often added in small amount to enhance densification (e.g. MgO added to Al_2O_3). From the above discussion, it is apparent that the optimal addition of second phase and sinter additive is necessary to impart ceramic with desired property combination.[5]

As far as the sintered density is concerned, the densification is dominated by the diffusion assisted mass transportation, which critically depends on both the sintering temperature and sintering time. The interplay among the process variable (sintering temperature and sintering time) and material variables (sinter-aid and second phase addition) therefore have a profound influence on both sinter density and grain size.[6,7] The complex interaction among the variables can not be assessed using conventional experimental approach by varying one parameter while keeping other parameters constant. It implies the importance of the quantitative modelling approaches with extensive statistical analysis. This aspect is limited in the ceramic community and, therefore, has been the major focus of the present study.

Five types of quantitative modeling approaches can be adopted to address material related problems. These approaches include full factorial design, fractional factorial design, Box-Behnken, response surface method and Taguchi method. In all such design approaches, factors and levels are used to define the design parameters. Factors are described as the number of input variables, but the level refers to a predefined range of the factors that are need to examine.[8]

In full factorial design approach, the level is restricted to two-level for less than or equal to four number of factors, which is also an expensive affair to run exponential number of sample size.

Jaworski et al.[9] was synthesised fine hydroxyapatite powder by using an aqueous solution of ammonium phosphate and calcium nitrate as precursors with the aid of full factorial design of experiments. The design of experimental matrix used two variables, namely ammonium hydroxide and calcium ions concentration and output responses, that is purity of HA powder and the mass of obtained batch. Herein, Ca^{+2} influences the yield, but higher concentration decreases the purity of HA.

Schlechtriemen et al.[10] reported optimization of rheological behaviour of monoclinic ZrO_2 and intermetallic compound $ZrSi_2$ of the powder mixture for the fabrication of net-shaped reaction-bonded ceramic microparts by low-pressure injection moulding. Full factorial central composite design was used to find the best combination of powder mixture for feedstock. For this manufacturing, $ZrSi_2$, ZrO_2, Al_2O_3, MgO, and two different paraffin were used as starting material and mixed by using the planetary ball mill method. With the consideration of input process variables, feedstock flowability temperature output responses like dynamic viscosity and yield point are optimized.From statistical analysis, it is revealed that feedstock mixture mainly influenced by the Zr/Si ratio, temperature, powder volume content, and the binder content.

The fractional factorial design is reported as an alternative approach to the full factorial, design approach, which reduces the number of runs but loses information due to the lack of effect on two-factor interactions.[11]

Zarate et al.[12] used the fractional factorial statistical design tool to prepare the precursory powders from spray granulation of ZrO_2 (3% Y_2O_3)/(10-95)% Al_2O_3. Solid content Al_2O_3, spraying pressure and exit temperature in the drying chamber considered as input process variables and utilized to find the effect on output responses such as green density, specific surface area and mean granule diameter. From the experimental design, it revealed that aspersion pressure was a most significant parameter on the average diameter of the granule (0.78 μm). Similarly, surface area (25.17 X 10^3 m^2/kg) and green density (3.08 X $10^3 m^2$/kg) of granules were highly influenced by the chamber temperature and solid content in the suspension.

Baldassari et al.[13] prepared the nano titanium oxide (TiO_2) powder through conventional and microwaved hydrothermal methods by using the $TiOCl_2$. Similarly, the fractional factorial design tool employed to determine the influence of input factors on suspension shear stress.

Herein, independent parameters, solid (wt %), mixing time (min) and hydroxypropylcellulose (wt %) optimized the rheological properties, and aqueous solution shear stress. The quantifying analysis was held between the two preparation methods and demonstrated that the synthesized powder consists of the same mineralogical composition. It demonstrated that solid content has the most significant influence on viscosity and shear stress of the suspension.

As another alternative, response surface design Box-Behnken designs was adapted, specially prepared and restricted to only 3 levels, coded as, -1, 0 and +1.

Kehoe et al.[14] employed Box-Behnken design of experiments to investigate the process parameter influence on the hydroxyapatite (HAP) synthesis by the chemical precipitation method. The factors have been studied at three levels that included, reaction synthesis temperature during precipitation, stirring speed, ripening time, acid addition rate, initial calcium concentration, and atmospheric environment (synthesis with and without a controlled atmospheric environment). These were evaluated against powder-related parameters such as phase purity, crystallinity, crystallite size (L_{002} and L_{300}), lattice parameters, and particle size of hydroxyapatite for orthopedic applications. As a result of DoE, there was an improvement in the purity levels in HAP from 47% to 85% at the ripening time (36-48 h) and stirring speed of 1200-1500 rpm.

In order to optimize the process parameters, Taguchi method is one of the popular statistical optimization tool. However, the interaction effect within factors is not effectively considered in this approach. In Taguchi method, orthogonal array deals with the consequence of individual factors efficiently on responses, while neglecting the interaction effect and consistency matrix. Interestinglya number of runs are reduced as compared to full factorial design and response surface method.[15]

Eltejaei et al.[16] studied the influence of new block copolymer surfactant PEG-PPG-PEG with having different molecular weight and PEG content on resultant output response ZrO_2 surface area, particle size and pore structure with help of Taguchi method. Aqueous ammonia (25%wt) was added drop wise at room temperature to an aqueous solution of zirconyl nitrate ($ZrO\ (NO_3)_2{\cdot}6H_2O$) and PEG–PPG–PEG block copolymer surfactant under rapid stirring. The influence of preparation conditions were considered in four levels for surfactant molecular weight (PEG %wt) and two levels for zirconium molar ratio, pH of precipitation, aging time, and zirconium molarity. An effective specific surface area 175 m^2/g of t-ZrO_2 was achieved in presence of surfactant molecular weight 8400, surfactant/Zr mole ratio 0.04, pH=11, aging time 38 h, and Zr molarity 0.03.

Mohanty et al.[17] used Taguchi statistical analysis to identify the relationship between output parameters, for instance developed crack length, healed crack length, hardness, fracture toughness, and resultant density were correlated with input parameters such as vol.% of both SiC and Y_2O_3, crack-healing temperature, healing time, compaction load, and indentation load of Al_2O_3/SiC ceramic composites. Alumina (0.4 μm) and SiC (63 μm) particles including Y_2O_3 sintering additive were used for this experiment. According to the design of experiments, various pellets were prepared by cold uniaxial pressing followed by the sintering at 1500°C for 12h in open air. The indentation was made on the sintered samples by Vickers indenter with a load range of 20 to 40 Kg. The intended and cracked specimens were further heat treated at 1300°C to heal the crack at different healing times. From this Taguchi statistical tool, it was revealed that interaction input parameters vol.% of SiC X indentation load, and linear parameters, healing time, compaction load and vol.% of SiC have a significant influence on the output parameters.

In addition, response surface methodology (RSM) is widely used to justify the individual and interaction among the design factors on the response, which is more appropriate for the current research problem.The name of such model can be justified as the model predictions provide a precise map, leading to successful optimisation of the composition, process, grain size, mechanical properties, etc.

Li et al.[18] reported that RSM comprises central composite design (CCD) and used to optimize the relative density and bending strength of MgO-PSZ by employing three independent variables such as heating rate, sintering temperature and holding time. The starting raw material baddeleyite powder (m-ZrO_2) was used after baddeleyite ore. The baddeleyite ore initially grinded to a particle size of 5.67 μm and followed the ball milling by the addition of 3 wt% MgO to baddeleyite powder. The composition was planetary milled for 24 h and reduced the particle size around 0.48 μm. Further, the dry powder was blended and uniaxial pressed to impart the desired bars and cylindrical pellets. As per the design of experiments, the pellets were sintered and measured relative density and bending strength. The maximum bending strength (260.7 MPa) and relative density (99.44%) of MgO-PSZ were accomplished at the sintering temperature, 1550 ^{o}C, holding time 5 h, and heating rate of 3 ^{o}C/min.

Fernandez et al.[19] studied the synthesis, and optimize the mechanical properties of glass-ceramic matrix biocomposites by reinforcing of yttria-stabilised zirconia (Y-PSZ) particles through melting process and used the RSM statistical tool. In this course, (wt%) 51.4 P_2O_5; 16 CaO; 9 Al_2O_3; 14.6 Na_2O; 1.8 F-; 4.5 ZrO_2; 2.7 TiO_2 chemical composition was used as precursors. Sintering temperature, time, and log time input process parameters were used to find out the effective sintering temperature and optimized mechanical properties. The bioglass was prepared through melting process and varied two different particle sizes (30%

<20 μm and 70% in the range of 106-20 μm).The glass powder and 17 wt% of Y-PSZ of the mixture were prepared with ethanol suspension and stirred until complete evaporation of the solvent. The green compacts of glass and Y-PSZ composition was prepared through uniaxial pressing. Two different sintering temperature 510-550°C and 720-760°C batches were considered to optimize the mechanical properties. Glass ceramic biocomposite without any phase change at 740°C for 30 min exhibits highest young's modulus and indentation fracture toughness, 76 GPa and 3 MPa $m^{1/2}$, respectively.

Li et al.[20] prepared the calcia partially stabilized zirconia (CaO-PSZ) samples through the solid-state sintering process by using the baddeleyite as a starting material. The RSM was used to optimize the relative density and bending strength of CaO-PSZ by using the pressureless sintering process parameters predominately heating rate, sintering temperature, and holding time as input parameters. The blended powder was compacted uniaxially and sintered according to the design of experiments. Observing the contour plot and variance analysis, the relative density (98.5%) and bending strength 165.7 MPa was optimized at sintering temperature 1540°C and with identical heating and cooling rate of 3°C.

In consideration of extensive literature, the sintered density, and grain size of a model ceramic, i.e., alumina are optimized through response surface modelling approach and elaborately discussed in Chapter 3. This is being pursued through multivariate regression analysis, interpretation of resulting polynomial equations and response surface/contour plots to adapt the central composite design for process optimization. It also provides the choice of order in RSM model and data economy in reducing the factorial experiments from a large number of parameter combinations to a far less number without losing any information including linear, quadratic and interaction effects. For the first time, this effort enlightens a rapid process optimization technique to develop highly dense oxide ceramic with finer microstructure.

2.2 Mechanical and Biological response of ZTA

In last few decades, the zirconia toughened alumina (ZTA) has gradually developed as an important structural material, specifically as hip prosthesis bio-implants because of their durability and properties better than other competing materials.[21,22] For instance, *in vivo* slow crack growth initiation and their failure is a major issue for low fracture toughness Al_2O_3 femoral ball head.[23] Also, alumina-alumina couplings experience high wear rate, often necessitating a revision surgery.[24,25] It is well known that Al_2O_3 has a low tensile strength, but femoral ball head requires high hoop strength at the blind end of taper hole. Alumina ceramics usually require additives which can impart better strength for such applications, for example, in an earlier study; Al_2O_3 ceramics were doped with tantalum in order to improve the wear resistance and durability of the femoral head that withstand the high hoop stress at blind end taper hole.[26]

In order to overcome the difficulties associated with monolithic Al_2O_3, ZTA composites have attracted widespread attention. Several powder synthesis processes, starting from inorganic precursors or powders are often adopted to develop sintered ZTA composites.[27,28,29] In a recent article, a rapid composition and sintering profile optimization processes are reported as an efficient technique to develop dense ZTA with fine grain size, starting from high purity commercial nano-powders.[30] In ZTA composite, the presence of ZrO_2 induces transformation toughening, increasing the fracture resistance properties. The intergranular zirconia grains with an optimum size, dispersed along alumina grain boundaries, are more prone to stress induced transformation than modular grains embedded into the alumina matrix.[31] Many studies have reported sintering and mechanical properties of various compositions of Al_2O_3-ZrO_2 composites.

Sarkar et al.[32] prepared ZTA composite powders by wet interaction process in an aqueous medium via the sol–gel method with starting materials of $Al(NO_3)_3.9H_2O$ and $ZrOCl_2.8H_2O$.The alumina matrix was reinforced with 5.9 wt. % ZrO_2 particles and pellets prepared by the uniaxial press and followed by cold isostatic press at 150 MPa. The green compactions were sintered at various temperatures of 1450 to 1600°C. It has been observed that the ZTA composite sintered at 1550°C for 4 h exhibited the highest hardness of 17 GPa and moderate fracture toughness of 4.8 MPa.$m^{1/2}$.

Casellas et al.[33] studied the hardness and fracture toughness of the alumina and ZTA with respect to the zirconia addition and coursing effect of zirconia at different sintering times. The reinforcement with 15 vol. % of t-ZrO_2 (doped with 3-mol% of yttria) was added to the alumina matrix, and the pellets were prepared by the cold isostatic press and sintered at 1600°C for different sintering times. Alumina and ZTA composites exhibited hardness of 17–18 GPa and 12–13 GPa, respectively. Similarly, the fracture toughness was increased from 4.5 - 5 MPa $m^{1/2}$ as a result of ZrO_2 particle coarsening and stress induced phase transformation.

Rao et al.[34] employed a sol-gel method to prepare ZTA composite with a composition of Al_2O_3–15 wt. % ZrO_2 as precursor materials. The calcined ZTA powder was pressed uniaxially followed by cold isostatic press and sintered at various temperatures. From the characterization, it is observed that the bending strength and fracture toughness (SEVNB) recorded 932 MPa at 1425°C and 8.5 MPa $m^{1/2}$ at 1475°C, respectively.

Huang et al.[35] studied the mechanical behaviour of the ZTA composite which was preparedby varying the 0-50 vol. % content 3Y-TZP in an alumina matrix. The sintering additives 1 wt.% MnO_2, 1 wt.% TiO_2 and 2 wt.% $CaO–Al_2O_3–SiO_2$ (CAS) glass were added to follow liquid phase sintering. The dry mixed powder was compacted uniaxially followed isostatic press at 200 MPa and then sintered in air at different peak sintering temperatures for 2h. From statistical analysis and experimentation data, it concluded that the obtained maximum bending strength and fracture toughness are 619 MPa and 7 MPa.m$^{1/2}$, respectively.

In view of the importance of ZTA composites in biomedical applications, a number of researchers have investigated *in vitro* and *in vivo* biocompatibility.

Roualdes et al.[36] studied the cytocompatibility and cell viability on ultrafine ZTA composite using human fibroblast cells (MG-63 cell). After the sterilization of ZTA disc samples, fibroblasts or osteoblasts cell culture medium were seeded on each sample and incubated under standard conditions for 2 h to proliferated the cell. MTT assay was used to calculate proliferated cells on ZTA discs directly. The result showed that good cell proliferation on ZTA composite when osteoblast and fibroblast cells were cultured.

He et al.[37] reported the biocompatibility of 3D inter-connected porous ZTA ceramics fabricated using direct forming method. Herein, the celluar response of untreated and treated porous ZTA composite was calculated in presence of human osteoblast cells (MG63) and cultured *in vitro*. All porous ZTA composite scaffolds were soaked in NaOH solution at 80^{o}C for different soaking times. The soaked specimens were used for culture and seeded the osteoblast cells for proliferation. The cellular culture showed that a better cellular response was observed with osteoblast cells when such ceramics were soaked in NaOH solution, i.e analogous to 1% NaOH in serum.

Vallée et al.[38] reported that the ZTA composite supports the absorption of laminin, an important protein fragment of relevance to epithelial cell adhesion and migration. ZTA and ATZ specimens both were treated with Ln-1 and Ln-5. The Human epithelial carcinoma cell line (HeLa) cells were seeded on respective samples and incubated for various times. Thereafter, cells were counted by automated cell counter, and MTT assay used to check the cell viability. This analysis revealed that ceramic compositesin presence of laminins exhibited better cellular activation.

Affatato et al.[39] studied laminin cellar functionality on ZTA composites in vitro conditions for dental restorative applications. Human osteoblast cells were seeded on the ZTA ceramic surface and examined for a week to assess the cell viability. ZTA nanocomposites, in comparison to monolithic alumina however, exhibit significantly better *in vitro* cytocompatibility property with reference to primary osteoblast proliferation.

A general literature analysis, however, could not reveal any study, reporting a broad spectrum of mechanical properties of ZrO_2 – toughened Al_2O_3 ceramics. More importantly, none of the earlier studies reported toughness measurement by SEVNB technique. In particular, we have selected highest dense ZTA composites for the present study (5 wt. % and 15 wt. % ZrO_2 and with 400 and 800 ppm MgO as sinter-aid). The strength properties are measured using Brazilian disk or diametral compression test (tensile strength) and using uniaxial compression. Other essential mechanical properties such as hardness or fracture toughness properties were also evaluated, in a reliable manner.

Summarising all the published literature, none has yet reported the combination of good fracture resistance through SEVNB technique along with muscle cell adhesion and proliferation on sintered ZTA composites. In view of this, one of the objectives of the present work is to report the reliable toughness measurement together with the cell attachment and growth of C2C12 mouse myoblast cells at the different time points of 24, 48, 72 h in culture.

2.3 Tribological Behaviour of ZTA

The hip joint is widely considered as a prime example of ball-in-socket joint in mechanical terms, as joint experience articulating motion with the socket placed at the pelvis and ball is another end of the thigh bone. The combination of these two bones generates the bearing action, which creates the relative rotational motion between the pelvis and thigh bone (femoral ball head) while transferring the load/body weight during walking/running/other physical activities. Due to this relative rotational sliding, such joints experience the rubbing action, leading to the friction and wear of the contact surfaces. Currently, the artificial hip joints are often implanted particularly in elderly human patients to replace the damaged or diseased hip joint. In last few decades, ceramic-on-polymer and ceramic-on-ceramic bearing pairs are being used for total hip joint (THR) replacement, because they have a right combination of mechanical and surface properties along with improved biocompatibility. In the context of our recent research program to develop ceramic based femoral head and acetabular socket, ZTA composite was fabricated and studied various mechanical and microstructural properties. The present work mainly focuses on tribological properties of optimized ZTA cylindrical disks (best combination of strength, toughness, and hardness property) against zirconia and stainless steel ball.

Esposito et al.[40]studied on the ZTA/Al_2O_3 sliding couple illustrated the influence of sliding speeds at a constant normal load of 32.8N. The tribocouple experienced less coefficient of friction (COF) 0.06 at 0.3 m/s sliding speed and COF increases to 0.26 at 0.7 m/s. In this tribotest, the material removal followed by surface fracture (intergranular and transgranular) produced a large quantity of debris.

Kerkwijk et al.[41]prepared the ZTA flat specimens by colloidal processing method and studied the tribological test using alumina pin. The normal loads were varied in between 3-17.5 N and sliding velocities in the range of 0.1 to 0.5 m/s. ZTA/Al_2O_3 system exhibited wear rate of less than 10^{-6} mm^3/ N.m and coefficient of friction was recorded as 0.5-0.6, where predominant wear mechanism influenced by abrasion and resulting debris is smeared out in the contact.

Bartolome et al.[42]demonstrated the fretting wear behavior of ZTA against MgO-partially stabilized ZrO_2 spherical ball with a sliding speed of 0.15 m/s and varying normal load in the range of 20 to 150 N. The wear rate of 22 vol% of zirconia containing ZTA composite was exhibited $>10^{-5}$ mm^3/N m. However, ZTA composite with consist of 14 and 7 vol.% zirconia exhibits $<10^6$ mm^3/N m wear rate at the normal load 20N. The wear mechanism was governed by microcracking and plastic deformation, indicating the dominance of abrasive wear.

Bueno et al.[43]used hemispherically tipped pins of 7 wt.% cobalt bonded tungsten carbide (WC) to determine the friction and wear properties of YTZP, alumina coated–YTZP (AF-YTZP) and alumina at a load of 10 N, and at the sliding speed of 0.15 m/s. The negative wear rate reported -1.9 and -5.7×10^{-6} g/N km for AF-YTZP and alumina, respectively. This wear behavior was attributed to the metallic cobalt (Co) transfer from pin to the ceramic samples. The residual compressive stress mismatch because of the variation in coefficient of thermal expansion between alumina and zirconia during cooling from sintering temperature is attributed to inter – and intra – granular fracture, that followed the resultant brittle fracture.

He et al.[44] reported that sliding wear of $ZrO_2 – Al_2O_3$ composites against the SiC ball under dry N_2 atmosphere. In particular, sinter-forged ZTA composite with 0.8 µm grain size exhibits wear rate of $1.44 X 10^{-6}$ mm^3/N.m and coefficient of friction of 0.33. On the contrary, the pressureless sintered ZTA composite with similar grain size exhibited wear rate of $3.4 X 10^{-6}mm^3$/N.m and coefficient of friction of around 0.37. The wear test was conducted at a sliding speed of 0.08 m/s and sliding time 130 min, with sliding distance and contact pressure of 5.8 km and 858 MPa, respectively. The ZTA composite is mainly subjected to grain pull-out from the worn surface.

In another study, Heet al.[45] investigated the friction and wear behaviour of the ZTA composite against the stainless steel ball with the aid of pin-on-plate reciprocating motion. The wear rate was recorded to be less than 10^{-6} mm^3/ N.m at a sliding distance of 6.8 km and sliding speed of 20 mm/s. ZTA composite exhibited mild wear rate together with a coefficient of friction of 0.75 after sliding for 4.5 km. The worn surface experienced grain pull out,and therefore, adhesive wear dominated.

Fan et al.[46] investigated the dry wear tribological properties of textured and untextured ZTA discs against stainless steel ball using pin-on-disc tribometer. Micro-dimples with different sizes were prepared on ZTA surface by pulsed Nd:YAG laser. Wear tests were conducted at various sliding speeds from 5 to 30 cm/s, sliding distance about 100 m and different loads applied 2 to 10N. It is observed that when the micro-dimples size increased to 34%, then frictional coefficient reduced to 0.4. Untextured ZTA surface experienced ploughing and adhesive wear, whereas the textured surface predominately exhibited mild wear.

Wang et al.[47] studied the tensile crack-controlled wear mechanism of ZTA composite specimen against Si_3N_4 balls under paraffin oil lubrication at room temperature using ball-on-flat tribometer. The wear test parameter normal load were varied from 170 to 340 N along with the different sliding velocity of 0.23 to 0.38 m/s. The wear rate of alumina sample $>10^6$ mm^3/N m and ZTA (15wt% Zirconia)$<10^6$ mm^3/N m were recorded. Permissible or critical tensile stresswas calculated by using maximum room temperature stress on grain due to thermal expansion, thermal stress between the alumina and zriconia phase, and internal stress induced by zirconia phase transformation. Similarly, the maximum or working tensile stress at the trailing edge of the contact was determined by normal load, Hertzian contactradius, and coefficient of friction of ZTA flat. It revealed that working tensile stresses were higher than the permissible tensile stresses as a result cracks induced on the ZTA flat and leads to the wear of sliding contact.

Hamilton et al.[48] studied about the tensile crack-controlled wear mechanism,which is triggered by maximum tensile stresses at trailing edge of the contact. When the tensile stress exceeds the critical damage stress, the cracking induced delamination leads to the wear of sliding contact.

In the above perspective, one of the objectives of present work is to assess the friction and wear properties of the optimized ZTA composite against zirconia and stainless steel using a ball-on-plate tribometer at different normal load and under identical dry sliding conditions. The wear tests were carried out by varying the normal load in dry sliding conditions. An attempt is made to correlate the observed wear mechanism with the established theory.

2.4 Status on THR Prototype Research

Material selection is a critical component to achieve analogous properties of hip bone. Bone is a complex natural composite of soft and strong protein collagen and brittle ceramic hydroxyapatite, respectively. Thus, it has anisotropic mechanical properties that differ in the longitudinal and transverse directions. Anatomically, the hip joint is described as a ball-on-socket joint at the juncture of the leg and pelvis, which comprises through (1) the acetabular socket affixed to the pelvis, (2) the femoral ball head attached to the stem, (3) the femoral stem, and (4) a fixation agent, that allows the attachment of the stem into femoral head and acetabular socket to the pelvis. This mechanical joint has a wide range of degrees of freedom that can allow the relative rotational motion in multiaxial directions by constraining the translator motion between the joint bones. Such continuous function leads to extensive wear at the ball/socket interface and related high friction, causing pain to the patients taken together, the synchronization of dimensional, mechanical, and chemical properties of new material is a challenging task since body environment can reject any foreign substance that causes inflammation to death. Hence, biocompatibility along with mechanical properties and their sustainability are major constraints. Herein, the prime focus has been concentrated in order to develop the articulating concave acetabular socket and convex femoral ball head made of high wear resistance ceramics.

2.4.1 Femoral Head

The convex shaped spherical femoral head of the femur represents the ball-and-socket hip joint with the concave cup shaped acetabulum socket of the coxal (hip) bone. The soft tissue cartilage is covered on the spherical femoral head to absorb the shock loads and to allow movement in almost any direction at the hip, including circumduction as well as rotation around its axis. When the uneven loads are exceeded in the hip joint, the absorbed energy can release through the fracture or dislocation of the femoral head from the mean position. Thus, partial or complete hip replacement is important to avoid the post-traumatic osteoarthritis. The above situation, demands the man-made prosthesis as bio-implantation to retrieve the function of the diseased or damaged part.

Yoshida et al.[49]investigated the pressure distribution on hip contact area during the daily living activities by finite element analysis (FEA). The joint forces were recorded by generic hip model and the discrete element analysis (DEA) used to calculate pressures on hip contact area. It was observed from the analysis that during slow walking, knee bending, walking down stairs, climbing up stairs, standing up from a chair and sitting down on a chair requires 3.3MPa, 3.7MPa, 3.8MPa, 5.7MPa, 8.8MPa and 9.4MPa compressive stress developed at articulating joints, respectively.

The femoral head deteriorates due to osteonecrosis. Because of that, the cortical bone of the femoral head can buckle and collapse into the cancellous bone supporting it. In order to assess the buckling and collapse scenario Volokh et al.[50] proposed a finite element analysis of a realistic femoral head model. The finite element model considered the brick elements for cancellous bone and triangular thin shell elements for cortical bone. The boundary conditions, contact pressure was calculated on the basis of normal walking (4.3 MPa) and sitting down pressure (9.4 MPa) by using the DEA and applied on the femoral head as acritical load. The Poisson's ratio chosen for cancellous and cortical bone was 0.25 and 0.3, respectively. The elastic modulus of cortical bone was chosen in decreasing order from 7 GPa, 4 GPa and 1 GPa to satisfy the necrosis conditions. Correspondingly, the thickness of cortical bone assumed declining from 3 mm to 1 mm. Similarly, the elastic modulus of the integral cancellous bone was 500 MPa. To mimic the cancellous bone deterioration, the modulus was assumed to decrease to 400, 300, 200, 100, 50, 10, and 1 MPa and applied the same in buckling analysis. From buckling analysis, the deteriorating cancellous bone is unable to prevent the unstable cortical bone from the buckling. The local buckling of the cortical shell seems to be the driving force of the progressive fracturing the femoral head leading to its entire collapse.

Daniel et al.[51] studied the diametrical effect on metal ions release from the metal-on-metal hip implants. In this work, the influence of bearing diameter on metal ions compared the cobalt and chromium levels in blood and urine at various intervals of times after the implantation are reported. Herein, different implantation, like 54 mm Birmingham hip resurfacing (BHR) and 28 mm Metasul total hip replacement (THR) were used to identify the cobalt level in blood and found 1.3 μg/l for the BHR and 1.7 μg/l for THR in the respective period. The confirmed that the bearing diameter did not influence metal ions release rate.

Jasty et al.[52] examined surface damage of the retrieved cobalt-chrome alloy femoral head collected from the revision surgery and post-mortem. In this arthroplasties, polyethylene acetabular socket liner and cobalt-chromium femoral head were used, where the uncemented porous acetabular socket cover was made of titanium fiber mesh or cobalt chrome beads. In another end, the cemented components were prepared with cobalt-chrome alloy. It was observed that the uncemented hip joints exhibited scratch depth from 0.1 to 2 μm and profound to third body abrasive wear. The analysis suggests that the surface damage of the femoral head was severe in hybrid and uncemented hip joints than the cemented prosthesis.

Najjar et al.[53] investigated the surface topography of titanium alloy (T4A6V) femoral head that retrieved after 4 years and 5 months due to osteolysis phenomenon. The hip joint implantation consists of UHMWPE acetabular liner received by the metallic shell and inserted 28 mm diameter of titanium alloy femoral head on a cemented femoral stem. From this investigation, it was identified that 30% surface lightly scratched, 20% severely scratched at polar and equator region and 50% moderately scratched on the femoral head. The surface roughness was reported to be 0.2 μm at polar and equator. Similarly, surface roughness at the region of lightly and moderately scratched regions was recorded less than 0.05 μm. These kind of surface degradation occurred because of third body abrasive wear that generated from the metallic femoral head.

The existing literature emphasizes that the metallic implants have less wear resistance for bearing applications, which are the cause of implant surface degradation. In order to overcome the aforesaid drawbacks, a focus has been concentrated on high wear resistance ceramics to establish next generation hip prostheses.

Researchers in Japan and Europe initially investigated alumina ceramic bearing materials due to their low friction, wear resistance and biocompatibility.[54] However, the first applications of alumina in orthopaedics were associated with high fracture rates.

Park et al.[55] studied the failure phenomena of the both alumina and polyethylene-alumina composite liners against alumina femoral head for the total hip bearing. Total hip arthroplasties liners were inserted within a titanium-alloy shell and coupled with alumina femoral head of 28 mm diameter. In a variation of the time limit, *in vivo* retrieved femoral heads were collected and analysed the mode of mechanical failure. In the early stage, an average of 36.8 months *in vivo* both the alumina head and alumina liner are subjected to fracture and needed revision surgery.

In the 1980s, zirconia (ZrO_2) was introduced in orthopaedics because of its improved fracture toughness and mechanical strength relative to alumina. Zirconia owes its higher fracture toughness to stress-induced phase transformation from its metastable tetragonal phase to its stable monoclinic phase at ambient temperatures.[56,57,58] During the 1990s, stabilized zirconia was widely used as ceramic femoral heads in ceramic-on-polyethylene bearings, because of its higher toughness and strength compared to that of alumina. However, depending on the manufacturing conditions and hydrothermal effects *in vivo*, the pure tetragonal zirconia may be unstable and can transform catastrophically into the monoclinic phase and hence failure of the component.[59]

Earlier, Matsunaga[60] disclosed a combined fabrication technique of alumina rich femoral head attached with metal rich femoral stem using a slurry compound of ceramic as well as metal or alloy powders in the US patent 5,336,465. In this invention, 35vol% of alumina ceramics powder having the average particle size of 60μm and 65vol% of stainless steel powder was mixed with 1wt% ammonium alginate, prior to casting through rotating and swinging mode of operation. The casted body showed composition gradient with a femoral head portion rich in alumina ceramics and a stem portion in stainless steel, which was further sintered in air upto 700˚C, followed by vacuum sintering ($1x10^{-5}$ torr) at 1300˚C for 3 hr. The obtained product consists of large particles near the inner wall of the mold, whereas it has a dense core consisting mainly of sintered fine particles. A hip prosthesis thus produced had a fully closed hollow interior and relative density of 95% at the outer shell portion.

In another patent (US patent 2002/0013625 A1), Abouaf[61] disclosed the invention of a biojoint prosthesis with one component having spherical ceramic head while the other component is a ceramic acetabular cup having a socket surface shaped to rotatably receive the outer surface of the ceramic head in. Herein, the submicron zirconia powder mixed with rare earth oxides followed by cold isostatic pressing at 400 MPa, followed by green machining and sintering in the temperature range of 1300-1500°C for about 1 to 4 hours to achieve density of at least 95% relative density. Eventually, the sintered component was hot isostatically pressed (HIPed) in argon atmosphere in the temperature range between 1300 to 1500°C for a time frame of 0.5 and 4 hours. The femoral head and ceramic socket exhibited near to 99.9% relative density with grain size ~1μm, which were finally polished to make mirror finish.

In and different patent, Glien[62] disclosed the endoprosthesis ceramic femoral head fabrication technique using aluminium oxide (Al_2O_3) and zirconium dioxide (ZrO_2) in (US patent 2005/0187638 A1). As part of this process, the compression mould was filled with different weight ratio of alumina and zirconia with up to 0.3 wt% of magnesium oxide, being continuously varied depending on design of the endoprosthesis component. After the shaping, thermal treatment was carried out in two steps. The sintering of the shaped component was carried out at 1300 to 1600°C to obtain a solid, graduated, and dense material composite of alumina and zirconia (monoclinic, tetragonal, cubic phase). In this prior art, a further compression by hot isostatic pressing (HIP) was also performed to achieve better densification of the product prototype.

Valdez et al.[63] studied the wear and phase transformation behaviour on the retrieved zirconia femoral heads after 13 years of implantation. Polyethylene acetabular cups and zirconia femoral heads were used for the implantation. It was observed that martensitic phase transformation occurred after 3 years implantation and accelerated monoclinic clusters at the pole of femoral head. This facilitated the femoral head surface damage and further enhanced after five years because of appreciable volume expansion, more roughness, and abrasive wear.

Chowdhury et al.[64] investigated the surface morphology and mechanical properties of aged 22.22mm zirconia femoral head and analysed the influence of phase transformation on mechanical properties. Four different zirconia femoral heads (0, 10, 50 and 78mol% m-ZrO_2 containing) were used and aged hydrothermally to understand the influence of transformation behaviour and thereafter resultant mechanical responses. Interestingly the surface to inner zone depth gradually increased upto 8μm for highest containing m-ZrO_2 after hydrothermally aging, which dramatically reduces the mechanical behaviour of resultant components. In the same time, the hardness is drastically diminished from 16.6 to 9.7 GPa and their elastic modulus reduced from 264 to 185 GPa.

Thus, low wear resistance and wear debris particles influenced by materials properties, have an adverse effect on performance, and this was one of the prime reasons for the *in vivo* failure of implants in early age. In the same line, better properties of acetabulum cup material are also needed to account for the minimization of the fretting wear, chipping and ultimate failure under. For a long time, biocompatible zirconia and alumina have been explored for developing femoral head, but alumina or zirconia material alone does not pass the necessary mechanical properties for an orthopaedic implant.

Hence, the optimum combinations of these two oxides will be explored to fabricate both the femoral head and acetabular cup for THR assembly in the present study. This has motivated us to develop zirconia toughened alumina (ZTA), wherein zirconia is dispersed in the alumina matrix. These ceramics exhibit superior strength and toughness compared to conventional alumina and zirconia.[65, 66, 67, 68] High fracture toughness, excellent wear characteristics and low susceptibility to stress assisted degradation of ZTA over alumina allows the manufacturing of thinner liners to improve stability.[69] Increasingly, the number of hip arthroplasty in human patients is on the rise around the world and ZTA femoral head can have an edge over conventional alumina femoral head.[70]

2.4.2 Acetabular Socket

The artificial acetabular socket is hemispherical in shape that performs as a sliding surface to the artificial joint. In order to prevent the dislocation of the hip joint, a proper depth of socket is necessary to accommodate the femoral head in position. Total hip replacements (femoral head – acetabular socket) are classified into various categories, such as metal-on-metal, metal-on-UHMWPE, metal-on-ceramic, ceramic-on-ceramic, and ceramic-on-UHMWPE. Some interesting information on metal, ceramic and polymer acetabular sockets and their analysis are summarized.

Zhil’tsova et al.[71] fabricated high density polyethylene (HDPE) acetabular cup by adopting the injection mould technique and studied the process parameters filling rate, packing time, packing pressure, and nozzle temperature impact on the dimensional stability, visual appearance and weight variation of the acetabular socket. Packing pressure is found to be the most significant parameter to control over dimension and weight of the components. However, low filling rate reduces the dimension stability and compact weight. The packing time and nozzle temperature effect was not significant on the component properties.

Singh et al.[72] employed investment casting to fabricate mild steel hip prosthesis with the help of acrylonitrile butadiene styrene (ABS) and conventional wax as pattern material separately, and analysed their dimensional accuracy. Statistical Taguchi method was chosen to predict the correlation between input and output variables. Fused deposition method (FDM) was used to prepare the ABS pattern to follow the investment casting. Similarly, the wax pattern was developed from the conventional die and casted the hip joint by mild steel. The prepared hip joint through ABS pattern exhibited good dimensional stability than the other methods.

Mathias et al.[73] proposed a novel state-of-art material, design, fabrication, and testing of acetabular socket. In this design concept, combined carbon fiber reinforced composite socket was introduced to balance the stress shielding effect including inner alumina linear to interact with the articulating surface and minimize the wear rate. The low modulus composite backing can avoid the stress shielding and assist to bone ingrowth when direct contact with the pelvis. Alumina cups were manufactured by hot isostatic pressing (HIP) and backing composite was fabricated by injection moulding and controlling the heating and cooling cycles to reduce the thermal shocks. Ultimate compressive strength, torque test, and fatigue tests were conducted on the fabricated unit. It observed that the acetabular cup is preferentially withstand compressive strength of 18.25 kN and the cup rotation was not observed in backing material even at the torque load of 6.4 kN.

Murr et al.[74] adopted electron beam melting (EBM, additive manufacturing) method to fabricate the patient specific bioimplant prosthesis, specifically total knee, hip, and intramedullary rods using the Co-29Cr-6Mo and Ti-6Al-4V metal alloys. In this method, additive manufacturing platform was used to maintain the layer thickness $\sim$50 to 100μm of the component. Multiple electron beams were employed to preheat the implant components layers at a temperature range of 600 to 800^{o}C. Further, tensile and hardness test was conducted on solid Co-29Cr-6Mo and Ti-6Al-4V alloys. The tensile strength of the Co-29Cr-6Mo and Ti-6Al-4V alloys was reported 1.45 GPa and 1.11 GPa, respectively. Similarly, hardness is also varied in the range of 4.6 and 4.1 GPa, respectively. Using EBM method, successfully porous knee and hip orthopaedic implants were fabricated.

In another research report, Maezawa et al.[75] investigated the cobalt and chromium release phenomenon from the implant into urine and serum. The cementless total hip arthroplasty was implanted in patients with various combinations of metal-on-metal (MoM) and metal-on-UHMWPE (MoP) according to the patient activities. Interestingly, metal-on-metal articulating joints release more chromium ions in urine compare to serum. For example, MoM and MoP are releasing 90.6% and 85.7% chromium ion in urine, respectively. However, the released chromium concentration is found near to three times less in serum under identical conditions.

Neveloset al.[76] reported the wear behaviour of the UHMWPE acetabular cup by varying the angle (anatomical position) with the alumina femoral head (ϕ 28 mm) in a physiological hip joint simulator. This study depicts the design aspects of prototypes. In the simulator, first two million cycles were maintained 45^o and remaining three million cycles changed to 60^o anatomical position between the hip prosthesis. It was observed that the volumetric wear of the acetabular cup is not significant by varying the anatomical positions from 45^o to 60^o.

Saikko et al.[77] studied the tribological behaviour of the CoCr-on-CoCr hip prostheses in a variation of steep angle of the acetabular socket. HUT-4 hip simulator was used to generate the biaxial rocking motion with an adduction-abduction angle range of 12^o, and extension-flexion range of 46^o to hip joint in the presence of serum lubrication. The diameter of the femoral head and the articulating surface of acetabular cup were 25.99 mm and 26.07 mm, respectively. Such a tribological couple is shown high wear resistance and low friction when the cup is in the right position. On the other hand, if the cup steep angle exceeded 60^o then it leads to the uneven contact area, followed by high wear rate.

Minguella et al.[78] introduced subjection system (work holding or supporting device) which permits the machining operations without damage of the presintered ZTA acetabular cup made of 75% alumina and 25% zirconia. Herein, the presintered ZTA cylinder was placed on the aluminium support to fix in a vice and machined outer surface of hemispherical cup prototype. In continuation to develop the articulating convex surface, the one end hemispherical dome shaped cylinder was rested on the plastic holder supported by the metallic box which holds rigidly and absorb the unnecessary loads during the machining. This new machining technique was invented to develop ceramic bioimplants.

In recent days, Caldarise[79] disclosed the ceramic bone prostheses more particularly acetabular socket and conventional casting processes was used for manufacturing the same. 3-D powder printing, additive manufacturing technology was used to fabricate a casting mould. Alumina powder was used to form layers of the mould and silica was used as a binder material. The negative image of acetabular shell was prepared as green casting mould that is used for the formation of implantable bone prostheses. The alumina green casting mould further fired at 1925°F for 2 h to improve the strength and thermal stability which defines the cavity size. The molten metal, titanium alloy/chromium cobalt/stainless steel was used to fill the mould cavity and the solidification casting material firmly attached to the irregular surface of the alumina mould and creating the bond. After the solidification, the disposable ceramic shell mould was removed from the external diameter of cast product. The densely packed alumina forms the articulation surface of the acetabular shell at inner diameter.

In another work, Kumar[80] disclosed the spraying manufacturing technique for the fabrication of the acetabular shell which consists of alumina as an articulating surface and titanium oxide/ titanium as an outer shell surface. In spray technique, the alumina slurry was sprayed on the mandrel upto a certain thickness around 5mm through spray gun. The alumina slurry consists of binders and deflocculating agents as desired quantity for achieving favourable slurry properties. After certain alumina slurry thickness accomplished the alumina slurry gradually reduces and increases the titanium oxide/titanium layer. The particle size of titanium increases to generate the porous outer surface on acetabular shell. Once the acetabular shell cast and separated from the mandrel, the green component kept in the oven at 175°C for 4 h followed by sintered at 1650°C for 8 h to densify the acetabular shell.

In the above perspective, one of the objectives of the present work was to develop a representative 26mm (OD) femoral ball head and 26.5mm (ID) acetabular socket of ZrO_2 toughened Al_2O_3 (ZTA) by an integrated manufacturing approach as well as to assess performance critical properties. This indigenous product development involves the following key stages- a) thermoplastic ABS polymer prototype development for THR, b) specific mould assembly for the manufacturing of biomedical devices and c) pre-sintering followed by machining and final stage sintering to obtain ZTA acetabular socket. As far as the manufacturing aspect is concerned, the optimization of near net shaped processing is an important feature, which is followed by uniaxial pressing, presintering, machining, and sintering.

2.4.3 Femoral stem

Truncated bore fitting of the femoral head and damaged femur mainly cancellous bone replacement demands artificial femoral stem prosthesis. The prime function of the femoral stem prosthesis is to bear the load of the implant and transfer to the compact bone without having any relative motion. To take such bearing load, the prosthesis must have elastic modulus matching with to that of cortical bone. Controlling over equivalent stiffness of implant and bone is a serious issue to avoid stress-shielding effect at the junction.[81] Well-known bioceramics are poor in ductility and not apposite for the artificial stem. In another end, the polymers are not in a position to withstand the fatigue loads that makes unsuitable for this specific application.[82] In view of the above application, metallic materials are fitted appropriately, because they have better ductility which absorbs the fatigue loads and yield before the fracture.[83] Stainless steel was employed for the preparation of femoral components in the early days and still preferred for a small number of active and young patients. A passive layer was formed on the surface due to chromium which can resist the corrosion.[84] In the long run, stainless steel releases the chromium, cobalt, and nickel ions, which are show an adverse effect after the implantation.[85] In the modern total hip joint, the replacement has been accomplished using femoral stems, which are fabricated from medical grade stainless steel (316 LS), cobalt-chrome (CoCr) and cobalt-chrome alloys (CoCrMb), titanium (Ti) and titanium alloys (TiAlV).[86,87]

2.5 Summary

Material selection is a critical component to achievecomparable properties of hip bone. Bone is a complex natural composite of soft and strong protein collagen and brittle ceramic hydroxyapatite, respectively. Thus, it has anisotropic mechanical properties that differ in the longitudinal and transverse directions. This mechanical joint has a wide range of degrees of freedom that can allow the relative rotational motion in multiaxial directions by constraining the translator motion between the joint bones. Such continuous function leads to extensive wear at the ball/socket interface and related high friction, causing pain to the patients taken together, the synchronization of dimensional, mechanical, and chemical properties of new material is a challenging task since body environment can reject any foreign substance that causes inflammation to death. Hence, biocompatibility along with mechanical properties and their sustainability are major constraints. Herein, the prime focus has been concentrated in order to develop the articulating concave acetabular socket and convex femoral ball head made of high wear resistance ceramics. Extensive literature review enlightens the limited research work on the process parameter and composition optimization for lab-scale processing of ZTA in the presence of MgO, followed by estimation of their mechanical, biological responses and prototypes fabrication. In order to justify the entire research objectives, ZTA materials are characterised for their mechanical, tribological, and in vitro cytocompatibility properties followed by design and fabrication of ZTA femoral head and acetabular socket prototypes.

2.6 References

---

[1] B. Basu, and K. Balani, "Advanced Structural Ceramics," Wiley & Sons, (2011).

[2] J. B. Wachtman, W. R. Cannon, and M. J. Matthewson, "Mechanical Behavior of Ceramics," Wiley & Sons, 2009.

[3] A. H. De Azaa, J. Chevaliera, G. Fantozzia, M. Schehlb, and R. Torrecillas, "Crack Growth Resistance of Alumina, Zirconia and Zirconia Toughened Alumina Ceramics for Joint Prostheses," Biomater., 23,937–945 (2002).

[4] B. Basu, "Toughening of Y-Stabilized Tetragonal Zirconia Ceramics," Int. Mater. Rev., 50, 239–256 (2005).

[5] S.J. Cho, Y.C. Lee, H.L. Lee, S.M. Sim, and M. Yanagisawa, "Chemical Inhomogeneity in Commercial Alumina Powders and its Effect on Abnormal Grain Growth during Sintering," J. Eur. Ceram. Soc., 23, 2281-2288(2003).

[6] W. D. Kingery, H. K. Bowen, and D. R. Uhlmann, "Introduction to Ceramics," 2nd Ed., Wiley-Interscience, New York, 1976.

[7] B. Basu, T. Venkateswaran and D.Sarkar, "Pressureless Sintering and Tribological Properties of WC-ZrO2 Composites," J. Eur. Ceram. Soc., 25, 1603-1610 (2005).

[8] R.H. Myers, D.C. Montgomery, and C.M. Anderson-Cook, "Response Surface Methodology: Process and Product Optimization using Designed Experiments," 3rd Ed., Willey, (1995).

---

[9] R. Jaworski, C. Pieriot, L. Pawlowski, M. Bigan, and M. Martel, “Design of the Synthesis of fine HA Powder for Suspension Plasma Spraying,” Surf. Coat. Tech., 203, 2092-2097 (2009).

[10] N. Schlechtriemen, J. R. Binder, R. Knitter, and J. Haußelt, “Optimization of Feedstock Properties for Reaction-Bonded Net-Shape Zircon Ceramics by Design of Experiments,” Ceram. Int., 36, 223-229 (2006).

[11] K. Rekab, and M. Shaikh, “Statistical Design of Experiments with Engineering Applications,” 4th ed., Boca Raton, Chapman and Hall, New York, 2005.

[12] J. Zarate, H. Juarez, M. E. Contreras, and R. Pe´rez, “Experimental Design and Results from the Preparation of Precursory Powders of ZrO_2 (3%Y_2O_3)/ (10-95) % Al_2O_3 Composite,” Powder Technol., 159, 135-141 (2005).

[13] S. Baldassari, A. B. Corradi, F. Bondioli, A.M. Ferrari, M. Romagnoli, and C. Villa, “DOE Analyses on Aqueous Suspensions of TiO_2 Nanoparticles,” J. Eur. Ceram. Soc., 28, 2665-2671 (2008).

[14] S. Kehoe and J. Stokes, “Box-Behnken Design of Experiments Investigation of Hydroxyapatite Synthesis for Orthopedic Applications,” J. Mater. Eng. Perform., 20, 306-316 (2011).

[15] R. L. Mason, R. F. Gunst, and J. L. Hess, “Statistical Design and Analysis of Experiments,” 2nd Ed., John Wiley & Sons, 2003.

[16] H. Eltejaei, J. Towfighi, H. R. Bozorgzadeh, M. R. Omidkhan, and A. Zamaniyan, “The Influence of Preparation Conditions on ZrO_2 Nanoparticles with different PEG-PPG-PEG Surfactants by Statistical Experimental Design,” Mater. Lett., 65, 2913-2916 (2011).

---

[17] D. Mohanty, A. Sil, and K. Maiti, "Development of Input Relationships for Self-Healing Al_2O_3/SiC Ceramic Composites with Y_2O_3Additives using Design of Experiments," Ceram. Int., 37, 1985-1992 (2011).

[18] J. Li, J. Peng, S. Guo, and L. Zhang, "Application of Response Surface Methodology (RSM) for Optimization of Sintering Process for the Preparation of Magnesia Partially Stabilized Zirconia (Mg-PSZ) using Natural Baddeleyite as Starting Material," Ceram. Int., 39, 197-202 (2013).

[19] C. Fernandez, E. Verne, J. Vogel, and G. Carl, "Optimisation of the Synthesis of Glass-Ceramic Matrix Biocomposites by the Response Surface Methodology," J. Eur. Ceram. Soc., 23, 1031-1038 (2003).

[20] J. Li, J. Peng, S. Guo, and L. Zhang, "Application of Response Surface Methodology (RSM) for Optimization of the Sintering Process of Preparation Calcia Partially Stabilized Zirconia (CaO-PSZ) using Natural Baddeleyite," J. Alloy. Compd., 574, 504–511 (2013).

[21] A. H. De Azaa, J. Chevaliera, G. Fantozzi, M. Schehl, and R. Torrecillas, "Crack Growth Resistance of Alumina, Zirconia and Zirconia Toughened Alumina Ceramics for Joint Prostheses," Biomaterials, 23, 937–945 (2002).

[22] S. M. Kurtz, S. Kocagöz, C. Arnholt, R. Huet, M. Ueno, and L. William, "Advances in Zirconia Toughened Alumina Biomaterials for Total Joint Replacement," J. Mech. Behav. Biomed. Mater., 31, 107-16 (2014).

[23] R. Huet, A. Sakona, and S. M. Kurtz, "Strength and Reliability of Alumina Ceramic Femoral Heads: Review of Design, Testing, and Retrieval Analysis," J. Mech. Behav. Biomed. Mater., 4, 476-483 (2011).

---

[24] G. Pezzotti, and K. Yamamoto, “Artificial Hip Joints: The Biomaterials Challenge,” J. Mech. Behav. Biomed. Mater., 31, 3-20 (2014).

[25] M. Slonaker, and T. Goswami, “Review of Wear Mechanisms in Hip Implants: Paper II – Ceramics IG004712,” Mater. Des., 25, 395–405(2004).

[26] T. S. Huang, M. N. Rahaman, and B. S. Bal, “Alumina–Tantalum Composite for Femoral Head Applications in Total Hip Arthroplasty,” Mater. Sci. Eng. C, 29, 1935–1941(2009).

[27] Y. Zheng, H. Li, T. Zhou, J. Zhao, and P. Yang, “Microstructure and Mechanical Properties of Al_2O_3/ZrO_2 Eutectic Ceramic Composites Prepared by Explosion Synthesis,” J. Alloy. Compd., 551, 475–480 (2013).

[28] B. Basu, J. Vleugels, and O. V. D. Biest, “ZrO_2–Al_2O_3Composites with Tailored Toughness,” J. Alloy. Compd., 372, 278–84(2004).

[29] H. Mills, and S. Blackburn, “Zirconia Toughened Aluminas by Hydro-Thermal Processing,” J. Eur. Ceram. Soc., 20, 1085-1090(2000).

[30] B. S. Reddy, D. Sarkar, B. Basu, Response Surface Modelling of Sintering Parameter and Compositional Optimization for Zirconia Toughened Alumina Composite,”(Unpublished data).

[31] B. Basu, J. Vleugels, and O.V.D. Biest, “Transformation Behaviour of Tetragonal Zirconia: Role of Dopant Content and Distribution,” Mater. Sci. Eng. A, 366, 338–347(2004).

[32] D. Sarkar, S. Adak, and N.K. Mitra, “Preparation and Characterization of an Al_2O_3–ZrO_2 Nanocomposite, Part I: Powder Synthesis and Transformation Behavior during Fracture,” Composites A, 38,124-131(2007).

---

[33] D. Casellas, M. M. Nagl, L. Llanes, and M. Anglada, “Fracture Toughness of Alumina and ZTA Ceramics: Microstructural Coarsening Effects,” J. Mater. Process. Tech., 143–144, 148–152(2003).

[34] P. G. Rao, M. Iwasa, T. Tanaka, I. Kondoh, and T. Inoue, “Preparation and Mechanical Properties of Al_2O_3–15wt.% ZrO_2 Composites,” Scripta Mater., 48,437–441(2003).

[35] X.W. Huang, S.W. Wang, and X.X. Huang, “Microstructure and Mechanical Properties of ZTA Fabricated by Liquid Phase Sintering,” Ceram. Int., 29, 765–769(2003).

[36] O. Roualdes, M. E. Duclos, D. Gutknecht , L. Frappart, J. Chevalier , and D. J. Hartmann, “*In vitro* and *In vivo* Evaluation of an Alumina-Zirconia Composite for Arthroplasty Applications,”Biomaterials, 31, 2043-2054(2010).

[37] X. He, Y.Z. Zhang, J. P. Mansell, and B. Su, “Zirconia Toughened Alumina Ceramic Foams for Potential Bone Graft Applications: Fabrication, Bioactivation, and Cellular Responses,” J. Mater. Sci. Mater. Med., 19, 2743-2749 (2008).

[38] A. Vallee, M.G. Faga, F. Mussano, F. Catalano, E. Tolosano, S. Carossa, F. Altruda, and G. Martra, “Alumina-Zirconia Composites Functionalized with laminin-1 and laminin-5 for Dentistry: Effect of Protein Adsorption on Cellular Response,” Colloids Surf. B Biointerfaces., 114, 284-293 (2014).

[39] S. Affatato, R. Torrecillas, P. Taddei, M. Rochhi, C. Fagnano, G. Ciapetti, and A. Toni, “Advanced Nanocomposite Materials for Orthopaedic Applications I. a Long-Term *In vitro* Wear Study of Zirconia-Toughened Alumina,” J. Biomed. Mater. Res. B Appl. Biomater., 78, 76-82 (2005).

[40] L. Esposito, R. Moreno, A. J. S. Herencia, and A. Tucci, “Sliding Wear Response of an Alumina-zirconia System,” J. Eur. Ceram. Soc., 18, 15-22 (1998).

---

[41] B. Kerkwijk, A. J. A. Winnubst, H. Verweij, E. J. Mulder, H. S. C. Metselaar, and D. J. Schipper, “Tribological Properties of Nanoscale Alumina–Zirconia Composites,” Wear, 225–229, 1293–1302(1999).

[42] J. F. Bartolome, C. Pecharroman, J. S. Moyaa, A. Martın, J. Y. Pastor, and J. Llorca, “Percolative Mechanism of Sliding Wear in Alumina/Zirconia Composites,” J. Eur. Ceram. Soc., 26, 2619-2625 (2006).

[43] S. Bueno, B. Ferrari, C. Melandri, G. De Portu, and C. Baudín, “Processing of alumina-Coated Tetragonal Zirconia Materials and their Response to Sliding Wear,” Ceram. Int., 36, 1545-1552 (2010).

[44] Y. J. He, A. J. A. Winnubst, A. J. Burggraaf, H. Venveij, P. G. T. V. D. Varst and G. D. With, “Sliding Wear of ZrO_2-Al_2O_3 Composite Ceramics,” J. Eur. Ceram. Soc., 00, 1371-80 (1997).

[45] Y. J. He, A. J. A. Winnubst, D. J. Schipper, P. M. V. Bakker, A. J. Burggraaf, and H. Verweij, “Friction and Wear Behaviour of Ceramic-Stainless Steel Couples under Reciprocating Sliding Motion,” Wear, 184, 33-43 (1995).

[46] H. Fan, T. Hu, Y., Zhang, and Y. Fang, “Tribological Properties of Micro-Textured Surfaces of ZTA Ceramic Nanocomposites under the Combined Effect of Test Conditions and Environments,” Tribol. Inter., 78, 134–141 (2014).

[47] Y. S. Wang, C. He, B. J. Hockey, P. I. Lacey, and S. M. Hsu, “Wear Transitions in Monolithic Alumina and Zirconia-Alumina composites,” Wear, 181-183, 156-164 (1995).

[48] G. M. Hamilton, “Explicit Equations for the Stresses beneath a Sliding Spherical Contact,” Proc. Inst. Mech. Engrs., 197 C, 53 (1983).

---

[49] Yoshida, H., A. Faust, J. Wilckens, M. Kitagawa, J. Fetto, and E. Y. S. Chao, "Three-Dimensional Dynamic Hip Contact Area and Pressure Distribution during Activities of Daily Living," J. Biomech., 39, 1996-2004 (2006).

[50] K. Volokh, Y., H. Yoshida, A. Leali, J. F. Fetto, and E. Y. Chao, "Prediction of Femoral Head Collapse in Osteonecrosis," J.Biomech.Eng.,128, 467-470 (2006).

[51] J. Daniel, H. Ziaee, A. Salama, C. Pradhan, and D. J. W. McMinn, "The Effect of the Diameter of Metal-on-Metal Bearings on Systemic Exposure to Cobalt and Chromium," J. Bone & Joint Surg., 88, 443-448 (2006).

[52] M. Jasty, C. R. Bragdon, K. Lee, A. Hanson, and W. H. Harris, "Surface Damage to Cobalt-Chrome Femoral Head Prostheses," J. Bone & Joint Surg., 76, 73-77 (1994).

[53] D. Najjar, M. Bigerelle, H. Migaud, and A. Iost, "About the Relevance of Roughness Parameters used for Characterizing Worn Femoral Heads," Tribol. Int., 39, 1527-1537 (2006).

[54] P. Christel, A. Meunier, J.M. Dorlot, J.M. Crolet, J. Witvoet, L. Sedel, and P. Boutin, "Biomechanical Compatibility and Design of Ceramic Implants for Orthopedic Surgery," Ann. N. Y. Acad. Sci., 523, 234-256 (1988).

[55] Y. S. Park, S. K. Hwang, W. S. Choy, Y. S. Kim, Y. W. Moon, and S. J. Lim, "Ceramic Failure after Total Hip Arthroplasty with an Alumina-on-Alumina Bearing," J. Bone & Joint Surg., 88, 780-787 (2006).

[56] A. H. De Aza, J. Chevalier, G. Fantozzi, M. Schehl, and R. Torrecillas, "Crack Growth Resistance of Alumina, Zirconia and Zirconia Toughened Alumina Ceramics for Joint Prostheses," Biomater., 23, 937-945(2002).

[57] R. Benzaid, J. Chevalier, M. Saâdaoui, G. Fantozzi, M. Nawa, L. A. Diaz, and R. Torrecillas, "Fracture Toughness, Strength and Slow Crack Growth in a Ceria Stabilized

---

Zirconia–Alumina Nanocomposite for Medical Applications," Biomater., 29, 3636-3641 (2008).

[58] S. Deville, J. Chevalier, G. Fantozzi, J. F. Bartolomé, J. Requena, J. S. Moya, R. Torrecillas, and L. A. Díaz, "Low-Temperature Ageing of Zirconia-Toughened Alumina Ceramics and its Implication in Biomedical Implants," J. Eur. Ceram. Soc., 23, 2975-2982 (2003).

[59] C. Piconi, W. Burger, H. G. Richter, A. Cittadini, G. Maccauro, V. Covacci, N. Bruzzese, G. A. Ricci, and E. Marmo, "Y-TZP Ceramics for Artificial Joint Replacements," Biomater., 19, 1489-1494 (1998).

[60] N. Matsunaga, K. Azeyanagi, I. Sogaishi, T. Katakura, Y. Ueda, and T. Ohsawa, "Method of Making Bone-Implants," US Patent 5336465, 1994.

[61] M. Abouaf, E. Lilley, D. Urffer, B. Cales, O. H. Kwon, and Y. Stefani, "Hip Joint Prosthesis Having a Zirconia Head and a Ceramic Cup," US20020013625 A1, 2002.

[62] W. Glien, T. Oberbach, and C. Ortmann, "Ceramic Endoprosthesis Components and Processes for their Production," US Patent 20050187638A1, 2005.

[63] A. A. N. Valdez, W. M. Rainforth, and T. D. Stewart, "Wear and Degradation on Retrieved Zirconia Femoral Heads," J. Mech. Behav. Biomed. Mater., 31, 145-151 (2014).

[64] S. Chowdhury, Y. K. Vohra, J. E. Lemons, M. Ueno, and J. Ikeda, "Accelerating Aging of Zirconia Femoral Head Implants: Change of Surface Structure and Mechanical Properties," J. Biomed. Mater. Res. Part B: Appl. Biomater., 81, 486-492 (2007).

[65] S. M. Kurtz, S. Kocagöz, C. Arnholt, R. Huet, M. Ueno, and W. L. Walter, "Advances in Zirconia Toughened Alumina Biomaterials for Total Joint Replacement," J. Mech. Behav. Biomed. Mater., 31, 107-116 (2014).

---

[66] R. Huet, A. Sakona, and S. M. Kurtz, "Strength and Reliability of Alumina Ceramic Femoral Heads: Review of Design, Testing, and Retrieval Analysis," J. Mech. Behav. Biomed. Mater., 4, 476-483 (2011).

[67] G. Magnani, and A. Brillante, "Effect of the Composition and Sintering Process on Mechanical Properties and Residual Stresses in Zirconia–Alumina Composites," J. Eur. Ceram. Soc., 25, 3383-3392 (2005).

[68] F. Sommer, R. Landfried, F. Kern, and R. Gadow, "Mechanical Properties of Zirconia Toughened Alumina with 10–24vol.% 1Y-TZP Reinforcement," J. Eur. Ceram. Soc., 32, 3905-3910 (2012).

[69] S. Affatato, R. Torrecillas, P. Taddei, M. Rocchi, C. Fagnano, G. Ciapetti, and A. Toni, "Advanced Nanocomposite Materials for Orthopaedic Applications. I. A Long-Term In Vitro Wear Study of Zirconia-Toughened Alumina," J. Biomed. Mater. Res. Part B: Appl. Biomater., 78 (1) 76-82 (2006).

[70] C. Piconi, G. Maccauro, F. Muratori, and E. B. O. Prever, "Alumina and Zirconia Ceramics in Joint Replacements," J. Appl. Biomater. Biomech., 1, 19-32 (2003).

[71] T. V. Zhil'tsova, M. S. A. Oliveira, and J. A. F. Ferreira, "Relative Influence of Injection Molding Processing Conditions on HDPE Acetabular Cups Dimensional Stability," J. mater. process. technol., 209, 3894-3904 (2009).

[72] R. Singh, S. Singh, and G. Singh, "Dimensional Accuracy Comparison of Investment Castings Prepared with Wax and ABS Patterns for Bio-medical Application," Proc. Mater. Sc., 6, 851-858(2014).

[73] M. J. Mathias, and K. Tabeshfar, "Design and Development of a New Acetabular Cup Prosthesis," Mater. Sc. Eng. C, 26, 1428-1433 (2006).

---

[74]L. E. Murr, S. M. Gaytan, E. Martinez, F. Medina, and R. B. Wicker, “Next Generation Orthopaedic Implants by Additive Manufacturing using Electron Beam Melting,” Int. J. Biomat., 2012, (2012).

[75]K. Maezawa, M. Nozawa, T. Hirose, K. Matsuda, M. Yasuma, K. Shitoto, H. Kurosawa, “Cobalt and Chromium Concentrations in Patients with Metal-On-Metal and other Cementless Total Hip Arthroplasty,” Arch. Orthop. Traum. Su., 122, 283-287 (2002).

[76]J. E. Nevelos, E. Ingham, C. Doyle, A. B. Nevelos, and J. Fisher, “The Influence of Acetabular Cup Angle on the Wear of “BIOLOX Forte” Alumina Ceramic Bearing Couples in a Hip Joint Simulator,” J. Mater. Sci. Mater. Med., 12, 141-144 (2001).

[77]V. Saikko, T. Ahlroos, H. Revitzer, O. Ryti, and P. Kuosmanen, “The Effect of Acetabular Cup Position on Wear of a Large-Diameter Metal-on-Metal Prosthesis Studied with a Hip Joint Simulator,” Tribol. Int., 60, 70-76 (2013).

[78]J. Minguella, D. Cuiñas, J. V. Rodríguez, and J. Vivancos, “Advanced Manufacturing of Ceramics for Biomedical Applications: Subjection Methods for Biocompatible Materials,” Proc. Eng., 63, 218-224 (2013).

[79] S. Caldarise, “Hip Joint Prostheses and Methods for Manufacturing the Same,” U.S. Patent 5,549,697, (1996).

[80] M. Kumar, “Plasma Spraying Working Surface (Mandreal) with Mixture of Al_2O_3 and TiO_2 and/or Ti, as Thickness Builds Up, the Relative Amount of Aluminum Oxide is Decreased such that the Composition is all Ti and TiO_2, after Desired Thickness, the Acetabular Shell is Extracted from Mandreal; Hip Implant,” U.S. Patent 7,655,162, (2010).

[81]E. S. N. Lopes, J. C. Rodrigo, S. T. Button, and R. Caram, “Femoral Hip Stem Prosthesis made of Graded Elastic Modulus Metastable β Ti Alloy,” Mater. Design, 69, 30-36 (2015).

---

[82] D. Abdelkader, B Mostefa, A. Abdelkrim, T. Abderrahim, B. Noureddine, and B. Mohamed, “Fatigue Life Prediction and Damage Modelling of High-density Polyethylene under Constant and Two-block Loading,” Procedia Eng., 101, 2-9(2015).

[83] G. K. Triantafyllidis, A. V. Kazantzis, and K. T. Karageorgiou, “Premature Fracture of a Stainless Steel 316l Orthopaedic Plate Implant by Alternative Episodes of Fatigue and Cleavage Decoherence,” Eng. Fail. Anal., 14, 1346-1350(2007).

[84] J. Geringer, B. Forest, and P. Combrade, “Fretting-corrosion of materials used as orthopaedic implants,” Wear, 259, 943-951(2005).

[85] G.A. Afolaranmi, J. Tettey, R. M. D. Meek, and M. H. Grant, “Release of Chromium from Orthopaedic Arthroplasties,” Open Orthopaed. J., 2, 10-18(2008).

[86] M. Semlitsch, “Titanium Alloys for Hip Joint Replacements,” Clin. mater., 2, 1-13(1987).

[87] V. Sansone, D. Pagani, and M. Melato, “The Effects on Bone Cells of Metal Ions Released from Orthopaedic Implants. A Review,” Clin. Case. Miner. Bone Met., 10, 34(2013).

Chapter 3

Composition and Process Optimization of ZTA

The properties and performance of a ceramic component significantly depends on the microstructue (grain size) and sinter density. While developing new ceramics for structural applications, it is therefore important to optimize both the process parameters (sintering temperature, sintering time) and material parameters (sinter–aid addition and reinforcement content) to tailor grain size and density, while obtaining tough and strong materials. The optimization of all these parameters is commonly pursued using trial-and-error approach or one-time-variable method. In this perspective, the present work demonstrates the effectiveness of response surface methodology (RSM) as a numerical tool to adequatly predict the sinter density and grain size of a model ceramic, Al_2O_3 which is densified using MgO sinter-aid together with ZrO_2 particulate addition (second phase). Based on the consideration of the fundamental densification-grain size relationship and using the predictive linear, quadratic or interactive response among the process and material parameters, the adopted approach is shown to provide excellent capability to predict sinter density and grain size with significant statistical correlation between experimental and predicted values. In view of the demostrated robustness, the adopted analytical approach can be extened to other ceramic systems.

3.1 Model description

3.2.1 Parameter identification and formulation of design matrix

The powder compaction by uniaxial pressing and the sintering of a powder compact is a common practice in lab-scale research as well as fabrication of small-scale commercial ceramic components. The identification of composition and sintering schedule has always been a challenging task for a particular application of interest. In the present work, the preparation of ZTA specimens has been pursued by the identification of process parameters and their optimization by design of experiment (DOE). DOE targets two types of factors (input variables), say qualitative and quantitative in order to achieve the best fit within experimental and predicted data. The factors including zirconia content, grain growth inhibitor MgO are considered as prime qualitative factors; whereas sintering temperature and sintering time represent quantitative factors. However, other processing factors such as particle morphology, surface area of particles, mixing time, PVA content, drying time, pressing load, pressing dwell time, heating rate, and cooling rate are kept constant.[1] Moreover, other external effects, like material mixing methods or tools, instrumental errors, measurement errors, operator errors, power surges, and furnace consistency are considered as uncontrollable or noise factor, as shown in Fig. 3.1.

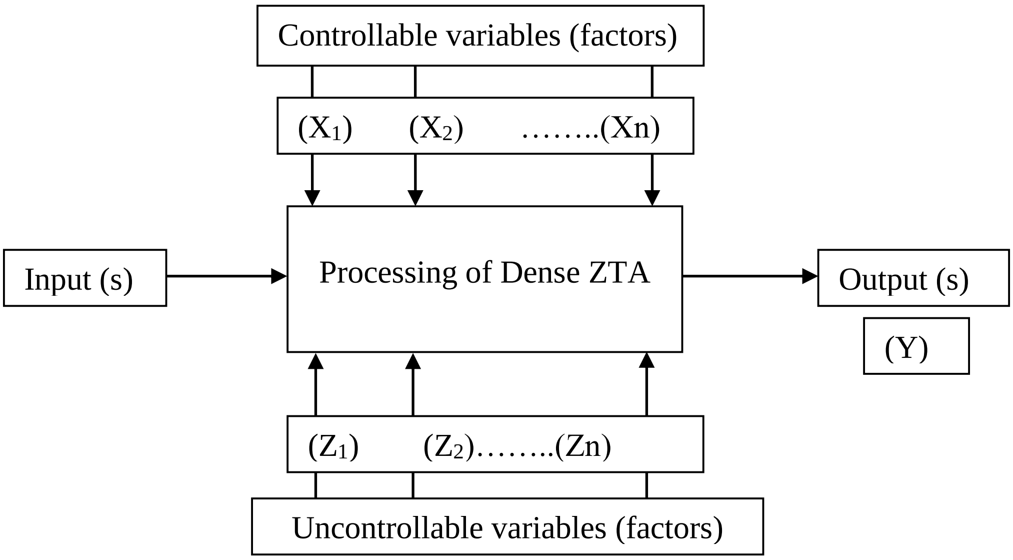

Fig. 3.1: General model for the processing of sintered ZTA; illustration of a relation within controllable, uncontrollable, input and output variables.

The level for qualitative factors is similar to quantitative factors since the source of ZrO_2 and MgO is constant in the proposed set of experiments. The present modelling approach, therefore, considers four factors and their five levels. For any valid prediction in pure experimental approach, one therefore has to carry out a large number of experiments (5^4 = 625) to arrive at a conclusion for the present case. The influence of one variable at-a-time has constrained to draw a conclusion on the output response when a large number of process variables and their interaction characteristics need to be considered. The selected process factors are varied over five levels as the high level (+2), low level (-2) and the intermediate levels (+1, 0, -1) since these ranges have connotation on both the targeted responses. The selected independent factors and their chosen region of levels are reported in the present work and are shown in Table 3.1.

Table 3.1: Description of input variables or factors (Temperature, Time, ZrO_2 and MgO content) and their assigned levels (1450 – 1650^{o}C, 0 – 8hr, 0 – 20wt% and 200 – 1000 ppm) with equal intervals.

Sl. No.	Input Factor	Denotation	Units	Levels coded -2	 -1	 0	 +1	 +2
1	Temperature	A	^{o}C	1450	1500	1550	1600	1650
2	Time	B	hours	0	2	4	6	8
3	Zirconia	C	wt%	0	5	10	15	20
4	MgO	D	ppm	200	400	600	800	1000

For the convenience of recording and processing the experimental data, the upper and lower levels of the factors are coded as +2 and -2, respectively, and the coded values of any intermediate level can be calculated using the following expression,

$$Xi \ = \frac{Xact - \ \bar{X}}{\frac{Xmax - Xmin}{4}} - -(1)$$

Where X_i is the required coded value of a parameter of any value X from X_{min} (lower level of the parameter) and X_{max} (upper level of the parameter). Similarly, X_{act} is the actual value of the parameter, and $\bar{X}$ is the average value of X_{max} and X_{min} value of the parameter. Herein, X_{min} and X_{max} are temperature (1450^{o}C and 1650 ^{o}C), time (0h and 8h), zirconia (0 wt% and 20 wt %) and MgO (200 ppm and 1000 ppm), and their background is given below.

Concerning sintering temperatures, two values i.e. 1450 to 1650^{o}C were considered as lower and upper limit, respectively. It has been observed that commercially accepted ZTA is a promising candidate for the development of orthopedic prosthesis like femoral ball head and acetabular socket.[2] The main purpose of ZrO_2 in alumina matrix is to restrict the grain size of the alumina matrix without any agglomeration and enhance the mechanical properties like fracture toughness. However, *in vivo* hydrolysis reduces the mechanical response of tetragonal zirconia.[3] In the same time, it is essential to select the zirconia content below the percolation threshold, i.e. below 22 wt.%, similarly, avoid the agglomeration of material that also restrict the ageing degradation of ZrO_2. Herein, an equal interval of 5wt% variation has been considered according to DoE. Similarly, MgO has chosen to minimize the abnormal grain growth of alumina and better densification through some degree of limit. However, an excess amount MgO can react with alumina matrix and form $MgAl_2O_4$ spinel that further may reduce the hardness and fracture toughness. Also, equal intervals of five levels (200 – 1000 ppm) upto 1000 ppm have been considered and limited in current state-of-art.[4,5]

Beyond the consideration of factors and levels, a design matrix is needed to generate from the selected factors and levels to conduct real life experiments and to understand the effects of input variables. In this circumstance, the mathematical model is generated with the aid of response surface methodology (RSM), because it is widely suitable for multi-level and multi-variable models. Central composite design (CCD) is a class of response surface methodology, which explains the basis of 31 sets of response data and their comparative analysis from the experimental runs. In the present case, this design model is scattered into 16 cube points, 8 axial points, 7 centre points, and alpha considered as 2, where complete randomized experimental design removes the experimental bias. The cube points are originated from a full factorial design using 2^{factors} (here factor = 4) and the combinations of +1 and -1 levels of the process parameters. Similarly, screen analysis is employed to design the axial points. It generates 2 x factors with sample points by using the $+ \propto$ or $- \propto$ for all factors and all other variables at their nominal value. The alpha is selected by the equation of the square root of factors.

Table 3.2: Design matrix including coded value represents different 31 set of experiments within restricted levels, and their estimated and predicted response Relative Density, Grain size are designated as RD and GS, respectively.

Serial No	Coded Form				Experimental RD	Predicted RD	% Error	Experimental GS	Predicted GS	% Error
	A	B	C	D						
1	-1	-1	-1	-1	87.92	87.78	0.16	1.24	1.31	-5.72
2	1	-1	-1	-1	92.66	92.04	0.67	2.38	2.25	5.56
3	-1	1	-1	-1	91.35	90.54	0.88	1.41	1.29	8.60
4	1	1	-1	-1	98.16	98.09	0.07	3.25	3.09	5.04
5	-1	-1	1	-1	88.97	88.06	1.02	1.18	1.15	2.51
6	1	-1	1	-1	91.82	92.67	-0.93	1.75	1.77	-0.86
7	-1	1	1	-1	89.29	88.98	0.34	1.24	1.10	11.78
8	1	1	1	-1	96.71	96.88	-0.18	2.77	2.58	6.94
9	-1	-1	-1	1	87.65	86.91	0.85	1.17	1.21	-3.44
10	1	-1	-1	1	92.77	92.87	-0.11	2.07	2.09	-1.20
11	-1	1	-1	1	90.41	89.35	1.18	1.49	1.36	9.14
12	1	1	-1	1	98.25	98.59	-0.35	3.23	3.11	3.80
13	-1	-1	1	1	87.78	87.64	0.16	1.04	1.08	-4.07
14	1	-1	1	1	93.71	93.95	-0.25	1.68	1.65	1.86
15	-1	1	1	1	88.18	88.23	-0.06	1.23	1.21	1.63
16	1	1	1	1	97.89	97.82	0.07	2.83	2.64	6.80
17	-2	0	0	0	81.17	82.81	-2.03	1.04	1.06	-1.26
18	2	0	0	0	97.54	96.67	0.89	3.17	3.43	-8.23
19	0	-2	0	0	87.96	88.26	-0.34	1.17	1.03	11.75
20	0	2	0	0	94.42	94.90	-0.51	1.58	1.99	-25.95
21	0	0	-2	0	92.19	93.30	-1.20	2.02	2.15	-6.61
22	0	0	2	0	93.15	92.82	0.36	1.38	1.52	-10.18
23	0	0	0	-2	92.66	93.18	-0.56	1.44	1.65	-14.79
24	0	0	0	2	93.00	93.26	-0.28	1.55	1.61	-3.95
25	0	0	0	0	90.29	91.60	-1.45	1.70	1.65	2.91
26	0	0	0	0	91.56	91.60	-0.04	1.60	1.65	-3.48
27	0	0	0	0	91.27	91.60	-0.36	1.57	1.65	-5.33
28	0	0	0	0	91.80	91.60	0.22	1.56	1.65	-6.21
29	0	0	0	0	92.31	91.60	0.77	1.63	1.65	-1.08
30	0	0	0	0	92.27	91.60	0.73	1.55	1.65	-6.42
31	0	0	0	0	91.70	91.60	0.11	1.96	1.65	15.52

However, experimental level enhances beyond the selection region to pursue the number of runs and subsequent formulation of their regression function for the developed region. The nominal design concept is used to generate the centre points, where all process variables are made at zero level. It is also called as consistent design matrix to check the predicted response value variance and tried to keep variance in the middle and edge nearly same. The CCD experimental design matrix and dependent responses are depicted in Table 3.2. The % error of the relative density and grain size describes how the experimental and predicted values are close each other. In order to calculate the % error, following formula was used.

$$\%\ \text{error} = \frac{\text{Experimental values} - \text{Predicted values}}{\text{Experimental values}} - -(2)$$

In obvious, the experimental and predicted (mathematical) values are not always same in practical. A wide range of calculation predicts the existence of both +ve and –ve signs for percentage (%) error. When the experimental values are greater than the predicted values, then % error sign is positive and vice versa. A close % error exhibits between the experimental and predicted values. Negative (-ve) % error indicates that still there is a chance to enhance the experimental values in compare with predicted values.

3.2.2 Evaluation of regression coefficients

This section describes a technique for the determination of regression coefficients from coded factors for the relative density and grain size. Least square method is typically used to estimate the regression coefficients in a second order polynomial regression model, where Y_1, Y_2....Y_{31} represents the experimental observation of responses for individual 1, 2....31 number of batches, respectively. The regression equations used in the present case can be represented as follows;

$Y_1 = \beta_0+\beta_1A_1+\beta_2B_1+\beta_3C_1+\beta_4D_1+\beta_{12}A_1B_1+\beta_{13}A_1C_1+\beta_{14}A_1D_1+\beta_{23}B_1C_1+\beta_{24}B_1D_1+\beta_{34}C_1D_1+$ $\beta_{11}A_1A_1+\beta_{22}B_1B_1+ \beta_{33}C_1C_1+\beta_{44}D_1D_1+\varepsilon_1$................. (3)

$Y_2 = \beta_0+\beta_1A_2+\beta_2B_2+\beta_3C_2+\beta_4D_2+\beta_{12}A_2B_2+\beta_{13}A_2C_2+\beta_{14}A_2D_2+\beta_{23}B_2C_2+\beta_{24}B_2D_2+\beta_{34}C_2D_2+$ $\beta_{11}A_2A_2+\beta_{22}B_2B_2+ \beta_{33}C_2C_2+\beta_{44}D_2D_2+\varepsilon_2$................. (4)

$Y_3=\beta_0+\beta_1A_j+\beta_2B_j+\beta_3C_j+\beta_4D_2+\beta_{12}A_jB_j+\beta_{13}A_jC_j+\beta_{14}A_jD_j+\beta_{23}B_jC_j+\beta_{24}B_jD_j+\beta_{34}C_jD_j+\beta_{11}A_jA_j+$ $\beta_{22}B_jB_j+ \beta_{33}C_jC_j+\beta_{44}D_jD_j+\varepsilon_j$................. (5) (where, $j = 1,2,3\ldots31$)

………………………………………..

....

$Y_{31} = \beta_0+\beta_1A_{31}+\beta_2B_{31}+\beta_3C_{31}+\beta_4D_{31}+\beta_{12}A_{31}B_{31}+\beta_{13}A_{31}C_{31}+\beta_{14}A_{31}D_{31}+\beta_{23}B_{31}C_{31}+\beta_{24}B_{31}D_{31}+$ $\beta_{34}C_{31}D_{31}+ \beta_{11}A_{31}A_{31}+\beta_{22}B_{31}B_{31}+\beta_{33}C_{31}C_{31}+\beta_{44}D_{31}D_{31}+\varepsilon_{31}$.................(6)

Where β_0 is the average of the observations; β_1, β_2, β_3 and β_4 are independent parameter related regression co-efficient; β_{12}, β_{13}, β_{14}, β_{23}, β_{24} and β_{34} are interaction parameter related regression co-efficient; β_{11}, β_{22}, β_{33} and β_{44}-square parameter related regression co-efficient. Thus, the least square normalised equation can be simplified by matrix notation $[Y]=X\beta+[\varepsilon]$, where Y is a vector of observations, ε is a vector of errors; X is the design matrix of the values of the design variables and β is the vector of regression coefficients. In the current model, a second order polynomial regression equation consists of 15 numbers of regression coefficients including empirical constant, linear, interaction and quadratic terms, which represent an as simple (15x1) matrix. Therefore, the developed design matrix (31x15) can be effectively reduced to (15x1) matrix by least square method, where error factor 'ε' is random and unobserved. It is worthy to mention that the following vector size has been considered in our model.

Y - column vector of size 31 x 1,

β -column vector of size 15 x 1,

X -column vector of size 31 x 15,

And ε- column vector of size 31 x 1.

Hence, $Y = X\beta + \varepsilon$ is reduced to $\beta = X^{-1} Y$, where $X^{-1} = [X^T X]^{-1}$ and $Y = [X^T Y]$. Based on four factors and their five levels, the design matrix (X) as well as the various relevant matrices are defined and discussed with the help of consecutive six tables, Table A1 to Table A6.

As discussed in above, various parameters in the design matrix (X) are defined in Table A1. As per the central composite design of RSM statistical tool, 31 number of experiments were conducted on the basis of the permutation and combination arrangement of four input variables temperature (A), time (B), zirconia (C) and magnesia (D) for 5 levels of these variables. Herein, the expected [31 x 5] matrix is enhanced upto the [31 x 15] due to the probable influence of individual and interaction of factors to predict the selective response characteristics. The same method of optimization has been followed for both the response relative density and alumina grain size of ZTA. In the second order polynomial regression equation, 31 algebraic equations are available with 15 unknown regression coefficients.

3.2 Experimental Validation

3.2.1 Sintering of ZTA

In reference to the design matrix of experiments, as given in Table 3.2, the samples were prepared with different compositions of alumina (Sumitomo, Japan, AKP – 5N, 120nm, 99.999% purity), zirconia (Tosoh, Japan, 3Y-E, 50nm, >99.9%), $Mg(NO_3)_2.6H_2O$ (Sigma Aldrich, >99.9% trace metal basis), and constant 3wt% of polyvinyl alcohol (PVA) binder. Thirty one sets and six disks for each set with different compositions were prepared from the above raw materials (see Table 3.2). The different compositions of powders were blended thoroughly and uniformly with a constant amount of 3 wt% PVA solution using standard powder metallurgical route and dried in an oven at 80°C for one hour. The dried mixed powder was poured in the mould of ϕ12 mm and pressed under hydraulic-uniaxial press at 5 ton load for 120 sec dwell time. The total number of (31 x 6 = 186) green specimens with approximate geometrical dimensions ϕ12 mm X ~4 mm in thickness were prepared. The relative green density was varied within the range of 50 ± 2%. The green specimens were sintered according to the experimental design matrix, as illustrated in Table 3.2. The sintering profile up to peak temperature and their cooling from the peak temperature were identical for each batch of specimens, where the binder removal and pre-sintering stages were maintained carefully and uniformly. Simple cylindrical shaped disc with 25 mm diameter, rectangular bar (length - 50mm, width - 7mm, thickness - 4mm), and complicated femoral head – acetabular socket was also prepared from optimized composition and process parameters.

3.2.2 Physical Properties Characterization

The density of sintered samples was determined by Archimedes' principle. Linear and volume shrinkage were also measured through geometrical method from before and after sintering of cylindrical disk specimens. Two sintered specimens from each batch were ground on silicon carbide 800, 1000 and 1200 grit mounted disks systematically prior to polishing by diamond paste. Diamond paste up to 1µm was used to achieve mirror polished specimens. All the specimens were cleaned by ethanol in ultrasonicator, followed by thermal etching for 30 minutes at a temperature below 50°C to peak sintering temperature. The microstructure was taken from different zone of the thermally etched specimens by scanning electron microscope (Jeol JSM 6480LV, Japan) at 15KV accelerating voltage in backscattered mode.

3.2.3 Microstructure Characterizations

Grain size was measured from the average of near to 500 numbers of grains from a different zone of microstructures. The measured alumina and zirconia grain sizes including other parameters of optimum dense specimens are shown in Table 3.3. Herein, the grain size measurement was further evaluated by rectangular intercept procedure consist of minimum1000 number of grains, and their average grain size, G, is represented by;

$$G = \sqrt{\frac{4A}{\pi\left(ni + \frac{no}{2}\right)}} - -(7)$$

Where, A is the area of rectangular, n_i and n_o are the grain numbers in the rectangular and on the rectangular boundary, respectively.[6] A standard deviation including average grain size has been measured and reported in Table 3.4. The obtained value is found near to the line intercept method.

Table 3.3: Highest relative density and grain size for both alumina and zirconia are optimized through RSM and listed with respect to factors.

Sample No.	Input Variable				Output Variables				
	Temperature (°C)	Time (h)	Wt% of Zirconia	MgO (ppm)	Bulk Density	Linear Shrinkage	Volume Shrinkage	Grain Size Al_2O_3	Grain Size ZrO_2
4	1600	6	5	400	98.16	20.25	49.34	3.25±1.00	1.24±0.33
8	1600	6	15	400	96.71	20.00	48.45	2.77±1.02	1.28±0.35
12	1600	6	5	800	98.25	19.83	48.68	3.23±1.11	0.90±0.26
16	1600	6	15	800	97.89	20.08	48.75	2.83±1.00	1.13±0.40

3.3 Results

3.3.1 FESEM micrographs of pure Al_2O_3 and ZrO_2 Powder

Fig. 3.2 a & b represents SEM micrographs of pure Al_2O_3 and TZ-3Y-E powders, respectively. As can be seen, the precursor Al_2O_3 powder revealed a homogeneous primary particle size near to 120 nm with consists of partial soft agglomeration (Fig. 3.2a). In another end, the TZ-3Y-E powder is formed of particles with a mean diameter of 50 nm (Fig. 3.2b) that appears near spherical in shapes. Taken together with this class of alumina and zirconia particles, details sintering study were conducted to optimize the density and relevant grain size of ZTA followed by fabrication of robust femoral head and acetabular socket prototypes.

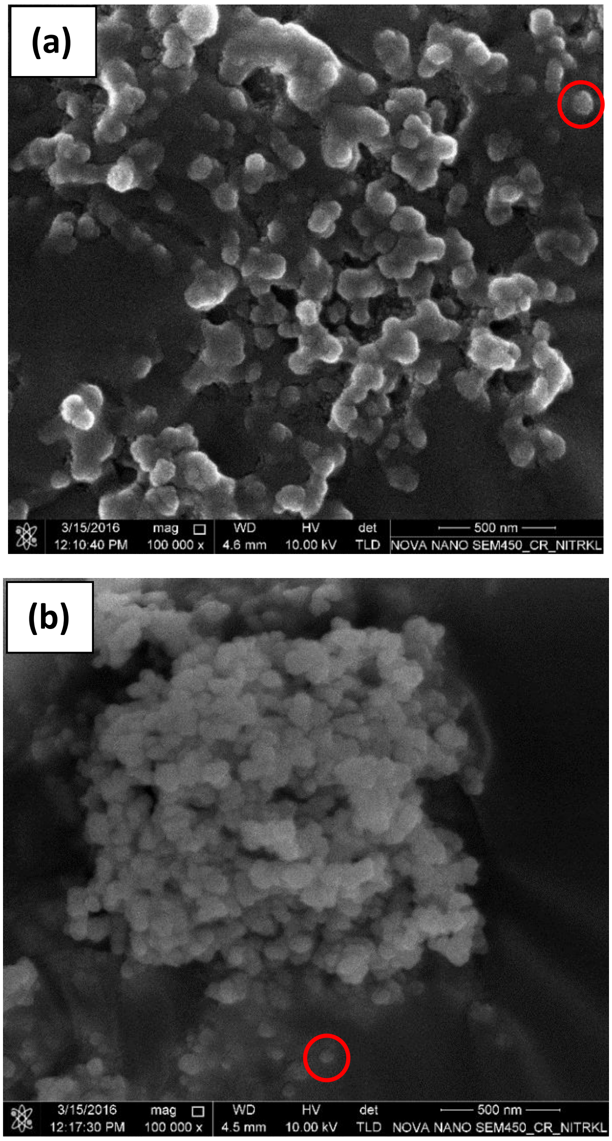

Fig. 3.2: FESEM image of starting particles of (a) Alumina and (b) Zirconia. The red circle indicates the morphology of single particle.

3.3.2 Data simulation and generation of the mathematical model

The response is either relative density (RD) or grain size (GS) of the ZTA specimens. The responses are represented as a function of input variables. The average grain size with standard deviation is demonstrated in Table 3.4 however, details microstructure is shown in later section.

Table 3.4: The alumina grain size with standard deviation

Sample Numbers	Alumina Grain size with Standard deviation
1	1.24±0.32
2	2.38±0.70
3	1.41±0.40
4	3.25±1.00
5	1.18±0.35
6	1.75±0.53
7	1.24±0.35
8	2.77±1.02
9	1.17±0.34
10	2.07±0.67
11	1.49±0.44
12	3.23±1.11
13	1.04±0.35
14	1.68±0.55
15	1.23±0.32
16	2.83±1.00
17	1.04±0.37
18	3.17±0.78
19	1.17±0.34
20	1.58±0.50
21	2.02±0.81
22	1.38±0.39
23	1.44±0.45
24	1.55±0.42
25	1.70±0.49
26	1.60±0.45
27	1.57±0.42
28	1.56±0.43
29	1.63±0.52
30	1.55±0.55
31	1.96±0.56

The experimental data obtained from the designed experiment were analyzed by response surface regression procedure using the following second order polynomial equation;

Relative Density (RD) = f (sintering temperature, sintering time, wt% ZrO_2, ppm MgO)

= f (A, B, C, D) ----- (8)

$RD = \beta_0 + \Sigma\ \beta_i X_i + \Sigma\ \beta_{ii} X_i^2 + \Sigma\ \beta_{ij} X_i X_j + \varepsilon$------------------ *(9)*

Where, X_i = coded values for i = A, B, C and D; X_iX_j= interactive terms. β_0 = the average of responses; β_i = linear regression co-efficient; β_{ii} = square regression co-efficient; β_{ij}= interaction regression co-efficient and ‘ε’ represents as the error term. By considering 4 process parameters, 5 levels and using experimental response data, the mathematical models for both relative density and grain size has been developed according to Eq. (7). Hypothesis testing (t-test) was used to determine the significance of the regression coefficient at 95% confidence level using the Minitab-14 software. The regression coefficients were determined from (31 x 15) matrix, and the relative density can be represented by an integrated equation involving polynomial, and interactive effect of factors;

Table 3.5: Analysis of variance table for Relative Density and Grain Size

	Relative Density				Grain Size			
Term	Coef	SE Coef	T	P	Coef	SE Coef	T	P
Constant	91.6000	0.3396	269.724	0.000	1.65157	0.07711	21.419	0.000
A: Temp	3.4650	0.1834	18.892	0.000	0.59238	0.04164	14.225	0.000
B: Time	1.6617	0.1834	9.060	0.000	0.24121	0.04164	5.792	0.000
C: ZrO_2	-0.1208	0.1834	-0.659	0.519	-0.15829	0.04164	-3.801	0.002
D: MgO	0.0183	0.1834	0.100	0.922	-0.01146	0.04164	-0.275	0.787
A^2	-0.4640	0.1680	-2.761	0.014	0.14758	0.03815	3.868	0.001
B^2	-0.0052	0.1680	-0.031	0.976	-0.03505	0.03815	-0.919	0.372
C^2	0.3648	0.1680	2.171	0.045	0.04583	0.03815	1.201	0.247
D^2	0.4048	0.1680	2.409	0.028	-0.00567	0.03815	-0.149	0.884
AB	0.8213	0.2246	3.656	0.002	0.21656	0.05100	4.246	0.001
AC	0.0875	0.2246	0.390	0.702	-0.07956	0.05100	-1.560	0.138
AD	0.4238	0.2246	1.886	0.078	-0.01306	0.05100	-0.256	0.801
BC	-0.4612	0.2246	-2.053	0.057	-0.00694	0.05100	-0.136	0.893
BD	-0.0825	0.2246	-0.367	0.718	0.04356	0.05100	0.854	0.406
CD	0.1112	0.2246	0.495	0.627	0.00994	0.05100	0.195	0.848

Coef. - Regression coefficients; SE Coef. - Standard error coefficient; T - t-test value; P- Probability of confidence;

Table A6 is representing the regression coefficients for relative density of ZTA samples. βo represents the regression constant coefficient. Similarly, β1, β2, β3, and β4 depict the regression coefficients of sintering temperature, sintering time, wt% of ZrO_2 and MgO, respectively. The variation of ZrO_2 and MgO is a part of design of experiments (DoE) which is used to enhance the densification and reduce the grain size of alumina. After the conducting the experiments by varying the multiple input parameters, and then the regression coefficients was calculated by using output (results) followed by least square method technique. The domination of the regression coefficients depends on the influence of the input parameters that results the output response. The relative density of the ZTA samples was mostly influenced by the sintering temperature and sintering time rather than material input parameters.

Similarly, the regression coefficients for grain size of alumina (see Table 3.5) were calculated by using the experimental values and least square mathematical method. βo represents the regression constant coefficient. Similarly, β1, β2, β3, and β4 describe the linear regression coefficients of sintering temperature, sintering time, wt% of ZrO_2 and MgO, respectively. From the Table 3.5 (grain size), the most influencing input parameters are sintering temperature, sintering time, and wt% of ZrO_2 on alumina grain size.

$RD = 91.6000 + 3.4650 (A) + 1.6617(B) – 0.4640(A^2) + 0.3648 (C^2) + 0.4048 (D^2) + 0.8213(A*B)$ --- (10)

In a similar fashion, the regression coefficients and other statistical parameters are also developed for grain size, as expressed in the following equation and both the data are represented in Table 3.5.

$GS = 1.65157 + 0.59238 (A) + 0.24121(B) – 0.15829 (C) + 0.14758 (A^2) + 0.21656 (A*B)$ --- (11)

The relative effect of each process variables on the final response is directly analysed by the regression coefficients as obtained using Eq. (10) and (11).

Table 3.6: Cumulative representation of statistical parameters for both responses and highlighted their significant and non-significant data.

Terms	Relative Density			Grain Size		
		F	P		F	P
Regression Model		34.37	0.000		20.69	0.000
Sum of squares (SS)	388.431			12.0541		
Degrees of freedom (df)	14			14		
Mean square (MS)	27.7451			0.86100		
Linear terms		109.86	0.000		62.61	0.000
Sum of squares (SS)	354.775			10.4227		
Degrees of freedom (df)	4			4		
Mean square (MS)	88.6939			2.60566		
Square terms		5.00	0.008		4.47	0.013
Sum of squares (SS)	16.158			0.7443		
Degrees of freedom (df)	4			4		
Mean square (MS)	4.0395			0.18608		
Interaction terms		3.61	0.019		3.55	0.020
Sum of squares (SS)	17.498			0.8871		
Degrees of freedom (df)	6			6		
Mean square (MS)	2.9163			0.14785		
Residual Error		----	----		---	---
Sum of squares (SS)	12.917			0.6659		
Degrees of freedom (df)	16			16		
Mean square (MS)	0.8073			0.04162		
Lack-of-Fit		2.14	0.182		2.62	0.125
Sum of squares (SS)	10.088			0.5418		
Degrees of freedom (df)	10			10		
Mean square (MS)	1.0088			0.05418		
Pure Error						
Sum of squares (SS)	2.830			0.1241		
Degrees of freedom (df)	6			6		
Mean square (MS)	0.4716			0.02069		
Whether the model is adequacy?	YES			YES		

F- Fisherman test value.

A positive sign for the regression coefficient in the fitted model indicates the ability of the factor to improve the response. However, a negative sign demonstrates the percentage error in predicted value.

3.3.3 Statistical parameters and their significance

Five important parameters, i.e. probability of confidence (p), coefficient of determination (R^2), standard error of coefficient (SEb), statistical significance of the regression equation (F), and lack of fit have been evaluated to analyse the influence on the responses. The significance of p-value describes the probability of obtaining the experimental results, which is often coupled with a significance or alpha ($\propto$) level and set in advance, usually at 0.05 (5%). Thus, p–value of less than 0.05 depicts high degree of statistically significant and consequent rejection of the null hypothesis. Other significance levels, such as 0.1 or 0.01, are also used depending on the field of study. Hence, an informal interpretation describes that, $p \leq 0.01$ has a very strong presumption against unbiased hypothesis, $0.01 < p \leq 0.05$ for moderate presumption, $0.05 < p \leq 0.1$ for low degree of presumption and $p > 0.1$ non-significant presumption. However, the utilization of p value is meaningful after performing adequate number of experiments and after regression analysis through proper formulation of matrix. Such an approach ultimately predicts the effect of factors on responses. R-square is a statistical measure of how close the data are to be fitted with the regression line or in another way. It may be noted that R-square is the percentage of the response variable variation explained by a linear model. Hence, R-square varies between 0 and 100%; where 100% indicates that the model explains all the variability of the response data around its mean and 0% for none of the variability of the response data around its mean. In general, higher R-square value represents the probability of model fit of the data. The coefficient of regression model including factors either in coded or uncoded form describes the ultimate equation and their coefficient of 'b'. However, a standard error of the computed coefficient 'b' (SEb) is an important factor that can guide the t–test value. A t–test for statistical significance of the coefficient is conducted by dividing the value of 'b' by its standard error. By rule of thumb, a t-value of greater than 2.0 is usually statistically significant. F is a test for statistical significance of the regression equation as a whole. It is obtained by dividing the explained variance by the unexplained variance. By rule of thumb, an F-value of greater than 4.0 is usually statistically significant. Lack of fit value is usually acceptable when its value is more than 0.1. The test for lack of fit compares the variation around the model with "pure" variation within replicated observations. This measures the adequacy of the specified model. Hence, a significant lack of fit will predict the requirement of refining the model.

3.3.4 Influence of statistical parameters on responses

An emphasis has been given to illustrate the influence of significance of aforementioned four statistical parameters derived from the hypothesis test and ANOVA regression analysis for both relative density and grain size. A combination of Table 3.5 and Table 3.6 describes the significance, including non-significant parameters. Linear, interactive and quadratic term of factors exhibit different probable ‘p’ values for both the responses, which varies within $0.000 \leq p \leq 0.976$ and $0.000 \leq p \leq 0.893$ for relative density and grain size, respectively. It is worthy to reiterate that ‘p’ value of less than 0.05 means confidence level above 95%. Linear terms, like individual sintering temperature and sintering time are dominant factors to synchronize the relative density. On the other hand, sintering temperature, time, and zirconia content have a control over grain size. Interaction terms like A B combine the effect of both relative density and grain size. In addition, the quadratic term involving common A^2 (temperature – temperature) has very less ‘p’ value in comparison to other quadratic parameters C^2 and D^2 within confidence label of data. Table 3.6 illustrates the significant and non-significant contribution in the responses of relative density and grain size by using the probability values (p) that is associated with F values for this analysis.

The regression model analysis for relative density and grain size reveals ‘F’ values to be 34.37 and 20.69, respectively. Such data indicate that regression quadratic models are significant on the basis of p-values, 0.000 and 0.000, respectively. Similarly, the lack of fit test compares the residual error to the pure error from replicated experimental design points. The p-values of greater than 0.05 for both relative density and grain size responses indicate that lack of fit for the model is insignificant. The lack of fit also indicates how well the model fits the data. Strong lack of fit ($p< 0.05$) is an undesirable property, because it indicates that the model does not fit the data well. It is desirable to have an insignificant lack of fit ($p>0.1$). The best model should have an insignificant probability value or $p>0.10$. R-Square is the multiple correlation coefficients for the model, which is expected to be one. Similarly, adjusted R-square represents the amount of variation that is explained by the model. In the above analysis, R-Sq and R-Sq (adj) for relative density and grain size are calculated to be as (96.8%, 93.9%), and (94.8%, 90.2%), respectively. Such results represent a good agreement between R-sq and adjusted R-sq for relative density and grain size responses.

3.3.5 Influence of individual parameter effects

The extensive statistical analysis suggests the strong correlation between factors and responses through linear, interaction of two factors and quadratic interaction within same factors (see Table 3.2). The objective is to find out the effective influence of the individual factors, their levels on response by using some meaningful plots. The response data mean is plotted with respect to individual factors, which intercepts a grand mean of response grain size reference line. Herein, a cumulative plot of the linear relation or main effect of several factors on particular relative density is shown in Fig. 3.3.

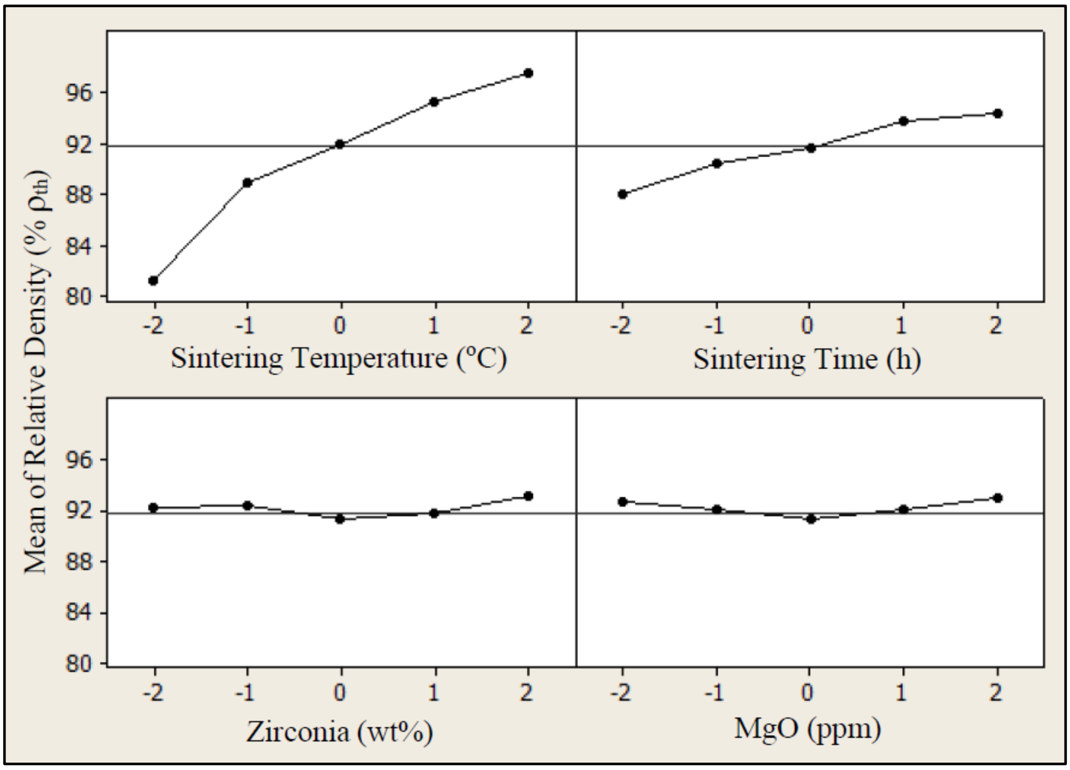

Fig. 3.3: Individual effects of input variable on relative density (gm/cc) including a representative mean of all obtained experimental data.

The plotted points are the mean of the experimental relative density response variable at the various levels of each factor and joined with a reference line drawn at the grand mean of the response data. The mean values of the relative density data are inclined in sintering temperature and sintering time zone to the reference grand mean line. This indicates that both factors have a significant effect on relative density. Other factors, such as zirconia and MgO do not have any significant linear effect because the response data mean lines are parallel to reference grand mean line.

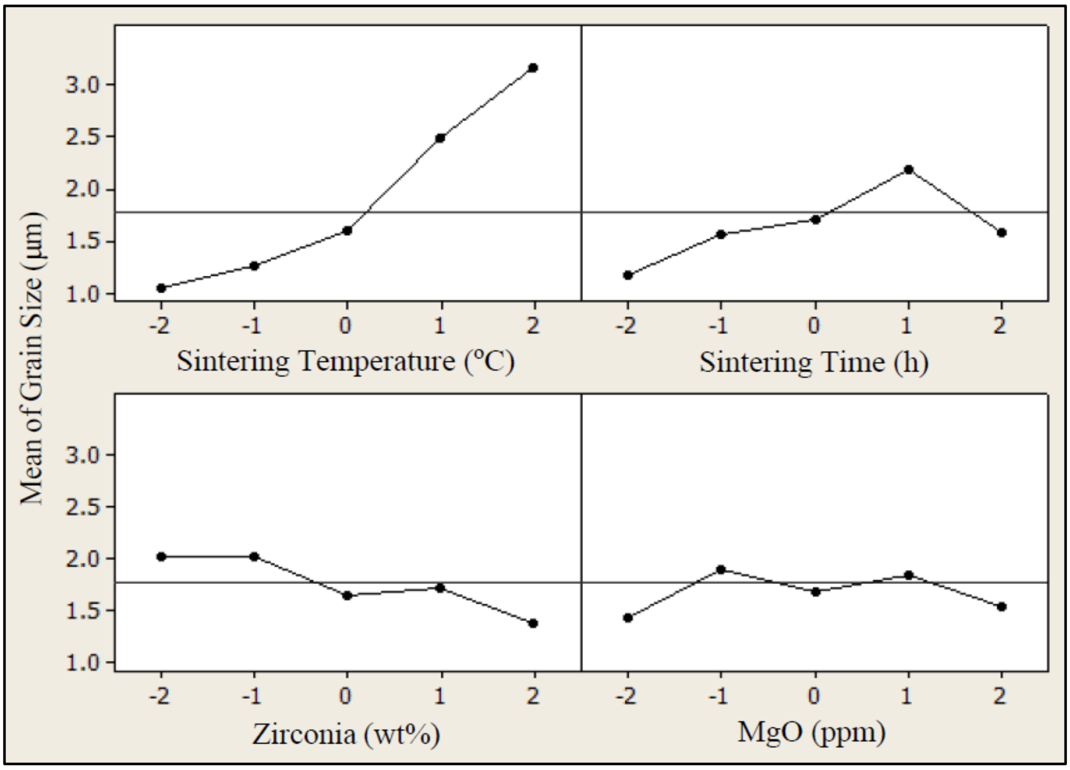

Fig. 3.4: Individual effects of input variable on grain size (μm) including a representative mean of all obtained experimental data.

Similarly, Fig. 3.4 depicts the main effect plots for the experimental grain size of ZTA composite. A closer observation of Fig. 3. 3 and Fig. 3. 4 reveals that sintering temperature, sintering time, and zirconia addition have a major influence on the control the grain size because the mean line is inclined to the grand mean reference line. MgO addition has less influence on the grain size of alumina when zirconia content is more than >1wt%. This is commensurate with the fact that zirconia addition as against MgO addition controls the grain size.[7]

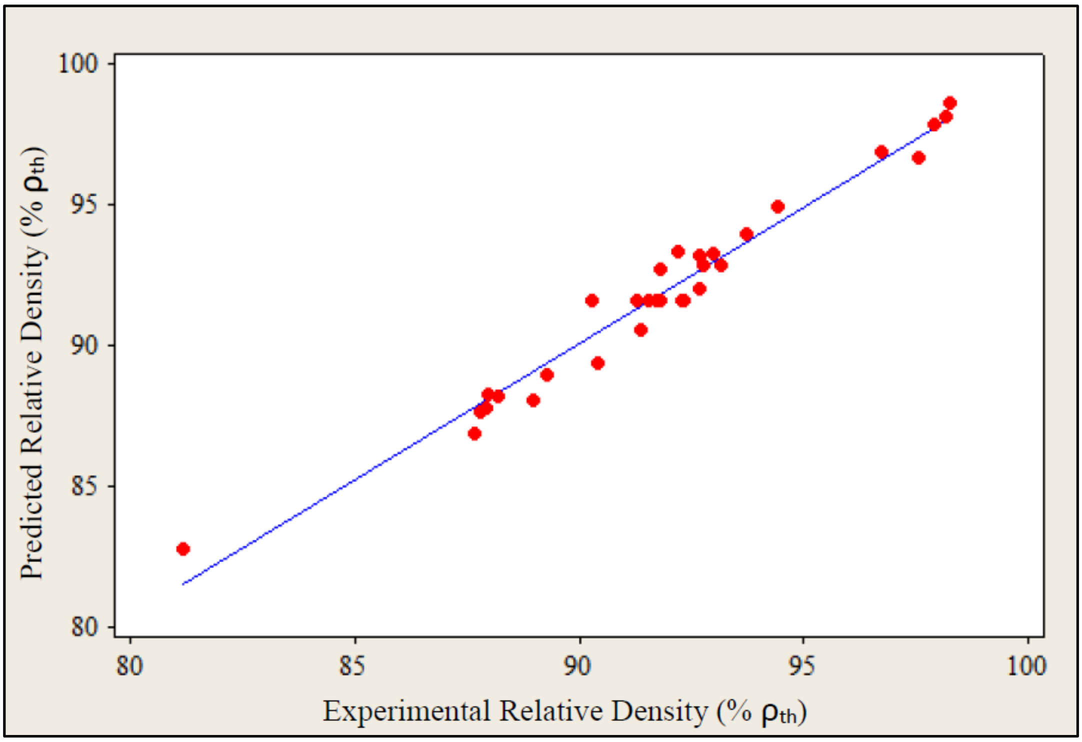

Fig. 3.5: Scatterplot for the predicted and experimental relative density (gm/cc) as obtained from RSM model and experiment data, respectively.

The scatter plot in Fig. 3.5 represents the relationship between experimental and predicted values of relative density, which are plotted on the horizontal and the vertical axis, respectively. In Fig. 3.5, the relative density point cluster appears to move from lower left corner to upper right corner. This suggests that there is a strong positive correlation between experimental and predicted relative density. This observation also implicates that the developed models are decent, and the predicted values are in full accord with the quantified data. Similarly, Fig. 3.6 demonstrates the scatter plot for grain size of alumina in ZTA system, which can identify the type of relationship between experimental and predicted grain size by utilizing the least square regression correlation line.

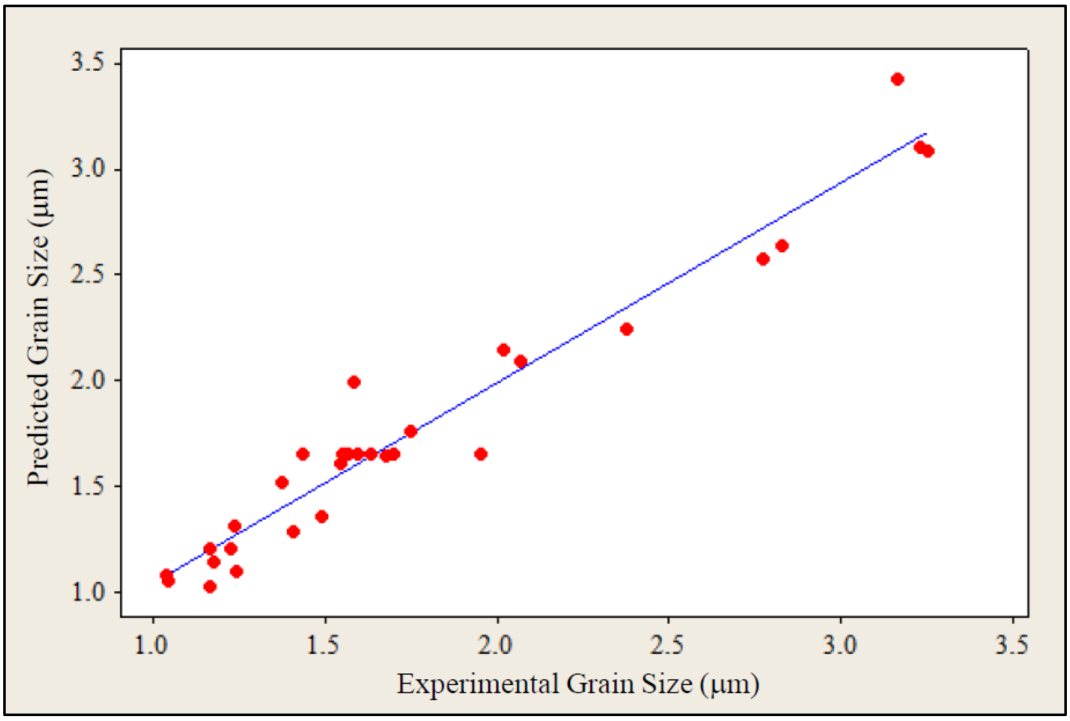

Fig. 3.6: Scatter plot for the predicted and experimental grain size (µm). As obtained from RSM model and experiment data, respectively.

It reveals that the intersecting points cluster can move from lower left corner to upper right corner and regression correlation line with the existence of a strong positive relationship and good agreement between experimental and predicted grain size (see Fig. 3.6).

3.3.6 Interactive effect of factors on responses by counter and surface plots

The counter and surface plots for particular two variables are important when other central design points remain constant. In the present case, sintering temperature, sintering peak isothermal time, zirconia content and MgO content are found as 1550°C, 4hr, 10wt% and 600ppm, respectively (see Table 3.1). Figs. 3.7 and 3.8 illustrate the counter plot for relative density and grain size, respectively. Such figures reveal the particular response characteristics when two variables are interactive and are plotted along x and y-axes keeping other two central design points constant.

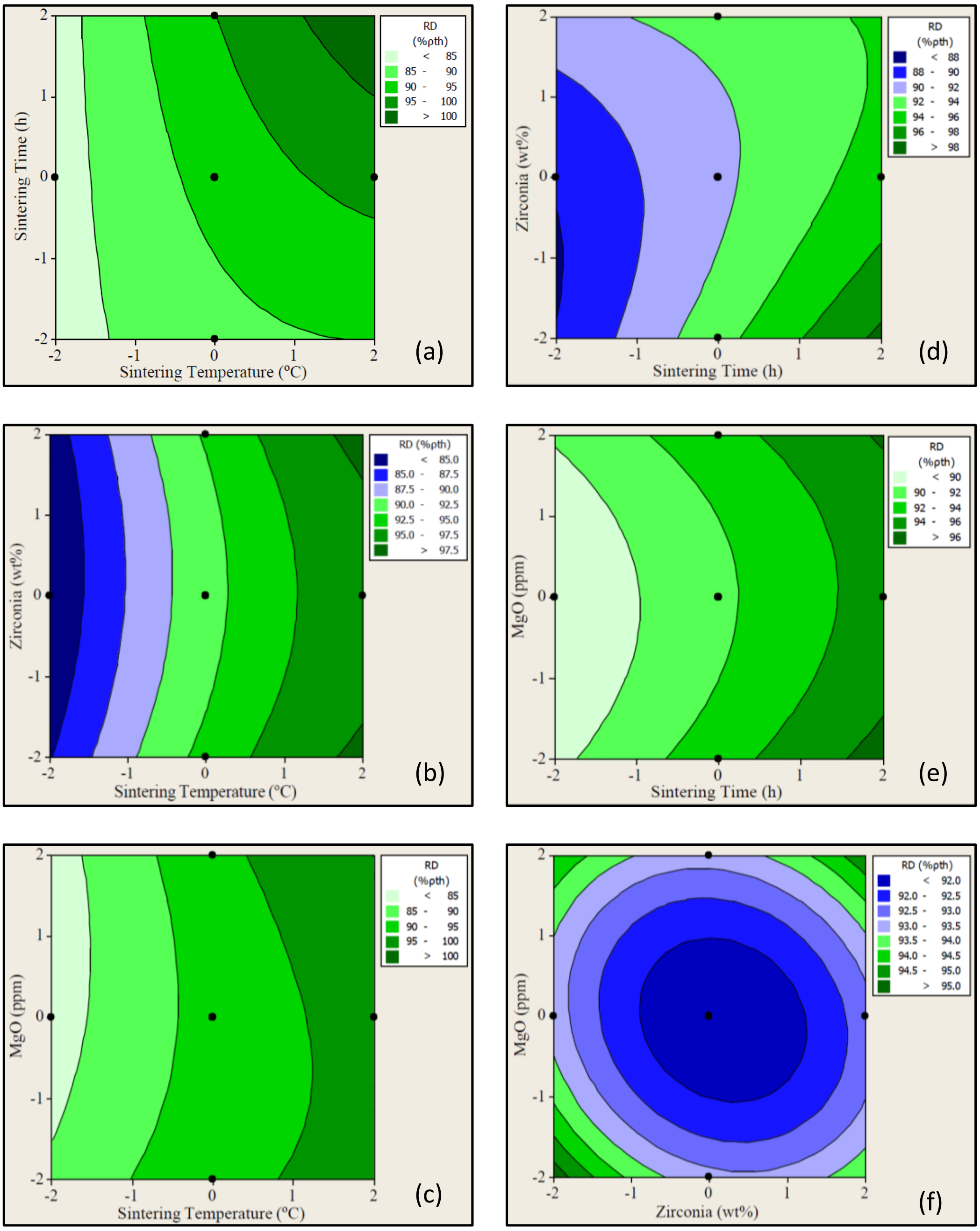

Fig. 3.7: Effect of sintering temperature, sintering time, zirconia and MgO content on relative density shown in contour plots. The relative density curved lines tend to bend towards the influencing input factors.

Fig. 3.7a reveals the contour plot when interaction effect of sintering peak temperature and sintering time are active (AB) on relative density, and other process variables like zirconia and MgO are detained at central design point. Contour is parallel to sintering time when relative density is in low side region. Hence, the sintering temperature has a significant influence, when compared to sintering time. However, the contribution of both temperature and sintering time have a major role in the high relative density region, since contours are curved for both the quantity factor axes. This interactive phenomenon agrees well with a p-value of 0.002. Fig. 3.7b is the representation of counter plot for the interactive effect within sintering temperature (A) and zirconia content (C) on relative density. Sintering temperature has a large influence on both the low and high density region, whereas a small curvature for zirconia depicts non-significant interactive effect. Herein, quantitative factor i.e. temperature is leading over qualitative factor, i.e. zirconia content. Similarly, an interactive effect within temperature and MgO is moderate ($p = 0.078$), whereas quantitative factor dominates the density behaviour of ZTA (Fig. 3.7c). The blue to green colour region indicates the density change from minimum to maximum, which is further influenced by quantitative factor i.e. sintering time, with ‘p’ value in the region of moderate presumption in Fig. 3.7d ($p = 0.057$). The characteristic feature of the counter plot is also identical for the interactive time and MgO, as shown in Fig. 3.7e. The interactive effect of qualitative factors (ZrO_2 and MgO) is not sensitive, when both the quantitative factors are constant at the central point design, as described in Fig. 3.7f. However, quantitative factor, i.e temperature has more significance, when quadratic term is needed to encounter. The influence of interactive factors further clarifies through surface plots. A close look at surface plot in Fig. 3.8a reveals that the optimal relative density can be achieved at sintering temperatures of 1600-1650^{o}C and sintering time of 6-8 h. The relative density of ZTA, therefore, increases because of the combined effect of sintering time and sintering temperature.

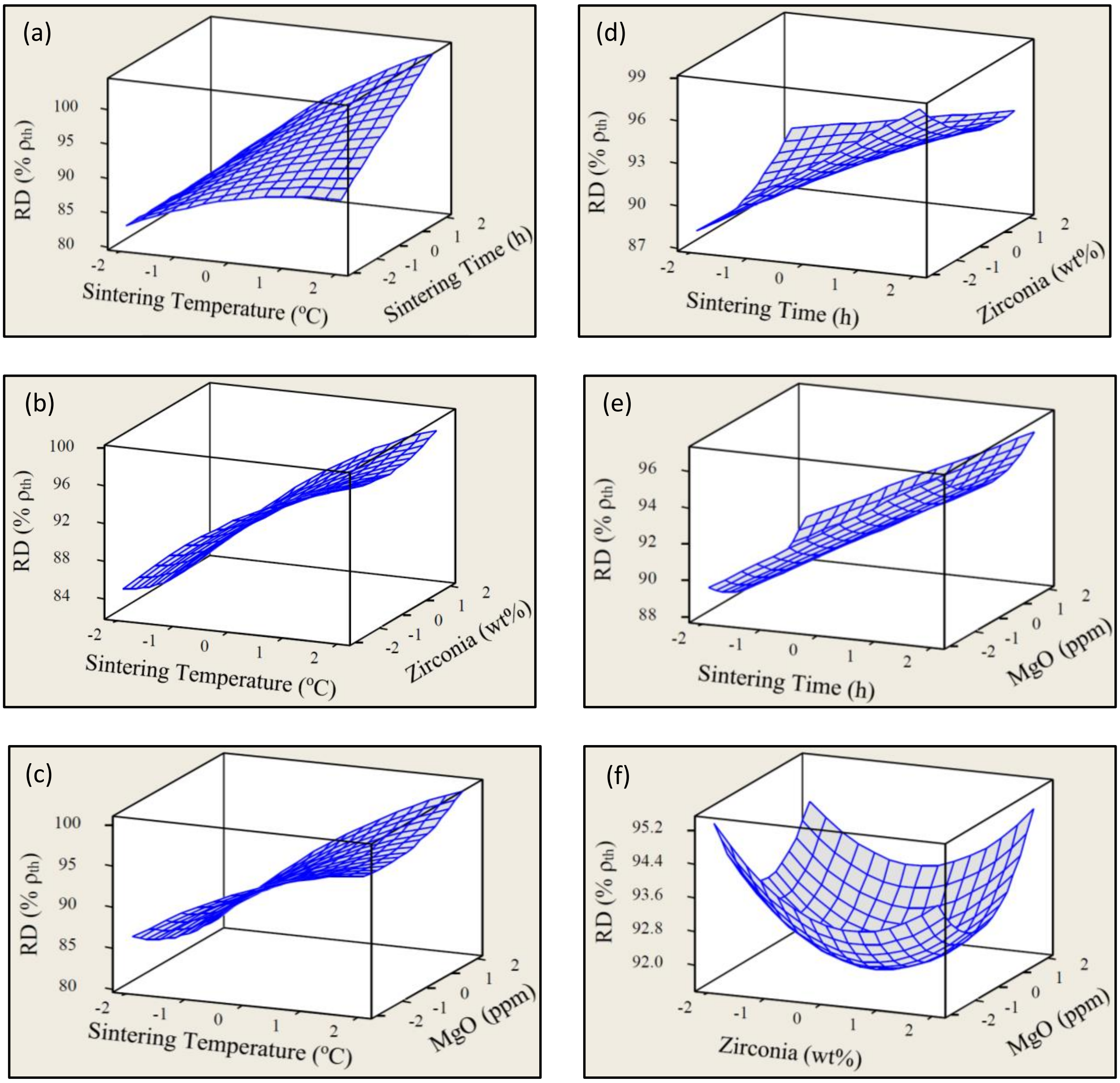

Fig. 3.8: 3D surface plots of the response variable relative density in the perspective of various input factors sintering temperature, sintering time, zirconia and MgO content. The inclination of blue colour wire frame represents the respective input parameters influence on relative density.

However, other surface plots, e.g. Fig. 3.8b-3.8f have no significant interactive phenomena as revealed by counter plot and regression analysis. Here, combined effect of factors on grain size is also analysed under similar central point design condition for the counter and surface plots for relative density. Fig. 3.9 represents the counter plots of all probable interactive effect of individual factors on the response grain size. The interaction of sintering temperature with sintering time also has a major role to control the grain size, which has been further demonstrated by surface plots in Fig. 3.10a. The interaction effect contours of small grain size are highly sensitive to the sintering time, whereas both the interaction factors are sensitive at higher grain size region. A close look at both the counter and surface plots demonstrates a rather weak response of interaction among all permutation – combination of input factors, except temperature – time (see Figs. 3.7 and 3.8). However, no significant influence has been observed for other interactive (AC, AD, BC, BD and CD) phenomenon.

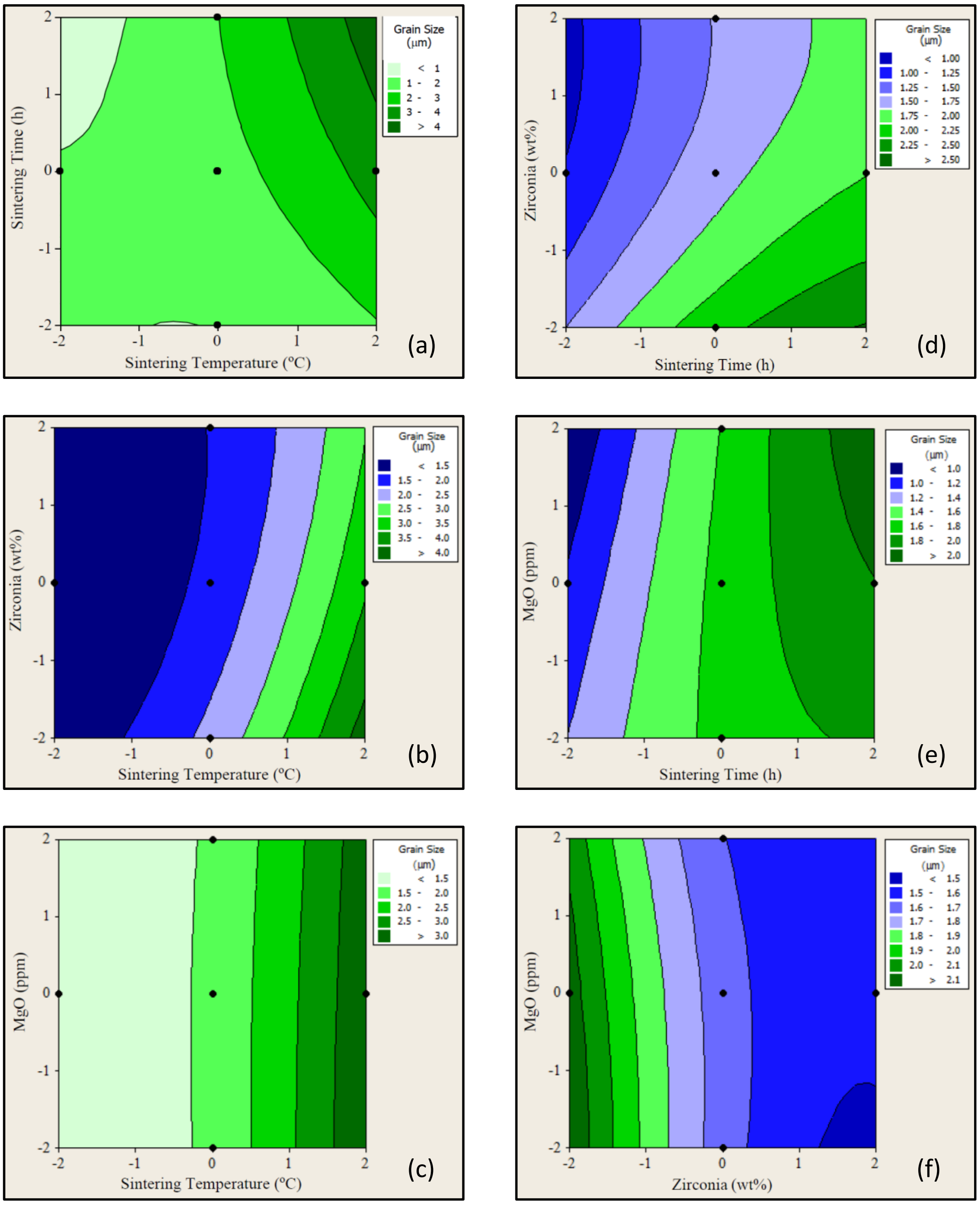

Fig. 3.9: Effect of sintering temperature, sintering time, zirconia and MgO content on grain size shown in contour plots. The grain size curved lines tend to bend towards the influencing input factors.

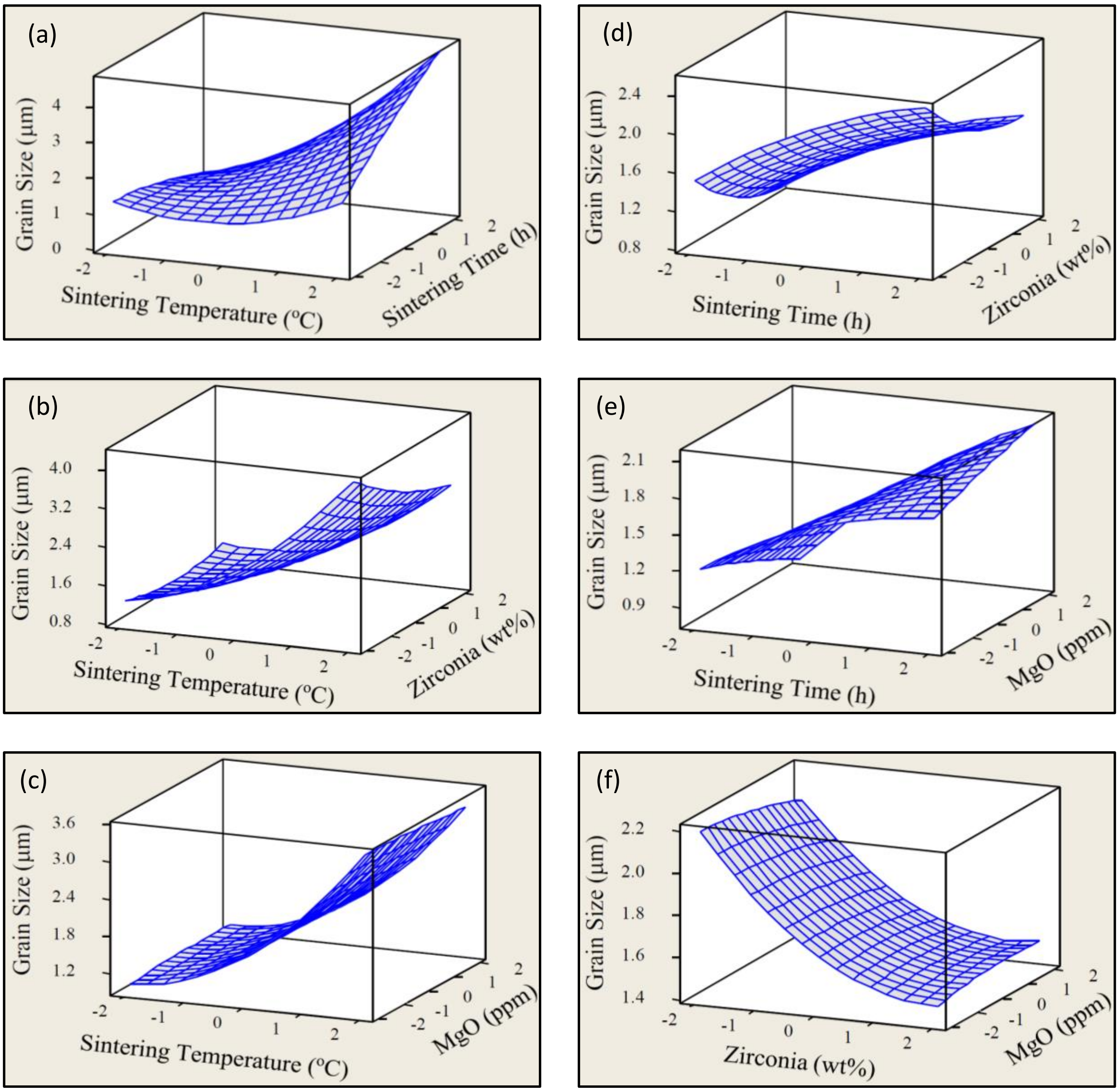

Fig. 3.10: 3D surface plots of the response variable grain size in the perspective of various input factors sintering temperature, sintering time, zirconia and MgO content. The inclination of blue colour wire frame represents the respective input parameters influence on grain size.

In contrast, individual parameters like A, B, C have more influence over counterpart D respectively (Fig. 3.9a-9f and Fig. 3.10a-10f). The explanation of such interactive behaviour of input factors on relative density is discussed in section 5.

3.3.7 Microstructure of Sintered ZTA

As an illustration towards the validation of numerical model prediction, scanning electron microscopic images of few specimens among 31 sets of specimens are shown in Fig. 3.11 and Figure 3.12.

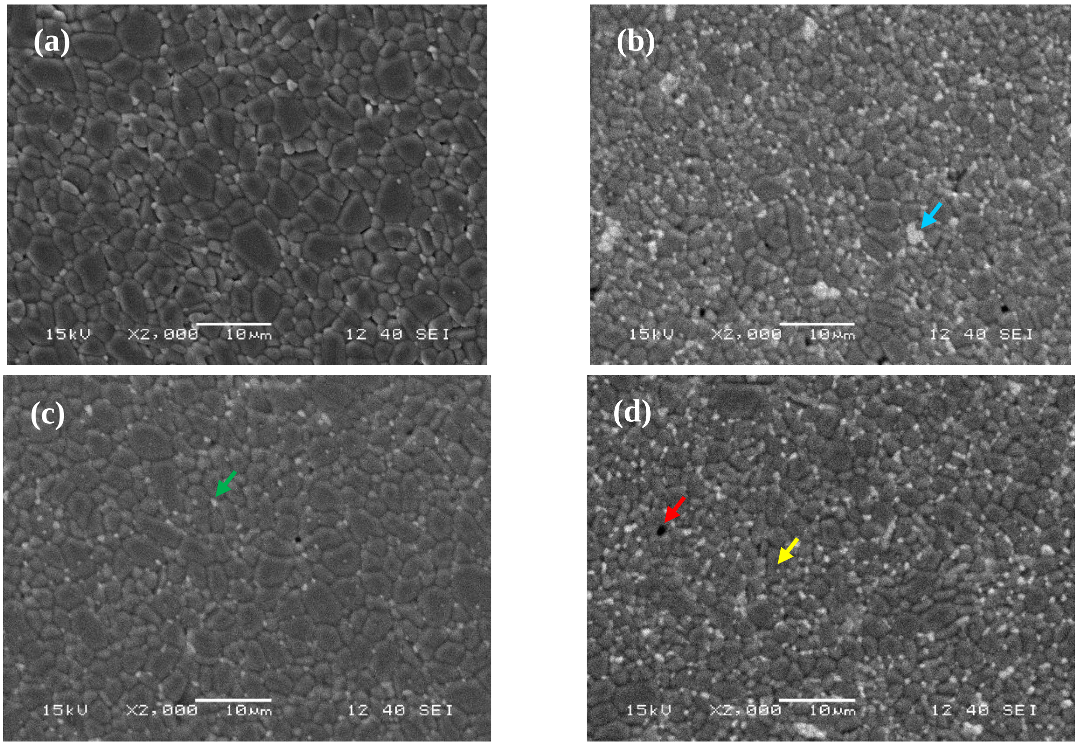

Fig. 3.11: SEM images for highest relative density specimens, (a) Number 4 - 1600°C for 6h, 5wt% ZrO_2 and 400ppm MgO, (b) Number 8 - 1600°C for 6h, 15wt% ZrO_2 and 400ppm MgO, (c) Number 12 - 1600°C for 6h, 5wt% ZrO_2 and 800ppm MgO, and (d) Number 16 - 1600°C for 4h, 15wt% ZrO_2 and 800ppm MgO. Relative large pore (red arrow), intragranular zirconia (yellow arrow) and zirconia grain cluster (cyan arrow) are found for high zirconia content compare to more uniform intergranular zirconia (green arrow) in low zirconia content.

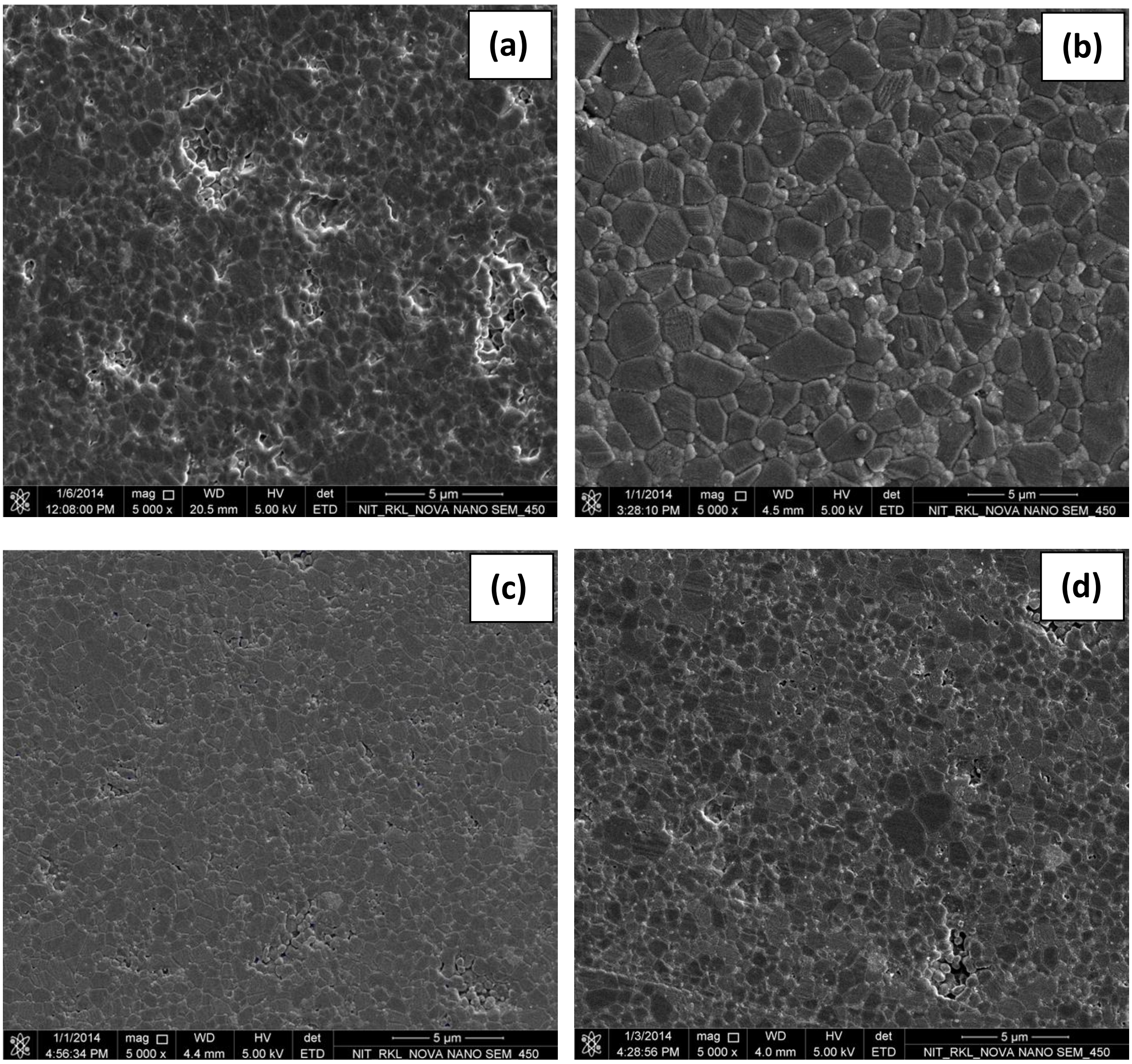

Fig. 3.12: Microstructure for the specimen (a) Number 5 - 1500^{o}C for 2h, 15wt% ZrO_2 and 400ppm MgO, (b) Number 18 - 1650^{o}C for 4h, 10wt% ZrO_2 and 600ppm MgO, (c) Number 22 - 1550^{o}C for 4h, 20wt% ZrO_2 and 600ppm MgO, and (d) Number 25 - 1550^{o}C for 4h, 10wt% ZrO_2 and 600ppm MgO.

Interestingly, we observe the optimal combination of temperature and time (1600^{o}C and 6h) to achieve the highest density also results in finer microstructure with lower grain size, as shown in Table 3.4. The effect of zirconia weight percentage has more influence on grain size than MgO content. However, irrespective of variation of qualitative factors, the linear and volume shrinkage are measured as 20 ± 1% and 48.8 ± 0.5%, respectively. An increase in zirconia grain size is also encountered when zirconia content is higher, but at the same time decreases the bulk density of ZTA.

3.4 Discussion

In the previous section, different set of statistical analysis and experimental data are reported with respect to a particular choice of input variables like sintering temperature, sintering time, zirconia weight percentage and ppm level MgO dopant to synchronise responses like relative density and grain size.The definitive mathematical model has been proposed for both the responses and regression analysis for the clarification of linear, interactive and quadratic effect. In this perspective, the basic premise of this discussion is to support the generation of regression coefficients and the utility of statistical tool for the development of ceramics from essential factors, and hence correlation with their responses.

Before going to extensive discussion on the influence of factors on achieved response, there is a need to concise the significant ‘p’ value and sign of coefficient for only effective factors, which have a strong influence on linear, polynomial or interactive phenomemon (Table 3.5). Relative density is influenced by linear [A (p-0.000), B (p-0.000)], polynomial [A^2 (p-0.014), C^2 (p-0.045)], [D^2 (p-0.028)], and interactive [AB (p-0.002), AD ($0.05<p<0.1$) and BC ($0.05<p<0.1$)], parameters respectively. Similarly, the grain size of alumina matrix strictly depends on linear [A (p-0.000), B (p-0.000), C (p-0.002)], polynomial [A^2 (p-0.001)] and interactive [AB (0.001)] phenomemon, respectively. According to the notification of mentioned ‘p’ values, it can be seen that both factors have different degree of influence. The input variables such as temperature and time have effective linear and interaction effect both on relative density and grain size. The powder compact of high purity alumina (>99.99%) and zirconia (>99.9%) undergoes solid state sintering in the presence of dopant MgO at different temperature schedule 1450 – 1650°C for the time duration of 2 – 8hr. In this perspective, the influence of temperature, time, zirconia and magnesia content need to be discussed to justify and to correlate the statistical model with experimental data for response parameters.

During the low temperature sintering (1450-1500°C) of MgO doped ZTA, the pore is gradually eliminated from the powder compact (e.g. *specimens 1,5,17, etc.*) (see Fig. 3.12 a). However, densification rate at final stage of sintering influences the elimination of closed pore through diffusion or coarsening of the grain size.[8] Hence, it is expected that the densification rate and grain size will depend on both the input parameters, temperature and time. During second stage of sintering (1500 - 1550°C) as illustrated in Table 3.2 and Fig.3.12 d (e.g. *specimens 25*), the developed pore strut at low temperature shrinks to unstable isolated form of spherical closed pores, followed by elimination of pores to achieve dense compact at final stage of sintering (1550 - 1600°C), as found in *specimens 4,8,12,16*. In reality, densification and growth both are competitive processes at or near to sintering temperature and hence, need to synchronize the adequate temperature and time for maximum density without compromising finer grain size. The above discussion can be further rationalised in the light of the following equation correlating the densification rate, grain size and relative density as proposed by Coble, for the densification of nanocrystalline ceramics;[9]

$$\frac{1}{\rho(1-\rho)}\left(\frac{\partial\rho}{\partial t}\right)_{T}=\frac{ADoexp\left(-\frac{Q}{RT}\right)}{G3}\frac{1}{G^{3}}---(12)$$

In the above equation, ρ represents instantaneous relative density, $\left(\frac{\partial\rho}{\partial t}\right)_{T}$is the densification rate at a constant temperature, A is a material constant, G is the instantaneous grain diameter, r is the instantaneous pore radius, and D_o exp (-Q/RT) is the diffusion related term, where Q the activation energy for diffusion, R the gas constant, T absolute temperature, and D_o the pre-exponential term. The above equation intuitively suggests that the densification can involve both simultaneous pore removal and grain growth. It is reported that with pore isolation during final stage of sintering, the density can be restricted to 94±1% ρ_{th} for nanocrystalline ceramics, like what happened for specimen 14 in the present case.[10] Such scenario is favoured when the diffusion path is short and along the grain boundaries without formation of intragranular trapping. In our study, the pore favourably resides along the grain boundary and are gradually eliminated during the final stage of sintering. However, higher sintering temperature (e.g. 1650°C) does not have further influence to eliminate the isolated closed pore, but induces the grain growth, as observed for the *specimen number 18* (see Fig. 3.12 b). Thus, abnormal grain growth associated with higher growth rate could be restricted in the presence of grain growth limiting additives, such as second phase particles (ZrO_2) along the grain boundaries.

In the present study, ZrO_2 as a second phase has more influence over ppm level addition of MgO on the grain size of Al_2O_3. Herein, zirconia particle plays two different roles at the alumina grain boundaries: pinning of grain boundary and relaxation of stresses.[11] It is worthy to mention that the Zr^{4+} diffusion for Y-TZP has an activation energy of 387 kJ/mol as compared to zirconia grain growth process (580kJ/mol).[12] Higher amount of zirconia segregated along the alumina grain boundaries can restrict the Al^{3+} diffusion within Al_2O_3 matrix and can lower their densification since activation energy for Al^{3+} diffusion (440kJ/mol) is higher than Zr^{4+} ion diffusion.[11] Due to this reason, ZTA specimens exhibit lower density, when zirconia content is higher (Table 3.2). Fig. 3.11c shows the microstructure of optimized ZTA specimens, where specimen 12 exhibits fairly homogeneous alumina grain size of 3.2μm, and zirconia grain size of 0.9μm at relative density of 98.6% ρ_{th}. Also, zirconia particles are isolated at grain boundaries between finer alumina grains.

In the perspective of dispersion and pinning efficiency of zirconia grains, an important relationship predicted by Hellman and Hillert can be considered, $d_{[A]} = \alpha d_{[Z]}/V^{1/3}$, where $d_{[A]}$ is ZrO_2 grain size, and V is the volume fraction of ZrO_2 and α depends on these constituents.[12,13] Applying this equation, the α value for *specimen number 12* is found as 1.4, which supports homogenous distribution and pinning by zirconia grains around alumina grain boundaries, as also reported by Moreno et al.[14] An additional influence of higher MgO content on zirconia grain size can be discussed. For example, ZTA with 5 wt% ZrO_2 exhibits lowest grain size (0.90 μm) with maximum density when MgO content is 800ppm. It is worthy to comment thatZTA with high zirconia content (20 wt.%) exhibits relatively larger grains (1.25 μm), which becomes more uniform in the presence of large amount of MgO, as observed for *specimen number of 8 and 16*. MgO is commonly used as a sinter-aid to restrict the Al_2O_3 grain boundary movement through solute-drag or solid–solution mechanism.[16] This mechanism has two fold advantages-discontinuous Al_2O_3 grain growth prevention and pore retention along grain boundaries until grain boundary and volume diffusion is active during the final stage of sintering. Harmer analysed various possible mechanisms of the solute effect using a microstructure development map, based on a plot of grain size versus density with the pore-separation area.[15] In the present study, MgO has an interactive influence to reduce zirconia grain size, which attributes the activation energy for Mg^{+2} ion diffusion towards ZrO_2 is 121 kJ/mol, which is less compared to the diffusion towards Al_2O_3 (210 kJ/mol) grain.[16,17] This assists the less segregation when both zirconia and MgO content are higher as relevant for *specimen number 12* in the present case. This phenomenon further supports uniform densification and significant pinning effect of Al_2O_3 grain boundaries to achieve the optimum density and grain size for structural applications. Moreover, such minimum content (5 wt%) of yttria doped zirconia will minimize the ion leaching *in vivo*, and, therefore, would be beneficial for transformation toughening.[18]

The robustness of the response surface modelling approach in developing ceramic components of various sizes and shapes has been demonstrated in Fig. 3.13.

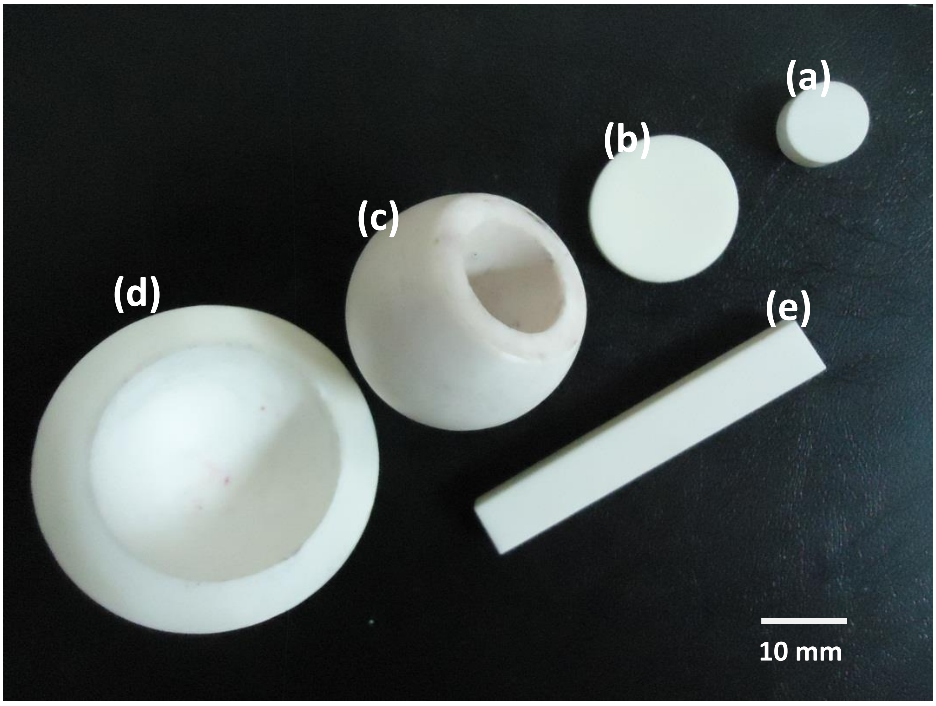

Fig. 3.13: ZTA based ceramic components and labscale specimens prepared through uniaxial pressing of powders from optimized $95Al_2O_3 – 5ZrO_2$ – 800ppm MgO composition (wt%) and sintered at 1600^oC for 6hr: (a) 9.65mm diameter sintered disk, (b)18 mm diameter sintered disk, (c) femoral head, (d) acetabular socket and (e) rectangular bar specimen for flexural strength/SEVNB fracture toughness testing. Both the material composition and sintering conditions were optimised using RSM approach.

Based on RSM analysis, the optimised composition for the best combination of sinter density and grain size is 95 w% Al_2O_3 with 5 w% $ZrO_2$and 800 ppm of MgO. This specific composition was subsequently sintered at 1600^0C for 6 hours (optimised sintering condition) to obtain ZTA ceramics of different sizes and shapes. It is worthwhile to mention that the sintering of small coupon ceramic at lab scale is relatively of less challenge compared to femoral ball head or acetabular sockets, which are of larger length scale with more complicated shape than cylindrical shaped samples of 10-20 mm diameter (see Fig. 3.13). It is therefore extremely significant to note that larger and complicated shaped ceramic components can be fabricated at the RSM predicted sintering condition with sinter density and grain size almost similar to that of small samples of either cylindrical or rectangular cross section. Summarizing, RSM approach, if adopted, appropriately can potentially solve much of the processing related challenges for difficult-to-sinter ceramics.

3.5 Conclusions

Based on the extensive interactive analysis among process variables (sintering temperature and sintering time) and material variables (MgO sintered-aid and ZrO_2 addition) using response surface methodology, we can arrive at the following major conclusions as per as predictive capability of the adopted model towards the densification and grain size is concerned.

(a) Grain size with standard deviation is found for the fabrication of ceramic composites, and a definite average grain size has used to optimize the process and compositions.

(b) The predicted sinter density and grain size computed at five different levels of process and material variables are found to be in excellent linear statistical correlation with the experimentally measured sinter density and average grain size, respectively.

(c) As far as the individual influence sinter density is concerned, the sintering temperature is found to have much more significant influence on densification than sintering time and the influence of either ZrO_2 addition or MgO sinter-aid is negligible.

(d) As far as the grain size is concerned, the sintering temperature has far more significant influence than sintering time. Importantly, ZrO_2 addition is predicted to have more effect on grain size than MgO addition.

(e) As far as the interaction among the investigated parameter is concerned, the response surface methodology predicts a greater influence of the combination of sintering temperature and sintering time on sinter density in statistically significant manner than any other combination of parameters.

(f) Importantly, the interaction of sintering temperature and sintering time followed by sintering time and ZrO2 addition has a larger influence on grain size than other combination of investigated parameters.

(g) The robustness of the response surface modelling approach in developing ceramic components of various sizes and shapes for the best combination of sinter density and grain size is 95 wt.% Al_2O_3 with 5 wt.% $ZrO_2$and 800 ppm of MgO.

Appendix - 1

Table A1: Summary of individual parameters (A, B, C and D) as well as their interaction of parameters to construct design matrix of [31x15].

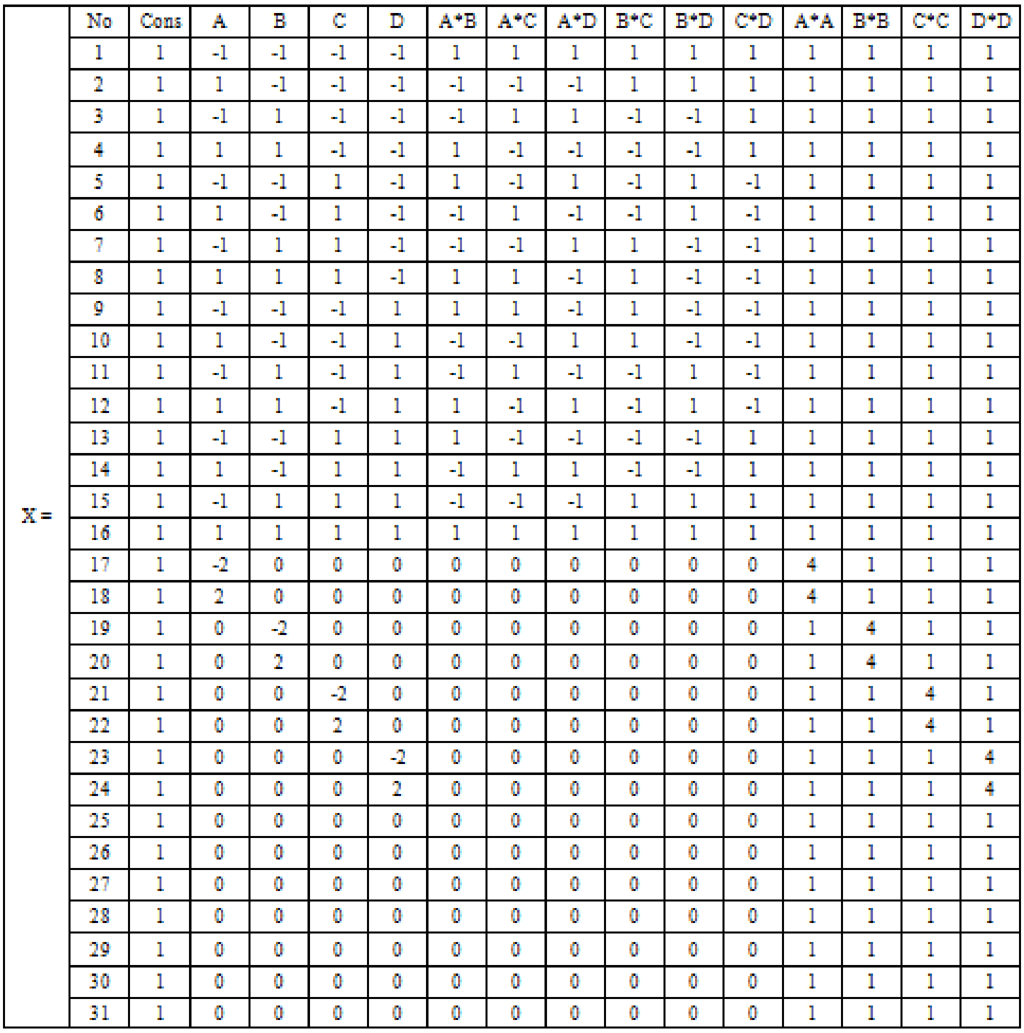

X =	No	Cons	A	B	C	D	A*B	A*C	A*D	B*C	B*D	C*D	A*A	B*B	C*C	D*D
	1	1	-1	-1	-1	-1	1	1	1	1	1	1	1	1	1	1
	2	1	1	-1	-1	-1	-1	-1	-1	1	1	1	1	1	1	1
	3	1	-1	1	-1	-1	-1	1	1	-1	-1	1	1	1	1	1
	4	1	1	1	-1	-1	1	-1	-1	-1	-1	1	1	1	1	1
	5	1	-1	-1	1	-1	1	-1	1	-1	1	-1	1	1	1	1
	6	1	1	-1	1	-1	-1	1	-1	-1	1	-1	1	1	1	1
	7	1	-1	1	1	-1	-1	-1	1	1	-1	-1	1	1	1	1
	8	1	1	1	1	-1	1	1	-1	1	-1	-1	1	1	1	1
	9	1	-1	-1	-1	1	1	1	-1	1	-1	-1	1	1	1	1
	10	1	1	-1	-1	1	-1	-1	1	1	-1	-1	1	1	1	1
	11	1	-1	1	-1	1	-1	1	-1	-1	1	-1	1	1	1	1
	12	1	1	1	-1	1	1	-1	1	-1	1	-1	1	1	1	1
	13	1	-1	-1	1	1	1	-1	-1	-1	-1	1	1	1	1	1
	14	1	1	-1	1	1	-1	1	1	-1	-1	1	1	1	1	1
	15	1	-1	1	1	1	-1	-1	-1	1	1	1	1	1	1	1
	16	1	1	1	1	1	1	1	1	1	1	1	1	1	1	1
	17	1	-2	0	0	0	0	0	0	0	0	0	4	1	1	1
	18	1	2	0	0	0	0	0	0	0	0	0	4	1	1	1
	19	1	0	-2	0	0	0	0	0	0	0	0	1	4	1	1
	20	1	0	2	0	0	0	0	0	0	0	0	1	4	1	1
	21	1	0	0	-2	0	0	0	0	0	0	0	1	1	4	1
	22	1	0	0	2	0	0	0	0	0	0	0	1	1	4	1
	23	1	0	0	0	-2	0	0	0	0	0	0	1	1	1	4
	24	1	0	0	0	2	0	0	0	0	0	0	1	1	1	4
	25	1	0	0	0	0	0	0	0	0	0	0	1	1	1	1
	26	1	0	0	0	0	0	0	0	0	0	0	1	1	1	1
	27	1	0	0	0	0	0	0	0	0	0	0	1	1	1	1
	28	1	0	0	0	0	0	0	0	0	0	0	1	1	1	1
	29	1	0	0	0	0	0	0	0	0	0	0	1	1	1	1
	30	1	0	0	0	0	0	0	0	0	0	0	1	1	1	1
	31	1	0	0	0	0	0	0	0	0	0	0	1	1	1	1

Direct estimation of these regression coefficients is relatively difficult through solving 31 algebraic equations. Thus, we have chosen *least square method* in matrix form in order to find out these coefficients. The main function of the least square method is the estimation of the regression coefficients of the model with reference to the experimental values, which finally accommodate the predicted values and best fitting straight line. In the present work, the least square method reduces the initial matrix to resultant [15 x 1] matrix and delivers the unknown regression coefficients. Table A1 – A6 describe the sequence of procedural steps as how to evaluate the regression coefficients.It can be noted that matrix (X) is a non-symmetric matrix with several non-zero and negative parameters.

Table A2: Defining the transpose of the design matrix X.

$[X^T]=$	No.	1	2	3	4	5	6	7	8	9	10	11	12	13	14	15	16	17	18	19	20	21	22	23	24	25	26	27	28	29	30	31
	Cons	1	1	1	1	1	1	1	1	1	1	1	1	1	1	1	1	1	1	1	1	1	1	1	1	1	1	1	1	1	1	1
	A	-1	1	-1	1	-1	1	-1	1	-1	1	-1	1	-1	1	-1	1	-2	2	0	0	0	0	0	0	0	0	0	0	0	0	0
	B	-1	-1	1	1	-1	-1	1	1	-1	-1	1	1	-1	-1	1	1	0	0	-2	2	0	0	0	0	0	0	0	0	0	0	0
	C	-1	-1	-1	-1	1	1	1	1	-1	-1	-1	-1	1	1	1	1	0	0	0	0	-2	2	0	0	0	0	0	0	0	0	0
	D	-1	-1	-1	-1	-1	-1	-1	-1	1	1	1	1	1	1	1	1	0	0	0	0	0	0	-2	2	0	0	0	0	0	0	0
	A*B	1	-1	-1	1	1	-1	-1	1	1	-1	-1	1	1	-1	-1	1	0	0	0	0	0	0	0	0	0	0	0	0	0	0	0
	A*C	1	-1	1	-1	-1	1	-1	1	1	-1	1	-1	-1	1	-1	1	0	0	0	0	0	0	0	0	0	0	0	0	0	0	0
	A*D	1	-1	1	-1	1	-1	1	-1	-1	1	-1	1	-1	1	-1	1	0	0	0	0	0	0	0	0	0	0	0	0	0	0	0
	B*C	1	1	-1	-1	-1	-1	1	1	1	1	-1	-1	-1	-1	1	1	0	0	0	0	0	0	0	0	0	0	0	0	0	0	0
	B*D	1	1	-1	-1	1	1	-1	-1	-1	-1	1	1	-1	-1	1	1	0	0	0	0	0	0	0	0	0	0	0	0	0	0	0
	C*D	1	1	1	1	1	-1	-1	-1	-1	-1	-1	-1	1	1	1	1	0	0	0	0	0	0	0	0	0	0	0	0	0	0	0
	A*A	1	1	1	1	1	1	1	1	1	1	1	1	1	1	1	1	4	4	0	0	0	0	0	0	0	0	0	0	0	0	0
	B*B	1	1	1	1	1	1	1	1	1	1	1	1	1	1	1	1	0	0	4	4	0	0	0	0	0	0	0	0	0	0	0
	C*C	1	1	1	1	1	1	1	1	1	1	1	1	1	1	1	1	0	0	0	0	4	4	0	0	0	0	0	0	0	0	0
	D*D	1	1	1	1	1	1	1	1	1	1	1	1	1	1	1	1	0	0	0	0	0	0	4	4	0	0	0	0	0	0	0

In Table A2, the transpose matrix of design matrix (X) is defined. According to the least square method, the design matrix was converted to transpose in order to make rows of transpose of the design matrix equal to columns of the design matrix. Such a transpose of design matrix was used to multiply the equation on both left and right side without changing the solution.

Table A3: The product matrix of the design matrix and its inverse for half of the design variables.

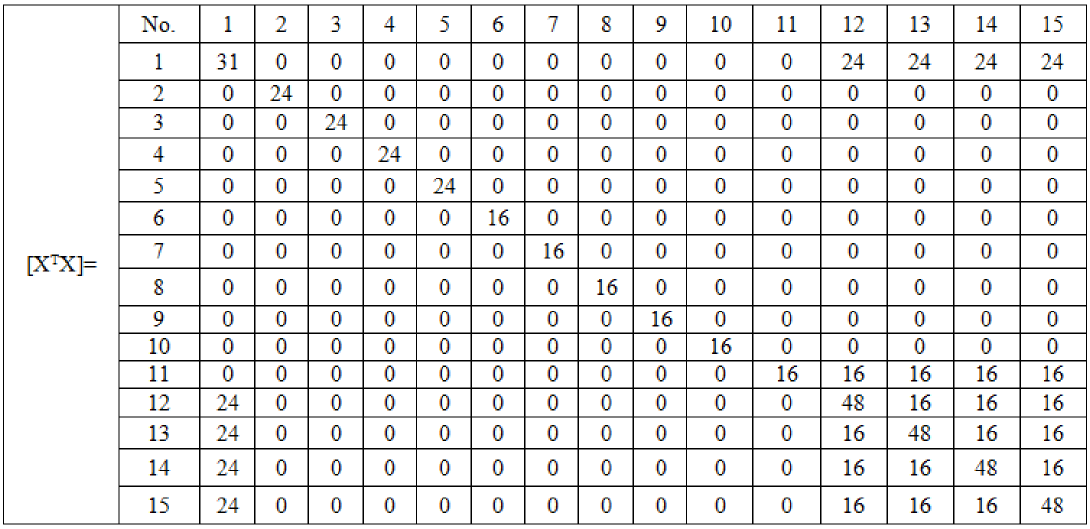

	No.	1	2	3	4	5	6	7	8	9	10	11	12	13	14	15
$[X^TX]=$	1	31	0	0	0	0	0	0	0	0	0	0	24	24	24	24
	2	0	24	0	0	0	0	0	0	0	0	0	0	0	0	0
	3	0	0	24	0	0	0	0	0	0	0	0	0	0	0	0
	4	0	0	0	24	0	0	0	0	0	0	0	0	0	0	0
	5	0	0	0	0	24	0	0	0	0	0	0	0	0	0	0
	6	0	0	0	0	0	16	0	0	0	0	0	0	0	0	0
	7	0	0	0	0	0	0	16	0	0	0	0	0	0	0	0
	8	0	0	0	0	0	0	0	16	0	0	0	0	0	0	0
	9	0	0	0	0	0	0	0	0	16	0	0	0	0	0	0
	10	0	0	0	0	0	0	0	0	0	16	0	0	0	0	0
	11	0	0	0	0	0	0	0	0	0	0	16	16	16	16	16
	12	24	0	0	0	0	0	0	0	0	0	0	48	16	16	16
	13	24	0	0	0	0	0	0	0	0	0	0	16	48	16	16
	14	24	0	0	0	0	0	0	0	0	0	0	16	16	48	16
	15	24	0	0	0	0	0	0	0	0	0	0	16	16	16	48

The number of non-zero parameters or elements is significantly reduced in the product matrix of the X^T and X, as can be seen in Table A3 with most of the off-diagonal terms as zero. It is interesting to note that the XX^T is a matrix of size is 31 x 31, whereas X^TX represents a matrix size of 15 x 15.

Table A4: The inverse of the product matrix, as defined in Table A3

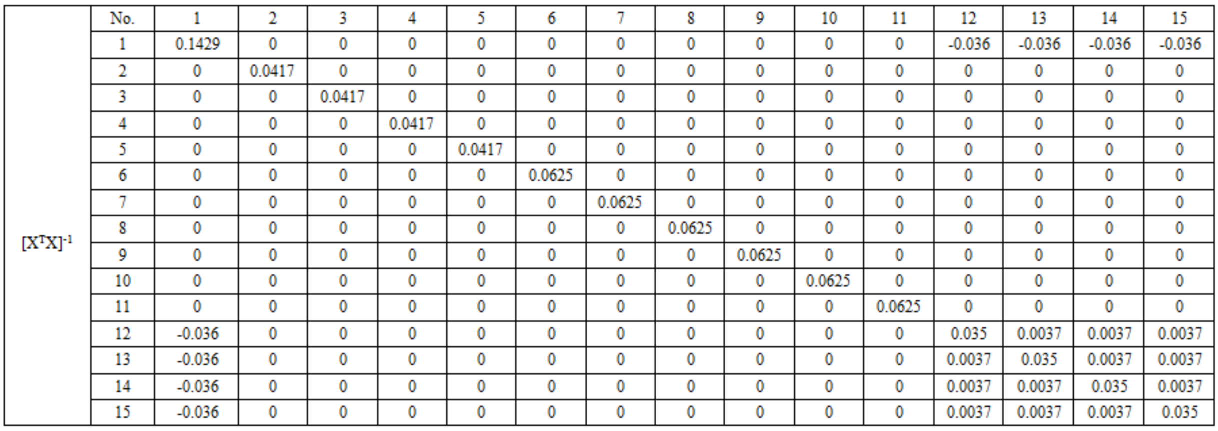

	No.	1	2	3	4	5	6	7	8	9	10	11	12	13	14	15
$[X^TX]^{-1}$	1	0.1429	0	0	0	0	0	0	0	0	0	0	-0.036	-0.036	-0.036	-0.036
	2	0	0.0417	0	0	0	0	0	0	0	0	0	0	0	0	0
	3	0	0	0.0417	0	0	0	0	0	0	0	0	0	0	0	0
	4	0	0	0	0.0417	0	0	0	0	0	0	0	0	0	0	0
	5	0	0	0	0	0.0417	0	0	0	0	0	0	0	0	0	0
	6	0	0	0	0	0	0.0625	0	0	0	0	0	0	0	0	0
	7	0	0	0	0	0	0	0.0625	0	0	0	0	0	0	0	0
	8	0	0	0	0	0	0	0	0.0625	0	0	0	0	0	0	0
	9	0	0	0	0	0	0	0	0	0.0625	0	0	0	0	0	0
	10	0	0	0	0	0	0	0	0	0	0.0625	0	0	0	0	0
	11	0	0	0	0	0	0	0	0	0	0	0.0625	0	0	0	0
	12	-0.036	0	0	0	0	0	0	0	0	0	0	0.035	0.0037	0.0037	0.0037
	13	-0.036	0	0	0	0	0	0	0	0	0	0	0.0037	0.035	0.0037	0.0037
	14	-0.036	0	0	0	0	0	0	0	0	0	0	0.0037	0.0037	0.035	0.0037
	15	-0.036	0	0	0	0	0	0	0	0	0	0	0.0037	0.0037	0.0037	0.035

Hence, the transpose of design matrix and design matrix becomes square matrix of [15 X15] in size. In order to express the design matrix in right of the equation, the inverse matrix is developed from the product matrix and represented in Table A4.

Table A5: The values of the elements of the product of the vector of observations (Y) and the transpose of design matrix (X).

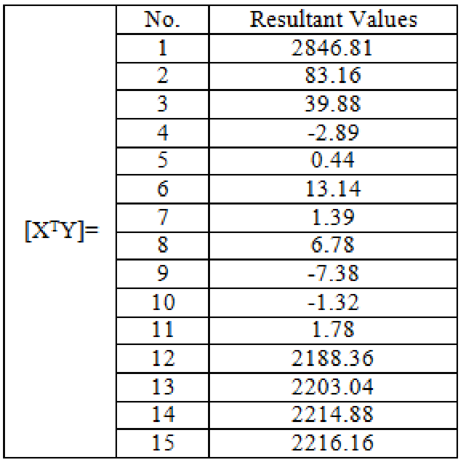

	No.	Resultant Values
$[X^TY]=$	1	2846.81
	2	83.16
	3	39.88
	4	-2.89
	5	0.44
	6	13.14
	7	1.39
	8	6.78
	9	-7.38
	10	-1.32
	11	1.78
	12	2188.36
	13	2203.04
	14	2214.88
	15	2216.16

The observation data matrix was multiplied with the transpose of design matrix and the resultant values are represented in Table A5.

Table A6: The summary of the regression coefficients obtained from the product of the inverse of the matrix defined in Table A3 and the matrix defined in Table A5.

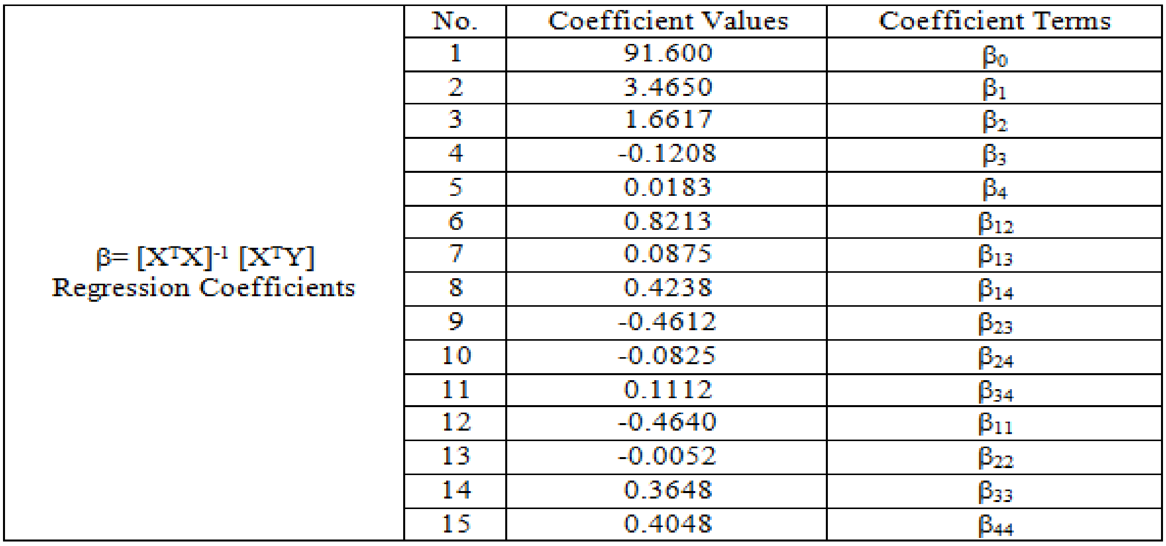

	No.	Coefficient Values	Coefficient Terms
$\beta= [X^TX]^{-1} [X^TY]$ Regression Coefficients	1	91.600	β_0
	2	3.4650	β_1
	3	1.6617	β_2
	4	-0.1208	β_3
	5	0.0183	β_4
	6	0.8213	β_{12}
	7	0.0875	β_{13}
	8	0.4238	β_{14}
	9	-0.4612	β_{23}
	10	-0.0825	β_{24}
	11	0.1112	β_{34}
	12	-0.4640	β_{11}
	13	-0.0052	β_{22}
	14	0.3648	β_{33}
	15	0.4048	β_{44}

The values of the regression coefficients are tabulated in Table A6, which are obtained from $\beta = [X^TX]^{-1}[X^TY]$.These coefficients are used to develop the equation 8 for the relative density, and similarly one can develop also equation 9 for alumina grain size.

3.6 References

---

[1] J. Antony, "Design of Experiments for Engineering and Scientists," Elsevier Science & Technology Books, (2003).

[2] C. Ortmann, T. Oberbach, H. Richter, and P. Puhlfürß, "Preparation and Characterization of ZTA Bioceramics with and without Gradient in Composition," J. Eur. Ceram. Soc., 32 777-785 (2012).

[3] S. Deville, J. Chevalier, G. Fantozzi, J. F. Bartolomé, J. Requena, J. S. Moya, R. Torrecillas, and L. A. Díaz, "Low-Temperature Ageing of Zirconia-Toughened Alumina Ceramics and its Implication in Biomedical Implants," J. Eur. Ceram. Soc., 23, (15) 2975-2982 (2003).

[4] H. Tomaszewski, "Toughening Effects in Al_2O_3 –ZrO_2System," Ceram. Int., 14, 117–125 (1988).

[5] A. Z. A. Azhar, H. Mohamad, M. M. Ratnam, and Z. A. Ahmad, "The effects of MgO Addition on Microstructure, Mechanical Properties and Wear Performance of Zirconia-Toughened Alumina Cutting Inserts," J. Alloy. Compd., 497 (1), 316-320 (2010).

[6] J. Luo, S. Adak, R. Stevens, "Microstructure Evolution and Grain Growth in the Sintering of 3Y-TZP Ceramics," J. Mat. Sc., 33, 5301-5309 (1998).

[7] M. Bengisu, "Engineering Ceramics," Springer, Springer-Verlag Berlin and Heidelberg New York, 2001.

[8] I. W. Chen, and X. H. Wang, "Sintering Dense Nanocrystalline Ceramics without Final-Stage Grain Growth," Nature, 404, 168–171 (2000).

[9] R. L. Coble, "Sintering Crystalline Solids. I. Intermediate and Final State Diffusion Models," J. Appl. Phys., 32, 787–792 (1961).

---

[10] A. S. Edelstein, and R. C. Cammarata, "Nanomaterials: Synthesis, Properties and Applications," 2nd edition (English), Taylor & Francis Group.

[11] J. D. Wang, and R. Raj, "Estimate of the Activation-Energies for Boundary Diffusion from Rate-Controlled Sintering of Pure Alumina, and Alumina Doped with Zirconia or Titania," J. Am. Ceram. Soc., 73, 1172–1175 (1990).

[12] P. Hellman, and M. Hillert, "On the Effect of Second-Phase Particles on Grain Growth," Scand. J. Metall., 4, 211–219 (1975).

[13] B. N. Kim, K. Hiraga, K. Morita, and Y. Sakka, "Superplasticity in Alumina Enhanced by Co-dispersion of 10% Zirconia and 10% Spinel Particles," Acta Mater., 49, 887–895 (2001).

[14] J. M. C. Moreno, M. Schehl, and M. Popa, "Superplastic Behavior of Zirconia-Reinforced Alumina Nanocomposites from Powder Alcoxide Mixtures," Acta Mater., 50, 3973–3983 (2002).

[15] M. P. Harmer, S. J. Bennison, and C. Narayan, "Microstructure Characterization of Abnormal Grain Growth Development in Al_2O_3," Mater. Sci. Res., 15, 309–320(1983).

[16] T. Bak, J. Nowotny, K. Prince, M. Rekas, and C. C. Sorrell, "Grain Boundary Diffusion of Magnesium in Zirconia," J. Am. Ceram. Soc., 85, 2244–2250 (2002).

[17] H. P. Liermann, and J. Ganguly, "Diffusion Kinetics of Fe_2 and Mg in Aluminous Spinel: Experimental Determination and Applications," Geochim. Cosmochim. Ac., 66, 2903–2913 (2002).

[18] D. Sarkar, S. K. Swain, S. Adhikari, B. S. Reddy, H.S. Maiti, "Synthesis, Mechanical Properties and Bioactivity of Nanostructured Zirconia," Mat. Sc. and Engg C, 33, 3413 – 3417 (2013).

Chapter 4

Mechanical and *in vitro* Cytocompatibility of ZTA

In view of the importance of the mechanical and biocompatibility properties in the performance and durability of femoral ball head in total hip joint replacement application, we have analysed such properties of sintered ZrO_2-toughened-Al_2O_3 (ZTA) composites with varying zirconia content of 5 and 15 wt.%. Depending on zirconia content and MgO addition (sintering additive), a range of hardness (upto 20 GPa) and indentation toughness (upto 6 MPa.m$^{1/2}$) was obtained. However, a more reliable measure of crack growth resistance was determined using Single Edge V-notch beam (SEVNB) technique and long crack toughness of 4.3 MPa.m$^{1/2}$ was measured. More importantly, a modest combination of tensile strength (up to 210 MPa) and compressive strength (up to 1100 MPa) was recorded with the investigated materials. In order to assess the cytocompatibility properties, C2C12 mouse myoblast cells were cultured on the ZTA composite having the best combination of mechanical properties. The cell viability results reveal an increase in the number of mitochondrially active cells with respect to control for a period of up to 72 hours. Fluorescence microscopy observations also confirm good cell attachment and cell-to-cell contact with cellular bridge formation after culture of 3 days. Summarising, the present study establishes that 5 wt.% ZTA sintered with 800 ppm MgO sinter-aid can exhibit a great combination of compressive strength (1100 MPa), tensile strength (200 MPa) and modest SEVNB fracture toughness (4.3 MPa.m$^{1/2}$) together with excellent cytocompatibility *in vitro*, thus establishing it as a favourable choice of material for biomedical applications.

In order to fulfil the targeted objective, several characterizations were conducted and their relevant results are summarized systematically in this chapter. Details data analysis further optimizes a selective composition with consist of combined mechanical and biological properties for further investigation and fabrication of prototypes.

4.1Experimental

4.1.1 Sintering and physical properties of ZTA

The ZTA composite preparation methodology starting from pure alumina and zirconia powders and their physical properties including microstructure measurement have been described in section 3.2.1. Herein, high dense specimens were selected to evaluate the mechanical and biological properties. The specimen nomenclature was given as 95A-5Z-400, 85A-15Z-400, 95A-5Z-800, and 85A-15Z-800 with respect to the composition, as summarised in Table. 4.1.

4.1.2 Phase Characterization:

The phase analysis of ZTA composites was conducted using X-ray diffraction (XRD, Pan Analytical, Netherlands) with Cu K$\propto$ radiation and a step size of 0.05°. The phase peaks were recorded from the polished surface and fracture surface of ZTA samples. The volume fraction of m-ZrO_2 and t-ZrO_2 were estimated in order to assess the influence of ZrO_2 phase on the mechanical properties.

4.1.3 Mechanical Characterizations

4.1.3.1 Diametral Compression and Uniaxial Compression Test

The average dimensions of the sintered pellets were 9.7mm/3.3mm (D/t) and 19 mm/10mm (L/D) for Brazilian disc test and compression test, respectively. Both Brazilian disc test (BDT) and uniaxial compression tests were carried out at room temperature using a universal testing machine (INSTRON SATEC 600 kN) with loading rate of 1kN/min. A thin aluminium foil was placed on top and bottom surfaces of the specimens and positioned between fixed and movable jaws of universal testing machine (UTM) in order to transfer the load uniformly throughout the specimen, while conducting the BDT and compression tests. For Brazilian disc tests, the cylindrical specimens were loaded along the diameter of the specimen. The diametral compressive strength was measured using the following expression,

$$\sigma_t = \frac{2P}{\pi D t} - (1);$$

Where P is the uniaxial load applied diametrically to pellets, D is the diameter of the pellet in (mm), and t is the height/thickness of ZTA disc pellets (mm). The Brazilian disc test shown schematically,

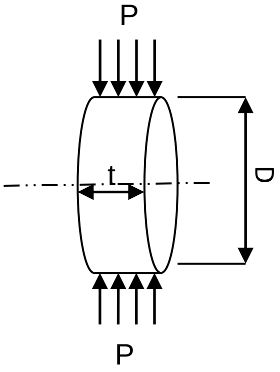

Fig. 4.1: The diametral compressive test (Brazilian disc test), the sample was uniaxially loaded (P) along the diametrically.

Similarly, the compressive strength was determined using the following expression,

$$\sigma c = \frac{F}{\frac{\pi D^2}{4}} - (2),$$

Where F is the uniaxial load applied along the axis of the cylindrical pellet (kN), D is the diameter of the pellet in (mm). The uniaxial compression test shown schematically,

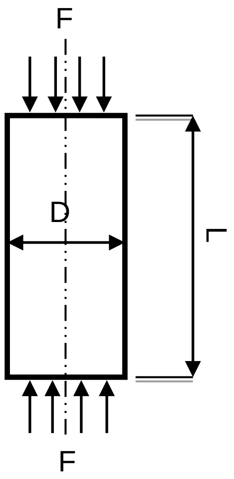

Fig. 4.2: Compressive test, the sample was uniaxially loaded (F) along the length (height axis) of the cylindrical specimen.

4.1.3.2 Hardness and Toughness

Another set of sintered specimens was polished and thermally etched to assess the Vickers hardness and indentation toughness. Vickers hardness of sintered ZTA samples was measured using a microhardness tester. The specimens were polished and thermally etched prior to the hardness tests under 10N load with dwell time of 10s. The average hardness of each specimen was calculated from 8 indentations. The corresponding hardness is measured by the following equation,

$$HV = 1.8544\left(\frac{F}{D^2}\right) - (3)$$

Where F is the load of indentation (N) and D is the length of the indentation diagonal on ZTA pellets in (mm). Similarly, the indentation toughness was determined at load of 50N using the following formula,

$$K_{IC} \; = \; 0.016\left(\frac{E}{H}\right)^{\frac{1}{2}}\left(\frac{P}{D^{\frac{3}{2}}}\right) - (4)$$

Where D is the crack length measured from the diamond indent centre (mm), P is the load of indentation (N), E is modulus of elasticity (GPa) and H is the hardness (GPa). It may be worthwhile to mention that the hardness was measured at an indent load, which does not cause any observable cracking, while fracture toughness was measured at higher indent load, which induces cracking from indent corners. For reliable measurement, SEM images of indents with appropriate magnification were used for hardness or toughness measurements.

4.1.3.3 SEVNB Fracture toughness

The long crack fracture toughness was determined by Single Edge V-notch Beam (SEVNB) method. Samples with rectangular cross-section with dimensions 5mm × 4mm × 15mm (height, width and length respectively) were cut from the sintered pellets using Isomet Low Speed Saw (Buehler, Germany). A v-notch of radius 15-30μm was introduced in the specimens with a commercial v-notch preparation machine (Scientific Testing Devices, Frankfurt, Germany) along with abrasive diamond paste to obtain a smooth and sharp notch. The samples were then loaded under 3-point bending condition with notched face under tensile stress. The test was carried out with a crosshead speed of 0.5 mm/min (UTM, Zwick Roell, Germany) and the fracture toughness (K_{Ic}) was calculated based on the following relationship,

$$K_{Ic} = Y \frac{3PL}{2bh^2} a^{1/2} \dots\dots\dots\dots\dots\dots\dots\dots\dots\dots\dots..(5)$$

Where P is the breaking load, L is the span length, b is the specimen thickness, h is the height, a is the total crack length and Y is the shape factor given by,

$$Y = \frac{1.99 - \alpha(1-\alpha)(2.15 - 3.93\alpha + 2.7\alpha^2)}{(1+2\alpha)(1-\alpha)^{3/2}}$$

Where α is the ratio of crack length (a) and height (h) of the specimen.

4.1.3.4 Cell culture

In order to evaluate the cytocompatibility of ZTA, C2C12 mouse myoblast cells (obtained from National Centre for Biological Science (NCBS), Bangalore) were used for all the *in vitro* tests. Prior to seeding of cells on the samples, the cells were revived from the cryo-preserved stock and grown in Dulbecco's Modified Eagle's medium (DMEM, Gibco), supplemented with 15% fetal bovine serum (FBS, Gibco), 1% antibiotic-antimycotic cocktail (Gibco) in CO_2 incubator (Sanyo, MCO-18AC, USA) kept at 37° C with 5% CO_2 humidified atmosphere. After incubation, sub-confluent monolayer of cells was trypsinized using 0.05% trypsin-EDTA (Gibco) and subcultured for further *in vitro* experiments. The samples used for cell culture studies were sterilized at 120^{o}C and 17psi in an autoclave and soaked in 70% ethanol for 2 h, exposed to UV for 30 min and finally washed with 1X Phosphate Buffer Saline (1X PBS, pH=7.4).

4.1.3.5 MTT assay

The cell viability was analysed using colorimetric MTT (3(4,5-dimethylthiazol-2-yl)-2,5-diphenyltetrazolium bromide, Sigma Aldrich) assay. 2000-3000 cells were seeded on each sterilized sample placed in a 12 well plate along with glass coverslips as control group and incubated for 24, 48 and 72 h in a CO_2 incubator (Sanyo MCO-18AC, USA) at 37° C, 5% CO_2 and 90% humidity. After the incubation period, the growth medium in the well plate was aspirated and samples were washed twice with 1X PBS. This was followed by an addition of 15% reconstituted MTT reagent (Sigma Aldrich) prepared in DMEM (without phenol red) to each sample and is further incubated for 3 h. The MTT reagent is reduced to insoluble formazan crystals by mitochondrial dehydrogenases of metabolically active cells on sample providing a measure of cell viability and metabolic activity. The formazan crystals were solubilized in Dimethyl Sulfoxide (DMSO, Merck) to give a purple solution. The absorbance was measured at 595 nm with a reference wavelength of 750 nm in a microplate reader (i-mark, BioRad laboratories, India).

4.1.3.6 Cell morphology

For cell morphological analysis, the sterilized samples and cover slips (control) were placed in 12 well plate and C2C12 myoblast cells were seeded approximately at a density of 3000-4000 cells/ well. The cells were cultured for 24 and 72 h, as described previously (paragraph 2.4.1). After completion of defined period of culture, the samples were washed twice with 1X PBS and adhered cells were fixed with 4% paraformaldehyde (PFA; SD Fine-Chem Lit) for 20- 30 min. After fixation, the cells were again washed with 1X PBS followed by their permeabilization with 0.1% Triton X-100 (Sigma Aldrich) solution for 8-10 min. Cells were blocked with 1% Bovine Serum Albumin (BSA) for 30 min to prevent nonspecific binding of dyes after a wash with 1X PBS. Cells were stained with Alexa Fluor 488 (Invitrogen) for 30 min to visualize actin filaments, while nuclei were stained with Hoechst stain 33342/ DAPI (Invitrogen). After washing the sample with 1X PBS, the cells were observed under fluorescence microscope (Nikon LV 100D, Japan) to study their morphological behavior.

4.1.3.7 Statistical analysis

Statistical analysis was performed by using SPSS 20 (IBM, USA) software. All *in vitro* experiments were run in triplicate and repeated for at least 3 times. The obtained cell viability data were presented as mean ± standard error and analysed statistically using a student’s *t* test. To determine the significance difference between the groups, the analysis of variance (ANOVA) method followed by post hoc multiple comparisons using Tukey test were performed. The value of *p* as 0.05 and 0.01 were considered to be significant against control.

4.2 Results and Discussion

The investigated ZTA samples were sintered at 1600°C for 6 h, and the measured densities as well as other properties are presented in Table. 4.1. All the samples exhibited more than 97% ρ_{th} and this can be corroborated to SEM analysis as explained later.

Table 4.1: The composition and sample designations of various investigated ZTA composites, sintered at 1600°C for 6 hours in atmosphere.

Sample No.	Al_2O_3 (wt. %)	ZrO_2 (wt. %)	MgO (ppm)	Sinter Density (% ρ_{th})	Grain Size (μm) with standard deviation	
					Al_2O_3	ZrO_2
95A-5Z-400	95	5	400	98.2±0.3	3.25±1.00	1.2±0.33
85A-15Z-400	85	15	400	96.7±0.2	2.77±1.02	1.3±0.35
95A-5Z-800	95	5	800	98.3±0.4	3.23±1.11	0.9±0.26
85A-15Z-800	85	15	800	97.9±0.1	2.83±1.00	1.1±0.40

The sintered samples are further characterised for phase analysis using XRD analysis and for microstructure using SEM analysis. SEM images of some selected ZTA composite are shown in Fig. 4.3. The alumina grains are revealed in dark gray, zirconia grains in bright contrast and pore in dark contrast. Alumina also appears as equiaxed grains and zirconia particles are distributed uniformly either at triple point or at grain boundaries of alumina, thereby inhibiting the alumina grain growth during sintering. The extensive quantitative image analysis reveals the average grain size of alumina in samples 95A-5Z-800 to be around 3.2μm.

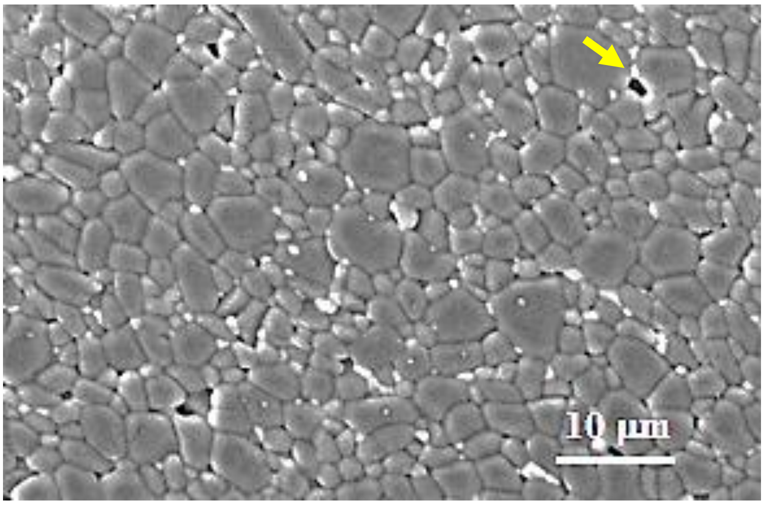

(a)

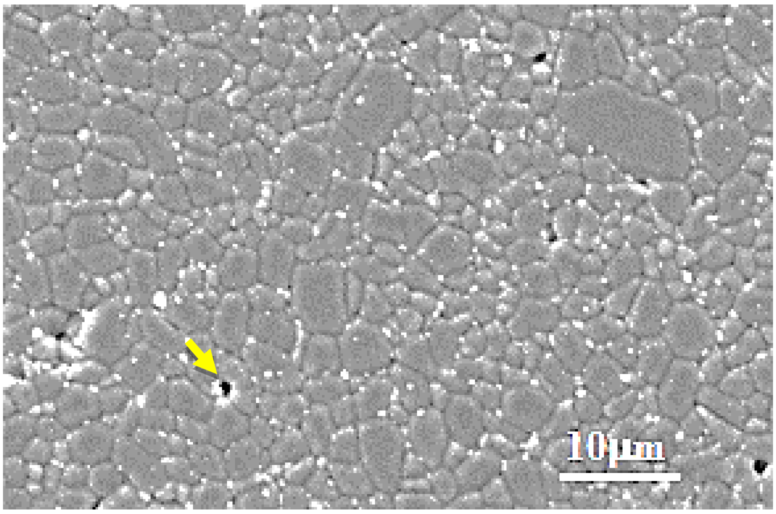

(b)

Fig. 4.3: SEM images of the polished and thermally etched microstructure of (a) 95A-5Z-400 (b) 95A-5Z-800. The residual porosity is indicated by bold arrow and the dispersion of ZrO_2 (bright contrast) in Al_2O_3 matrix can be noted.

In Fig. 4.4 (a), XRD analysis of sintered surfaces for various ZTA compositions is presented. The characteristics peaks of $\alpha - Al_2O_3$ (PDF # 42-1468) are marked at $2\theta = 35.2°$, 43.3°, and 57.5° and that of t-ZrO_2 (PDF # 79-1768) are identified at $2\theta = 30.2°$, 50.2°, and 59.9°. In view of importance of m-ZrO_2 on mechanical properties, an effort has been made to quantify its presence. The m-ZrO_2 peaks the characteristics peaks of m-ZrO_2 (PDF # 34-1484) are located at $2\theta = 28.2°$ and 31.2°.

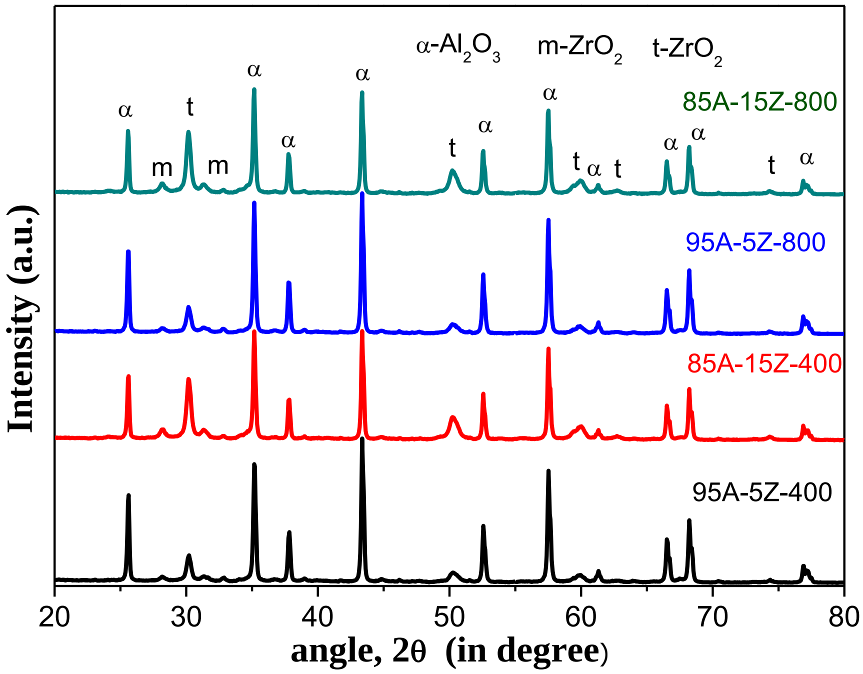

(a)

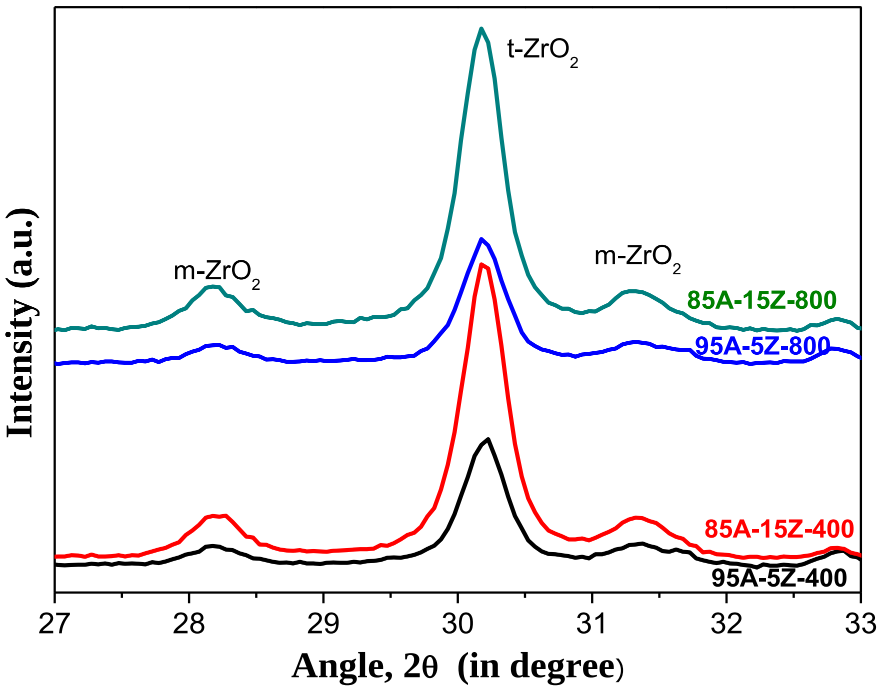

(b)

Fig. 4.4: XRD analysis for the sintered surfaces of 95A-5Z-400, 85A-15Z-400, 95A-5Z-800, and 85A-15Z-800 of ZTA composites (a), and the transformation of t-ZrO_2 to m-ZrO_2 was quantified by critical analysis of the XRD patterns after fracture in the composites (b).

Based on the following formulation, the amount of monoclinic zirconia (X_m) was further calculated [1],

$$(X_m) = \frac{I_{m1} + I_{m2}}{I_{m1} + I_t + I_{m2}} - - - (5)$$

Where I_{m1} and I_{m2} are the intensities of m-ZrO_2 peaks at 2θ = 28.2° and 31.2°, respectively and I_t is the intensity of t-ZrO_2 peak at 2θ = 30.2°. The volume fraction of the m-ZrO_2 (V_m) is calculated by using the reflections of the monoclinic and tetragonal phase peak according to the formula[2],

$$Vm = \frac{1.311X_m}{1 + 0.311X_m} - - - (6)$$

Where X_m is the %m-ZrO_2. While adopting above formulation, suitable background correction was made. Subsequently, % transformability is defined as the difference in m-ZrO_2 content (V_m) measured on the fracture and polished surfaces.

4.2.1 Mechanical Characterization

4.2.1.1 Tensile and compressive strength analysis

The diametral compressive deformation response as measured using Brazilian disc test of 95A-5Z-800 is shown in Fig. 4.5 (a). The test sample dimensions for Brazilian disc test is around 9.6 mm × 3.3 mm and the loading rate was 1kN/min. In this Brazilian disc or indirect tensile test, the load-displacement curves exhibit linear response up to the point of failure and such behaviour is displayed in all the samples. This type of linear behaviour is the evidence of lack of plasticity and the brittleness at room temperature. The 95A-5Z-800 exhibited superior tensile failure strength of 213MPa. The inset of Fig. 4.5a, the macroscopic image of the fractured samples after Brazilian disc test is shown for 95A-5Z-800. The triple-cleft fracture mode occurred, with the specimen being split into three or four main pieces normal tensile fracture mode along the loaded diameter. The tongue and groove shapes are the characteristic of this type of fracture. It should be noted that for secondary cracks to propagate, either the loading contact with the disc or compressive crushing of the specimen must occur to achieve an arc of contact or a planar surface.

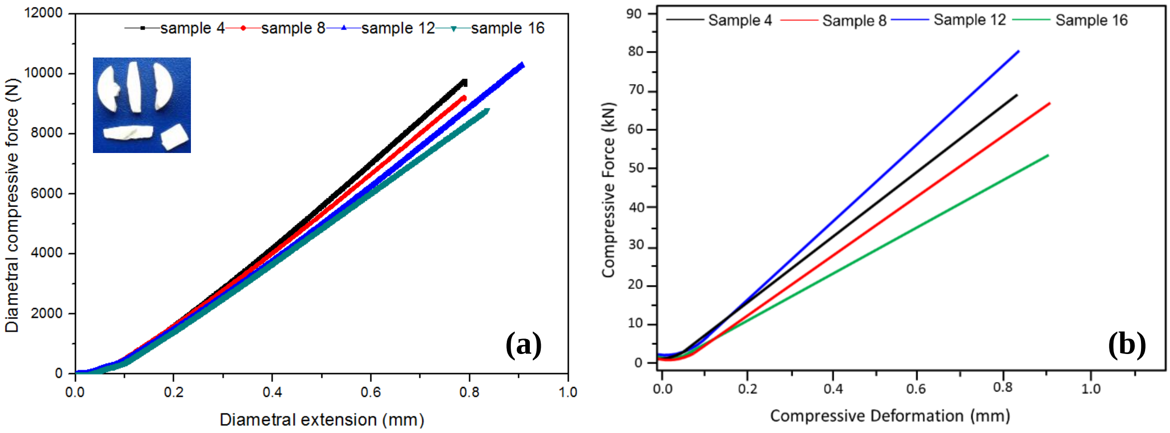

Fig. 4.5: The loading response of all samples under (a) diametral compression and (b) uniaxial compression. In early state, a small inconsistency noticed during compression due to packing of additional aluminium metal foil in order to avoid permanent damage of original platen of the equipment (UTM).

For all the compression test samples length (L) to diameter (D) ratio are greater than 1.5 and the loading rate was 1 kN/min. Fig. 4.5 (b) shows the representative response for all samples. Among the investigated samples, 95A-5Z-800 exhibits the highest compressive strength of 1101 MPa (see Table 4.2).

Table 4.2: Comparison of mechanical properties of selected ZTA composites in the present work with previous studies. Toughness is mostly measured using indentation cracking method, unless otherwise mentioned.

ZTA-Composition (ZrO_2 addition)	Sintering Conditions	Fracture Toughness (MPa. $m^{1/2}$)		Vickers Hardness (GPa)	Tensile Strength (MPa)	Compressive Strength (MPa)	Reference
5 wt.%	1600°C; 2h; (CIP)	7.5$^+$		--	--	--	[3]
5 wt.%	1710°C; 1h	3.8*		--	--	--	[4]
5 wt.%	1600°C; 2h;	4.25		17.48			[5]
15 wt.%	1710°C; 1h	2.0*		--	--	--	[4]
15 wt.%	1600°C; 2h;	4.43		17.38			[5]
15 wt%	1500°C; 2h;	4.7$^+$		--	--	--	[6]
	1450°C; 15 min; F.S.	7.4$^+$		--	--	--	
5 wt.% ZrO_2 + (400 ppm MgO)	1600°C; 6h;	4.4	3.5±0.24*	19.1	195.1	877.9	Present Work
15 wt.% ZrO_2+ (400 ppm MgO)		5.7	3.3±0.30*	18.4	195.3	927.2	
5 wt.% ZrO_2 + (800 ppm MgO)		4.5	4.3±0.15*	19.3	213.3	1101.1	
15 wt.% ZrO_2 + (800 ppm MgO)		5.9	3.1±0.41*	18.5	91.1	786.1	

*measured using single edge V-notch beam technique; $^+$ measured using single edge notch beam technique; CIP - Cold isostatic press; F.S. Forged Sintering.

The examination of the microstructure of fractured surfaces (see Fig. 4.6) leads us to conclude that compressive failure followed intergranular and transgranular. As mentioned in the introduction section, the comprehensive mechanical property measurements of ZTA ceramics are not reported in open literature despite several years of research on this class of material. Concerning compression property, only study has earlier reported the compression strength to be around 500 MPa.[7] In contrast, we have obtained much higher compressive strength of 800-1100 MPa in the present work with the highest for the 95A-5Z-800 composition. In the absence of any previous diametral compression study on ZTA, we cannot compare the tensile strength of our ZTA samples with any earlier results. The tensile strength in the present case varies around 200 MPa with the highest of 213 MPa recorded with 95A-5Z-800 ceramics. Interestingly, 85A-15Z-800 ceramic exhibits both lower tensile and compressive strength properties among the presently investigated ZTA.

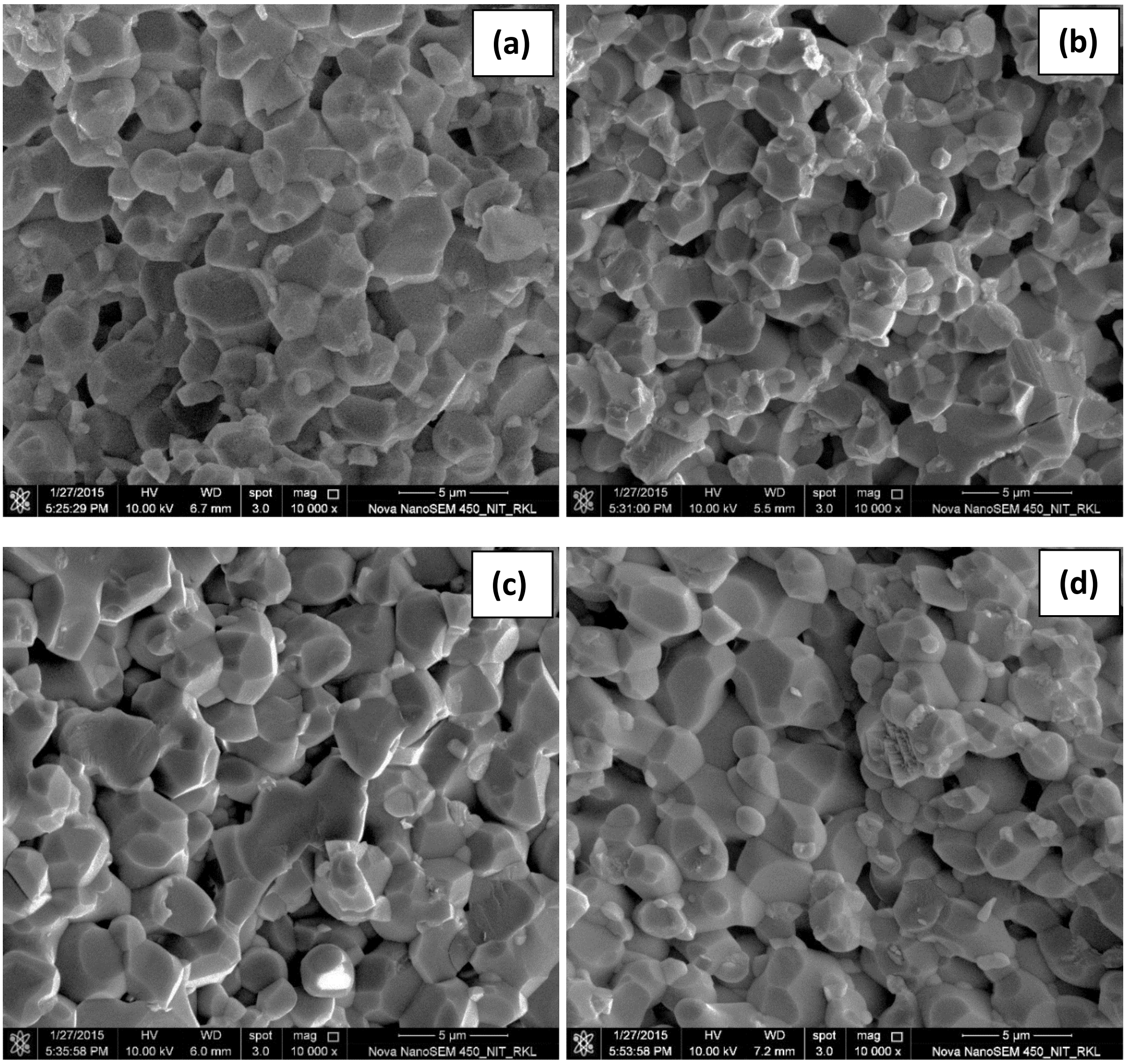

Fig. 4.6: The fractograph after compressive mode of failure of specimens (a) 95wt%Al_2O_3 – 5wt%ZrO_2, 400ppm MgO, (b) 85wt%Al_2O_3 – 15wt%ZrO_2, 400ppm MgO, (c) 95wt%Al_2O_3 – 5wt%ZrO_2, 800ppm MgO, (d) 85wt%Al_2O_3 – 15wt%ZrO_2, 800ppm MgO, all are sintered at 1600^{o}C for 6h.

4.2.1.2 Hardness and fracture toughness properties:

SEM micrographs of Vickers indentations on the polished ZTA composite samples are shown in Fig. 4.7. Using average diagonal length (d) of a number of indents, the hardness is calculated by Eq. (3). On the other hand, the cracks originating from indent edges are used to evaluate the fracture toughness. As per Eq. (4), indentation toughness is determined and presented in Table. 4.2. Further, the cracks are observed in higher magnification of the indented samples and are illustrated inset Fig. 4.7. Fig. 4.7 illustrates the indentation, plastic deformation, and cracking of various ZTA samples. In contrast, indentation loading leads to a plastic deformation and pore collapse in ZTA samples that promote energy absorption. The closing of pores in the ZTA reduces material pileup around the indent periphery. Further the applied energy disappeared through the cracking from indent edges. In sample 95A-5Z-400 and 85A-15Z-400, multiple cracks are initiated from the indent corners.

Many of the previous reports concur that SEVNB method of estimating the crack growth resistance is more reliable than indentation toughness.[8,9,10] In view of this, the SEVNB fracture toughness results are reported together with indentation fracture toughness in the present study. The SEVNB fracture toughness is calculated from the Eq. (5), after subjecting the notched beam to load in 3-point bending until fracture.

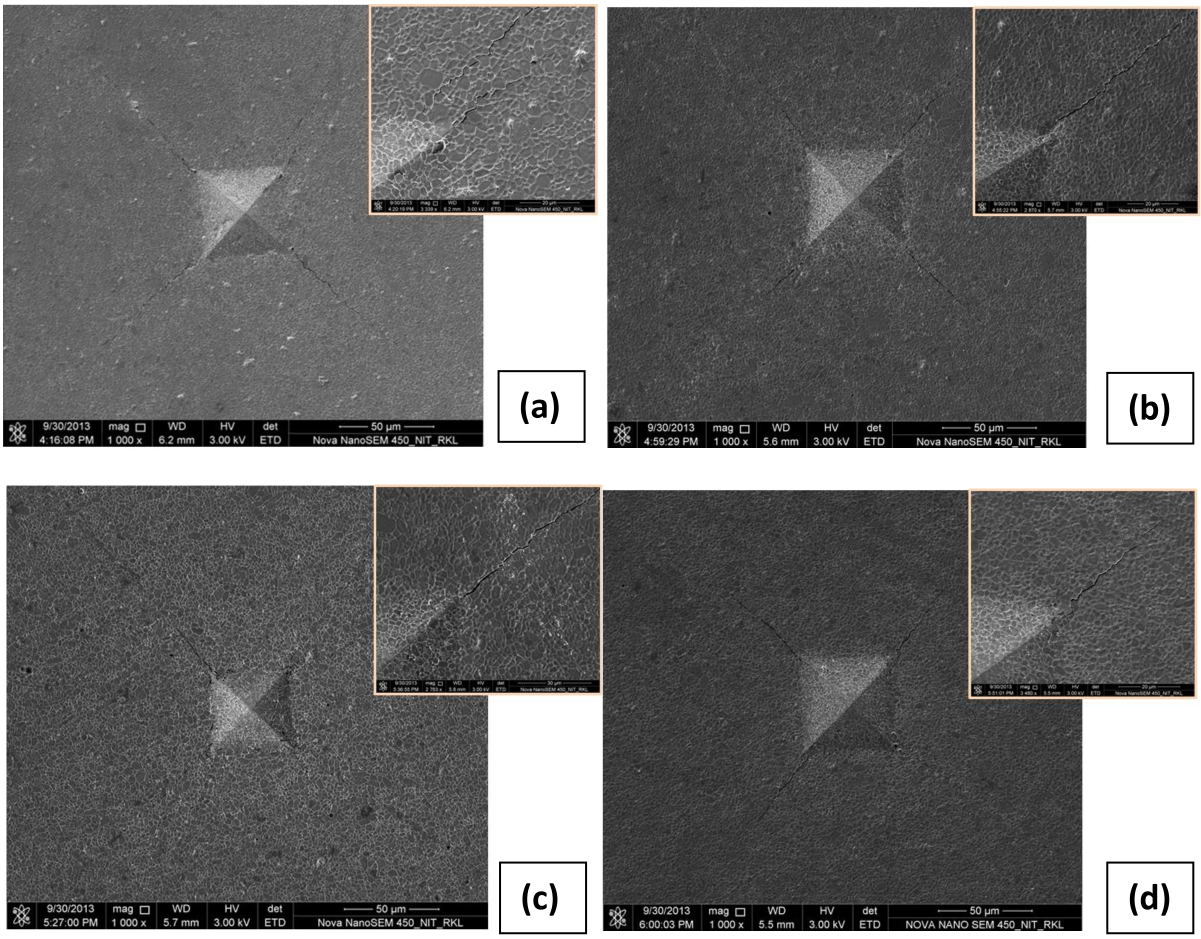

Fig. 4.7: The Vickers indented image for (a) 95wt%Al_2O_3 – 5wt%ZrO_2, 400ppm MgO, (b) 85wt%Al_2O_3 – 15wt%ZrO_2, 400ppm MgO, (c) 95wt%Al_2O_3 – 5wt%ZrO_2, 800ppm MgO, (d) 85wt%Al_2O_3 – 15wt%ZrO_2, 800ppm MgO, all are sintered at 1600°C for 6h. The inset indicates corresponding crack deflection behaviour.

A comparison in terms of the mechanical properties among the ZTA ceramics reported in literature as well as with that of the presently investigated ceramics is presented in Table. 4.2. The ZTA ceramics with varying amounts of ZrO_2 additive (5 wt. % and 15 wt.%) and MgO as sinter-aid (400 ppm and 800 ppm) are sintered at 1600 ^{0}C for 6 h. As far as the hardness properties are concerned, the hardness of earlier developed ZTA varies largely around 16-17 GPa. In the present work, we achieved much higher hardness of around 19

GPa, which was reliability measured by precisely determining indent diagonal lengths from SEM images of the indented surfaces. Also, the variation in hardness among our ZTA ceramics is within 1 GPa. The use of nanopowders as well as the retention of finer scale microstructure attribute to the attainment of higher hardness in the present case (see Fig. 4.3).

The indentation toughness of ZTA shows a higher fracture toughness values in composites with 15% ZrO_2 content (85A-15Z-400 and 85A-15Z-800) with 5.7 and 5.9 MPa.m$^{1/2}$ respectively. The indentation toughness of composites with 5% ZrO_2 is determined to be 4.4 and 4.5 MPa.m$^{1/2}$ for 95A-5Z-400 and 95A-5Z-800, respectively. It is to be noted that the composites which show the highest indentation toughness have lesser density, higher ZrO_2 grain size (see Table. 4. 1) and inferior tensile and compressive strengths (see Table. 4.2).

The SEVNB technique on the other hand, provides a lesser value of fracture toughness for all ZTA composites. This is expected as it measures the bulk crack growth resistance, of the material, whereas the indentation toughness measures the crack growth resistance over a small test volume. The fracture toughness of ZTA composites determined by SEVNB method is the highest for the composition 95A-5Z-800 with 4.25 MPa.m$^{1/2}$ and toughness between 3 and 3.5 MPa.m$^{1/2}$ for other compositions. The composition which exhibited the highest fracture toughness in SEVNB test also possessed the highest tensile and compressive strengths among the ZTA composites (see Table. 4.2). This indicates that not only has the composition 95A-5Z-800 achieved the highest density but also an excellent combination Al_2O_3 and ZrO_2 grain sizes (3.23 μm and 0.9 μm respectively). A representative microstructure of the fracture surface after SEVNB test is shown in Fig. 4.8a. The Back Scattered Electron (BSE) image of the fracture surface reveals the presence of ZrO_2 particles mainly at the grain boundaries of Al_2O_3 matrix, where it can arrest the crack growth effectively (see Fig. 4.8b).

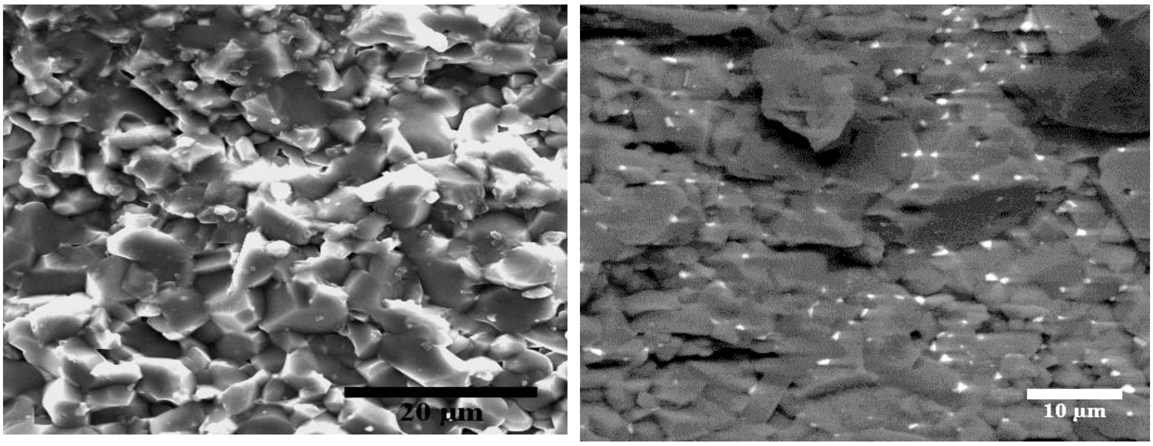

(a) (b)

Fig. 4.8: SE image of the fractured surface after SEVNB test (a). BSE image of the fracture surface showing ZrO_2 particles along the intergranular cracks in Al_2O_3 matrix and (b)

Any comparison in terms of toughness properties among ceramics needs to be made with some caution in view of the availability of multiple measurement techniques to quantify such property. The toughness values reported in Table. 4.2 are largely measured using indentation microcracking method, while adopting different empirical relations as found in the respective literature references. In the present study itself, toughness values obtained by indentation cracking and SEVNB technique cannot be compared with each other. While indentation toughness is highest for 85A-15Z-800 (5.9 $MPa.m^{1/2}$), SEVNB results show that the same composition has the least toughness (3.1 $MPa.m^{1/2}$). Also 95A-5Z-800 composite with the highest toughness (4.3 $MPa.m^{1/2}$) has a lesser indentation toughness (4.5 $MPa.m^{1/2}$) among the ZTA composites. Nevertheless, as SEVNB results are more reliable, the composition 95A-5Z-800 with highest SEVNB toughness, hardness, compressive and tensile strengths can be considered to exhibit the best combination of properties. As far as the fractures toughness is concerned, the toughness of our ZTA composites is lower than that reported in some of the earlier studies with toughness measured using techniques other than SEVNB. Such difference in toughness can be primarily attributed to the ZrO_2 content or more specifically the volume fraction of the transformable ZrO_2 as well as their transformability. Even among ZTA ceramics with comparable ZrO_2 content, the difference in toughness can be attributed to the difference in grain size of t-ZrO_2 phase.

4.2.1.3 Role of m-ZrO_2 on mechanical properties

The toughness in ZTA composites is influenced by the extent of transformation from t-ZrO_2 to m-ZrO_2 during the crack propagation. Such a transformation in the crack path increases the volume of ZrO_2 thereby blunting the crack tip. The transformation was quantified by critical analysis of the XRD patterns after fracture (see Fig. 4.4 b). The volume fraction of m-ZrO_2 was calculated by the Eqs. 4 and 5 and compared with the amount of m-ZrO_2 in the composites before fracture to determine the transformability of t-ZrO_2 during crack propagation. The results tabulated in Table. 4.3 and represented graphically in Fig. 4.8 show that there is a direct correlation between the transformability of t-ZrO_2 and fracture toughness.

Table 4.3: The volume fraction of m-phase on ZTA before (polished surface) and after fracture determined by quantitative XRD analysis.

Sample Name	m-phase on polished surface (%V_f)	m-phase after fracture(%V_f)	Amount of t-ZrO_2 transformed to m-ZrO_2
95A-5Z-400	7.7	13.9	6.2
85A-15Z-400	5.5	9.5	3.9
95A-5Z-800	13.3	22.7	9.4
85A-15Z-800	16.4	18.5	2.2

The highest SEVNB fracture toughness in 95A-5Z-800 can be attributed in part to the extent of transformation of t-ZrO_2 to m-ZrO_2 (9 vol.%), which is highest among the ZTA composites in the present study. It is also to be noted that, though the composites with 85A-15Z have a low transformation (2 and 3 vol.%), they still show moderate toughness due to the higher ZrO_2 content. This indicates that extent of transformation of t-ZrO_2 to m-ZrO_2 around the crack tip and not the content of ZrO_2 induces higher degree of toughening in ZTA composites. The modest SEVNB toughness can therefore be attributed to limited transformation toughening contribution, as can be predicted from the lower transformability (see Table 4.3 and Fig. 4.8).

The influence of ZrO_2 grain size also influences transformation toughening contribution. Following an earlier review on transformation toughening of ZrO_2,[11] it is clear that t-ZrO_2 phase with grain size in the range of 0.9-1.3 μm should have transformation potential in the monolithic ZrO_2. However, such potential can be restricted when ZrO_2 is constrained in another non-transforming matrix, like Al_2O_3. Also, the fact that larger the t-ZrO_2 grain size, larger would be the transformation toughening contribution – this fact unfortunately could not be established with the limited datasets for ZTA in the present work (see Table 4.1 and 4.3). Nevertheless, modest SEVNB toughness values with % transformability in the present case (see Fig. 4.8).

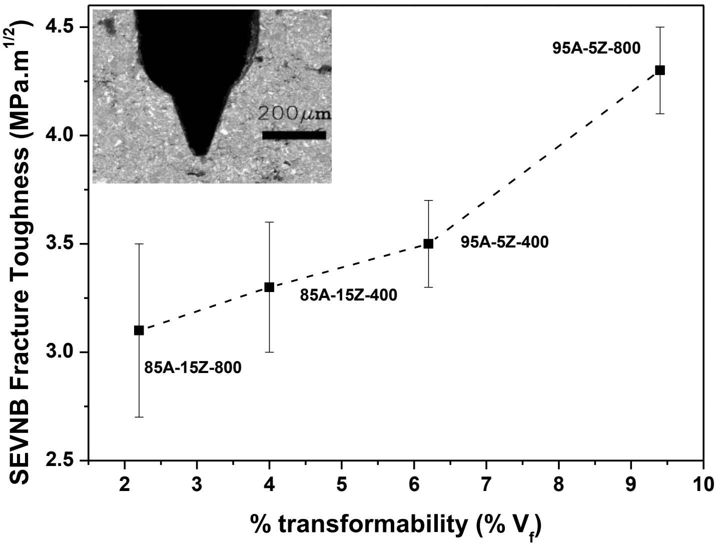

Fig. 4.9: SEVNB fracture toughness of ZTA composites with respect to % transformability (V_f) of t- ZrO_2 after fracture. Inset represents the typical notch shape and dimensions.

The hardness of ZTA composite varies in the window of 18-19 GPa. The observed variation in hardness properties can be correlated with m-ZrO_2 content in the as sintered ceramics as well as minor difference in the sinter density. As far as the tensile strength is concerned, the reduction in tensile strength from 213 MPa (95A-5Z-800) to 91 MPa (85A-15Z-800) is remarkable. Such significant reduction in strength can be attributed to larger m-ZrO_2 content as well as the agglomeration of higher amount of ZrO_2 in alumina matrix in 85A-15Z-800 ceramic. It is known that the second phase agglomerates cause microcracks at the interface with another ceramic phase during cooling from sintering temperature. However, the reduction in tensile strength from 195 MPa (95A-5Z-400) to 185 MPa (85A-15Z-400) is far less significant. In reference to the compressive strength, no significant variations could be recorded between 95A-5Z-400 and 85A-15Z-400 composite. The difference in compressive strength between 95A-5Z-800 (1102 MPa) and 85A-15Z-800 ceramic (786 MPa) is however extremely significant. The reduction in strength properties can be arguably attributed to the presence of agglomeration of finer ZrO_2 particles, which potentially cause the formation of micro-cracks. Concerning indentation toughness, an interesting observation is that an increase in ZrO_2 from 5 to 15 wt. % considerably increases the toughness at the expanse of significance reduction compressive/tensile strength properties [compare 95A-5Z-800 vs 85A-15Z-800].

4.2.2 *In vitro* cytocompatibility properties

In order to assess the cytocompatibility property of the ZTA (95A-5Z-800), we performed *in vitro* cell culture experiments using C2C12 myoblast cell for different periods of upto 72 h to assess cell adhesion and proliferation. The reasons behind using C2C12 murine myoblast cell line are as follows,

(a) These cells are the typical type of cells, which exhibits a distinct morphology in differentiated and undifferentiated form.

(b) Also, these myoblast cells have a contractile nature, which allow them to easily adhere and proliferate in a reproducible manner on both softer and stiffer surfaces of the biomaterials.

4.2.3 Cell Viability

In the present study, we have analysed the viability and proliferation of C2C12 myoblast cells after their seeding on ZTA (95A-5Z-800) ceramic substrate. The total metabolic activity of cells was assessed by MTT reagent, which is reduced to an insoluble, coloured product (formazan) by an enzyme known as mitochondrial succinate dehydrogenase. This reduction of MTT into formazan can only occur in metabolically active cells. Therefore, the quantified absorbance of this coloured formazan product reflects the level of activity of cells, which directly indicate the extent of cell viability. Fig. 4.10 shows the cell viability on ZTA at different time points (24, 48 and 72 h), compared to control (0.2% gelatine coated cover slip). Presently, our results reveal that the myoblast proliferation on ZTA ceramic substrate (95A-5Z-800) is higher at each time point when compared to their respective controls. According to the Anova test, the proliferation of cells on 95A-5Z-800 samples increased markedly after 48 h ($p < 0.05$) and 72 h ($p < 0.01$) of culture when compared to 24 h of culture. In contrast, no significant difference ($p > 0.05$) was found between the viability of cell amongst 95A-5Z-800 samples cultured for 48 h and 72 h. However, for the controls, the proliferation of cells was significantly higher after 48 h ($p < 0.01$) and 72 h ($p < 0.01$) of cultures when compared to the 24 h of culture. A significant increase in cell growth was also observed after 72 h ($p < 0.01$) of culture when compared to 48 h of culture. These results demonstrate that 95A-5Z-800 is highly compatible with myoblast cells, as indicated by the regular increase in cell growth from 24 h to 72 h of culture.

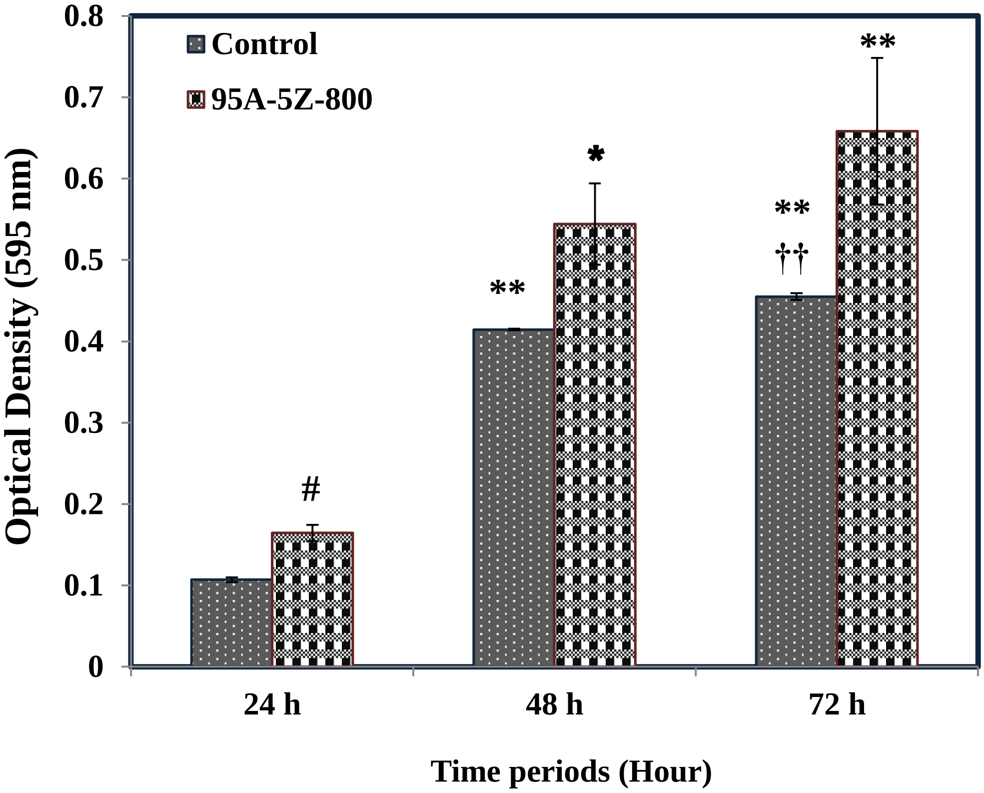

Fig. 4.10**:** Plot showing MTT analysis of C2C12 myoblast cells cultured on 95A-5Z-800 samples for the periods of 24, 48 and 72 h. Statistical difference from control: # significant at p≤0.05; Statistical difference (intra group) from the 24 h of cell culture: *significant at p≤0.05; ** significant at p≤0.01using one way Anova followed by post hoc tukey test. Statistical difference (intra group) from the 48 h of cell culture: †† significant at p≤0.01 using one way Anova followed by post hoc tukey test. Each value was represented as mean±standard error.

4.2.4 Cell adhesion and proliferation

Apart from the quantification of the myoblast proliferation or viability on 95A-5Z-800 ceramic, we also investigated the cell adhesion and proliferation by morphological analysis of myoblast cells. The morphology of adhered cells was also found to be normal with shuffle differences with that of control.

The florescent staining images in Fig. 4.11 reveal the cellular morphology, in particular the cytoskeletal (actin filaments) structure and shape of nuclei, which were respectively stained withAlexa Fluor 488 and Hoescht stain (Invitrogen). One can easily observe a marked difference between densities, morphology and cytoskeletal organization of myoblast cells proliferated for a period of 24 h on the surface of 95A-5Z-800 ceramic from that recorded on control (Fig. 4.10a & b). The cells showed good cell-cell contact and had an elongated appearance (lamellipodia), which reflects the projection of cytoskeletal protein, actin on the leading edge of the cell (Fig. 4.11b). Lamellopodia structures generally helps in the propagation of cells over the ZTA substrates. On completion of 72 h of incubation, a complete confluency was attained by myoblast cells on the surface of 95A-5Z-800 composite as compared to control (Fig. 4.11c-d). Cells were seen to proliferate throughout the surface of ZTA sample and actin filament stained with Alexa Fluor 488 were found to be highly aligned along a specific direction, which shows aligned growth pattern of cells leading to cellular bridge formation. In contrast, the cultured cells appear to be evenly distributed with non-aligned actin filaments, as visualized under fluorescence microscope. The observations such as increase in cell proliferation and highly organized cytoskeletal elements in cells cultured upto a time period of 3 days substantiates that ZTA ceramic sample can provide good support for increasing the expression levels of NDRG2 (N-myc downstream-regulated gene 2), growth related gene which has been linked to increased myoblast growth and skeletal muscle development.[12]

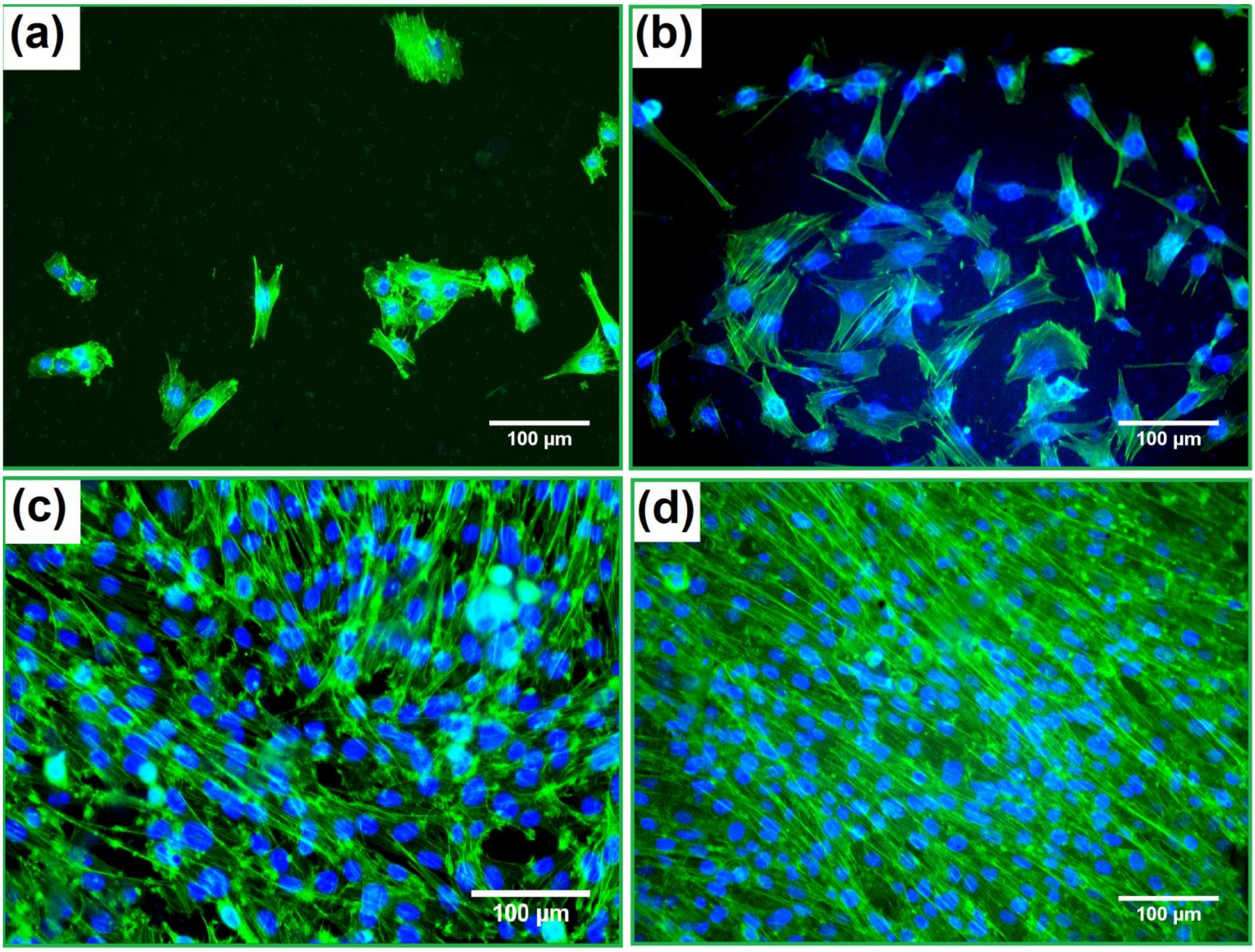

Fig. 4.11: Representative fluorescence microscopic images of C2C12 myoblast cells cultured on (a) control and (b) 95A-5Z-800 for the time period of 24 h and for the time period of 72 h on (c) control and (d) 95A-5Z-800.

The results of the *in vitro* analysis have shown promising cellular response with 95A-5Z-800 substrates. This aspect has been reflected by enhanced cell proliferation, cell attachment, cell spreading and cell-to-cell interaction with specific alignment and organisation of cytoskeleton elements. Therefore, it can be confirmed that the investigated ZTA composite is cytocompatible *in vitro*.

4.3. Conclusions

Based on the wide spectrum of reliable mechanical property measurement and *in vitro* cytocompatibility assessment, the following key points emerge,

(a) Depending on zirconia content, a high compressive strength of 1100 MPa and tensile strength of 200 MPa were recorded with sintered ZTA containing 5 wt.% zirconia and 800 ppm MgO. Also, the SEVNB toughness for this particular composite was determined to be 4.3 MPa.m$^{1/2}$, highest among the composites.

(b) The long crack fracture toughness scales with % transformability of t-ZrO_2 for the investigated ZTA. The difference in fracture toughness among the presently investigated ZTA however could not be explained solely on the basis of difference in grain size or ZrO_2 content.

(c) MTT results confirm that the ZTA composite with the best combination of mechanical properties can support the growth of mitochondrially viable mouse myoblast cells *in vitro* with the viability increasing in statistically significant manner for a period of 72 h in culture.

(d) The fluorescence microscopic observations support the evidence of good cell to cell and cell to substrate attachment, cell spreading, cell elongation and cytoskeletal rearrangement and alignments of the adhered cells leading to cellular bridge formation. All these observation together indicate good cytocompatibility property.

(e) At the closer, the present work establishes that Al_2O_3 – 5 wt.% ZrO_2 – 800 ppm MgO can exhibit the best combination of a wide spectrum of reliable mechanical properties, including long crack fracture toughness (4.3 MPa.m$^{1/2}$), compressive strength (1100 MPa), tensile strength (213 MPa) and hardness (19.3 GPa), together with good muscle cell compatibility, *in vitro*.

4.4. References

---

[1] R. Guo, D. Guo, D. Zhao, Z. Yang, and Y. Chen, “Low temperature ageing in water vapor and mechanical properties of ZTA ceramics,” Mater. Lett., 56, 1014-1018 (2002).

[2] L. Gremillard, L. Martin, L. Zych, E. Crosnier, J. Chevalier, A. Charbouillot, P. Sainsot, J. Espinouse, and J. L. Aurelle, “Combining ageing and wear to assess the durability of zirconia-based ceramic heads for total hip arthroplasty,” Acta Biomaterialia, 9, 7545-7555 (2013).

[3] M. Schehl, L. A. Dıaz, and R. Torrecillas, “Alumina Nanocomposites from Powder–Alkoxide Mixtures,” Acta Materialia 50, 1125-1139 (2002).

[4] H. Tomaszewski, “Toughening effects in Al_2O_3-ZrO_2 System,” Ceram. Int., 14, 117-125 (1988).

[5] M. C. C. D. S. Moraes, C. N. Elias, J. D. Filho and L. G. D. Oliveira, “Mechanical Properties of Alumina-Zirconia Composites for Ceramic Abutments,” Materials research, 7, 643-649 (2004).

[6] Y. J. He, A. J. A. Winnubst, H. Verweij, and A. J. Burggraaf, “Improvement of Mechanical Properties of Zirconia-Toughened Alumina by Sinter Forging,” J. Mater. Sci. 29, 5868-5874 (1994).

[7] A. N. Rascon, A. A. Elguezabal, E. Orrantia, and M. H. B. Bernal, “Compressive Strength, Hardness and Fracture Toughness of Al_2O_3 Whiskers Reinforced ZTA and ATZ Nanocomposites: Weibull Analysis,” Int. J. Refract. Metals Hard Mater., 29, 333-340.

[8] H. Fischer, and R. Marx, “Fracture Toughness of Dental Ceramics: Comparison of Bending and Indentation Method,” Dent. Mater., 18, 12-19 (2002).

[9] S. S. Scherrer, Isabelle L. Denry, and H. W. A. Wiskott, “Comparison of Three Fracture Toughness Testing Techniques using a Dental Glass and a Dental Ceramic,” Dent. Mater., 14, 246-255 (1998).

---

[10] H. Wang, P. Pallav, G. Isgrò, and A. J. Feilzer, "Fracture Toughness Comparison of Three Test Methods with Four Dental Porcelains," Dent. Mater., 23, (2007): 905-910.

[11] B. Basu, "Toughening of Yttria-Stabilised Tetragonal Zirconia Ceramics," Int. Mater. Rev., 50, 239-256 (2005).

[12] V. C. Foletta, M. J. Prior, N. Stupka, D. H. Segal, S. Jones, C. Swinton, S. Martin, D. C. Smith and K. R. Walder, "NDRG2, a Novel Regulator of Myoblast Proliferation, is Regulated by Anabolic and Catabolic Factors," J. Physiol., 587, 1619-1634 (2009).

Chapter 5

Tribological Behavior of ZTA against ZrO_2 and Steel

In view of the importance of the wear resistance properties in the performance and durability of femoral ball head and acetabular cup in total hip joint replacement (THR) application, we have analyzed such properties of sintered ZrO_2-toughened-Al_2O_3 (ZTA) composites with zirconia content of 5 wt.%. The unlubricated sliding wear experiments reveal that a combination of steady state COF of 0.54- 0.62 and wear rate of the order of 10^{-9} $mm^3/N.m$ can be achieved with ZrO_2 counterbody. The wear mechanism is dominated by abrasive wear and cracking induced delamination of tribolayer, when worn against zirconia counterbody. Negligible wear of ZTA against stainless steel is also recorded, which is presumably due to the transfer of oxidized iron transfer film on ZTA and subsequent adhesive wear at the sliding contact. The severity of the wear induced damage was further quantified using the critical analysis of bearing ratio and surface roughness related statistical parameters. Using the established theories for brittle fracture, the theoretical calculations revealed that the maximum tensile stress at the training edge of sliding contact on ZTA is higher than critical damage stress, independent of normal load. Summarising, the combination of tribological properties suggest that the investigated ZTA can be used for load bearing articulating joints, particularly against ZrO_2 mating surface.

Details mechanical and biological response of an optimum zirconia toughened alumina facilitates their acceptability in order to develop high strength – high hardness robust prototypes. However, prior to fabricate bioimplants, friction and wear behaviour against two tribocouples say cubic zirconia (Hv – 21 GPa) and steel (Hv – 2 GPa) has been evaluated and analysed to understand the feasibility of product performance in target to fulfil the objective. The details background of such study is described in section 5.2.

5.1 Experimental

5.1.1 ZTA disc preparation and Characterization

The preparation of ZTA composite from precursor materials has been described in section 3.2.1. The optimized ZTA composition was used for tribological characterization. Importantly, the bearing curve of the original bare and worn surface was determined with an attempt to analyse the load dependent changes in surface roughness parameters.

5.1.2 Tribological Properties Evaluation

The ball-on-disc type wear tester (model - TR-208-M1, Ducom) was used to determine the tribological properties of zirconia-toughened-alumina composites. The optimized ZTA disc specimen was used as a flat sample and fixed in the sample holder, and such arrangement enables the flat sample to rotate at a constant speed. For each and every test, a new counterbody, either cubic ZrO_2 ball or stainless steel ball was fixed to the rigid arm that keeps at stationary and placed in contact with a rotating flat sample under the influence of a normal load. The counterbodies were cleaned using the ultrasonic bath to remove the surface contamination before the test. All the counterbodies were in the form of 10 mm balls and the stable contact between the tribocouple pair was maintained throughout the test. The relative sliding speed of 30 rpm (sliding velocity 6 mm/s) was maintained, while varying the normal loads of 5, 10, 15N. The selection of the corresponding angular speed (3.14 rad/s) mimics the steady state walking of a human.[1,2]

The wear test was carried out at unlubricated conditions (ambient atmosphere) and repeated at least three times. The total test duration was 120 min for all the tribocouple pairs. The total sliding distance for one tribocouple was 45 m. During the wear test, the coefficient of friction and corresponding wear test parameters were recorded with the help of data acquisition card and software *windcum 2006*. After the wear test, the wear scar surface roughness parameters were measured by stylus profilometer. Field emission scanning electron microscopy (FESEM) was used to evaluate the surface topological analysis of worn surfaces. Stylus profilometer (Veesco Dektak 150) attached with Dektak 150 software was used to determine the topographical feature of wear track of ZTA and various statistical roughness parameters. The Hertzian contact pressure was calculated by the following equation[3]:

$$P_{\boldsymbol{hertz}} = \frac{1}{3\pi}[\frac{3\mathrm{FE_r^2}}{\mathrm{R_r^2}}]^{1/3} --(1)$$

Where F is applied normal force in N, E_r is reduced elastic modulus; R_r is reduced radius of the ball in mm. E_r and R_r are defined by following expression:

$$E_r = \frac{2}{\frac{1-\nu_1}{E_1}+\frac{1-\nu_2}{E_2}} --(2)$$

Where $\nu_1$and ν_2 are Poisson’s ratios and E_1 and E_2 are elastic modules of ball and disc materials, respectively. The reduced radius (R_r) $=\frac{R}{2}$; where R is radius of the curvature of the ball. Contact radius estimated by using the radius of the counter body (R), applied normal load (F), and reduced elastic modulus (E_r) by the equation.

$$a = \sqrt[3]{\frac{3FR}{4\,E_r}} --(3)$$

The average specific wear rate was determined using the following formula,[4]

$$K_w = \frac{V_w}{F\,S} - -(4)$$

Where F is the applied normal load (N), S is the sliding distance (m), V_w is the wear volume (mm^3) measured by using a stylus profilometer. The counterbody worn surface was also analyzed through FESEM images in order to understand the wear mechanism between the sliding pairs and further conducted chemical compositional analysis through energy dispersive X-ray analysis (EDS).

The linear bearing ratio curve or material ratio curve is a graphical representation of the bearing ratio parameter in relation to the profile section level. Using the linear bearing area curve we can characterize surface roughness, bearing capacity, and forecast the behavior of the surface produced in different wear conditions. The detailed surface topographical analysis of the worn surfaces is carried out by the measuring the linear bearing curve obtained using stylus profilometer. The linear bearing ratio curve is formed by establishing the amount of material that would rest on a reference plane on relative to the entire cross section of the surface for each height from the highest to the lowest point of the surface. It gives the material or bearing ratio, which is material-filled length to the evaluation length at the given profile section level. The linear bearing area curve, measured using the stylus profilometer is plotted in Fig. 5.10 and the corresponding roughness parameters are mentioned in Table 5.3.

5.2 Results

5.2.1 Microstructural and sliding conditions

It is worthwhile to reiterate that the investigated ZTA is characterized by a combination of better mechanical properties, including high hardness (19.3 GPa), compressive strength (1100 MPa) and tensile strength (200 MPa). Such an array of properties can be attributed to the optimal selection of ZrO_2 addition (5 wt%) as well as sintering parameters (1600 ^{0}C, 6h). All these parameters were optimized based on the response surface modeling approaches, as described elsewhere.[5] Considering the fact that the microstructure influences both the mechanical and the tribological properties, SEM images of ZTA flat and ZrO_2 ball are shown in Fig. 5.1. A close look at Fig. 5.1a reveals the distribution of submicron ZrO_2, mostly at the triple grain junctions of Al_2O_3 matrix (average grain size – 3.2 μm). In Fig. 5.1b, the microstructure of ZrO_2 ball shows equiaxed ZrO_2 grains of around 0.7 μm. As summarized in Table 5.1, the selection of two mating materials, i.e. ZrO_2 or steel can be rationalized in terms of three aspects: a) both steel or Al_2O_3 are used as femoral ball head in THR applications and the presently investigated ZTA can be shaped to acetabular socket, b) Al_2O_3 and steel vary in terms of elastic modulus and therefore, a different range of Hertzian contact stress can be expected to prevail at sliding contacts against two different counterbodies and c) considering the hardness difference between ZTA and Al_2O_3 / steel, the mating couple of ZTA/ Al_2O_3 can be approximated as more like self-mated tribocouple, while adhesive wear can be expected for ZTA/steel.

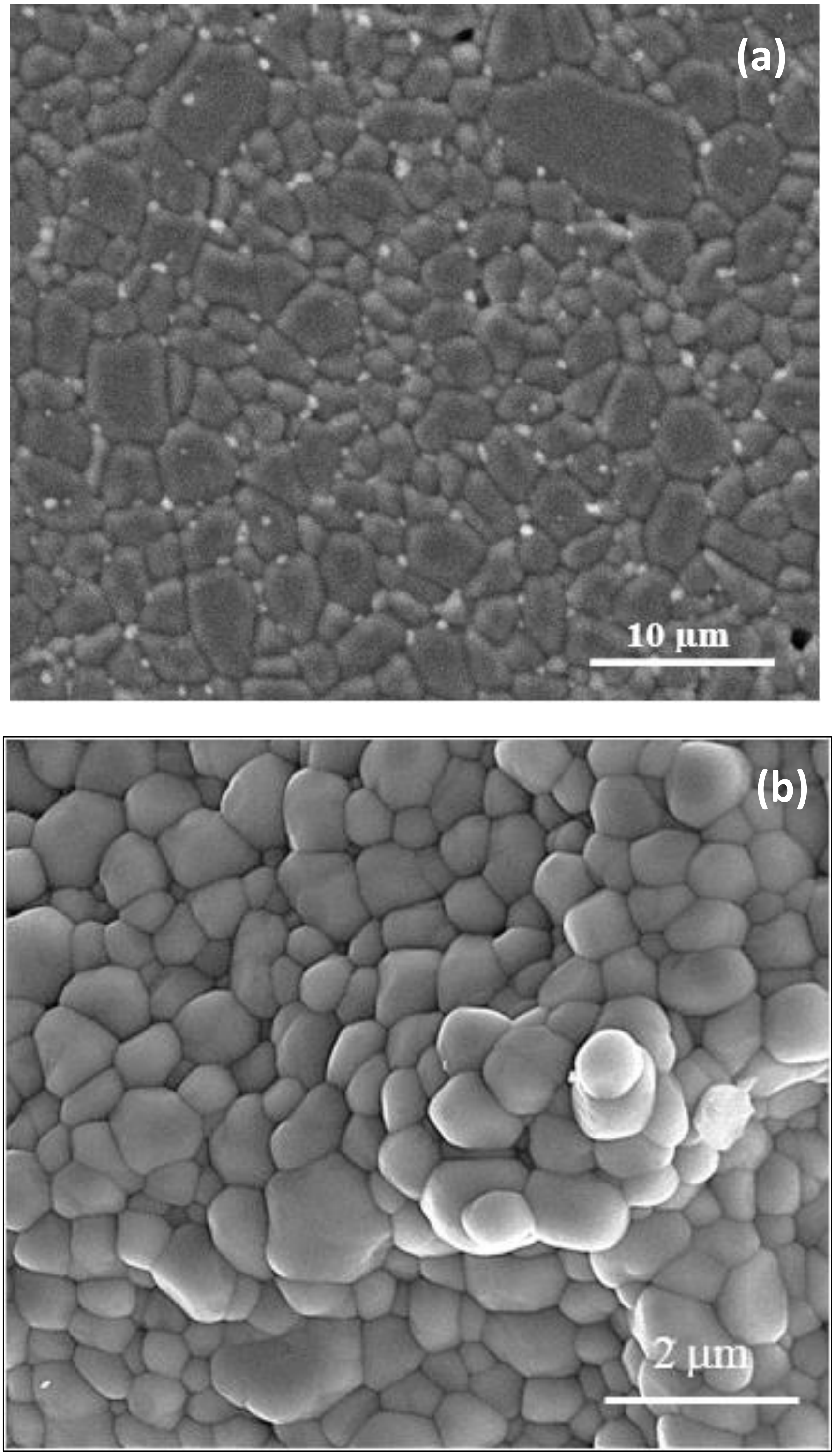

Fig. 5.1: Microstructures of ZTA disk specimens (a) and cubic ZrO_2 ball (b).

Table 5.1**:** Properties of ZTA, ZrO_2 ball and stainless steel ball.

Properties of materials	**ZTA**	**ZrO_2 ball**	**Steel ball**
Hardness (GPa)	19.3	21	2.0
Toughness MPa√m	4.2	13	--
Elastic modulus (GPa)	364	210	200
Compression strength (MPa)	1100	2500	--
Tensile strength (MPa)	200	--	215

Based on the sliding wear parameters as well as on the basis of Eq. (1) (2), and (3), the Hertzian contact stress and contact radius can be determined. The values so obtained are summarized for ZTA/ Al_2O_3 tribocouple in Table 5.2. The Hertzian mean contact pressures are estimated to vary in the range of 390 to 560 MPa. Considering that during the course of sliding, the contact pressure decreases in commensurate with the corresponding increase in contact diameter, it is however important to realize that Hertzian contact pressure is far below the quasi-static compressive strength of ZTA (see Table 5.1). In the following, we describe the friction and wear results, when ZTA was slided against ZrO_2 or steel.

Table 5.2: The Hertzian contact pressure and calculated maximum tensile stress (σ_{max}) at the trailer edge of ZTA against ZrO_2 ball, and critical stress in ZTA composite (σ_S)

Counterbody	Normal load	Contact radius (a) μm	Hertzian contact pressure	σ_{max} (MPa)	σ_S (MPa)
ZrO_2	5	38	389	2930. 8	280
	10	48	490	3532. 1	
	15	55	561	4094.9	

5.2.2 Friction behaviour against ZrO_2 and stainless steel ball

Figs. 2a and 2b illustrate the frictional behaviour of ZTA disc against cubic zirconia ball and stainless steel ball at varying normal loads. Other test parameters such as sliding distance, sliding time and sliding speed were kept constant. From Fig. 5.2, it is clear that the frictional behaviour of the ZTA disc strongly depends on the normal load as well as on mating material. In Fig. 5.2a, the coefficient of friction systematically increases to higher values at the initial running-in-period, and thereafter, the steady state frictional behavior was maintained. This canbe attributed to the fact that the initial surface asperities of the disc and counterbody get continuously knocked off until the smoothing of the contact surface. In effect, the steady state coefficient of friction (COF) is attained after first 0.69, 0.41 and 0.27 hours of sliding time against ZrO_2. Similarly, Fig. 5.2b reveals the frictional behaviour of ZTA disc against steel ball. It is observed from Fig. 5.2b that the COF increases gradually to a steady state level, until the initial surface asperities are knocked off from the tribocouple contact surface. In particular, the steady state COF of 0.41, 0.39 and 0.42 was attained at various normal loads of 5, 10 and 15 N, respectively. These COF values are relatively less than the ceramic-on-ceramic contact. The difference in steady state COF between ZTA and counterbodies are suggested to be related to the interfacial wear mechanism.

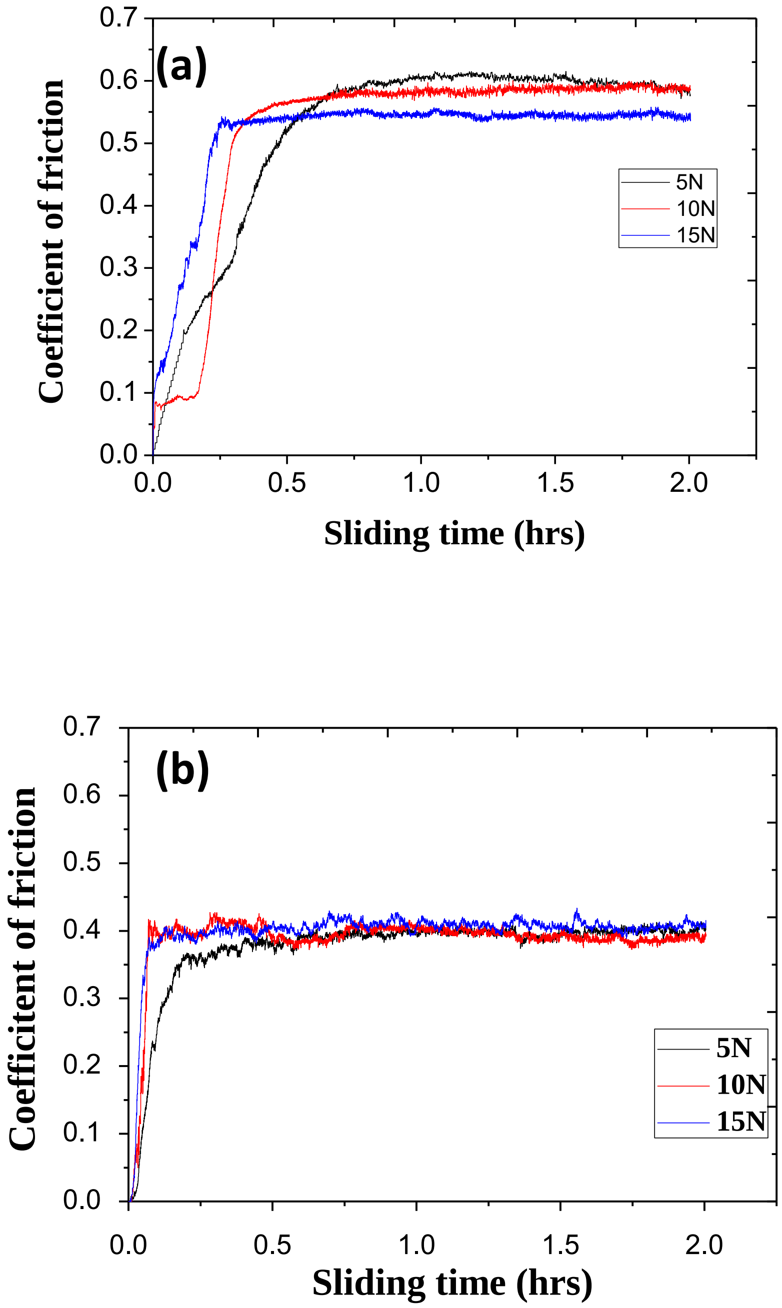

Fig. 5.2: Frictional behaviour of ZTA sintered compact against cubic ZrO_2 ball (a) and against stainless steel ball (b) with varying load (the sliding speed 30 rpm, and duration 2 hrs were maintained during this experiment).

5.2.3 Quantification of ZTA wear rate

The wear rate of ZTA was measured in order to understand the influence of load and friction behavior on wear resistance property. The wear volume, measured using stylus surface profilometer is normalized with respect to normal load and sliding distance to obtain the specific wear rate of ZTA. The wear rate of ZTA flat against two counterbodies, such as ZrO_2 and steel ball are plotted against normal load in Fig. 5.3.

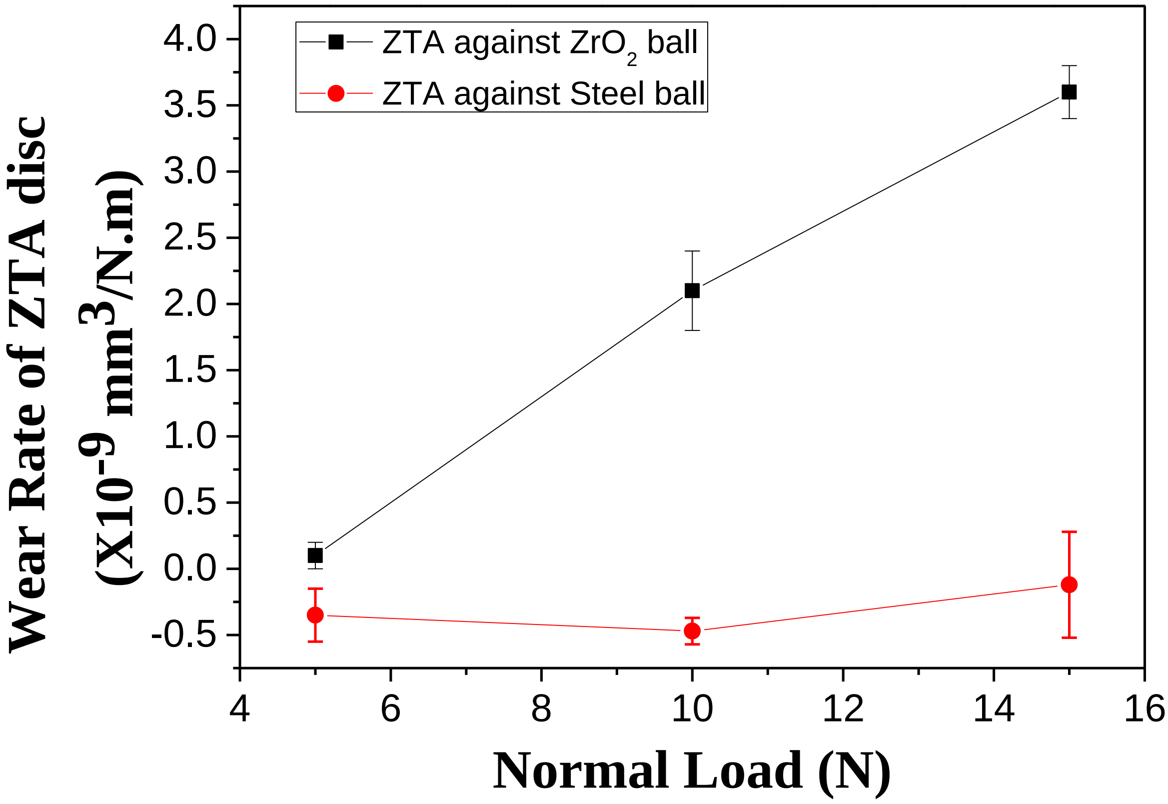

Fig. 5.3: Specific wear rate of ZTA sintered disc specimen at a particular normal load when subjected to rotational slide against ZrO_2 and steel ball (the sliding speed 30 rpm, and duration 2 hrs were maintained during this experiment).

Observing the data in Fig. 5.3, it is clear that the wear rate of ZTA against ZrO_2 varies over the same order of magnitude, i.e. 10^{-9} mm^3/N.m. At the lowest load regime (5N), the specific wear rate is 0.1 X 10^{-9} mm^3/N.m and -0.35 X 10^{-9} mm^3/N.m against ZrO_2 and steel ball, respectively. A similar negative wear rate of alumina coated-YZTP and alumina vs WC and ZTA with Cr (C10Z10) vs steel ball tribocouple has been reported by Carter et al. and Scheppokat et al.[4,6] A Systematic linear increase in wear with respect to load of ZTA against ZrO_2 with load reflects a signature of abrasive wear. In contrast, negligible or negative wear against steel suggests adhesive wear mechanisms mediated by the transfer of oxidised iron transfer film on ZTA and subsequent interaction with the transfer film. The difference in wear rate w.r.t. load in case of ZrO_2 counterbody can be rationalized in the light of the differences in Hertzian contact pressure. The Hertzian contact pressure is directly proportional to applied normal load and inversely proportional to the reduced radius of the contour body. When the normal load increases from 5 to 15 N, similarly, the Hertzian contact pressure also increases from 389 to 561 MPa.

5.2.4 Topographical features of ZTA worn surface

SEM analysis together with surface profilometer analysis was used to understand the counterbody dependent sliding damage on the investigated ZTA flat. In view of the highest wear rate measured 15 N load with ZrO_2 counterbody, we have chosen the worn surface analysis at such sliding condition, as shown in Fig. 5.4. Apart from the expected concentric sliding wear tracks, we do observe the presence of wear debris particles on and around the wear tracks. While assessing the wear induced damage, some representative surface profiles taken at four different locations (marked as A, B, C, D in Fig. 5.4a) are shown in Fig. 5.4. Overall, the surface roughness in terms of the maximum depth of valleys on the worn ZTA is around 3-4 μm. Also, the width of worn region or maximum depth of worn surface at those chosen locations vary within a narrow window, indicating homogeneity in wear induced damage of ZTA against ZrO_2.

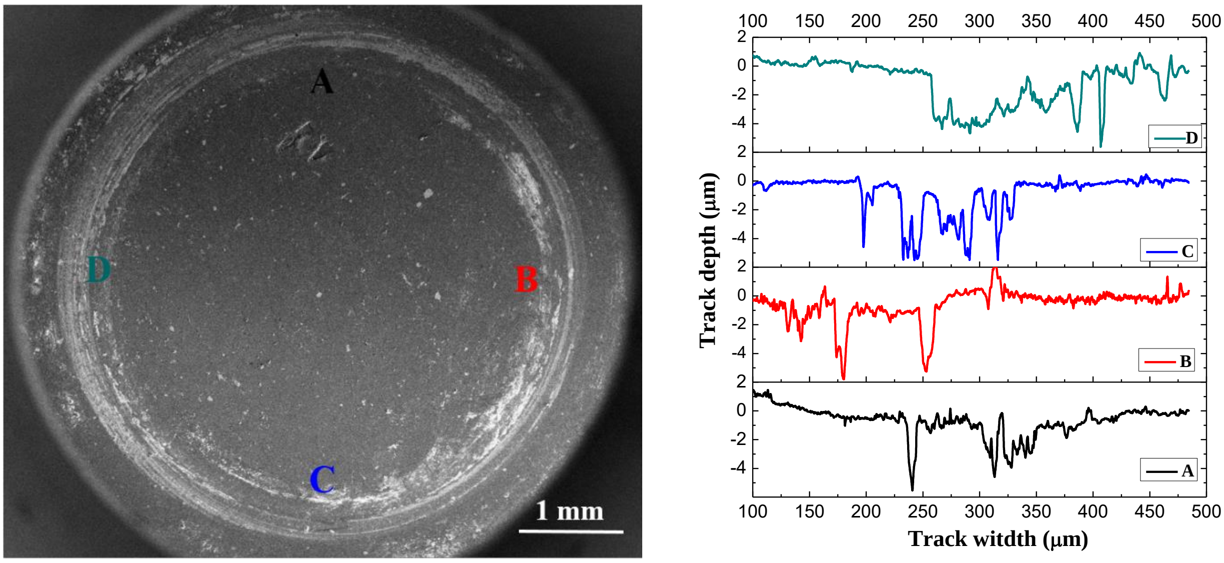

Fig. 5.4: SEM image of the entire wear track on ZTA after slided against cubic ZrO_2 ball (center). The different surface profiles were taken at various locations (A, B, C, and D) to understand the depth of wear removal phenomenon. The sliding conditions were normal load 15 N, sliding speed 30 rpm, and duration 2 hrs.

In contrast, the representative worn surface profile taken from any random location on worn ZTA after sliding against steel clearly indicates the adhesion of transfer layer and as such, the transfer layer forms as a collection of wear fragments from steel counterbody in different sizes, as revealed from the spikes on the surface profile (see Fig. 5.5).

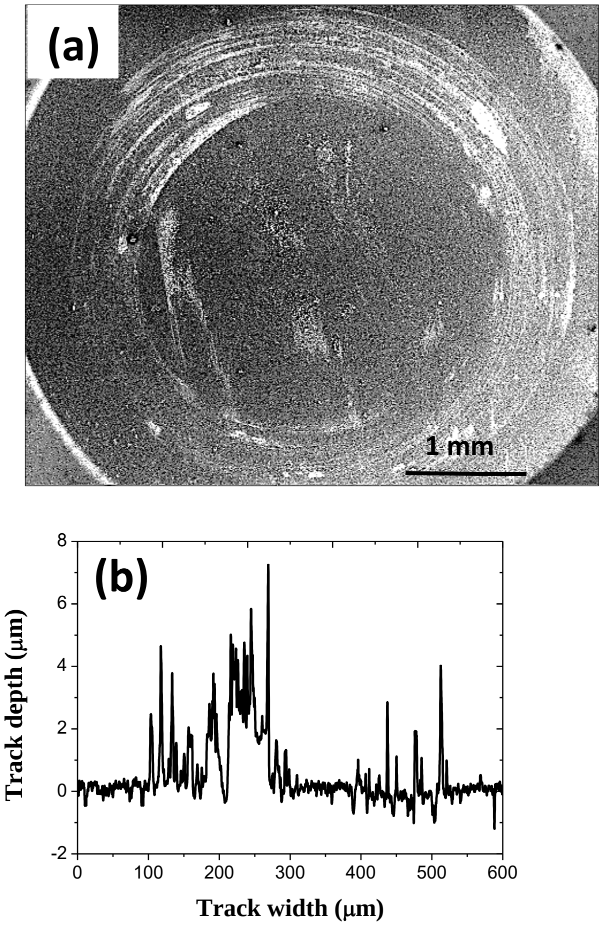

Fig. 5.5: SEM image of the entire wear track on ZTA after slided against commercial available stainless steel (Cr – 20 wt%) ball (a). The surface roughness profile depicts the signature of adhesion of transfer layer and localised adhesion on abrasive grooves (b). The sliding conditions were normal load 15 N, sliding speed 30 rpm, and sliding duration 2 hrs.

The details of the worn surface on ZTA after sliding against ZrO_2 are displayed in Fig. 5.6. In addition to the underlying abrasive grooves, the presence of abraded layer or the third body appearing in different contrast can be clearly seen in Fig. 5.6a. In Fig. 5.6b, the cracking induced spalling at the worn surface can be noticed. The cracks are branched and also propagate more along a direction perpendicular to sliding direction. The size distribution of wear debris particles can be seen in Fig. 5.6c and some coarser or flake-like debris particles are also observed.

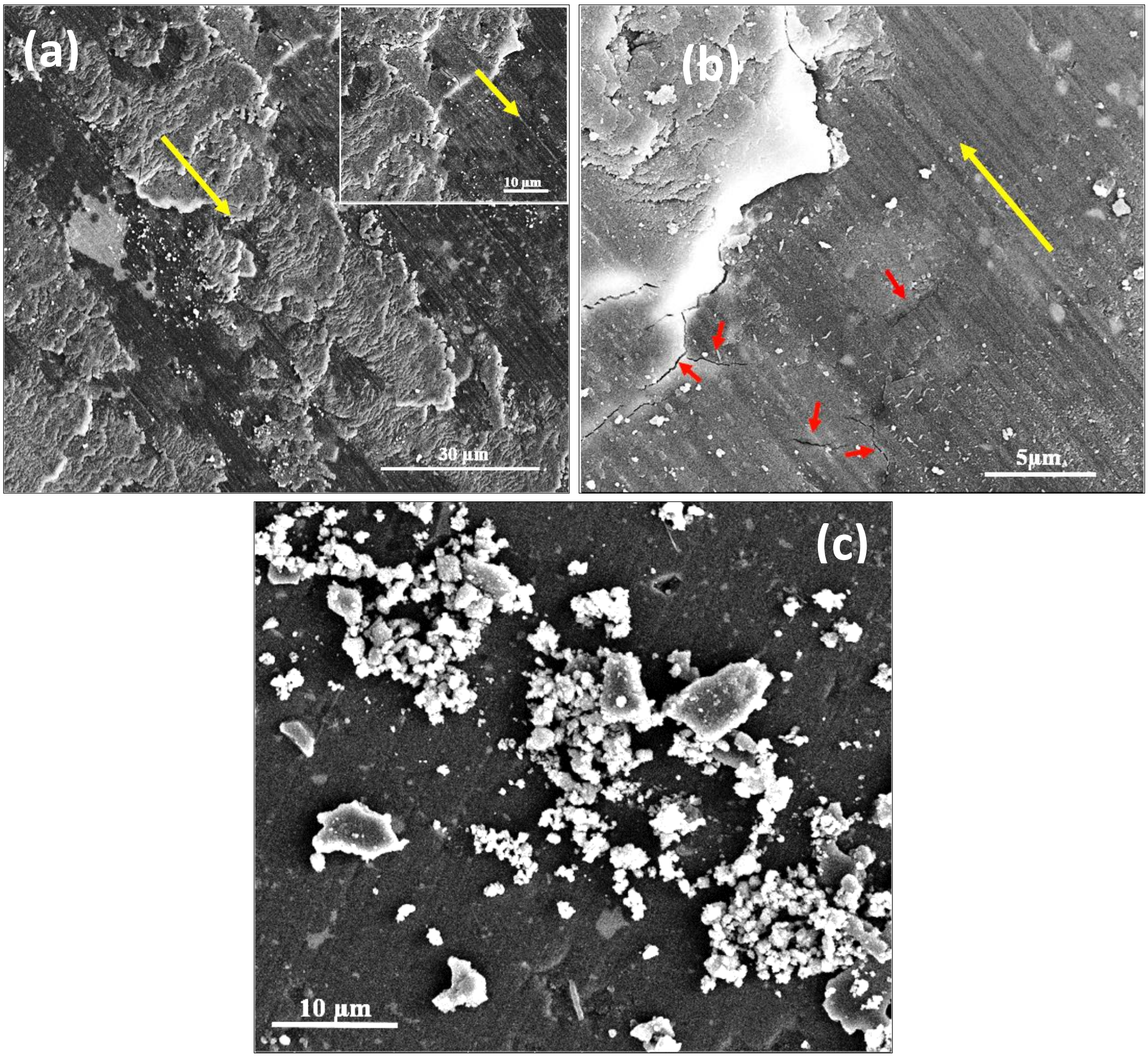

Fig. 5.6: SEM images of the debris fragment layer adhered on the worn surface of ZTA sample against ZrO_2 ball and the micrograph of tribolayer at higher magnification is shown in the inset (a); the cracks on the worn surface which are due to tensile stress at trailing edge of contact surface of sliding pairs (b); the debris accumulated on the worn surface (c).The sliding conditions were normal load 15 N, sliding speed 30 rpm, and sliding duration 2 hrs.

The details of worn surfaces on ZTA after sliding against steel are illustrated in Fig. 5.7. In Fig. 5.7a, the accumulation of steel transfer layer (see also EDS analysis in Fig. 5.7c) onto the abrasive grooves can be seen. In Fig. 5.7b, the presence of steel transfer layer with certain characteristic features can be seen.

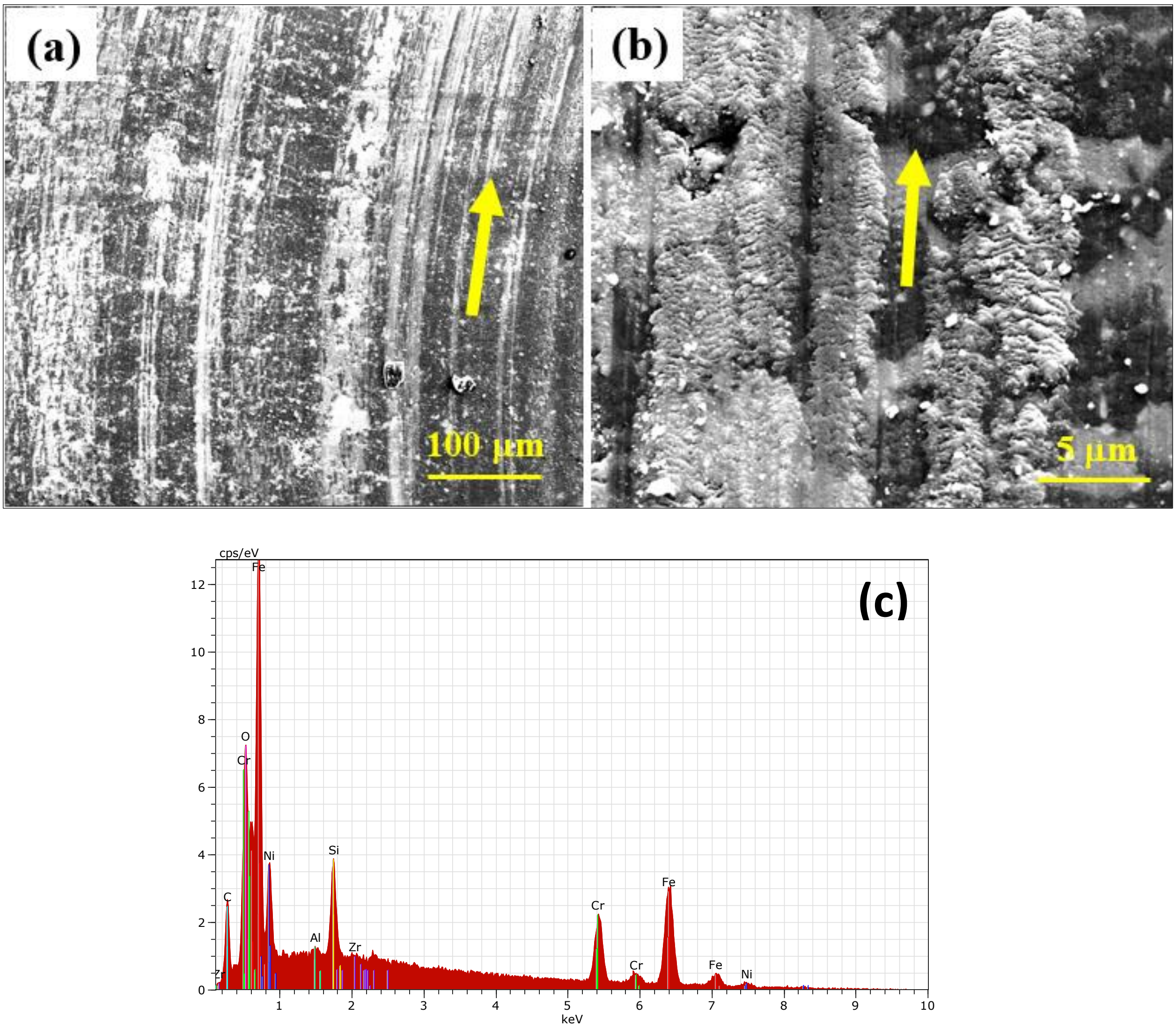

Fig. 5.7: SEM micrographs wear scar of ZTA (a) against steel ball at 15 N normal load and different magnification of wear scar (b) contains debris adhered like a film on the wear surface and compositional analysis (c). Sliding direction shown by an arrow. The sliding conditions were normal load 15 N, sliding speed 30 rpm, and sliding duration 2 hrs.

The wear induced damage of counterbody was also investigated. The worn surface on ZrO_2 ball shows the cracking induced spalling (see Fig. 5.8a and 8b). Interestingly, EDS analysis taken from the presence of Al-peak, indicating some material transfer from ZTA flat (see Fig. 5.8c). The damage of steel counterbody was not very significant, when compared to ZrO_2 counterbody, under similar sliding conditions. While the abrasive scars are seen, but those are mostly covered with steel tribolayer, as evident from EDS compositional analysis (see Fig. 5.9). Therefore, no material transfer from ZTA flat took place in case of steel counterbody.

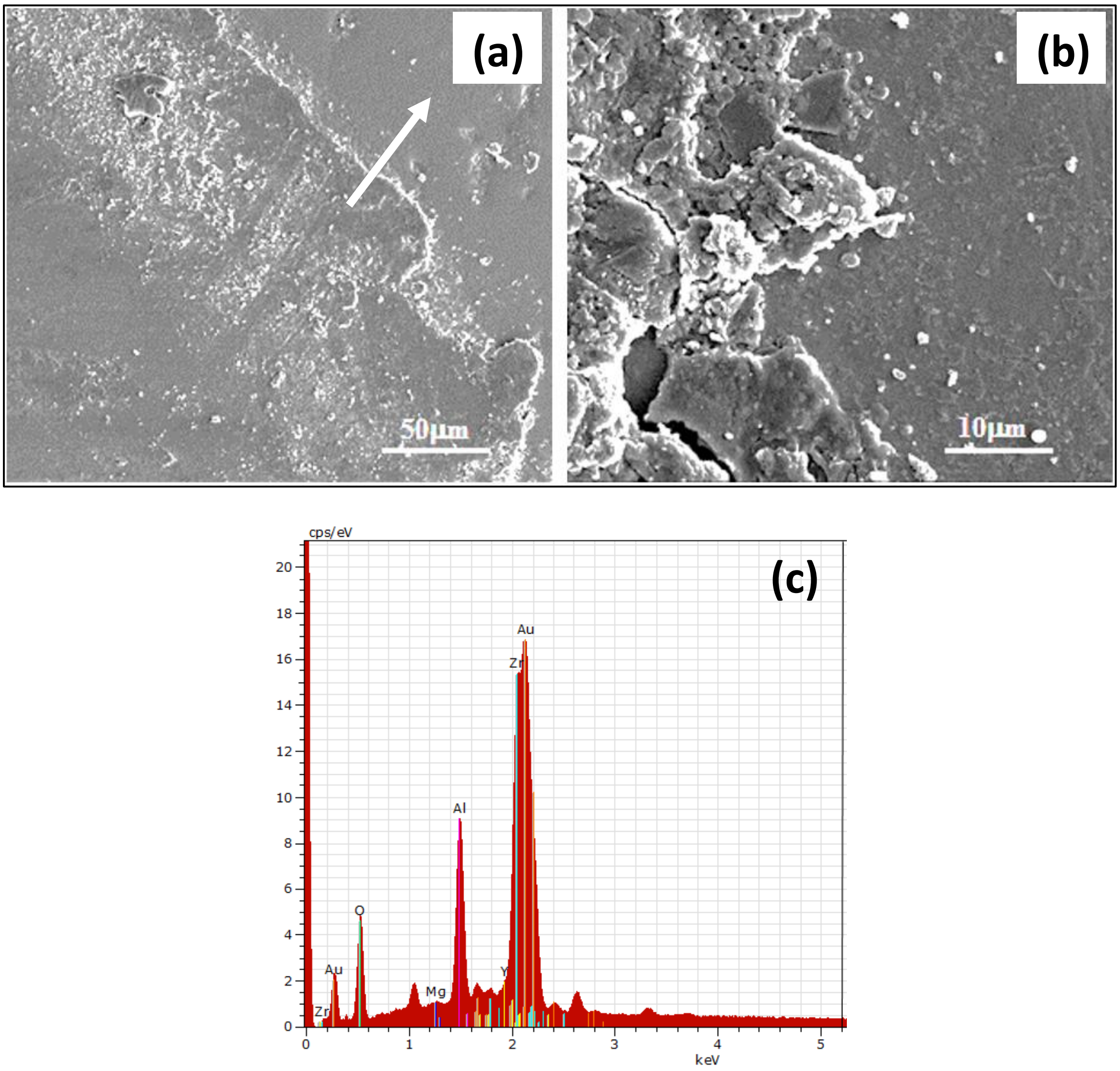

Fig. 5.8**:** The worn surface micrograph of cubic ZrO_2 ball (a) tested against the ZTA disc specimen at 15N and high magnification micrograph of debris fragment layer at the edge of the same worn surface (b) indicates abrasive wear mechanism followed between the sliding pairs. Compositional analysis of wear debris on ZrO_2 counterbody after wear test (c). The presence of Al gives the evidence of material transfer from disc specimen to ZrO_2 ball. The sliding conditions were normal load 15 N, sliding speed 30 rpm, and sliding duration 2 hrs.

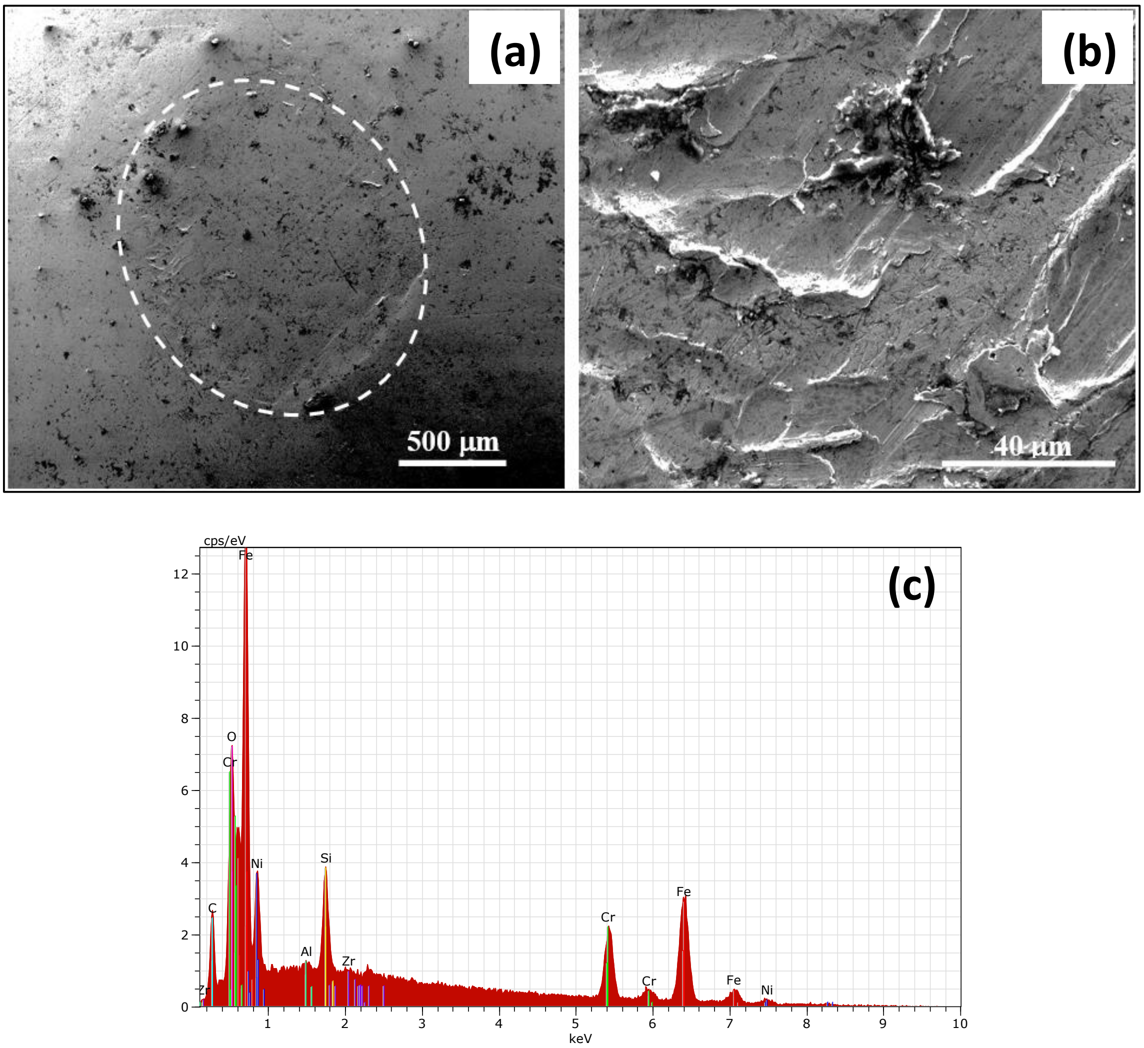

Fig. 5.9: The worn surface micrograph of stainless steel ball (a) tested against the ZTA disc specimen at 15N and wear marks indicates plastic deformation on ball surface (b). Compositional analysis on the same worn surface (c). The sliding conditions were normal load 15 N, sliding speed 30 rpm, and sliding duration 2 hrs. Very minute amount of transferred metallic Al and Zr is noticed during tribological test.

5.2.5 Bearing Ratio analysis and surface roughness parameters

Detailed surface topographical analysis of the bare and worn surfaces is compared through linear bearing ratio curve obtained using stylus surface profilometer. The bearing ratio curve of worn ZTA surface against ZrO_2 and steel ball measured using stylus profilometer is plotted in Fig. 5.10 and the corresponding roughness parameters are summarised in Table 5.3. In Table 5.3, various surface roughness parameters such as reduced peak height, reduced valley depths and material ratio are specified for the worn surface of the various ZTA samples. It can be noted that roughness parameters are measured in X, Y direction individually and their average of parameters are only taken. While discussing the surface roughness profilometer results, the concept of linear bearing area curve and various important associated parameters are needed to be defined. For example, R_{pk} is the surface roughness parameter of reduced peak height that leads to high-stress concentration points on the initial contact area. These high asperities on the worn surface may be knocked off during the operation. Similarly, R_{vk} is the reduced valley depths of the worn surface, which is measured below the core roughness. R_{vk} indicates the valleys that can hold the debris to consequently reduce the friction. Correspondingly, R_k is the core roughness of the worn surface and determines the nominal surface roughness. The material ratio is the ratio of the intersecting area of a plane passing through the surface at a given height to the cross-sectional area of the evaluation region. Material ratio (Mr_1 and Mr_2) determines the level of the peak area and valley area of the worn surface texture of ZTA sample that can support the load between the reduced peak height, reduced valley depth and reduced core height.[7]

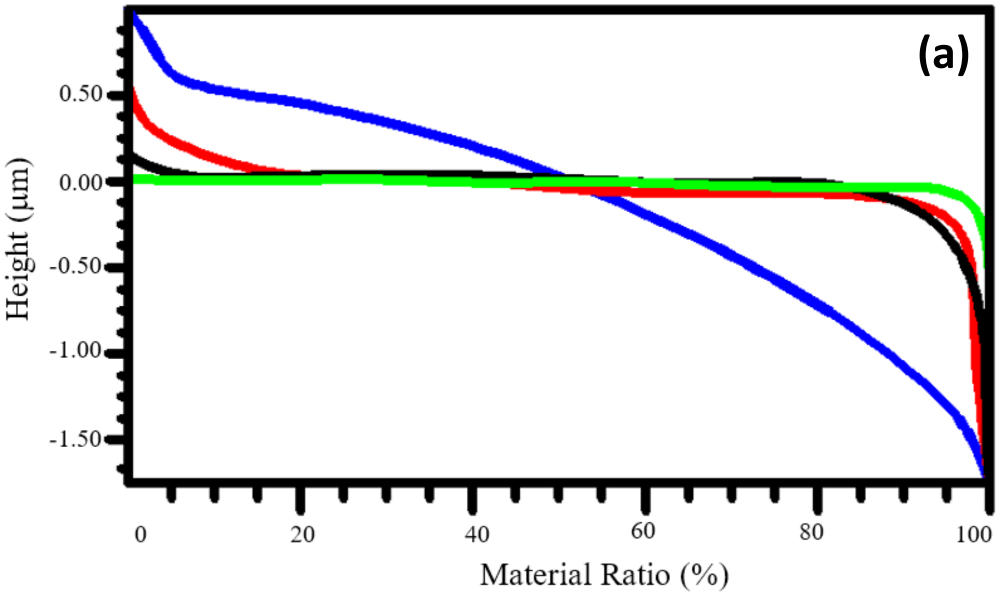

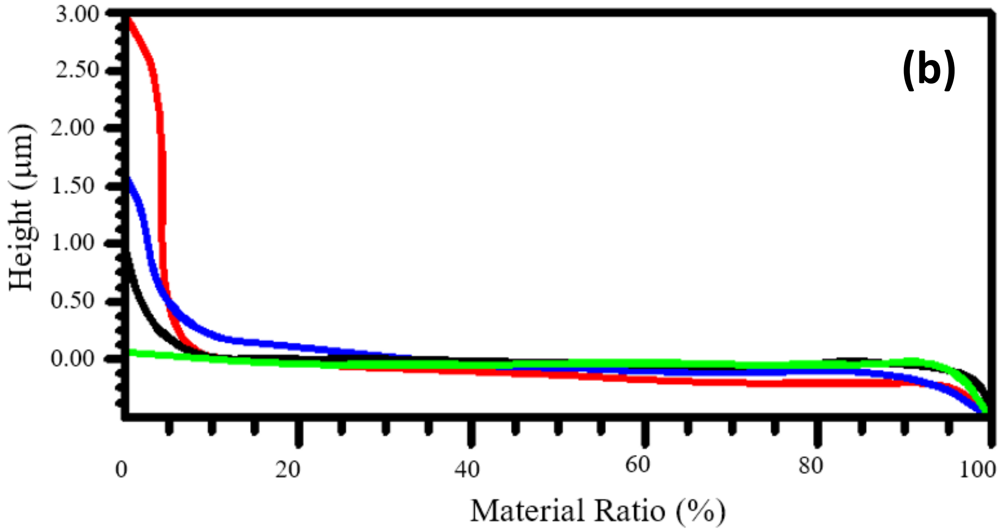

Fig. 5.10: Bearing ratio curves measured on ZTA specimens after it was slided against cubic ZrO_2 ball (a) and stainless steel ball (b) at three different normal loads. A reference bearing ratio for bare surface is also given for the comparative study. Black, red and blue colours are corresponding to 5, 10 and 15N, respectively. Green line represents the bare ZTA surface (sliding conditions include, sliding speed of 30 rpm and duration of 2 hrs).

Table 5.3: Influence of load on the bearing ratio parameters measured on ZTA after sliding against cubic zirconia ball and steel ball at different loads with sliding speed 30 rpm.

Counterbody →		ZTA worn surface at different load and counterbodies					
		against ZrO_2 ball			against Steel ball		
Parameters	Unworn surface	5N	10N	15N	5N	10N	15N
Roughness average R_a(μm)	0.012	3.33	3.67	5.58	3.44	3.00	7.25
Root mean square R_q(μm)	0.019	4.74	2.79	9.32	4.57	2.98	5.58
Surface skewness, R_{sk}	0.06	-0.86	-1.21	-1.47	-0.46	-0.22	1.97
Surface kurtosis, R_{ku}	3.19	2.85	0.14	0.37	2.41	0.95	0.66
Reduced peak height, R_{pk} (μm)	0.005	4.00	4.20	8.60	3.32	3.26	4.00
Reduced core height, R_k (μm)	0.027	1.48	4.11	6.70	1.26	1.15	1.67
Reduced Valley height, R_{vk} (μm)	0.046	4.78	2.09	12.83	0.74	0.83	2.83
Material ratio 1 (Mr1%)	6.37	9.0	22.8	4.45	4.8	16.9	9.71
Material ratio 2 (Mr2%)	82.46	80.4	75.1	72.2	91.4	96.8	92.3

In Table 5.3, various surface roughness parameters of unworn surface and worn surface of ZTA flat. From the bearing ratio curve as shown in Fig. 5.10, the bare surface (green color line) has near to linear characteristics with low value of R_{pk} and R_{vk}, indicating uniform asperities on the unworn surface.Observing the Fig. 5.10a and Table 5.3, it is evident that the surface of ZTA is being severely damaged in contact with zirconia. However, bearing ratio plot (see Fig. 5.10b) for ZTA/steel contact depicts reverse behavior because of steel transfer to ZTA surface (negative wear as discussed in section 3.4). Except the expected variation in R_a and R_q with respect to load increment and different counterbodies, an interesting observation on skewness and kurtosis can be observed, while critically assessing the data in Table 5.3. The resultant surface peak height distribution is measured as negative skew for ZTA/zirconia contact. This indicates the development of fairlydeep valleys on ZTA worn surfaces with an increment of the load. However, this feature becomes more positive for ZTA/steel tribocontact, because of more adherence of transfer layers and fairly high spikes that protrude above a flatter average. Correspondingly, kurtosis (R_{ku}) is used to measure the shape of amplitude distribution function of the worn surface. Since R_{ku} is less than 3, the shape of the peak in amplitude density function (ADF) is broad and flat compared to a normal

Gaussian height distribution. The reduced peak height (R_{pk}) corresponding to top 25% material ratio (Mr1) of the worn surface increases to four to eight times with similar variation in normal load for ZTA/ZrO_2 contact. However, it is relatively less, when the surface is adhered by more transferred layer from steel. Larger peak roughness implies that the wear has been more at 15 N load and also the contact stress will be more at 15 N load, which would cause significant material removal on further wear at the interface. The reduced valley height (R_{vk}), corresponding to bottom 25% material ratio (Mr2) also increases with load under the chosen sliding conditions. This indicates a larger valley depth, leading to the entrapment of more wear debris at the sliding interface.

5.3 Discussion

5.3.1 Influence of load on friction and wear mechanism

In this subsection, we will now analyze the load and counterbody dependent friction and wear behavior. A closer look at Fig. 5.2c clearly reveals the following aspects:

a) ZTA/ ZrO_2 sliding pair experiences much higher steady state COF (0.55-0.62) than that of ZTA/steel tribocouple (0.38-0.42). Therefore, it is expected that ZTA/ ZrO_2 pair at an articulating joint would also cause more frictional noise.

b) The load dependence of frictional behavior is more evident in case of ZTA/ ZrO_2 tribopair, both in terms of steady state COF as well as the way COF rises in the running-in-period to the steady state. The transition from running-in-period takes place over longer time duration with an increase in load.

c) The frictional behavior ZTA/steel tribopair is found to be insensitive to the normal load applied during sliding tests. Considering the fact that the steady state COF of self-mated steel is around 0.5, the frictional behavior, as shown in Fig. 5.4b together with SEM analysis of worn surfaces, therefore suggest the steel tribolayer transfer to ZTA does not make the sliding contact to purely self-mated configuration (i.e. steel vs. steel), but the response of underlying ZTA flat also contributes to the observed frictional behavior.

Concerning the wear resistance properties, the following points emerge while critically assessing the results presented in Figs. 5.3-5.5:

a) The systematic linear increase in wear rate of ZTA against ZrO_2 with load establishes the dominance of abrasive wear.

b) The adhesive contribution to wear of ZTA/steel leads to negative wear.

5.3.2 Correlation of observation of cracking with theoretical model prediction

The following analysis is based on the assumption that sliding damage induced stresses would trigger crack nucleation or crack growth of pre-existing flaws, if the tensile stress field at trailing edge of a sliding contact exceeds the critical damage stress. Cho et al.[8] particularly commented that the damage stress ‘augments’ the pre-existing stresses in a multiphase microstructure and often triggers the transition from mild to severe wear at an early timepoint during sliding or effectively lowers the critical grain size for transition to severe wear.

The observation of cracking on the worn surfaces, as shown for example in Fig. 5.6, can be rationalized on the basis of stresses around Hertzian contact zone. Considering the presence of 5% ZrO_2 in Al_2O_3 for the presently investigated ZTA, some elements of the following calculations are based on the values of pure Al_2O_3, but not limited to the entire calculation. Based on the established theory, the maximum tensile stress at the trailing edge of the contact (σ_{max}) can be expressed as,

$$\sigma_{max} = \frac{3F}{2\pi a^2}[\frac{1-2\vartheta}{3} + \frac{(4+\vartheta)\pi\mu}{8}] - -(5)$$

Where F is the normal load, a is the Hertzian contact radius, ϑ is Poisson's ratio and μ is the coefficient of friction. Based on the presently used sliding condition and material parameters, the values of σ_{max} can be determined and summarised in Table 5.2. Following an earlier analysis reported elsewhere,[9] the critical tensile stress (σ_s) induced for microcrack propagation can be expressed by the following equation,

$$\sigma_s = \sigma_I^* \left(\frac{d^*}{d}\right)^{1/2} - \sum_{i=0}^{n} \sigma_{Ii} - -(6)$$

In the above expression, the second term on the right hand side essentially represents the summation of the internal stresses in a given microstructure and the first term is the grain size – normalized frictional stresses at a grain size (d) with respect to critical grain size (d^*). The internal stresses, σ_{I1} due to thermal expansion anisotropy in polycrystalline alumina can be given by the following equation:

$$\sigma_{I1} = \frac{1}{2}\, \Delta\alpha\, E_M\, (T_e - T_{Room}) - -(7)$$

Where the critical temperature T_e is the characteristic temperature above which all stresses can be relaxed. $\Delta\alpha$ is the change in the coefficient of thermal expansion between the a- and c-axes.[10] For alumina, the maximum thermal-expansion-anisotropy stress can be obtained as $\sigma_{I_1}^{max}$ = 299 MPa.

As far as other source of residual stress is concerned, the thermal stresses between the alumina and zirconia phases (σ_{I2}) at the grain boundary (see for example, Fig. 5.1a) can be defined using the following equation,[11]

$$\sigma_{I2} = \frac{\Delta\alpha\Delta T}{\frac{1+\vartheta_m}{2E_m}} + \frac{1-2\vartheta_p}{E_p} - -(8)$$

Where the subscripts m and p refer to matrix alumina and particle zirconia, respectively, $\Delta\alpha$ is the differential thermal expansion coefficient ($\alpha_p - \alpha_m$), $\Delta T = 1575^{o}C$ is the temperature range of cooling, ϑ and E are Poisson's ratio and elastic modulus, respectively. For ZrO_2 – toughened – Al_2O_3, $\alpha_m = 9 \text{ X } 10^{-6}$ K^{-1} and $\alpha_p = 10 \text{ X } 10^{-6}$ K^{-1}, respectively,[12] and E_m = 380 GPa and E_p = 210 GPa, ϑ_m = 0.3 and ϑ_p = 0.3. For such a set of values, we compute, σ_{I2} = 920 MPa.

Finally, the transformation of ZrO_2 phase from tetragonal to monoclinic ZrO_2 phase generates the compressive stresses (σ_{I3}), that can be determined using the following formula:

$$\sigma_{I3} = -E_p \frac{\Delta V}{V} \frac{V_v}{3(1-\vartheta_p)} - -(9)$$

Where E and ν are the Elastic modulus and Poisson's ratio of ZrO_2, V_v is the volume fraction of ZrO_2 and ΔV/V is the fractional volume change due to ZrO_2 – phase transformation.[13] If we use typical values for ZrO_2 phase transformation, i.e. ΔV/V = 0.007, E = 210 GPa, V_v = 0.03, and ν = 0.3, then it can be estimated that σ_{I3} = -23.2 MPa, assuming the absence of stress relaxation.

Now we will estimate the first term on the right hand side of Eq. (5). Considering the presence of only 5 % ZrO_2, the frictional stress, (σ^*_1) can be approximately taken as that of pure Al_2O_3, as reported in literature.[8] With such assumptions of σ_I^*= 132 MPa, d^*= 400μm, d=3.2μm (average grain size Al_2O_3 = 3.2 μm), the value of $\sigma_I^* \left(\frac{d^*}{d}\right)^{1/2}$ can be estimated to be 1475.8 MPa. It may be worthwhile to mention that d^* in the above calculation is the critical grain size for spontaneous microcracking/microfracture even in the absence of sliding, as reported by Cho et al.[8]

On the basis of the estimates of various components of internal stresses in ZTA microstructure, the critical damage stress was further determined using Eq. (5). After incorporating various stress values, we obtain, σ_s= 280 MPa, which does not depend on load applied during sliding. The above discussion also signifies that σ_s will be sensitive to ZrO_2 content Al_2O_3 matrix as well as on sintering temperature. Looking at data in Table 5.2, it would appear that σ_{max} surpasses σ_s at the highest load of 15 N. However, one should also note that the calculation of σ_{max} is valid for initial Hertzian contact and under dynamic conditions, σ_{max} would vary from the values calculated from eq. (4). Nevertheless, it is clear that the σ_{max} has similar or higher magnitude than σ_s to trigger cracking induced abrasive damage at sliding contact.

At the closure, the present work demonstrates the possibility of achieving a better wear resistance property of Al_2O_3- 5% ZrO_2 ceramics (wear rate- 10^{-9} mm^3/Nm) against ZrO_2 at sliding conditions similar to that experienced at load bearing articulating joints. It may be worthwhile to mention that the wear rate of conventional ceramic composites mostly vary in the range of 10^{-6} to 10^{-7} mm^3/Nm. A higher wear resistance is presumably due to a better combination of hardness and fracture toughness properties, which to a large extent is due to the fine grained microstructure. More importantly, an attempt has been made to rationalize the cracking induced spalling in abrasive wear dominated material removal to the critical damage stress. The correlation of the theoretical model with experimental observation also shows that a similar approach can be followed while evaluating wear resistance properties for other brittle materials.

5.4 Conclusions

Based on the analysis of the experimental results, the following key points emerge,

a) The load dependence of frictional behavior is more apparent for ZTA/ZrO_2 sliding couple that ZTA/steel. Under the investigated sliding conditions, steady state COF of 0.5-0.6 was recorded with ZTA/ZrO_2 tribocouple, while a much lower COF of 0.4 was obtained for ZTA/steel. The transferred metallic layer prevented direct contact between metal and ZTA ceramic, and therefore that controlled the friction and wear behaviour of the sliding couples.

b) A better sliding wear resistance with wear rate varying in the range of 10^{-9} mm^3/Nm can be achieved with ZTA/ZrO_2. From the wear data, the ZTA sample exhibited high wear resistance due to high hardness and material adherence on the worn surface. The more homogeneous microstructure of the ZTA disc leads to a significant improvement in wear resistance. On the other hand, ZTA/steel tribocouple exhibited a negative wear rate, which indicates that occurrence of mass transfer from the metal ball to ZTA.

c) The observed load dependence of wear rate together with the closer analysis of worn surface morphology establishes abrasive wear as the predominant mode of wear mechanism for ZTA/ZrO_2. The morphology of the surface of the counter body is the main cause for the abrasion. In contrast, adhesive wear plays a major role in case of ZTA/steel.

d) The load dependence of wear rate also corroborates well with the load dependent increase in multitude of bearing curve related statistical surface roughness parameters.

e) Based on the consideration of several internal stresses including thermal residual stress and t-ZrO_2 transformation stresses, the critical damage stress is found to be larger than the maximum tensile stresses at the trailing edge of sliding contact on ZTA, when worn against ZrO_2.

f) The theoretical analysis therefore is in close correlation with the experimentally observed cracking induced material removal mechanism. The contact area between the two harder ceramic surfaces will be less than that between relatively softer ceramic surfaces. The contact stresses are therefore larger and, consequently, the tendency for fracture wear is larger.

5.5 References

---

[1] F. Liu, Z. Jin, P. Roberts, and P. Grigoris, “Importance of Head Diameter, Clearance, and Cup Wall Thickness in Elastohydrodynamic Lubrication Analysis of Metal-on-Metal Hip Resurfacing Prostheses,” J. Eng. Med., 220, 695-704 (2006).

[2] L. Mattei, F. D. Puccio, B. Piccigallo, and E. Ciulli, “Lubrication and Wear Modelling of Artificial Hip Joints: A Review,” Tribol. Int., 44, 532–549(2011).

[3] K. L. Johnson, "Contact Mechanics," Cambridge University Press, 1985.

[4] F. Kern, P. Palmero, F. G. Marro, and A. Mestra, "Processing of Alumina–Zirconia Composites by Surface Modification Route with Enhanced Hardness and Wear Resistance," Ceram. Int., 41, 889-898 (2015).

[5] B. Basu, B. S. Reddy, K. Ravikumar, N. Bhaskar, and D. Sarkar, “ZrO_2 toughened Al_2O_3 Biocomposites with Reliable Fracture Resistance and Muscle Cell Compatibility property,” (Unpublished Data).

[6] S. Scheppokat, R. Hannink, R. Janssen, G. D. Portu, and N. Claussen, “Sliding Wear of Cr–Al_2O_3–ZrO_2 and Mo–Al_2O_3–ZrO_2 Composites,” J. Eur. Ceram. Soc., 25, 837–845 (2005).

[7] B. Basu and M. Kalin, " Tribology of Ceramics and Composites: A Material Science Perspective," Wiley, 2011.

[8] S. J. Cho, B. J. Hockey, B. R. Lawn and S. J. Bennison, “Grain-Size and R-Curve Effects in the Abrasive Wear of Alumina,” J. Amer. Ceram. Soc., 72, 1249-52 (1989).

---

[9] G. M. Hamilton, “Explicit Equations for the Stresses beneath a Sliding Spherical Contact,” Proceedings of the Institution of Mechanical Engineers, Part C: J. Mech., Eng. Sci., 197, 53-59 (1983).

[10] J. E. Blendell, and R. L. Coble, "Measurement of Stress due to Thermal expansion Anisotropy in Al_2O_3," J. Amer. Ceram. Soc., 65, 174-178 (1982).

[11] B. R. Lawn, “Fracture of Brittle Solids,” Cambridge university press, 1993.

[12] D. R. Uhlmann, H. K. Bowen, and W. D. Kingery, "Introduction to Ceramics," Wiley, (1976).

[13] D. J. Green, R. H. J. Hannink, and M. V. Swain, "Transformation Toughening of Ceramics," CRC Press, (1989).

Chapter 6

Fabrication and Properties of ZTA Femoral head and Acetabular Socket

Despite several decades of research for new materials for articulating joints in orthopedic applications, the efforts to develop patient-specific prototype of such biomaterial devices are rather limited. While addressing this aspect, the present work demonstrates an integrated manufacturing approach to fabricate femoral head and acetabular socket prototypes of zirconia-toughened alumina (ZTA) with specific composition (Al_2O_3-5 wt% ZrO_2 (3 mol % Y_2O_3 stabilised)). In commensurate with the computer aided-design (CAD) of prototypes, the custom made modular steel-die mould assembly was utilised to obtain high strength green powder compact of without any geometric distortion at a uniaxial pressure of 18 - 22 ton. Subsequently, the green compact of the femoral head and acetabular socket was presintered at 1200^{o}C in air for 2h in a conventional sintering furnace and the presintered compact was computer numerical control (CNC) machined to a limited extent. The final stage of prototype development involved the multi-stage sintering with final holding at 1600^{o}C for 6h in air, followed by polishing using tailor-made machine. The process quality was closely monitored by measuring dimensional changes at each stage as well as the circularity measurement of final polished prototypes. The microstructures as well as the physical properties in terms of hardness, fracture toughness and burst strength are also reported. Taken together, the present manufacturing approach appears to be a scalable and commercially viable fabrication strategy to make bioceramics based femoral ball head and acetabular socket for total hip joint replacement surgery.

In continuation of composition optimization and their physical, mechanical and biological properties evaluation of coupon disks or bar shaped specimens, this chapter deals with the designing and fabrication aspects of zirconia toughened alumina femoral head and acetabular socket bioimplants including their characterization to some extent. The detail study eventually depicts a new technique in order to fabricate the ceramic prototypes.

6.1. Design of ABS femoral head and acetabular socket prototypes

6.1.1 Design of prototype

The preparation of a ceramic femoral head and acetabular socket from zirconia-toughened alumina according to the desired design not only involves the preparation of a complex shape using powder-based sintering, but also several machining processes. In general, these machining processes are different from the conventional machining of machine design components, as various regions of the components were subjected to involve rotational grinding or polishing processes. The choice of tooling for this operation is often a balance between optimum surface quality and geometry, according to the designed shape and tolerances. The fabrication of prototype involves the design concepts, manufacturing capabilities and product valiadation. For the targeted 26 mm (OD) ZTA femoral head and 26.5 mm (ID) ZTA acetabular cup fabrication, the following specific steps were involved.

6.1.2 Designing of 3D - CAD femoral head and Acetabular Socket

The geometrical shapes of the femoral head was designed from the respective clinical models in terms of diameter, truncated head height, depth of the blind hole, open and blind end diameter of femoral head blind hole. To ensure perfect fixing and removal during revision arthroplasty of the femoral stem into the femoral head, the Morse taper angle of $2^{o}48'$ was maintained throughout the length of the femoral head bore hole. Similarly, acetabular socket dimensions were derived in terms of inner and outer diameter and hemispherical height. Using these geometrical properties and features, three dimensional femoral head and acetabular socket was designed in Pro/E molding software (see Fig. 6.1 a & b) and consider as targeted geometrical feature of selective ceramic prototypes. In view of shrinkage behaviour associated with powder-based sintering, other allowance namely material shrinkage allowances, machining and finishing allowances were added to the target model dimensions, while tailoring the dimensions to green specimen. In view of the above, modified design concept, other allowances were incorporated to the targeted component dimensions and presented as orthogonal and isometric projection of the prototype femoral head and acetabular socket shown in Fig. 6.2 a & b. Such a femoral head and acetabular socket dimensions and shape were used further to develop the multi-piece integrated cavity steel mould for uniaxial pressing of the powder.

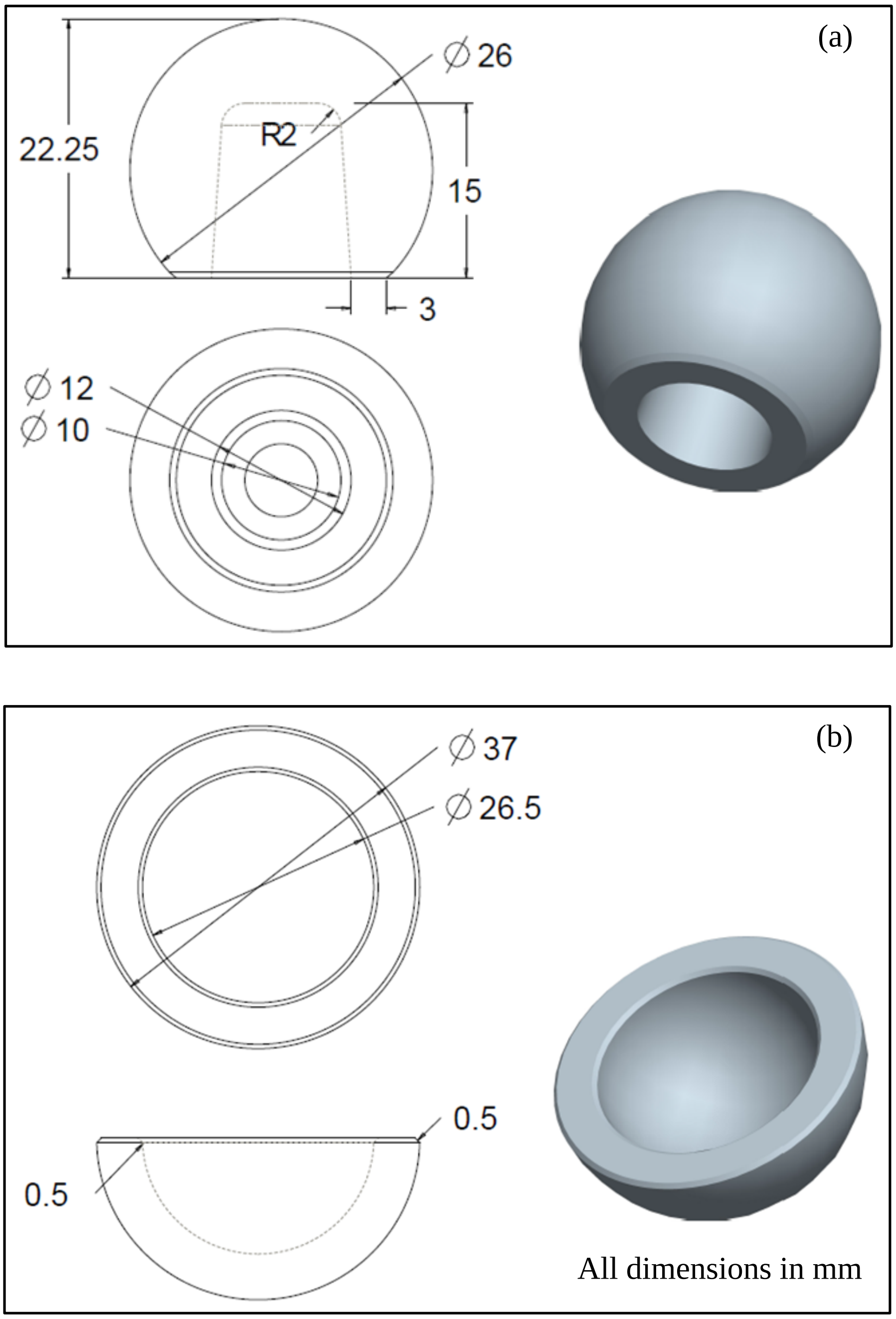

Fig. 6.1: Computer aided design (CAD) originated orthographic and isometric projection of targeted 26mm ZTA femoral head (OD) with consist of tapered cylindrical blind hole and fillet curvature (a) and 26.5mm inner diameter (ID) acetabular socket (b).

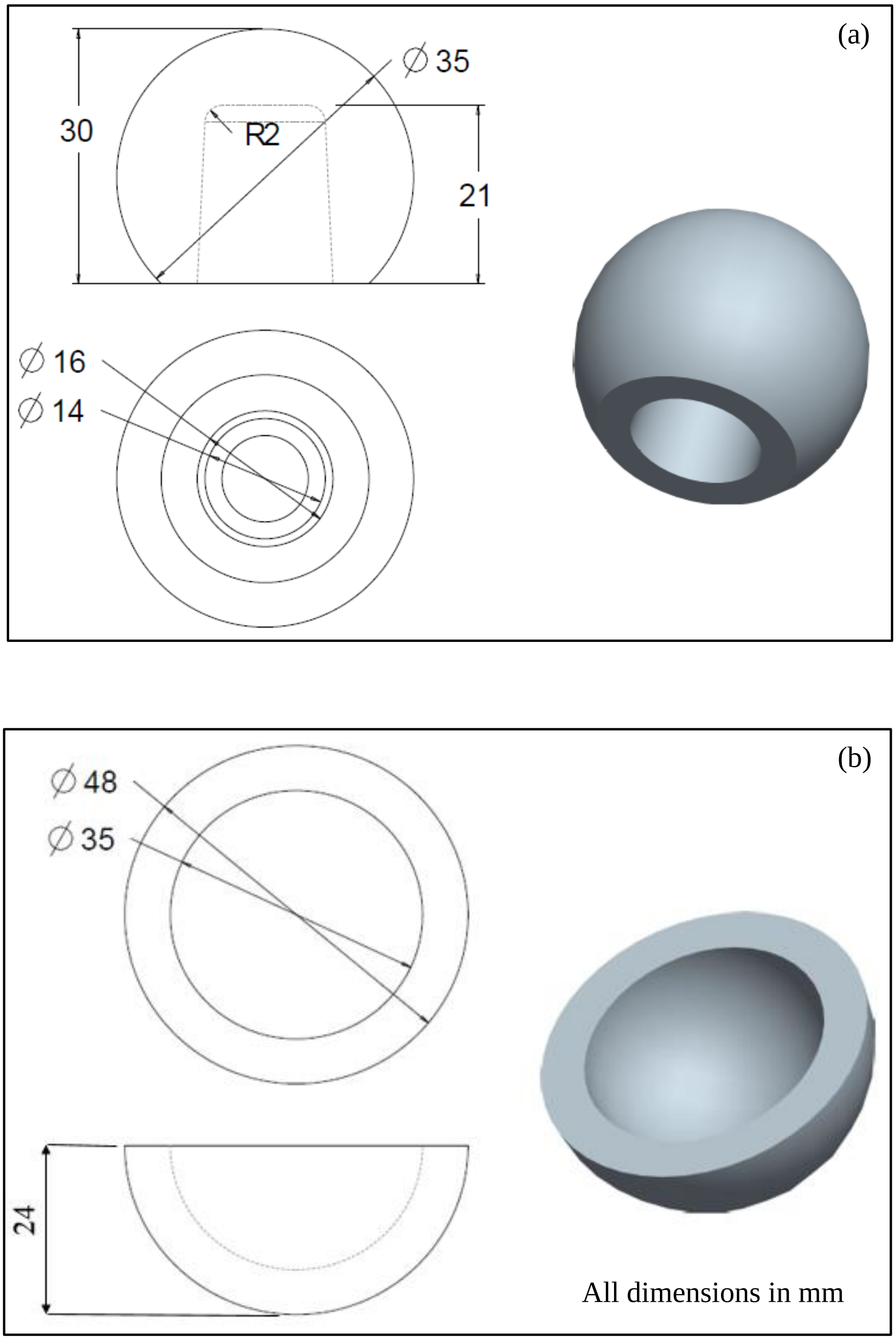

Fig. 6.2**:** Computer aided design (CAD) originated orthographic views and isometric model in the perspective of the development of 26 mm outer diameter (OD) femoral head (a) and 26.5mm inner diameter (ID) acetabular socket (b) including of shrinkage, machining and polishing allowances.

6.1.3 Pre-process and generation of STL file

Pre-process is a technique that makes the 3D virtual model of standard triangularization language (STL) file ready for the development of components through fused deposition molding (FDM).[1] Pre-process in rapid prototype method was categorised into three steps, namely creating standard tessellated language (STL) file, build supports and slice the STL file into layers.[2] Using the 3D modelling software Pro/E, the 3D solid femoral head and acetabular socket was converted into *.stl file with the help of deviation control units, chord height 0.0057 mm, the distance between component surface to tessellated surfaces and angle control of 0.5^o, which allows the angular deviation between adjacent planar triangles, saved in binary format. The smaller chord height means less deviation from the original surface to tessellated surface. This format represents a three dimensional surface as mesh of planar triangles. The file contains the coordinates of the planar triangle vertices and the direction of the outward normal of each triangle.[3]

6.1.4 Materials for Polymer rapid prototypes

Fused deposition modelling (FDM) is a well-established rapid prototype technique particularly for the development of a 3D prototype of any complicated shape. It uses two types of materials; one is the support material that acts as a scaffolding to support the printed product as described earlier and the second one is modelling material of the same composition as the final product. The support is required to a develop product in order to avoid the unnecessary mechanical vibrations at the time of operation, to prevent the floating layers, to support the overhanging and twisted surfaces and to improve the stability to the system with the final aim being that the finished part can be removed easily from the working platform. In the present work, a soluble support of polyphenylsulfone (PPSF) was used, which can dissolve into hot amino liquid at ultrasonic heating tank for 4 hours. This type of soluble support is used for acrylonitrile butadiene styrene (ABS) grade model materials. In fused deposition modelling, self-support angle of upto 45^o was used for the required support.[4] Similarly, the product building material is in the form of wire filament, which consists of 1.8 mm in diameter. The final product accuracy of layer thickness and vertical dimensions mainly depend on feeding the rate of material and nozzle diameter. Thermoplastic materials are most commonly used and these include ABS with different colours. The physical and mechanical properties of building material are tabulated in Table 6.1.

Table 6.1: Properties of ABS Plus (P430) thermoplastic material.[5]

Properties	**Specifications**
Structure	Amorphous
Specific gravity	1.04
Tensile Strength (MPa)	33
Flexural Strength (MPa)	58
Rockwell Hardness	109.5

6.1.5 Slicing and base support build-up

After importing the planar triangular meshed femoral head and acetabular socket from Pro/E, the 3D volume of the design was sliced into very thin layers using the catalystEX software[6]. The individual layer thickness was maintained about 0.254 mm, which indicates the Z-direction movement of the working platform per every deposition of one layer. The slicing of the femoral head and acetabular socket was followed by the stereo lithography contour. This slicing shows the cross section area of the acetabular socket in a particular direction of orientation, where the material injection nozzle follows the same contour. The model interior material deposition is adopted to raster sparse-high density. The support material was selected as smart (break away) type of support style. The orientation of the femoral head and acetabular socket was chosen such that it reduces the usage and removal of support material without damaging the build components.[7] The build time for head was 1hr 05 min and the estimated volume of support material was consumed 1.44cm^3 for head. In the same way, estimated build time and consumed material volume for acetabular socket was 1hr 30 min and 2.12 cm^3, respectively. A typical ABS polymer prototype for both the femoral head and acetabular socket equivalent to details dimension described in Fig. 6.2 was fabricated prior to mould design.

6.2. Design and Manufacturing of Mould

6.2.1 Mould Material

In the present work, the femoral head and acetabular socket prosthesis was fabricated using the powder compaction technique in a novel method of uniaxial pressing. For such a uniaxial pressing of the femoral head and acetabular cup, two different multi-piece integrated cavity mould was designed and manufactured with EN 24 alloy steel. EN24 is a popular grade alloy steel, which is readily machinable during softened condition.[8] It is mostly suitable for the manufacture of single and multi-piece mould tools. After the machining, raw stock into the final desired shape of the mould, and subsequently carried out heat treatment in terms of quenching and tempering to enhance mould hardness and wear resistance. The hardness was maintained Rockwell hardness number 55.

6.2.2 Design and Fabrication of multi-piece steel mould

Articulated designs include a wide variety of geometrically connected surfaces depending on type of joints. For example, hip joint, which consists of femoral head and acetabular socket. Spherical joint allows for rotation in all direction simultaneously. Such a articulated components fabrication are not so easy with conventional moulds. The joint needs to realize by very precisely assembling many individual pieces is call multi-piece moulds.[9,10] Multi-piece mould fabricated with number of partining surfaces and directions to provide the enough number of degrees of freedom to the bottom and top dies and prepared like subassembly parts in order to operate the various surface of the componet. These subassemblies assembled together to form the cavity and demould the green compact by dissembled the mould parts. Moreover, integrated cavity mould tooling cost is relatively low and also mould design enables the fabrication of the complex shaped ceramic components.

The dimensional accuracy, circularity of the moulded femoral head and acetabular socket component is very important; in this particular case, the design of the multi - piece mould must consider the shrinkage of the green component. Linear and volume shrinkage values were obtained from the sintered ZTA pellets and can be used as a guideline to design of mould.[11] The cavity dimensions of the mould included the nominal dimensions, shrinkage and machining allowances. The multi-piece mould included a facility for the release of air trapped in the mould cavity.

6.3 Fabrication of Ceramic Prototypes

6.3.1 Uniaxial pressing to make ZTA green compacts

The newly designed and fabricated moulds were used for femoral head prototypes through uniaxial pressing of powder mixtures. Uniaxial hydraulic pressing performs the compaction of ZTA powder in cavity of the multi-piece mould to form hip prosthesis by applying pressure in a single axial direction through a plunger cum mandrel. The optimized ZTA composition was designed using the response surface modelling approach. Herein, the optimized ZTA composition is 95 wt%, Al_2O_3, 5 wt% ZrO_2-800 ppm MgO. The commercial grade alumina (Sumitomo, Japan, AKP – 5N, 120nm, 99.999% purity), Zirconia (Tosoh, Japan, 3Y-E, 25nm, >99.9%) and $Mg(NO_3)_2.6H_2O$ (Sigma Aldrich, >99.9% trace metal basis) were used without any further modification.[11] The aforesaid ZTA composition of around 70 g were blended thoroughly by the addition of 3wt% polyvinyl Alcohol (PVA) organic binder for two components and made it dried. The dried and free flowing powders were poured into the mould cavity, which was assembled as multi-piece moulds together by high tension bolts along the different directions. Before starting the compaction, the steric acid was applied on the cavity and plunger walls that serves as a lubricant. Subsequently, heavy-duty silicone spray was applied to release a green body from the mould cavity walls without any distortion and breakage. The compaction force of 18 and 22 tons for equal dwell time of 120 seconds was applied to transfer the load uniformly throughout the powder compact and to obtain sufficient strength in the green compact of femoral head and acetabular socket. After compaction, the plunger was removed and the multi – parts mold was carefully dismantled to get the perfect shape of the green components in commensurate with the ABS prototype model.

6.3.2 Sintering and Machining

Ceramic components are effectively machined before the final sintering stage either in the green compact state or in the presintered state. While the sintering the ceramic components subjected to shrinkage and warping, those are not allow to, get precise dimensional tolerances and surface finish in the sintered state. Moreover, machining of presintered ceramic parts is quite economical and safer than the green sintered state.[12] In this regarding, the demoulded green compacts further pre-sintered at 1200°C for 2h to improve the green strength in order to gain the good machinable characteristics. The presintering condition was optimized from continuous sintering at different level of peak temperature starting from 800 – 1600°C with an interval of 100°C. The pre-sintered femoral head and acetabular socket was machined by using the modern machines, like CNC machine tools, to impart precise geometrical shape and properties which provide the circularity and good surface finish to the articulating surfaces.[13] The pre-sintered and machined components were finally sintered at 1600°C for 6h to get highly dense compacts. The sintered ceramic parts were polished in order to remove the excessive material and to get the mirror surface, which will reduce the interaction among the asperities between the convex femoral head (D) and concave acetabular socket (inner ID).

6.3.3 Polishing of femoral head and acetabular socket

Excellent geometrical smooth surface finish of the femoral head is a primary requirement, since it undergoes significant tribological interaction with the acetabular socket in THR assembly. After achieving accurate shape and dimension of the product through machining and sintering, further attempt was made in order to achieve a better surface finish maximum R_a value in the range of 0.2μm. Polishing was carried out with sequentially varying diamond paste of grit sizes (10 – 1 μm) to obtain smooth outer surface of spherical dome-shaped object. The dome shaped machined femoral head was mounted on the rotating spindle and pressed against a spring-loaded rotating attachment at a given load. The rotation of the spindle was carefully varied while polishing the final prototype.

The finishing processes are an important perspective to be considered to meet the final goals like tolerances, and smooth surface of the articulating surface of the acetabular socket. Since the acetabular cup made of ZTA composite is 3-D complex surface, so conventional finishing process (polishing) such as grinding and honing might not be feasible solution as it uses solid cutting tools. Thus, in the present research work polymer rheological abrasive semi solid medium type of cutting tool is used for acetabular socket. This polymer rheological abrasive medium possesses three unique properties such as self-deformability, better flow ability, and good abrading ability.[14] Therefore, this medium can flow to each and every corner while finishing when applied very low forces and abrades the surface to nano scale. On the contrary, the polymer rheological abrasive medium consists of multiple semi solid soft polymers (silicone polymer, styrene polymer), rheological additives (plasticizers and softeners), and silicon carbide abrasives of particle size 15 μm. Base polymers possess dominating elastic characteristics and partial viscous characteristics. To impart the required viscous component, rheological additives are blended. Hence, this medium becomes viscoelastic with required viscous and elastic component. Where viscous component assist the abrasive particles along the direction of motion (exert axial force) and elastic motion tries to indent in nano scale on the workpiece surface (exert radial force).[15] Thus, because of radial and axial forces, nano surface finishing can be achieved on the workpiece.

6.4 Evaluation of Physical Properties

The bulk density of sintered femoral ball heads and acetabular socket was determined by Archimedes' principle. The geometric dimensional stability, including a targeted tolerance limit of ± 50μm for 26mm (OD) diameter femoral head and 26.5mm (ID) acetabular socket was measured using co-ordinate measuring machine (CMM). Coordinate measuring machine (CMM) was used to measure the geometrical properties and form accuracy in terms of circularity. The CMM basic concept is three coordinate axes movements in *x*, *y*, and *z* directions are possible. Each directional axes are fitted with a linear measurement transducer. The transducers are sense the direction of movement and gives digital display. In the present case, bridge type CMM was used for the measure the dimensional accuracy of the acetabular socket prosthesis. In this travelling bridge CMM, the table carries the quill (z-axis) along the x-axis. Such a motion is controlled by a joystick and a stylus an input device in the probe of CMM. It is the sensory part of a CMM responsible for sensing different parameters required for the measurement. The profile data were plotted on a polar graph to determine the circularity within stipulated tolerance limit. The entire process was repeated in several locations to identify the shape and size stability.

6.5 Evaluation of Femoral head Burst Strength

A typical burst test was used to measure the uniaxial compressive strength of the femoral ball head in accordance with the ISO 7206-10 guideline.[16] The dummy femoral stem and metal cone were manufactured with mild steel. Prior to burst test, the femoral ball head was mounted on the dummy femoral stem neck and was loaded hydraulically against 100° metal female cone. To reduce the local stress and smooth transfer of load between the femoral head and 100° cone geometry, a metallic copper ring was also used. The cone support and copper ring fixture are assembled to mimic the in-vivo fracture behaviour.[17] Five sets of femoral ball heads were used to test the strength at a loading rate of 1 kN/sec using universal testing machine (Instron Satec 600 kN, USA).

6.6 Results and Discussion

6.6.1 Design aspects of THR and clinical perspective

It can be reiterated that significant current research on THR focuses on developing biomaterials for bearing surfaces to reduce wear debris and osteolysis, and thereby improve longevity of the prosthesis. Thus, there is a need of patient specific acetabular components with differing outer dimensions for revision arthroplasty. There will be a great need in the future as the number of revision arthroplasty surgeries is bound to increase in proportion to the primary arthroplasty of the hip or knee in our country. Herein, we have demonstrated to develop ZTA 26 mm OD femoral head and 26.5 mm ID acetabular socket (ceramic – ceramic) prototype to establish the cost effective new manufacturing technology for the development of patient -specific ceramic bearings for THR (Fig. 6.1 and Fig. 6.2).

A typical process chart represents a sequential operation in order to achieve the final product with desired dimension and mechanical properties (Fig. 6.3 a & b). Lab scale research to patient specific THR femoral head and acetabular socket development is a critical association of material science and technology, mechanical engineering and biological science, which have been cumulatively divided into three major sections in Fig. 6.3 a; [I] Composition and process optimization including mechanical and biological response assessment, [II] Tribological study with different tribocontacts, and correlation with microstructure and properties, and [III] Fabrication of both femoral head and acetabular socket from optimized process conditions.

In the first phase, response surface modelling approaches to predict the sinter density and grain size of alumina through multivariate regression analysis, interpretation of resulting polynomial equations and response surface/contour plots to adapt the central composite design for process optimization. It also provides the choice of order in RSM model and data economy in reducing the factorial experiments from a large number of parameter combinations to a far less number without losing any information including linear, quadratic and interaction effects.[18] Based on RSM analysis, the optimised composition for the best combination of sinter density and grain size is 95 wt% Al_2O_3 with 5 wt% ZrO_2 and 800 ppm of MgO. This specific composition was subsequently sintered at 1600°C for 6 hours (optimised sintering condition) to obtain ZTA ceramics of different sizes and shapes. Following that the cytocompatibility properties, C2C12 mouse myoblast cells were grown on the ZTA composite having the best combination of mechanical properties combination of compressive strength (1100 MPa), tensile strength (200 MPa) and modest indentation toughness (4.5 MP $m^{1/2}$).[19] In continuation of earlier research program on composition and process optimization, the wear resistance properties in the performance and durability of femoral ball head and acetabular socket in total hip joint replacement the unlubricated sliding wear experiments with commercial zirconia, and steel counterbody reveal that a combination of steady state COF of 0.5 and wear rate of 10^{-9} mm^3/N m can be achieved with ZTA composite having the best combination of mechanical properties.[20] While material and process optimized with respect to density, microstructure, mechanical properties and *in vitro* biological response a critical process has been developed and discussed systematically to obtain the resultant compacts. In brief, starting from 3D model generation to component fabrication from optimized process has been illustrated in Fig. 6.3b and more elaborately discussed in following sections.

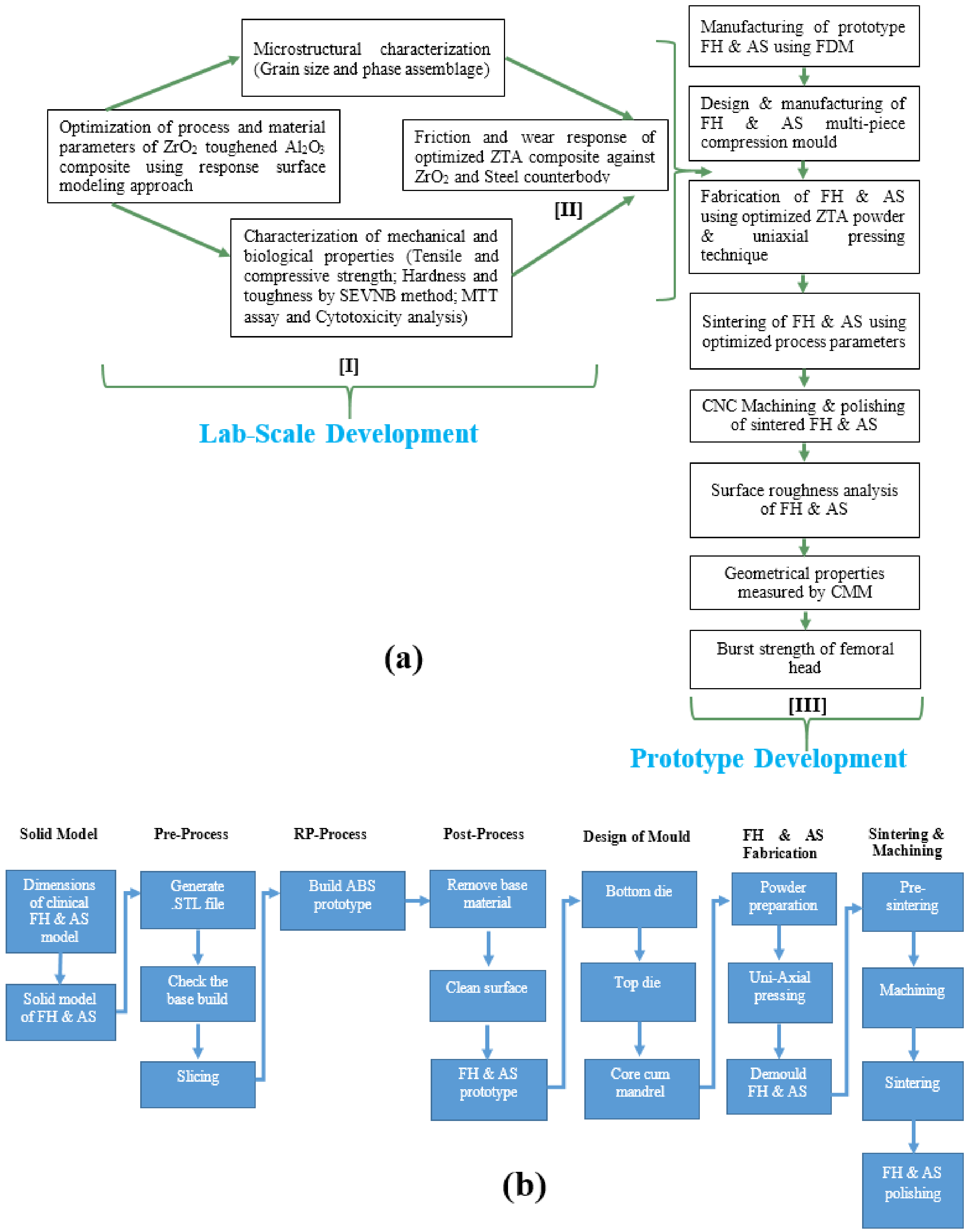

Fig. 6.3: Flowchart, showing the lab-scale to ZTA prototype development of ZTA femoral head (FH) and acetabular socket (AS) for the ultimate HIP joint replacement (a) and process chart for the fabrication of femoral head and acetabular socket (b).

6.6.2 Polymeric prototypes and mould fabrication

Based on the part’s function, the user must select the appropriate orientation to balance or optimize surface finish, strength or build time of the part. Orientation impacts build time and material consumption, proper orientation can reduce both. Orienting the part so that curved or angled surfaces are built parallel to the Z-axis will result in smoother surfaces.[21] Part orientation can affect support material usage and build speed of the part shown in Fig. 6.4.

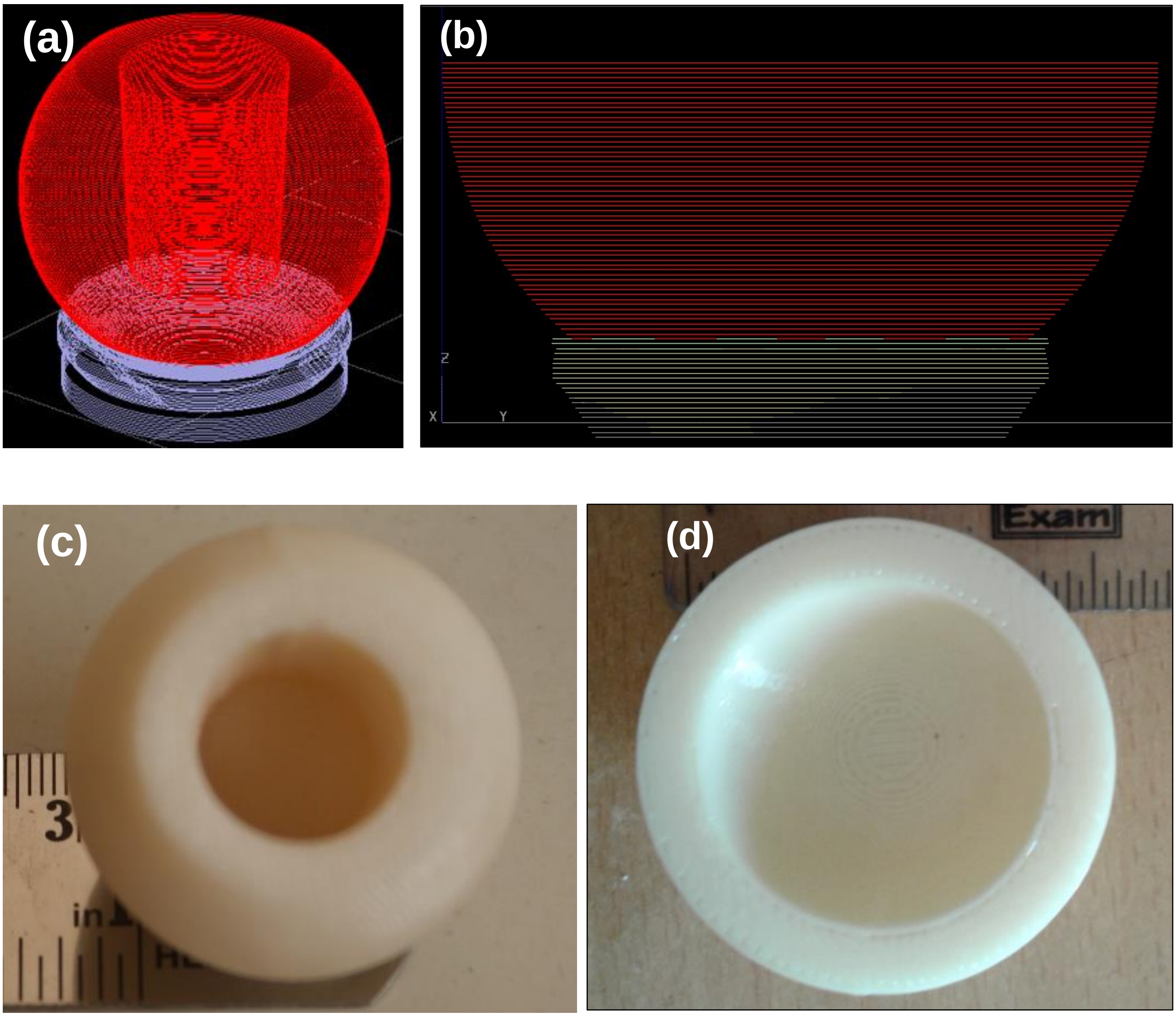

Fig. 6.4: Mode of fused deposition including slicing and orientation during deposition of 3D-printing for femoral head (a) and acetabular socket (b). Fabricated ABS model made of femoral head (c) and acetabular socket (d). Dimension fixed up with consideration of volume shrinkage of green compacts of alumina zirconia nanopowder mixture.

The layer thickness was maintained around 0.254 mm which indicates the Z-direction movement of the working platform per every deposition of the one layer. The slicing of femoral head and acetabular socket was followed the stereolithography contour. Such a slicing indicates the cross section area of the femoral head and acetabular socket in the particular direction of orientation where the material injection nozzle also follows the same contour. The model interior material deposition was chosen raster sparse-high density. The Fig. 6.4 a & b shows optimize orientation to fabricate the hip prosthesis and that reduces the usage of support material. The material addition takes place in Z-direction by laying the cross sectional area as a layer.

In a typical FDM system, the semi-molten thermoplastic wire material was passed through the extrusion liquefier nozzle on top of the working platform in horizontal and vertical direction in order to draw the cross section of the sliced 3D CAD model. The ejected semi-molten thermoplastic was cooled and hardened within a fraction of seconds. If the first layer was completed, the base platform moves downward, i.e. Z-direction, usually by about one layer height and makes it ready to place the next layer of material. During printing, these materials take the form spools, where the spools were unwound and made it passed through a liquefier and then to an extrusion nozzle. The liquefiers melt the filaments and extrude them further onto a base, earlier designated as build platform or table.[22] Numerical control machine was used to monitor the movements of extrusion nozzle and platform in X, Y and Z translational directions. After completion of the product, the post processing was done to remove the support or base material by soaking in water at 90^{o}C. Moreover, Fig. 6.4 c & d shows the fabricated ABS femoral head and acetabular socket. It was followed very close dimensional tolerance (35 mm) of femoral head diameter and ID of acetabular socket. Furthermore, the ABS hip prosthesis was used for designing of multi-piece integrated cavity mould.

Two different multi-piece integrated cavity moulds were designed and manufactured with the aid of ABS femoral head and acetabular socket prototype dimensions, which is assisting the fabrication of ZTA green compacts through powder compaction method. With the aid of ABS polymeric 3D prototype model and their geometrical properties, multi-piece integrated cavity mould was designed and machined for the fabrication of ZTA green femoral ball head and acetabular socket through powder compaction method. Fig. 6.5 a & b demonstrates the partitioned bottom and top cavity dies for the femoral head.

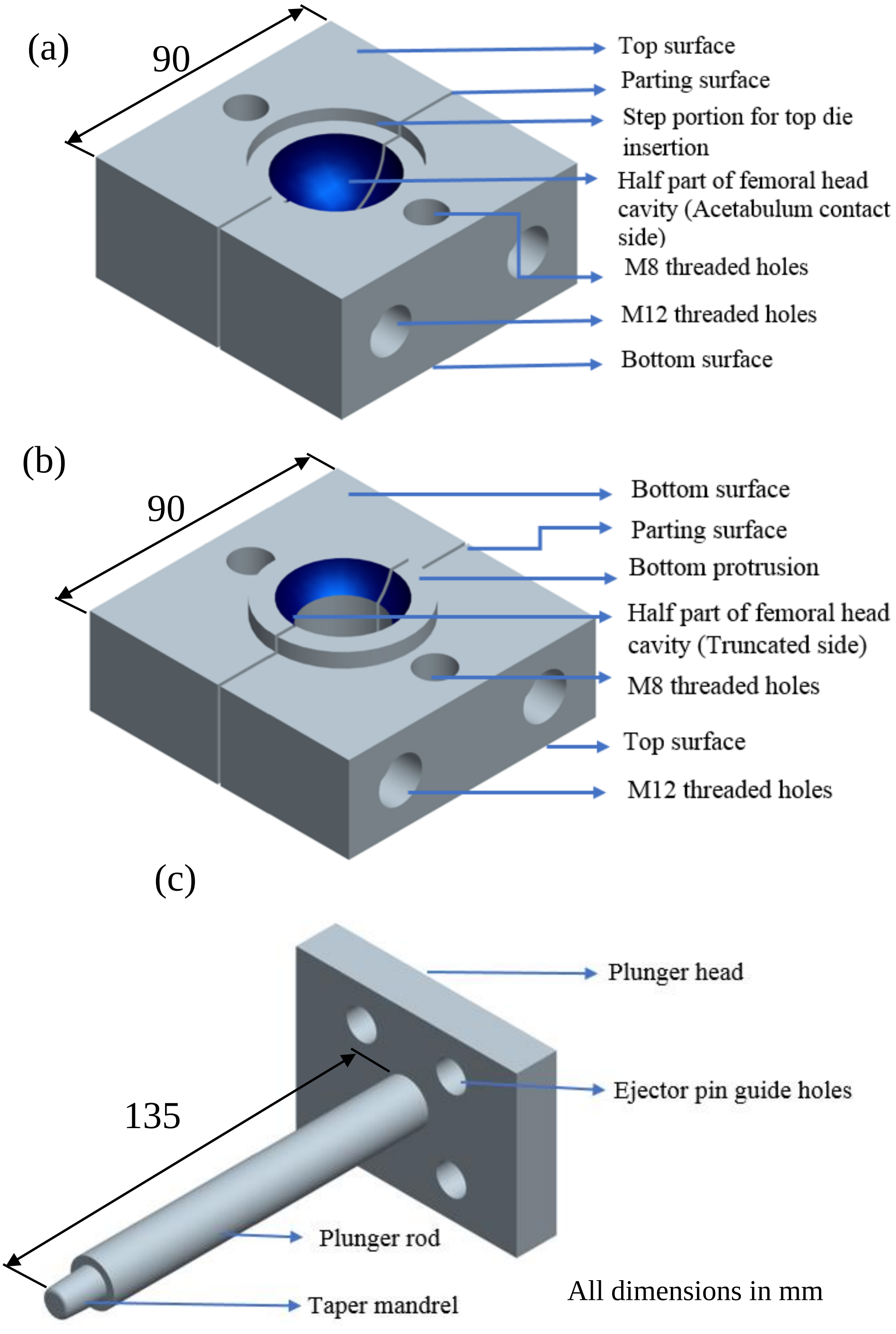

Fig. 6.5: Typical multi-piece steel die fabricated with consideration of polymer prototype component dimension, where design and drawing of cavity including plunger are shown for femoral head, where (a) bottom die, (b) top die, and (c) plunger cum mandrel.

The parting surface was maintained at zero draft, which will minimize the powder penetration between the interactive surfaces during the powder compaction process. This cavity portion creates uniform pressure gradient during powder compaction. From the top surface of cavity a step portion is maintained to provide the room to insert the top die and such arrangements allows one to avoid powder insertion between the mating surfaces within top and bottom die. The parting surface of the bottom dies are fastened together by the high tension M12 bolts. Similarly, M8 thread hole is produced at the bottom of the die and also in the vertical direction in order to hold the top die, as well as powder and plunger guide die. Similarly, the top die was partitioned into two symmetrical halves, which were used to separate the die along the parting direction. The bottom surface of the top die consists of protrusion, which was used to insert into the step portion of the bottom die. Similarly, the bottom surface of the top die had another projection that can insert into the bottom surface of the powder and the plunger guide die slot. The truncated side of the femoral head is used as the top die because the plunger was allowed to move and compress the powder in the mould cavity to create the perfect blind hole within parallel positioned both of the fixed and moveable platforms. The plunger-cum mandrel (core) was manufactured to compact the ZTA powder in the pressure zone of mould cavity as well as to generate the blind hole in the femoral head. One end of the plunger one end was consisted of taper mandrel, which penetrated into the powder to create cylindrical blind hole on the truncated side of the femoral ball head (see Fig. 6.5c). Another end of the plunger consists of a head, which guides the ejection pins.

Similarly, Fig. 6.6 a, b, & c describe the partitioned bottom cavity die, powder cum plunger guide die and core cum mandrel (plunger) of the multi-piece acetabular socket mould. The bottom acetabular socket cavity die consists of a partitioned surface which is used to access the one surface of the acetabular socket and to demould the green compact without any damage. The partitioned surface was prepared with zero draft that reduces the powder penetration and produces the uniform pressure while the powder compaction. A female step portion was prepared on the top surface of bottom die to insert the powder cum plunger guide die (see Fig. 6.6 b) which has male step portion. Such step arrangement restricts the powder penetration during compaction. The bottom acetabular socket die was fastened together by the high-tension M12 bolts. The bottom and plunger guide die was fixed firmly by the M8 bolts in vertical direction.

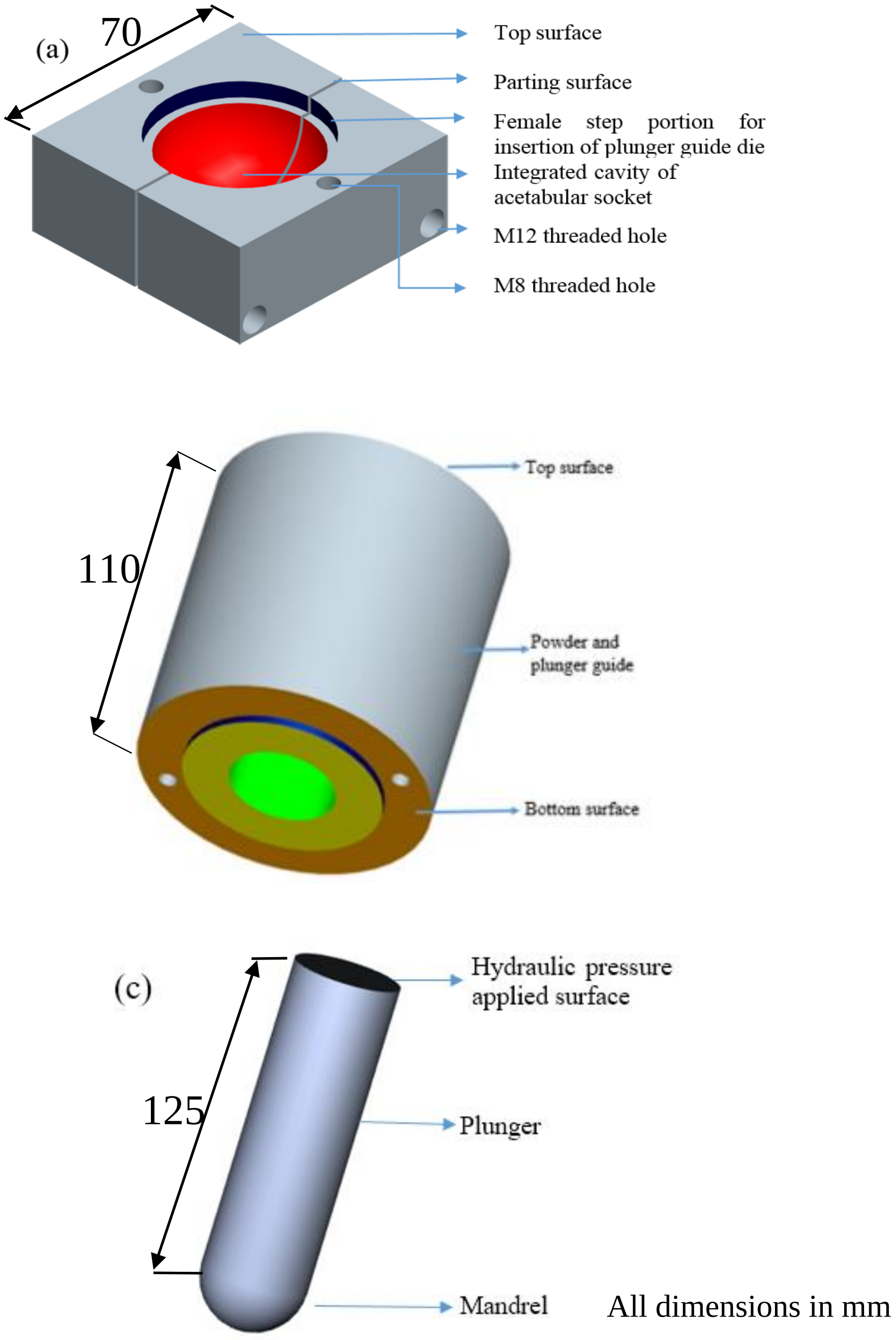

Fig. 6.6: Typical multi-piece integrated steel die fabricated with consideration of polymer prototype component dimension, where design and drawing of cavity including plunger are shown for acetabular socket. Multi-piece integrated cavity mould for acetabular socket (a) bottom die (b) powder cum plunger guide die and (c) plunger.

Fig. 6.6 c depicts the core cum mandrel which was used for the compaction of ZTA powder in the pressure zone of acetabular socket cavity. The plunger one end consists of mandrel that creates the pressure on the powder for compaction and the second end is receiving the load from the movable jaw of the hydraulic uniaxial compressor. With the aid of ABS polymeric 3D prototype model and their geometrical properties, multi-piece integrated cavity mould was designed and machined for the fabrication of ZTA green femoral ball head and acetabular socket through powder compaction method.

6.6.3 Dimensional validation of ZTA femoral head and acetabular socket prototypes

The transformation of a green compact to polished prototype of femoral head and acetabular socket requires one to adopt several steps manufacturing in conjunction with different degree of shrinkage, machining and polishing tolerances. Further, demonstrate the different dimensional features for femoral head, and assembly with acetabular socket. In order to relate the achieved dimension at different stages of manufacturing, the geometrical features are summarized in Table 6.2.

Table 6.2: Geometrical features at different stages for both femoral head and acetabular socket starting from green compaction to polished components.

Stage	Femoral ball head	Dimensions in mm
Green (Digital Vernier Calliper)	Diameter of femoral head	35.49
	Truncated height	30.65
	Depth of the blind hole	21.62
	Open end diameter of blind hole	16.21
	Blind end diameter	14.30
Machined and Sintered (Digital Vernier Calliper)	Diameter of femoral head	26.02
	Truncated height	22.53
	Depth of the blind hole	14.98
	Open end diameter of blind hole	12.09
	Blind end diameter	10.65
Polished (Dimension measured by CMM)	Diameter of femoral head	26.00 ±0.02
	Truncated height	22.25 ±0.01
	Depth of the blind hole	15.0 ±0.03
	Open end diameter of blind hole	12.05 ±0.03
	Blind end diameter	10.4 ±0.06

The dimensions of the obtained green component are varied within ±2% from ABS polymer prototype dimensions, as described in Fig. 6.4 a. An appreciable green strength without dimensional deviation was observed after drying at 70^{o}C for 6h.

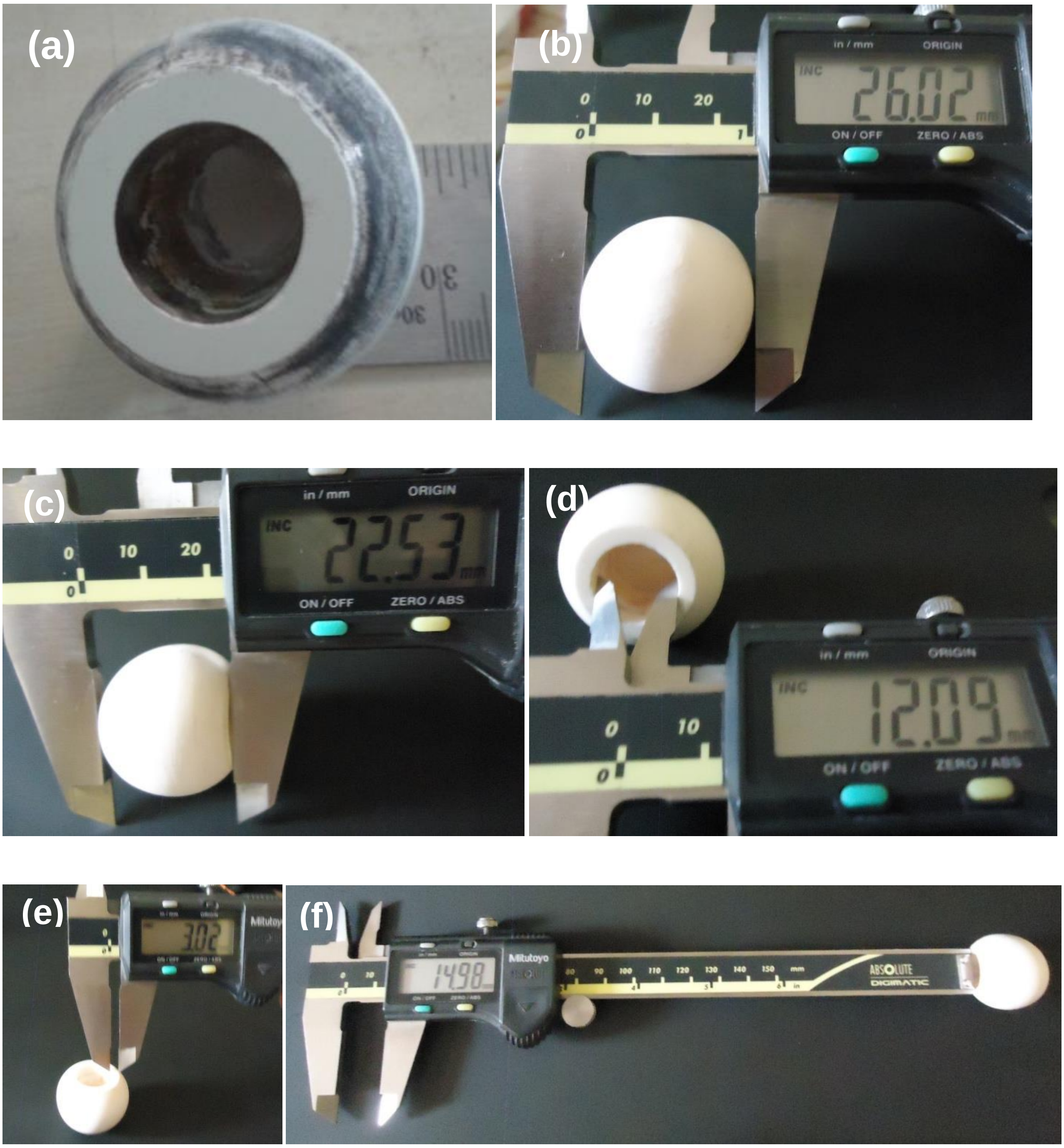

Figure 6.7: Isometric view of (a) green compact through uniaxial press. From b to f all dimensions are near to CAD generated model and these are representing top view, side view, tapered entrance of femoral stem neck, thickness of wall at truncated zone and blind hole depth of machined and sintered femoral head, respectively.

Fig. 6.7 a reveals the isometric view of truncated shaped spherical green compacts with perfect tapered blind hole depth and dimension. A closer to targeted dimension was achieved after presintering (1200°C/2hr), CNC machining and final sintering at 1600°C for 6h. This feature is demonstrated in terms of various aspects (diameter, truncated height, open end diameter of blind hole, circumference width and depth of the blind hole) in Fig. 6. 7b-f.

On the other hand, dimensional and shape tolerances are the fundamental importance for the design and construction of patient specific acetabular socket component. Fig. 6.8 illustrates the ZTA acetabular socket prototype of the various green and sintered stages.

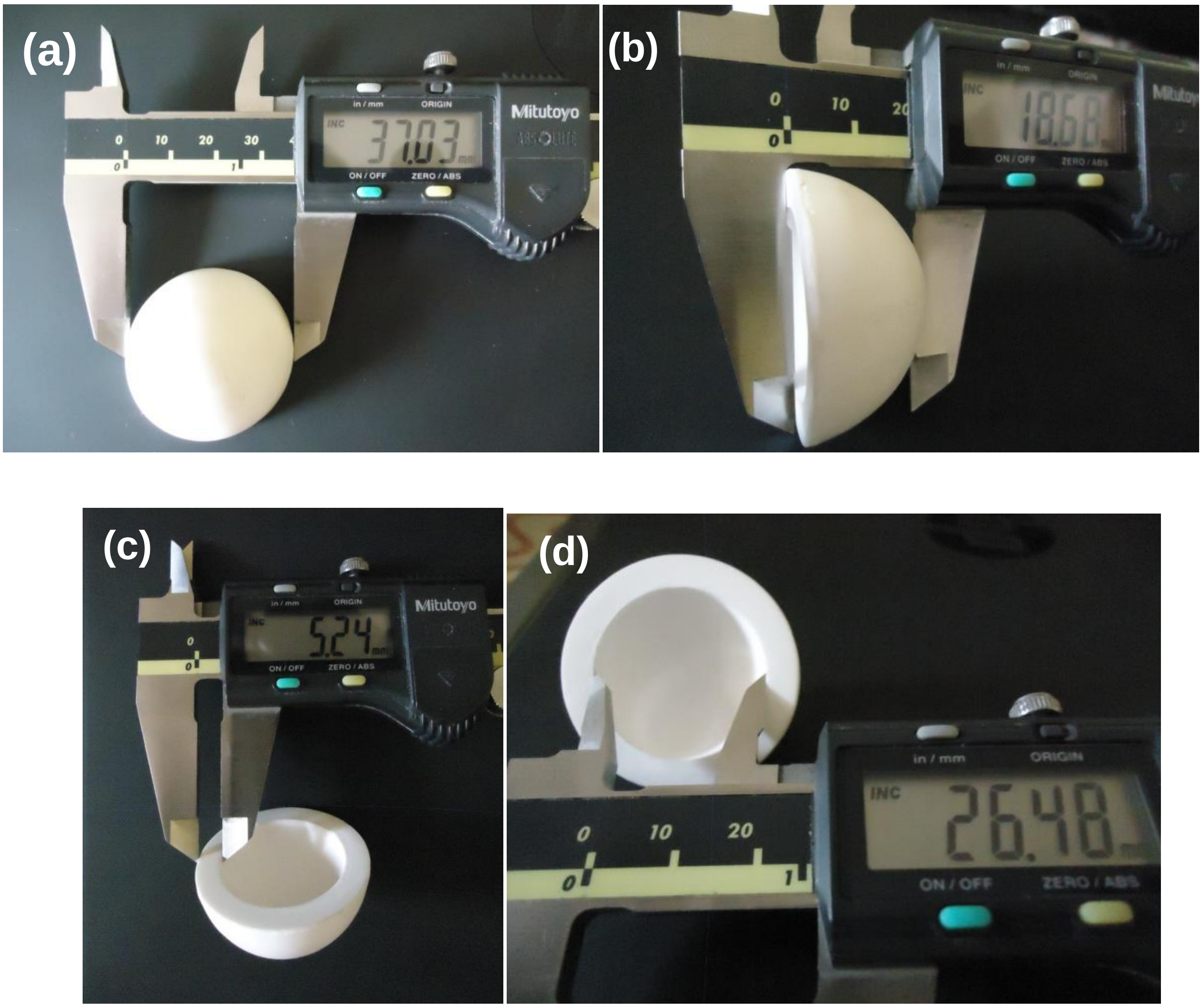

Figure 6.8: Different projected view of machined and sintered acetabular socket, where (a) top view, (b) side view, (c) wall thickness and (d) femoral head accommodate space. All achieved dimensions are near to CAD originated product.

The closely monitored and measured dimensional properties of different stages are defined in Table 6.3. The demoulded green acetabular socket was made to dry at 70°C for 6h in order to remove the lubricants which were applied on mould cavity walls for easy removal. Fig. 6a reveals dimensions of the outer diameter of green stage acetabular socket and similarly other geometrical properties such as inner diameter, thickness, and height were measured and summarised in Table 6.3. Further, green acetabular cup was presintered at 1200°C for 2h and done the CNC machining to achieve the form accuracy of roundness and remove the excessive material. Machining of sintered ceramic components is highly energy consuming process, cutting tool cost, and not that much economical. However, presintering stage is quite economical for the design and fabrication of patient specific ZTA acetabular cup. The presintered and machined acetabular cup geometrical properties were tabulated. The machined component moreover sintered for final densification at 1600°C for 6h. The sintered cup geometrical properties were measured in terms of outer diameter, inner diameter, thickness, and height (see Table 6.3). A closer look reveals the different orthogonal projection along with geometrical features and slight deviation (<±1%) compared to the projected dimension of the product (see Fig. 6.1).

Table 6.3: Geometrical features at different stages for acetabular socket starting from green compaction to polished components.

Stage	**Acetabular socket**	**Dimensions in mm**
Green (Digital Vernier Calliper)	Outer diameter	48.62
	Inner diameter	35.52
	Thickness	6.56
	Height	24.21
Machined and Sintered (Digital Vernier Calliper)	Outer diameter	37.03
	Inner diameter	26.48
	Thickness	5.24
	Height	18.68
Polished (Dimension measured by CMM)	Outer diameter	36.7 ±0.07
	Inner diameter	26.6 ±0.05
	Thickness	5.1 ±0.05
	Height	18.5 ±0.05

6.6.4 Polishing and dimensional measurement of femoral head and acetabular socket

It is worthy to mention that the machining of ceramic components are relatively difficult compared to metallic and polymeric materials, because of high hardness and low fracture toughness. In this context, a suitable pre-sintering is an essential step to conduct necessary machining to the prototype compact. A closer look reveals the different orthogonal projection along with geometrical features and slight deviation (<±1%) compared to projected dimension of the product (see Fig. 6.1). More accurate configuration without any distortion or deformation was ensured after polishing the near net-shaped ZTA femoral head (see Fig. 6.9).

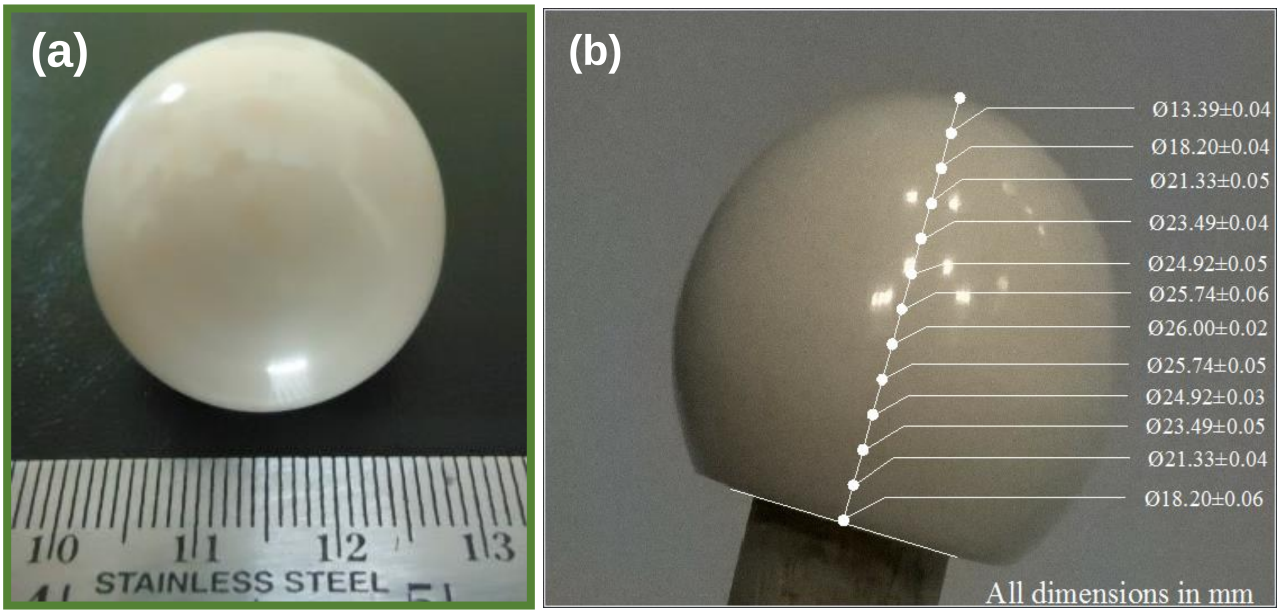

Figure 6.9: The femoral head was polished after machining and sintering, where (a) top view of polished femoral head, and (b) dimension analysis by co-ordinate measuring method (CMM).

Fig. 6.9 a shows the top view of polished surface, whereas the side view including geometrical dimension as measured by CMM method is mentioned (see Fig. 6.9 b). The measured dimensions of polished femoral head are tabulated in Table 6.2.

The same workpiece is polished using a specially fabricated single polar articulating tool is made of aluminium alloy whose shape is converse to the shape of articulating surface of acetabular cup (see Fig. 6.10a). The acetabular cup is held by a wooden fixture so as to arrest the relative motion when tool rotates (see Fig. 6.10b).

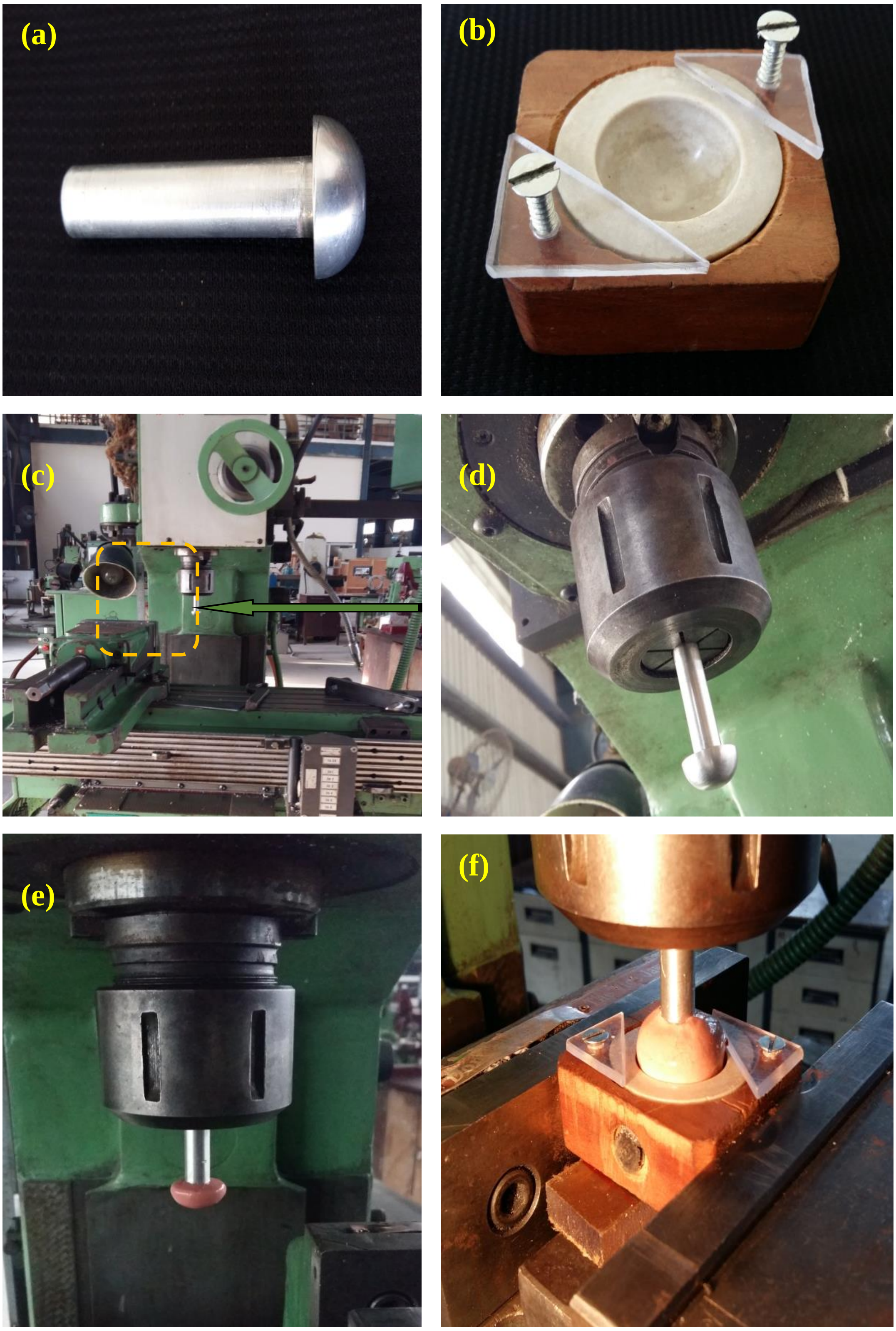

Figure 6.10: (a) Single polar articulating tool, (b) Workpiece holding fixture, (c) Overview of experimental set up, (d) Single polar tool with tool holder, (e) Single polar tool with polymer rheological abrasive finishing medium and (f) Double polar finishing tool with workpiece held by fixture.

Polishing experiments are done using an end milling machine tool. Medium is filled in the acetabular cup, single polar tool is rotated at 50 RPM, and sequences of operations are demonstrated in Fig. 6.10c-e. The acetabular inner surface articulating tool was maintained 50 RPM because to retain the medium and to avoid the excessive centrifugal force on medium.

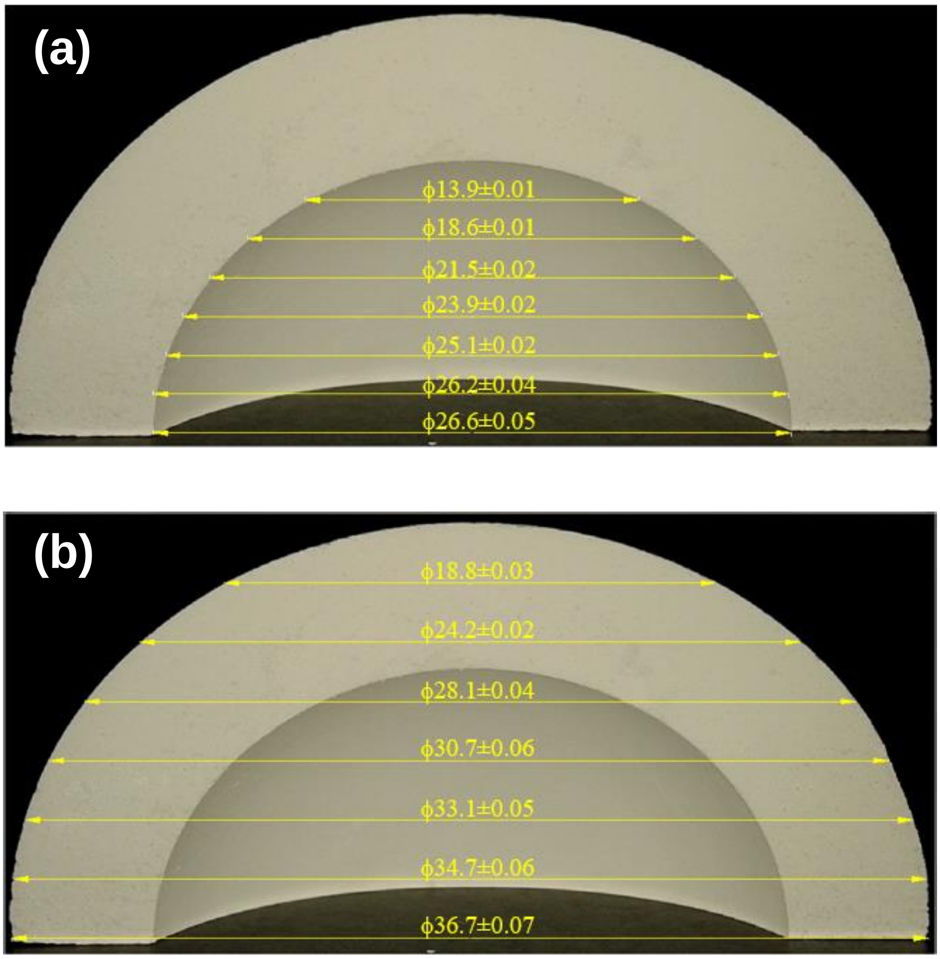

Figure 6.11: Cross sectional view of the acetabular socket and a dimensional analysis of articulating surface (a) and outer shell (b) diameter measured by the co-ordinate measuring machine (CMM).

Furthermore, the polished acetabular socket was used to measure the dimensional tolerances of the polished articulating surface and outer shell by CMM. Acetabular cup, articulating surface receive the femoral head bearing surface and allows the relative rotational motion between them. For getting the smooth relative motion between the mating parts, need enough dimensional tolerance which could avoid the fixing and functionally developed unnecessary concentrated stress. Fig. 6.11 displays the cross section view, measured dimensions of the acetabular socket, and marked at appropriate location. The measured dimensions of polished articulating surface and outer shell of the acetabular cup are tabulated in Table 6.3.

6.6.5 Property Validation of Ceramic Prototype

For the purpose of product validation, the density variation and the microstructural characterisation as well as the mechanical properties are also studied. The sintered components exhibited more than 98% ρ_{th} at various mechanical sections. The expected powder flow behaviour and density gradient and different parts of sintered femoral head are given in Fig. 6.12.

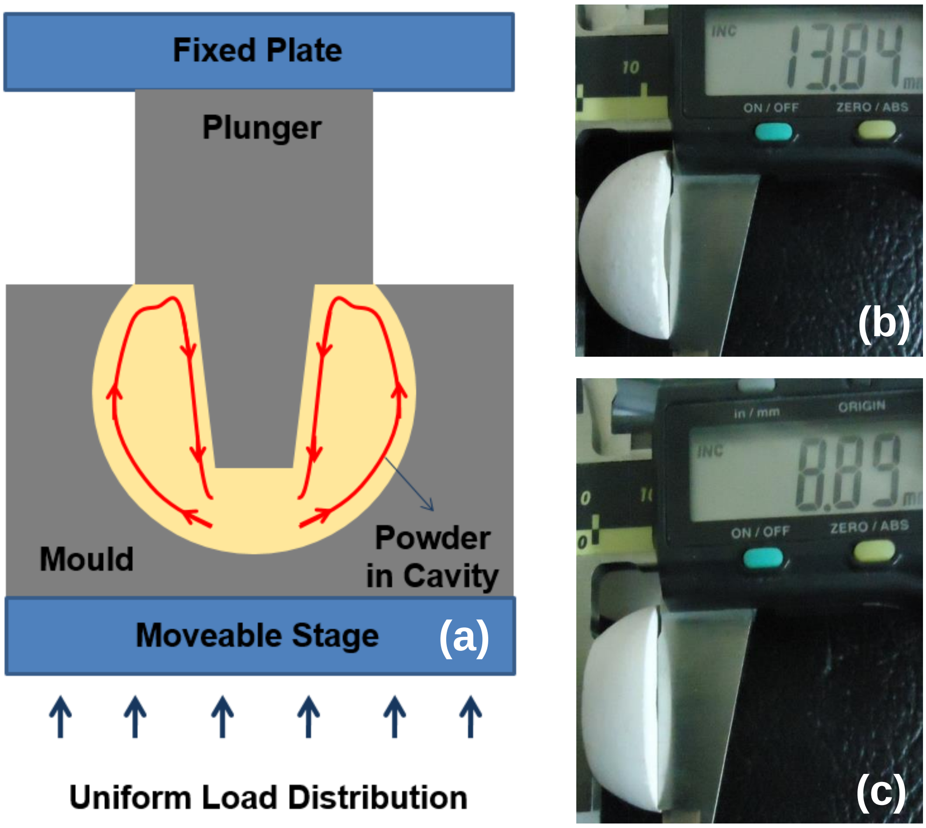

Fig. 6.12: Probable particle flow and compaction mechanism (a) and density pattern for upper and lower halves of femoral machined and sintered head (b & c).

When the steel mould is placed between the movable and fixed jaw of the uniaxial hydraulic pressing machine, the movable jaw applies the force to the plunger, leading to compaction of the green compact in the die cavity until the final femoral head and acetabulur socket shape are formed (see

Fig. 6.12a). The complicated shape, such as femoral head also exhibits the absence of any density gradient, irrespective of pressure direction. Fig. 6. 12 b & c represents the upper part of femoral head, which is expected to be in conformal contact with acetabular socket and lower halve to accommodate femoral stem, respectively. Interestingly, both of the parts have near identical relative density variation of 98.5±0.5 %. On the other hand, sintered ZTA acetabular socket achieved 98% relative density.

SEM images of sintered ZTA femoral head is shown in Fig. 6.13 a and acetabular socket shown in Fig. 6.13 b. The alumina grains are revealed in dark grey, zirconia grains in bright contrast and pore in dark contrast. Alumina also appears as equiaxed grains and zirconia particles are distributed uniformly either at triple point or at grain boundaries of alumina, thereby inhibiting the alumina grain growth during sintering. The extensive quantitative image analysis reveals the average grain size of alumina to be around 3.2 μm and zirconia grain size on an average is 0.9 μm.

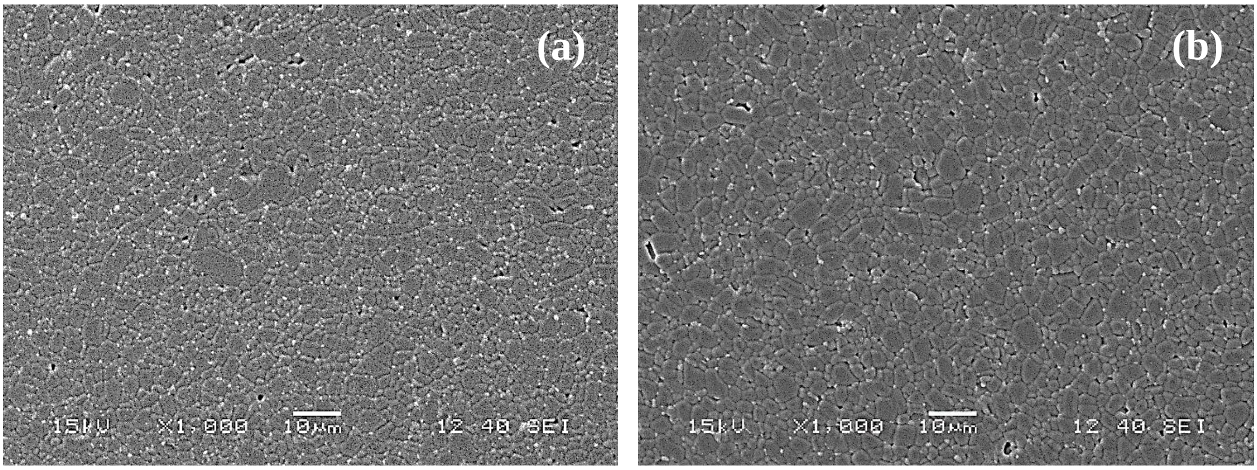

Fig. 6.13: Microstructure of sintered ZTA femoral head (a) and acetabular socket (b), where different contrast indicates the uniform distribution of zirconia particulate (white) in alumina (grey) matrix.

With increasing demand for the hard ceramic materials as wear-resistance of bearing applications, it becomes necessary to define the mechanical properties of ZTA composite of hip prosthesis. From presintered ZTA femoral head and acetabular socket a small part portioned and grinded on the SiC paper to prepare like square pellets. The presintered square pellets were sintered at 1600°C for 6h to densify. The polished square pellets were undergone various mechanical characterizations. The hardness is determined by Eq. 1 using an average diagonal length (d) of an of indents on a ZTA polished surface by diamond indenter. On the contrary, the fracture toughness is calculated by Eq. 2 with the aid of average cracks length originating from indent edges, elastic modulus and hardness of the material. The determined hardness is around 19 GPa, and fracture toughness is 4.5 MPa.m$^{1/2}$. The use of nanopowders as well as the retention of finer scale microstructure attribute to the attainment of higher hardness in the present case. As far as the indentation fracture toughness is concerned, the toughness of our ZTA is lower than that reported in some of the earlier studies only for lab scale sintered disks or bars for SEVNB. The achieved in toughness can be primarily attributed to the ZrO_2 content or more specifically the volume fraction of the transformable ZrO_2 as well as their transformability.[23]

In order to assess the surface quality of prototypes, we measured the roughness parameters for part of femoral head. These mating surfaces are expected to experience small amplitude relative interfacial displacement during normal functioning of THR device. Apart from obtaining several 2D/3D surface topographical images via 3D non-contact profiling, several roughness parameters, e.g. arithmetic mean deviation (R_a), Root mean square deviation (R_q), maximum peak height (R_p), and maximum valley depth (R_v) using high resolution optical profilometer (TalySurf CCI, 4155C, UK) were also critically analyzed. Some representative topography images and analysis are represented in Fig. 6.14 and Table 6.3.

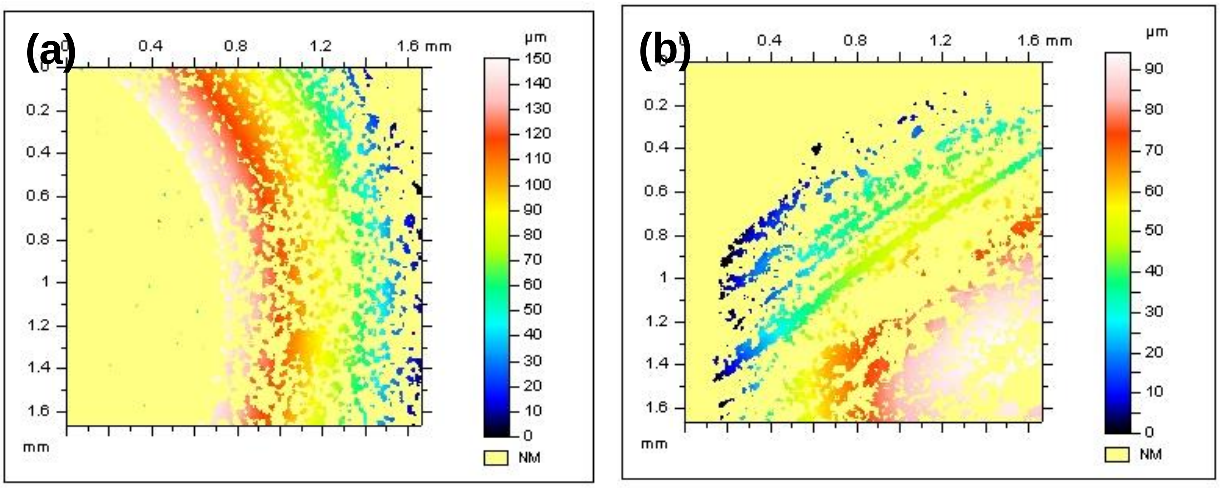

Fig. 6.14: 2D optical profilometric image for the specific area of (a) convex head of 26 mm after machining and sintering and (b) convex head of 26 mm after machining, sintering, and polishing of femoral head.

During measuring either concave and convex surface, a surface with 0.01 nm resolution in Z-direction over a full scan range plus a 0.4 nm lateral resolution, with over 1,000,000 data points were maintained.[24] A closer look at the color spectrum corresponding to various depth profiles reveals smooth surface of the newly developed socket/femoral head. For example, R_a values, as summarized in Table 6.4 indicate equivalent roughness parameters for femoral head before and after polishing.

Table 6.4: Surface roughness parameters of femoral head and acetabular socket at different stages of fabrication.

Type of Biomedical devices	**Region of interest (Optical Profilometer analysis)**	**R_a (µm)**	**R_q (µm)**	**R_p (µm)**	**R_v (µm)**
ZTA Femoral Head	Machined and Sintered 26 mm convex head	1.01	1.25	2.01	2.91
	Machined, Sintered and polished 26 mm convex head	0.20	0.26	0.62	0.54
ZTA Acetabular Socket	Machined and Sintered 26.5 mm concave socket	0.49	-	-	-
	Machined, Sintered and polished 26.5 mm concave socket	0.01	-	-	-

However a significant improvement of surface finish is achieved after successful polishing of femoral head. The polishing reduces R_a by 3-4 times to 0.20μm. This feature can be achieved for other identical dense prototypes. The other parameters e.g, R_q, R_p and R_v can vary with respect to machining and polishing conditions. Table 6.4 also illustrates that the polishing reduces the roughness parameters (R_a, R_q, R_p and R_v) by 3-5 times with respect to as-machined convex surfaces of femoral head. The root mean square roughness of polished head is 0.26 μm, which is close to R_a value. Also, the maximum peak and valley height is nearly equal and therefore, the micro-asperities on the polished functional mating surface of convex head is similar to that of an isotropic surface.

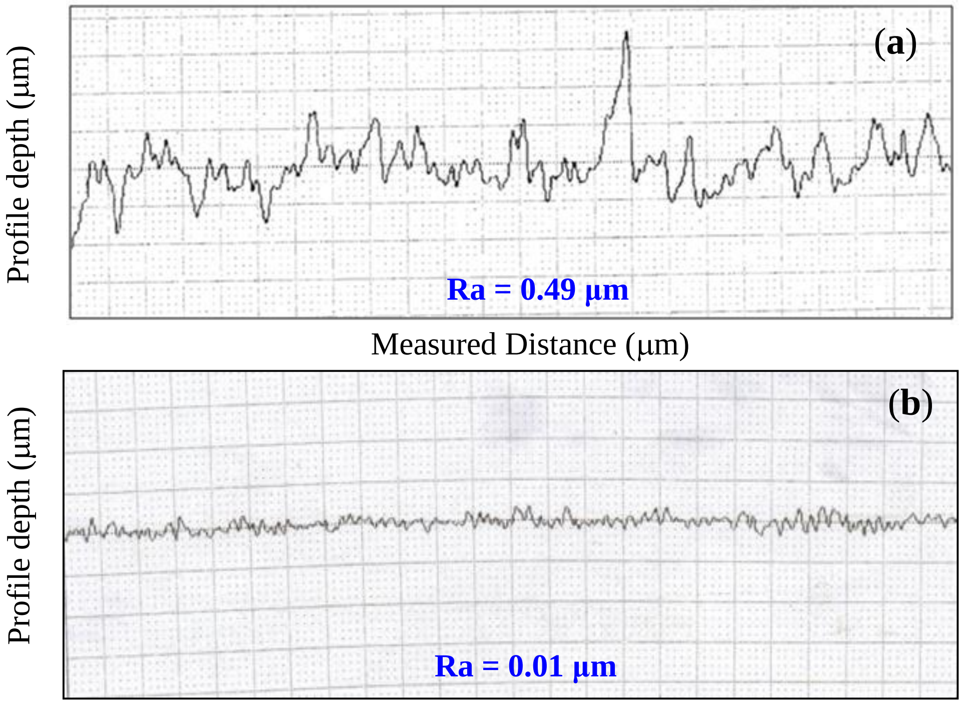

Fig. 6.15: Average initial (a) and polished (b) surface roughness profile of the articulating surface of acetabular cup

First, initial surface roughness of the acetabular cup is measured using mechanical stylus type surface analyzer (Surftest SJ 400, Make: Mitutoyo) and found to be 0.49 μm (see Fig. 6.15a). Thus, a very fine nano surface roughness (0.01μm) on the acetabular cup is achieved (see Fig. 6.15b). The percentage change in surface roughness is 98% and the achieved nano surface greatly improves the lifespan of the acetabular cup from the tribological point of view by reducing the friction. The polished ZTA acetabular cup dimensions were presented in Table 6.3.

In this research work, vertical direction compressive stress in assistance of mild steel dummy femoral stem has been conducted (according to ISO standard) to understand the feasibility of fracture load accommodate capability of femoral head at a loading rate of 1 kN/sec. CAD generated isometric projection and details dimension for burst test arrangements are shown in Fig. 6.16 a & b.

The machined and sintered ZTA femoral head (without polishing) was placed on copper ring cone during burst strength measurement under compression by mild steel dummy stem (see Fig. 6.16c). A typical fracture load near to 15 kN is obtained for this femoral head and shown in Fig. 6.16 d. Initial stage of non-linear deviation is associated with the ductility behaviour of Cu compare to mild steel.[25] The obtained fracture or damage load 15±3 kN during burst strength measurement of identical five specimens is slightly lower compare to the minimum fracture load acceptable limit 20 kN by the US Food and Drug Administration (FDA) guidance draft.[26] In actual, this committed level of force is relatively higher compare to the normal activities, even more daily activity including fall and impact also experiences less force.[27] However, it is expected the obtained fracture strength will further improve when minimize the surface roughness and their relative contact through proper polishing of machined specimens. Synchronization of transformation toughening phenomenon is another issue for further enhancement of fracture strength. However, a point load on alumina femoral head against a steel hard plate is found to be almost identical peak load of 18.5 kN.[28] In recent another group of researcher measured the burst strength of commercial grade alumina femoral head in presence of titanium alloy TiAl6V4 dummy stem and reported relatively higher value compare to the recent set of data.[29] Surface damage at the interactive conformal contact within femoral head and cone assembly has recorded under incremental fracture load (see Fig. 6.16 d).

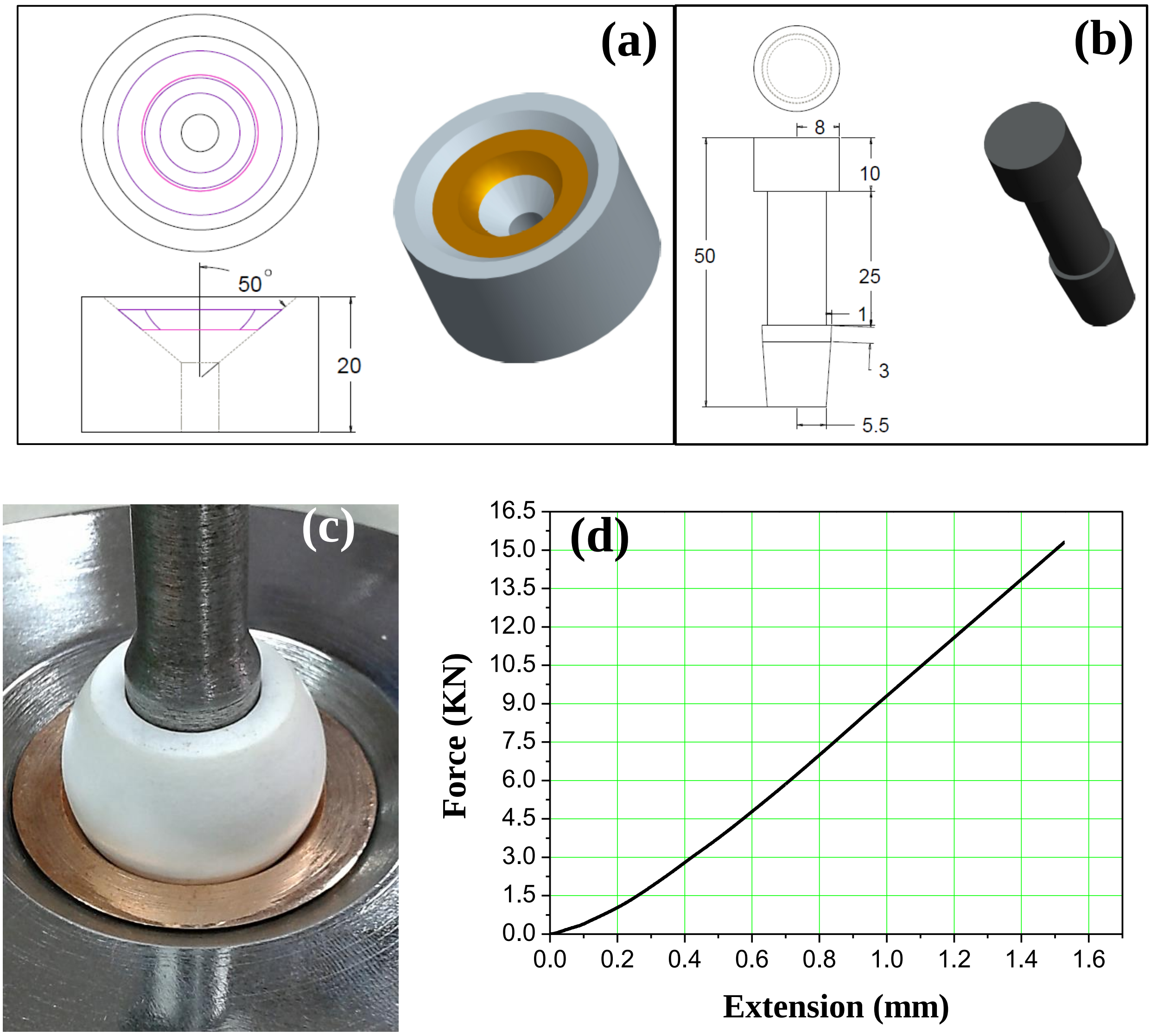

Fig. 6.16**:** Computer aided design (CAD) originated assembly to conduct the burst test, in which (a) bottom base consist of 100° cone according to ISO-7206-10, ZTA femoral head and tapered dummy femoral head, (b) dummy stem to accommodate in blind hole of femoral head during burst test and (c) front view of the assembly prior to conduct the burst strength of fabricated femoral head. (d) force versus displacement plot during burst strength measurement of femoral head. A small deviation in early from linear plot is due to the copper ring.

The inspection of different angle of fracture cleavage after burst test indicates asymmetric four pieces (see Fig. 6.17) resulting from relative displacement during compaction between ball head and mild steel dummy stem. The highest level of tensile stress in service is expected near to taper zone of ceramic femoral head and thus fracture initiate at this inter phase.

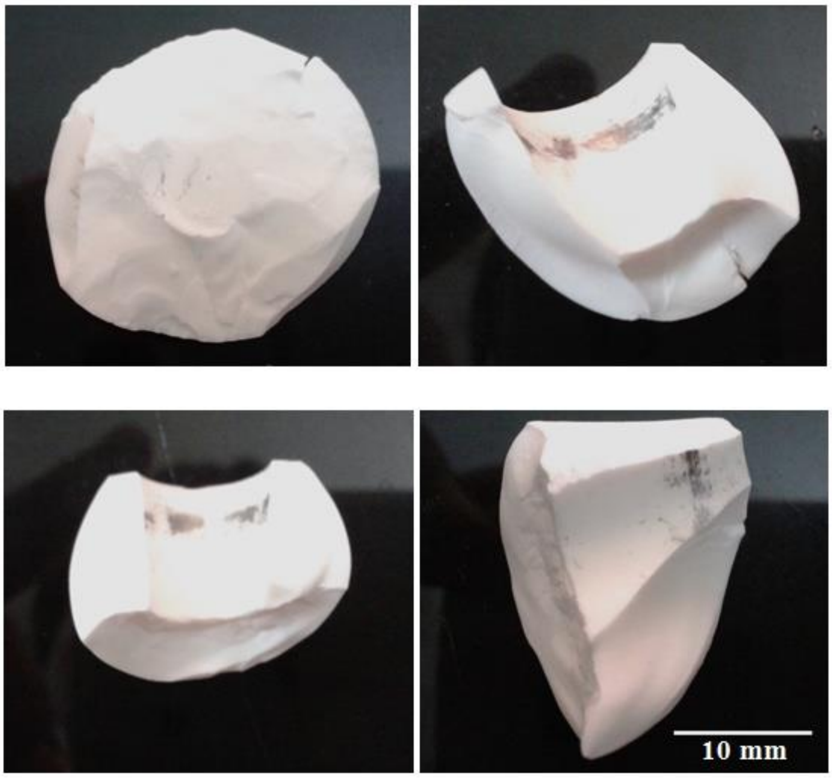

Fig. 6.17: Different mode of exposed fractured surface after performing the burst strength at the peak load of 15.3kN at the loading rate of 1kN/sec.

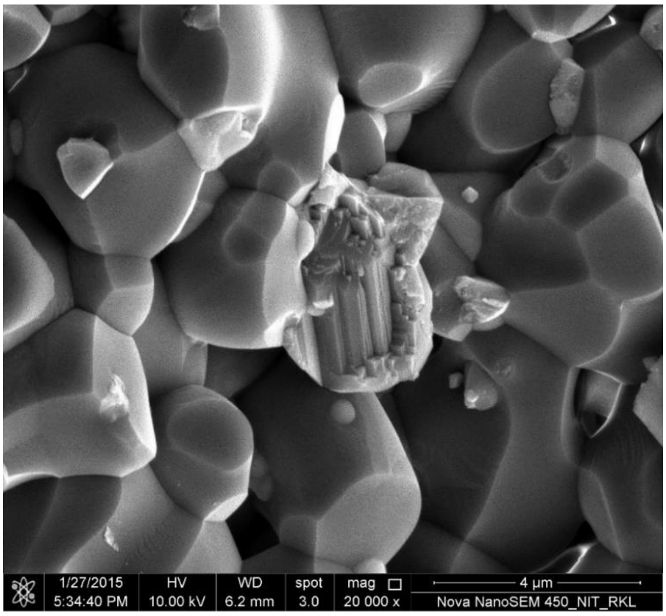

Fig. 6.18**:** Fractograph of femoral head, where different contrast indicates the uniform distribution of zirconia particulate (white) in alumina (gray) matrix.

In recent, this postulation has been confirmed when the surface damage is predominated because of the blind hole cone replacement by a flat plate. The fractured surface micrograph of femoral head after burst strength measurement is represented in Figure 6.17. Microstructure (Figure 6.18) depicts the grains are supposed to follow intergranular and transgranular fracture that is initiated from top of the femoral head under compression mode of loading.

6.6.6 Product validation and significance of current research

6.6.6.1 Zirconia toughened Alumina (ZTA) Femoral head

A representative femoral head and acetabular socket with the tolerance limit of 0.5mm was maintained and represented in Figure 6.19.

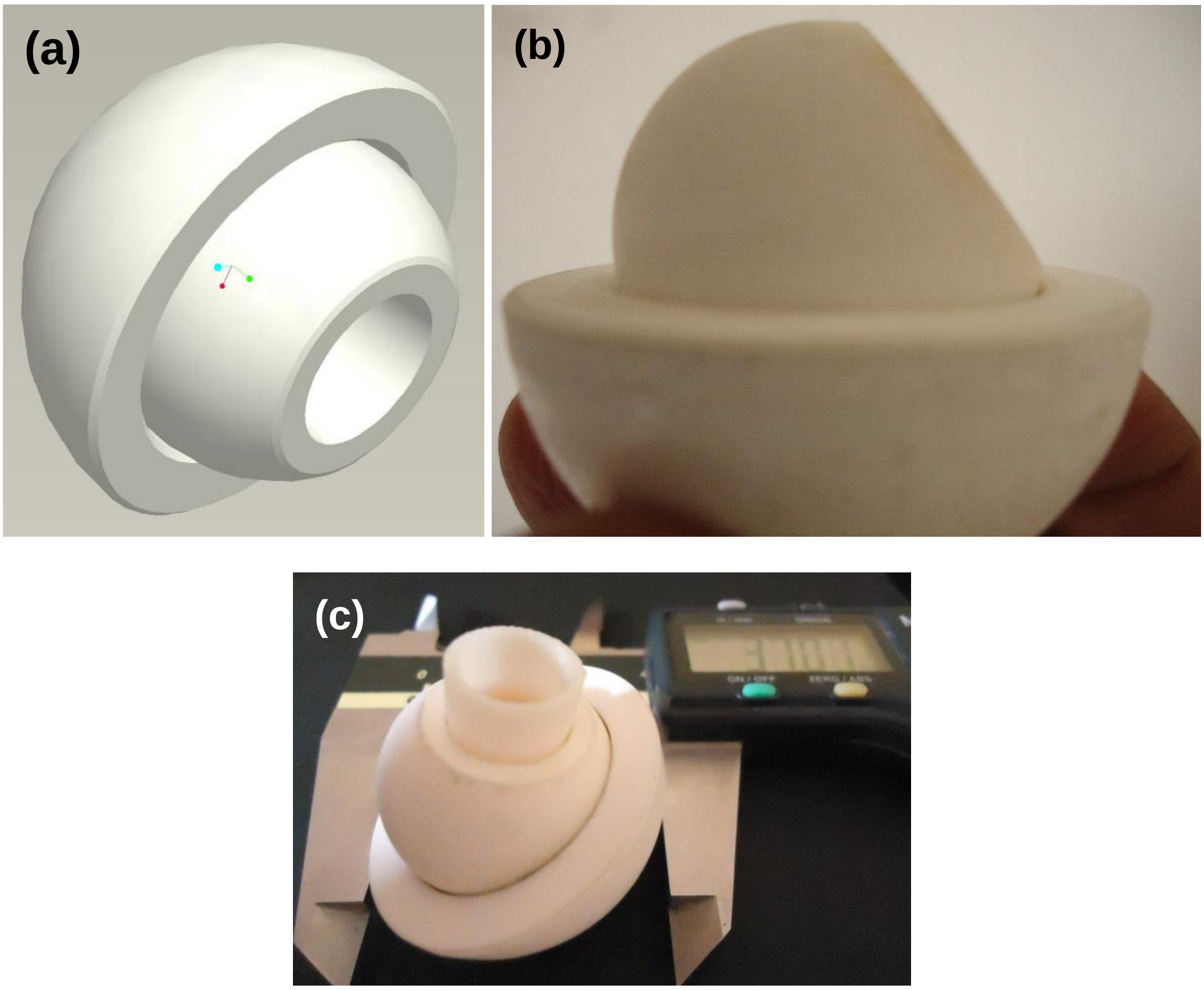

Figure 6.19: CAD originated model (a), sintered both femoral head and acetabular socket prototype in commensurate with the achieved near net shaped dimension as well as the geometrical conformation (b & c). A polymeric (ABS) sleeve analogous to femoral neck shape was inserted to ensure the taper geometry and probable fitting of stem in blind hole.

Fig. 6.19a illustrates the virtual assembly model of femoral head and acetabular cup which were generated through the solid modeling software Pro/E. Similarly, the fabricated ZTA femoral head 26 mm (OD) and acetabular cup 26.5 mm (ID) was assembled THR bearing and different views of assemblies are shown in Fig. 6.19 b and c. As shown in Fig. 6.19, the product assembly elucidate the importance of our research in the perspective of bioimplant prototype development.

6.6.6.2 Zirconia toughened Alumina (ZTA) Acetabular socket

In order to demonstrate the product conformity in reference to dimensional stability and performance for total hip replacement, a set of ZTA ceramic femoral head and acetabular socket and ABS polymer stem prototype have been prepared. As shown in Fig. 6.20, the product assembly elucidate the importance of our research in the perspective of bioimplant prototype development. The details of ZTA based acetabular socket development will be discussed in our coming research publication. An exposed concave surface of acetabular socket with 26.5 mm (ID) demonstrating the ease of accommodating the male part of 26 mm (OD) femoral head,[30] together in geometrical conformity with a polymer prototype femoral stem (see Fig. 6.20 a). In continuation, a short 135 mm in total length of femoral stem was prepared, which consist of different neck geometry to accommodate the blind hole of 26 mm (OD) femoral head (see Fig. 6.20 b).

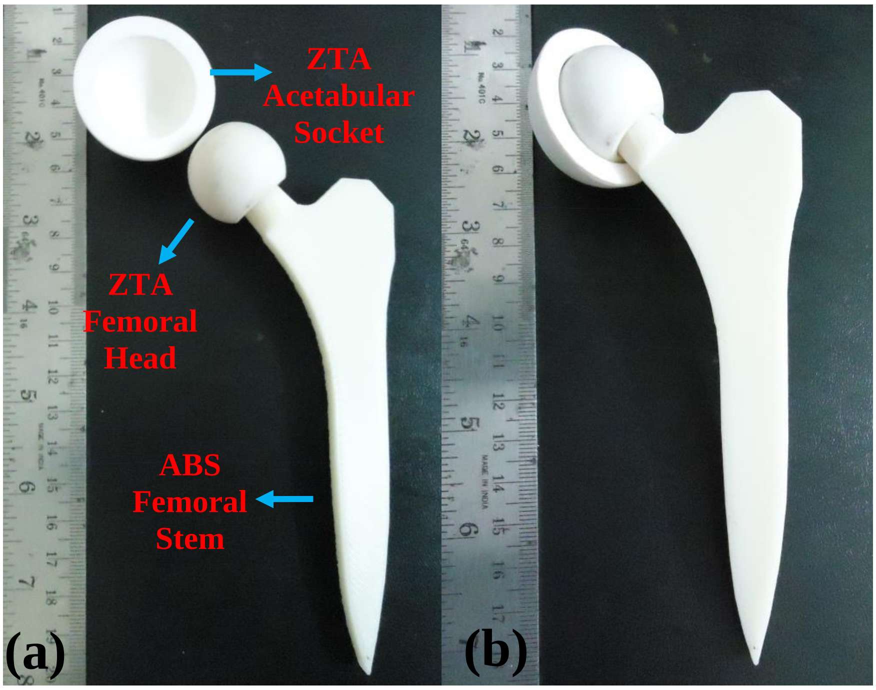

Figure 6.20: A probable THR biomedical devices, where (a) an exposed ZTA acetabular socket and ABS femoral stem (135mm) inserted ZTA femoral head, and (b) complete assembly of ceramic socket – ceramic head including dummy femoral stem of ABS Plus (P430).

Apart from the above described fabrication results for both of the femoral head and acetabular socket, an extensive literature analysis could not reveal any report of the manufacturing of the patient specific femoral ball head and acetabular socket with closely controlled dimensional features as well as good surface finish and material properties. We strongly believe, the adopted fabrication strategy can be implemented in case of other bioceramics with material-specific appropriate change in process parameters. Also, a number of ZTA femoral head and acetabular socket prototypes were reproducibly manufactured using the above-described method and this provides us the confidence that the reported fabrication method is scalable. Apart from these inventions other materials and different processing techniques have also been adopted by several schools and justified the applied research in light of product development concern where multidiscipline knowledge including material science, manufacturing technology, mechanical engineering, and orthopedic biomechanics are essential.

6.7 Conclusions

Based on the design and experiments to develop ceramic prototypes for THR components, we can arrive at the following major conclusions;

a) Using a specially designed cold compaction steel mould from ABS polymer prototype, the green compacts of the femoral head and acetabular socket was obtained at a pressure of 18 - 22 ton.

b) An intermediate manufacturing step of pre-sintering of green compacts at 1200^{o}C for 2hr was found to be useful to impart small scale machining in order to closely control dimensional stability of prototypes.

c) An important result is that the multi-stage sintering of the pre-sintered compact with final holding at 1600^{o}C for 6h could enable us to obtain dense (~98% ρ_{th}) prototypes without any density variation across the component. The sintering conditions were optimized using response surface methodology and were validated at lab-scale experiments to obtain dense samples of similar composition but with much lower geometrical complexity.

d) The detailed surface analysis using optical profilometer confirmed that convex mating surface of femoral head with sub-micron (R_a - 0.2μm) and articulating surface of acetabular socket achieved R_a-0.01μm of surface roughness can be obtained after polishing.

e) The extensive dimensional analysis of the prototypes at various stages of manufacturing ensured a close control over dimensional stability of head with respect to the patient-specific design of respective THR component.

g) The circularity measured using co-ordinate measuring methods also ensured the geometrical conformity of the convex surface of femoral head and acetabular socket within the tolerance limit of ±50μm.

h) Geometrical conformity of the convex as well as concave shape was measured by the co-ordinate measuring method, and ensured that articulating contact between femoral head (26 mm) and acetabular cup (26.5 mm).

Summarising, the present work demonstrates that the adopted manufacturing protocol involving mould design using polymer prototype and optimised pre-sintering as well as multi-stage final sintering successfully fabricated near-net shaped Al_2O_3 - 5wt% ZrO_2 based femoral head with ultra smooth roughness and circularity properties. Although femoral head of 26 mm outer diameter and acetabular socket of inner diameter of 26.5 mm obtained in this work, we believe that the integrated manufacturing approach can be extended to fabricate patient-specific THR components of different geometry and/or different materials.

6.8 References

---

[1] I. Stroud, and P. C. Xirouchakis, “STL and Extensions,” Adv. Eng. Softw., 31, (2) 83-95 (2000).

[2] D. Rypl, and Z. Bittnar, “Generation of Computational Surface Meshes of STL Models,” J. Comput. Appl. Math., 192, 148-151 (2006).

---

[3] M. Szilvśi-Nagy, and G. Y. Matyasi, “Analysis of STL Files,” Math. Comput. Model., 38, 945-960 (2003).

[4] K. Hu, S. Jin, and C. C. L. Wang, “Support Slimming for Single Material Based Additive Manufacturing,” Comput. Aided Design, 65, 1-10 (2015).

[5] Stratasys, MSS_FDM_ABSplusP430.pdf.

[6] Automation Assembly, “Stratasys Adds High-Performance PPSF Plastic,” Assembly Automation, 23, (4) (2006).

[7] K. Thrimurthulu, P. M. Pandey, and N. V. Reddy, “Optimum Part Deposition Orientation in Fused Deposition Modeling,” Inter. J. Mach. Tool Manuf., 44, 585-594 (2004).

[8] M. Korat, and N. Agarwal, “Optimization of Different Machining Parameters of EN24 Alloy Steel in CNC Turning by use of Taguchi method,” Int. J. Eng. Res. Appl. 2, 160-164 (2012).

[9] L. S. Gyger, P. Kulkarni, H. A. Bruck, S. K. Gupta, and O. C. Wilson, “Replamineform Inspired Bone Structures (RIBS) using Multi-Piece Molds and Advanced Ceramic Gelcasting Technology,” Mater. Sci. Eng. C, 27, 646-653 (2007).

[10] A. C. Lin, and N. H. Quang, “Automatic Generation of Mold-Piece Regions and Parting Curves for Complex CAD Models in Multi-Piece Mold Design,” Comput. Aided Design, 57, 15-28 (2014).

[11] B. S. Reddy, D. Sarkar, and B. Basu, “Response Surface Modelling of Sintering Parameter and Compositional Optimization for Zirconia Toughened Alumina Composite,” (Unpublished Data).

[12] S. Mohanty, A. P. Rameshbabu, S. Mandal, B. Su, and S. Dhara, “Critical Issues in near Net Shape Forming via Green Machining of Ceramics: A Case Study of Alumina Dental Crown,” J. Asian Ceram. Soc., 1, 274-281 2013.

[13] L. C. Zhang, E. C. S. Kiat, and A. Pramanik, “A Briefing on the Manufacture of Hip Joint Prostheses,” Adv. Mater. Res., 76, 212-216 (2009).

[14] V. S. Sooraj, and V. Radhakrishnan, “Fine Finishing Of Internal Surfaces using Elastic Abrasives,” Int. J. Mach. Tool Manu., 78 (2014): 30-40.

---

[15] M. R. Sankar, V. K. Jain, J. Ramkumar, and Y. M. Joshi, “Rheological Characterization of Styrene-Butadiene Based Medium and its Finishing Performance using Rotational Abrasive Flow Finishing Process,” Int. J. Mach. Tool Manu., 51, 947-957 (2011).

[16] ISO 7206-10: Implants for Surgery - Partial and Total Hip-Joint Prosthesis: Determination of Resistance to Static Load of Modular Femoral Heads, 2003

[17] S. Begand, T. Oberbach and W. Glien, “Mechanical Properties of Hip Joint Heads Made of the Dispersion Ceramic-Alumina Toughened Zirconia,” Key Eng. Mater., 309, 1257-1260 (2006).

[18] B. S. Reddy, D. Sarkar, and B. Basu, “Response Surface Modelling of Sintering Parameter and Compositional Optimization for Zirconia Toughened Alumina Composite,” (Unpublished Data).

[19] B. Basu, B. S. Reddy, K. Ravikumar, N. Bhaskar, and D. Sarkar, “ZrO_2 toughened Al_2O_3 Biocomposites with Reliable Fracture Resistance and Muscle Cell Compatibility property,” (Unpublished Data).

[20] B. S. Reddy, D. Sarkara, and B. Basu, “Differential wear response of sintered ZrO_2-toughened-Al_2O_3 against ZrO_2 and Steel: influence of load and microstructure,” (Unpublished Data).

[21] D. T. Pham, S. S. Dimov, and R. S. Gault, "Part Orientation in Stereolithography,” Int. J. Adv. Manuf. Tech., 15, 674-682 (1999).

[22] R. Singh, S. Singh, and G. Singh, “Dimensional Accuracy Comparison of Investment Castings Prepared with Wax and ABS Patterns for Bio-medical Application,” Procedia Mater. Sci., 6, 851-858 (2014).

[23] H. Fischer, and R. Marx, "Fracture Toughness of Dental Ceramics: Comparison of Bending and Indentation Method,” Dent. Mater., 18, 12-19 (2002).

[24] D. Chappard, I. Degasne, G. Hure, E. Legrand, M. Audran, and M. F. Basle, “Image Analysis Measurements of Roughness by Texture and Fractal Analysis Correlate with Contact Profilometry,” Biomaterials, 24, 1399-1407 (2003).

[25] J. Gührs, A. Krull, F. Witt, and M. M. Morlock, “The Influence of Stem Taper Re-Use upon the Failure Load of Ceramic Heads,” Med. Eng. & phys., 37, 545-552 (2015).

---

[26] US Food and Drug Administration, "Guidance document for the preparation of Premarket Notification for Ceramic ball hip systems," US Food and Drug Adminstration, Medical Devices 5-3 (2009).

[27] A. Fiorentino, G. Zarattini, U. Pazzaglia, and E. Ceretti, “Hip Prosthesis Design. Market Analysis, New Perspectives and an Innovative Solution,” Procedia CIRP 5 310-314 (2013).

[28] C. Affolter, B. Weisse, A. Stutz, S. Köbel, and G. P. Terrasi, “Optimization of the Stress Distribution in Ceramic Femoral Heads by Means of Finite Element Methods,” Proceedings of the Institution of Mechanical Engineers, Part H: J. Eng. in Med. 223, (2) 237-248 (2009).

[29] U.S. Food and Drug Administration (http://www.accessdata.fda.gov/cdrh_docs/pdf3/P030022b.pdf)

[30] D. Sarkara, B. S. Reddy, S. Mandal., D.C. Sundaresh, B. Basub, “A Novel Manufacturing approach to Fabricate Near-Net Shape Femoral Head of ZrO_2-toughened-Al_2O_3,” (Unpublished data).

Chapter 7

Summary and Future Scope of Work

This concluding chapter summarises the key points of this dissertation. All the four proceeding chapters individually have a conclusion section and therefore this chapter briefly reiterates some of these important points to provide readers a final outlook. The scope for future work is also highlighted. Overall, the research results of this dissertation have major implication for human health care and in particular, for load bearing component (femoral head and acetabular socket) in total hip replacement to improve the functionality and life of the prosthesis.

7.1 RSM of process optimization

This dissertation demonstrates the robustness of response surface methodology (RSM) approach to quantitatively establish the optimised sintering and material parameters of ZrO_2-toughened Al_2O_2 with ultrafine microstructure and properties.

i) In accordance with response surface method, the predicted sinter density and grain size computed at five different levels of process and material variables follows linear statistical correlation with the experimentally obtained average grain size and relative density data.

ii) Sinter density (>98%) of the ZTA composite is highly influenced by the temperature than other parameters, whereas, temperature and ZrO_2 content have more effect on the Al_2O_3 grain size (3.2μm).

iii) Concerning the interaction variables, sintering temperature and sintering time significantly influenced the sinter density. The interaction of sintering temperature and sintering time followed by sintering time and ZrO_2 addition has a larger effect on grain size than other combination of investigated parameters.

7.2 Mechanical and Tribological properties

For load bearing orthopedic application (articulating joints), the potential materials need to have the designed combination of mechanical and tribological properties. This constitutes an important part of the present dissertation.

i) The present work also establishes that Al_2O_3 – 5 wt.% ZrO_2 – 800 ppm MgO can exhibit the best combination of a wide spectrum of reliable mechanical properties, including long crack SEVNB fracture toughness (4.3 MPa.$m^{1/2}$), compressive strength (1100 MPa), tensile strength (213 MPa) and hardness (19.3 GPa).

ii) Concerning the tribological properties, the load dependence of frictional behavior is more apparent for ZTA/ZrO_2 sliding couple than ZTA/steel. A better sliding wear resistance with wear rate varying in the range of 10^{-9} mm^3/Nm can be achieved with ZTA/ZrO_2 and in contrast, a negative wear rate for ZTA/steel.

iii) Abrasive wear was found to be the predominant mode of wear mechanism for ZTA/ZrO_2. In contrast, adhesive wear plays a major role in case of ZTA/steel.

iv) The critical damage stress is found to be larger than the maximum tensile stresses at the trailing edge of sliding contact on ZTA, when worn against ZrO_2.

7.3 *In vitro* cytocompatibility properties

In view of the predominant significance of biocompatibility property, some *in vitro* cell culture experiments were also conducted and muscle cells were grown on ZTA for different time points of upto 3 days in culture.

i) In reference to cytocompatibility (*in vitro* biological response), MTT results confirm that the ZTA composite with the best combination of mechanical properties can support the growth of mitochondrially viable mouse myoblast cells (muscle cells) *in vitro* with the viability increasing in statistically significant manner for a period of 72h in culture.

ii) The fluorescence microscopic observations support the evidence of good cell to cell and cell to substrate attachment, cell spreading, cell elongation and cytoskeletal rearrangement and alignments of the adhered cells leading to cellular bridge formation. All these observation together indicate good cytocompatibility property of optimized composites.

7.4 Design and Prototype Fabrication

Despite several decades of research for new materials for articulating joints in orthopedic applications, the efforts to develop patient-specific prototype of such biomaterial devices are rather limited.

(i) While addressing this aspect, the present work demonstrates an integrated manufacturing approach to fabricate femoral head and acetabular socket prototypes of zirconia-toughened alumina (ZTA) with specific composition (Al_2O_3-5 wt% ZrO_2 (3 mol % Y_2O_3 stabilised)).

(ii) In commensurate with the computer aided-design (CAD) of the patient-specific prototype, the custom made modular steel-die mould assembly was utilised to obtain high strength green powder compact without any geometric distortion.

(iii) The process quality was closely monitored by measuring dimensional changes at each stage as well as the circularity measurement of final polished prototype. Apart from measuring a robust combination of hardness and reliable fracture toughness, the burst strength, one of the key performance-limiting property, was measured and the as-fabricated femoral head exhibits a value of 15 kN, with the fractographs revealing characteristic features as those of fractured femoral heads, *in vivo*.

(iv) The extensive analysis confirms homogeneous distribution of ZrO_2 across the volume of the defect-free prototype. Furthermore, details dimensional and microstructure analysis enables us to understand the influence of processing technique on the resulting microstructure. Taken together, the present processing approach appears to be a scalable and commercially viable fabrication strategy to develop near-net shaped bioceramics based femoral ball head for total hip joint replacement surgery.

Summarising, the present work demonstrates that the adopted manufacturing protocol involving mould design using polymer prototype and optimised pre-sintering as well as multi-stage final sintering successfully fabricated near-net shaped Al_2O_3 - 5wt% ZrO_2 based femoral head with ultra smooth roughness and circularity properties. Although femoral head of 26 mm outer diameter and acetabular socket of 26.5 mm inner diameter was obtained in this work, we believe that the integrated manufacturing approach can be extended to fabricate patient-specific THR components of different geometry and/or different materials.

7.5 Future Scope of work

In the following, some of the immediate aspects to be pursued in a follow up work are highlighted.

7.5.1 To enhance the fracture toughness of ZTA

In the present dissertation, 3 mol% Y_2O_3-stabilised ZrO_2 was used as a reinforcement to Al_2O_3. In future, the ZrO_2 particle dopant composition can be tailored w.r.t. amount and distribution so that K_{IC} can be enhanced further. It is expected that such strategy can be adapted to obtain ZTA femoral head with better burst strength.

7.5.2 To assess the change of wear rate with Zirconia addition

An optimized (95wt%Al_2O_3-5wt%ZrO_2-800ppmMgO) ZTA composition has been chosen in order to develop the bioimplants. However, a basic understanding on the wear behaviour can be done with variation of zirconia content in alumina matrix.

7.5.3 To assess *in vitro* tribological behaviour using HIP simulator

Different physical properties, like hardness, fracture toughness, and compressive strength are already reported in this thesis. The *in vitro* tribological study should be carried out on the polished surface against highly cross-linked UHMWPE using HIP simulator.

7.5.4 To study the *in vivo* osseointegration in rabbit model

The optimized composition needs to be further implanted into femoral defects in rabbit animal model. In rabbit animal model, the osseointegration will be quantified using micro CT analysis. After the hip simulator study, ZTA femoral ball head against UHMWPE socket for upto 5 million cycles, the cytotoxicity of the wear debris particles needs to be analyzed using bone cells.

7.5.5 Clinical trials on ZTA prototype

After the successful completion of the above aspects, limited clinical trials in human patients at a single institute followed by multi-institutional clinical trials are to be pursued after obtaining necessary ethical clearances. This will pave the way for the commercialisation of ZTA based femoral head and acetabular sockets.

In practice, the current 26mm femoral head and relative acetabular socket is commercial available product that are using for patient specific demand. In obvious the developed technology can be implemented for any patient specific use in future.

Curriculum Vitae

Name: Bhimavarapu Sambi Reddy
Permanent Add: 3-174/A, Gundimeda,
Via. Nutakki, Guntur, Andhra Pradesh 522303
Ph: +91-9493041090
E-mail: bsreddy.design@gmail.com

Date of Birth: 11th July, 1982

Academic Credentials

- Ph.D. Department of Ceramic Engineering from National Institute of Technology Rourkela, 2012 – till date.
- M. Tech in Design Engineering 2008 from Kakatiya Institute of Technology & Science, Warangal.
- BE in Mechanical Engineering 2004 from Sri Padmavathi College of Engineering, Kanchipuram, Madras University
- Diploma in Mechanical Engineering 2001 from VKR & VNB Polytechnic College, Gudivada, SBTET, Hyderabad.
- SSC 1997 from Aravinda High School, Kunchanapalli, Board of Secondary Education, Hyderabad.

Research Interest: Product Design and Development in Engineering field.

Publications and Patents

Patents:

1. D. Sarkar, B. S. Reddy, D. C. Sundaresh, B. Basu, *Design and prototype development of near-net shaped uniaxial pressed ceramic femoral head and acetabular socket*, Indian patent No. 201641004257, 5th Feb, 2016.

Publications:

1. Bhimavarapu Sambi Reddy, Debasish Sarkar, Bikramjit Basu, *Response Surface Modeling of Sintering Parameter and Compositional Optimization for Zirconia Toughened Alumina Composite*, submitted to Acta Materialia. Manuscript number: A-16-189.
2. Bikramjit Basu, Bhimavarapu Sambi Reddy, NituBhaskar, Debasish Sarkar, *ZrO_2-toughened Al_2O_3 biocomposites with reliable fracture resistance and muscle cell compatibility property*, submitted to Journal of the American Ceramic Society. Manuscript ID: JACERS-38040.
3. Bhimavarapu Sambi Reddy, Debasish Sarkar, Bikramjit Basu, *Differential wear response of sintered ZrO_2-toughened-Al_2O_3 against ZrO_2 and Steel: influence of load and microstructure*, submitted to Journal of the European Ceramic Society. Manuscript number: JECS-D-16-00097.
4. Debasish Sarkar, Bhimavarapu Sambi Reddy, D.C. Sundaresh, Bikramjit Basu, *An Integrated Manufacturing approach to Fabricate Patient-specific Near-Net Shape Femoral Head of ZrO2-Toughened-Al2O3*, submitted to Acta Materialia. Manuscript number: A-16-594.
5. Bhimavarapu Sambi Reddy, D.C. Sundaresh, Bikramjit Basu, Debasish Sarkar, *Patient-specific near-net shaped ZrO2-toughened Al2O3-based acetabular socket for total hip replacement surgery*, submitted to Advanced Engineering Materials. Manuscript number: 201600250. (Accepted).